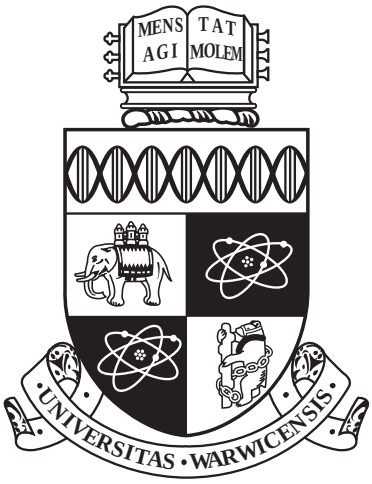

Investigation of the Structure of the Perovskite System (1-x)BiFeO3-(x)(K0.5Bi0.5)TiO3

by

Daniel William Nye

Thesis

Submitted to the University of Warwick

for the degree of

Doctor of Philosophy

Physics

July 2017

THE UNIVERSITY OF
WARWICK

Contents

List of Tables

List of Figures

Acknowledgments

I would like to start by thanking my supervisor, Professor Pam Thomas, for the opportunity to conduct this PhD and for the extremely helpful meetings we have had over the years - I've always walked away with a much better understanding of where I'm going with my research and with the motivation to get there. These have been especially useful given some of the very interesting results gathered regarding the BFO-KBT system!

Some of the powders used and the room temperature measurements made on those powders were produced by a pair of project students, K. Zahra and S. M. Johari, and I'd like to thank them for their contributions. In addition, the BFO-KBT crystals were received by Pam from Noguchi's group at the University of Tokyo, without which the single crystal measurements would not have been possible, but I was unable to find a paper on their synthesis to reference. The KBT crystals were made by Dr. G. Jones, a previous student here and the BFO crystals were received from Prof. M. Alexe in the department, so I would also like to extend my gratitude for the opportunity to experiment with these materials.

I am also extremely grateful for all the help given to me by Dr. Steven Huband, who has really gone above and beyond in helping me rapidly shift from the project initially envisaged for my PhD (which was a study into photostriction in BFO) to the current form, both showing me the ropes of various techniques used in this thesis which I hadn't used before and being on hand to be perplexed by some of the results with me and then suffering through reading sections of my thesis for his trouble. There are some people thanked here I feel I owe a drink; by that metric, I probably owe Steve approximately a distillery. He may have to settle for

a multipack though.

I'd also like to thank Dr. David Walker for all his help understanding the equipment, the measurements and the programs related to them,
and Dave Hammond for sorting them out whenever they went wrong, and his help with the thermal analysis and mass spec. measurements. I'd like to thank Dr. Dean Keeble for his initial help on starting my PhD, guidance in the initial photostriction studies and most recently his help in the single crystal experiments at Diamond Light Source. I'd like to thank Dr. Iain Dunn for joining our regular research meetings and being enjoyable company in the office.

I'd like to thank my friends for all of their support, especially Ben and Heather Hall who gave up part of their New Years Eve and New Years Day to help copy edit the whole of my thesis (Don't worry; there was a break in between) and certainly are owed one of the aforementioned drinks. I'd like to thank my housemates, especially Dan Cook, with whom I have had many late night crystallography discussions. I'd like to thank the Comedy Society at Warwick for a good laugh, back when I had free time.

Finally, I'd like to thank my family for all of their support (and financial aid), without whom I wouldn't have had the chance to finish.

This thesis was typeset with LaTeX 2_ε[1] by the author.

[1] LaTeX 2_ε is an extension of LaTeX. LaTeX is a collection of macros for TeX. TeX is a trademark of the American Mathematical Society. The style package *warwickthesis* was used.

Declarations

I declare that the work contained in this thesis is my own, except where stated otherwise (Specifically, several samples were prepared by project students, K. Zahra and S. M. Johari, who also took the room temperature powder x-ray diffraction measurements for those same samples. These samples are explicitly pointed out in the text. In addition, the thermal and mass spectroscopy measurements were set up by David Hammond). This work was carried out in the physics department at the University of Warwick between October 2012 and January 2017 under the supervision of Prof. Pam Thomas. The research reported here has not been submitted wholly or in part for consideration as part of another higher degree at this institution or any other.

It is planned that some parts of the research contained within will form part of several papers to be submitted in the future.

Abstract

The (1-x)$BiFeO_3$-(x)$(K_{0.5}Bi_{0.5})TiO_3$ (BFO-KBT) system has been investigated with respect to composition and temperature. Powder samples have been synthesised by the traditional solid state method at regular intervals across the compositional range. High resolution powder x-ray diffraction measurements have been made on these powders between room temperature and up to 950°C. The data from these measurements have been analysed by the Rietveld method, and the results of these refinements have been used to construct a phase diagram of the BFO-KBT system.

It was found that there are no sharp transitions in the phase diagram, either with composition or with respect to temperature, and that aside from the BFO end member, all samples investigated were best fitted with a mixed phase model. At low mol% KBT, it was found that the mixed phase model that best described the system was a mix of rhombohedral $R3c$ and cubic $Pm\bar{3}m$. As the mol% KBT was increased, the cubic phase increased, becoming dominant between 15% KBT and 20% KBT. The rhombohedral phase diminished with increasing mol% KBT and was no longer a component in the mixed phase system beyond 60% KBT. At 70% KBT, the room temperature system could still not be modelled with a single phase. A mix of cubic $Pm\bar{3}m$ and monoclinic $P1m1$ was used to model the system. At 90% KBT, the model was again found to be best fitted by a different mix of phases, specifically a mix of monoclinic $P1m1$ and tetragonal $P4mm$ phases were used to model the data. The tetragonal phase was found to become more dominant from this point with increasing mol% KBT, but even the KBT end member was found to be best modelled with a mix of monoclinic $P1m1$ and tetragonal $P4mm$ phases.

It was found that all samples become more cubic with increasing temperature. It was found that the temperature at which the change to a cubic state occurred decreased with increasing mol% KBT. It was also found that at high mol% KBT and high temperature, there was phase separation into a two-cubic mixed phase model instead of the expected single $Pm\bar{3}m$ cubic phase. This phase separation has been linked to the reported morphotropic phase boundary in the material. The BFO-KBT system was found to change little with respect to temperature below 500°C, which makes it an attractive material for high temperature device applications if doped with a material with a stronger piezoelectric response.

In addition, single crystal x-ray diffraction of BFO-KBT crystals has been undertaken with laboratory-based and synchrotron systems. It was found that the latter was necessary to obtain good results from a refinement of the data in SHELXL due to the absorption of the BFO-KBT system, minimised through the use of a much higher energy x-ray beam. It was found in JANA2006 that the BFO-KBT system was best fit with anharmonic atomic displacement parameters, which was linked to the difference between the short range and long range order in the material.

Abbreviations

ADP	Atomic Displacement Parameter
BFO	Bismuth Ferrite, $BiFeO_3$
BFO-KBT	(1-x)$BiFeO_3$-(x)$(K_{0.5}Bi_{0.5})TiO_3$
hkl	Miller indices
KBT	Potassium Bismuth Titanate, $(K_{0.5}Bi_{0.5})TiO_3$
MPB	Morphotropic Phase Boundary
PZT	Lead Zirconate Titanate ($Pb(Zr_xTi_{1-x})O_3$)
XRD	X-Ray Diffraction

An x-ray haiku:
Diffraction techniques
Atomic decorations
The ray is no more

Chapter 1

Introduction

This investigation is interested in the structure of the (1-x)$BiFeO_3$-(x)$(K_{0.5}Bi_{0.5})TiO_3$ system, investigating based on powder x-ray diffraction (powder XRD) experiments and single crystal x-ray diffraction (single crystal XRD) experiments.

In this chapter, the concepts underpinning these investigations are introduced, along with an in depth discussion of the literature regarding bismuth ferrite ($BiFeO_3$, BFO), bismuth potassium titanate ($(K_{0.5}Bi_{0.5})TiO_3$, KBT) and the (1-x) $BiFeO_3$-(x) $(K_{0.5}Bi_{0.5})TiO_3$ (BFO-KBT) solid solutions that comprise the bulk of this thesis. The theory behind the experimental techniques used on the materials to build the phase diagram and probe the structure of BFO-KBT are described in Chapter 2.

One of the major focuses of this thesis is the creation of a temperature-composition phase diagram for the material. This is achieved by first investigating the changes present with respect to composition at room temperature through powder XRD, analysed with Rietveld refinement techniques (Chapter 3), then expanding this work to investigate with respect to temperature (Chapter 4). This is then further investigated with single crystal XRD (Chapter 5), before the final conclusions are drawn in Chapter 6.

1.1 Crystal Structure

A crystal is a periodic 3-D arrangement of atoms represented by a unit cell that repeats in space to make up the whole crystal structure. The periodic repetition of the cell is given by the lattice function, which is an underlying mathematical construct. There are 7 crystal systems, as displayed in Table 1.1.

The way in which the peaks in a powder XRD pattern are split can be

Table 1.1: The seven crystal systems.

Structure	Defining symmetry	Lattice parameter constraints	Split Peak {100}	Split Peak {110}	Split Peak {111}
Cubic	Four intersecting 3-fold rotations (or $\overline{3}$-axes)	$a = b = c$, $\alpha = \beta = \gamma = 90$			
Tetragonal	One four-fold rotation (or $\overline{4}$-axis)	$a = b \neq c$, $\alpha = \beta = \gamma = 90$	✓	✓	
Trigonal	One three-fold rotation (or $\overline{3}$-axis)	$a = b \neq c$, $\alpha = \beta = 90, \gamma = 120$		✓	✓
Hexagonal	One six-fold rotation (or $\overline{6}$-axis)	$a = b \neq c$, $\alpha = \beta = 90, \gamma = 120$		✓	✓
Orthorhombic	Two-fold rotation or mirror plane or both along each axis	$a \neq b \neq c$, $\alpha = \beta = \gamma = 90$	✓	✓	
Monoclinic	One two-fold rotation or mirror plane	$\alpha = \gamma = 90, \beta \neq 90$	✓	✓	✓
Triclinic	No defining symmetry	unrestricted	✓	✓	✓

used to eliminate possible single structures, so these have been highlighted for the {100}, {110} and {111} peaks in Table 1.1. Whether the peaks are split or not depends on the differences in the lattice parameters; where the parameters are the same, they will be overlapped in a powder XRD measurement, so will not be split. While the exact nature of these split peaks are more subtle than the binary yes/no presented here, this is sufficient for eliminating crystal systems from being able to fully model the observed data. This also becomes more complicated when multiple phase structures are present, as is often found in mixed perovskite materials or impure samples.

1.1.1 Cubic Perovskite Cell

A perovskite is a material of the form ABX_3, where in general A is a large metal cation, B is a smaller metal cation and X_3 is oxygen for oxide structures (such as those considered in this thesis) but can also be other materials, such as fluorine. As the materials considered here are all oxides, for the rest of this thesis a structure of ABO_3 will be assumed (which is also the most common perovskite form). These atoms are arranged such that in the $Pm\overline{3}m$ cubic perovskite cell, the
A-site represents the corners of the cube, the B-site represents the body-centre of the cell and the O-site appears in the centre of each cubic face, forming an octahedron around the B-site, shown in Figure 1.1 [1].

From this cubic cell, deformations or distortions can be used to construct other cells. At high temperature, most perovskites will form the $Pm\overline{3}m$ cubic perovskite cell with $a \approx 3.8$Å [2], but at lower temperatures many will form other

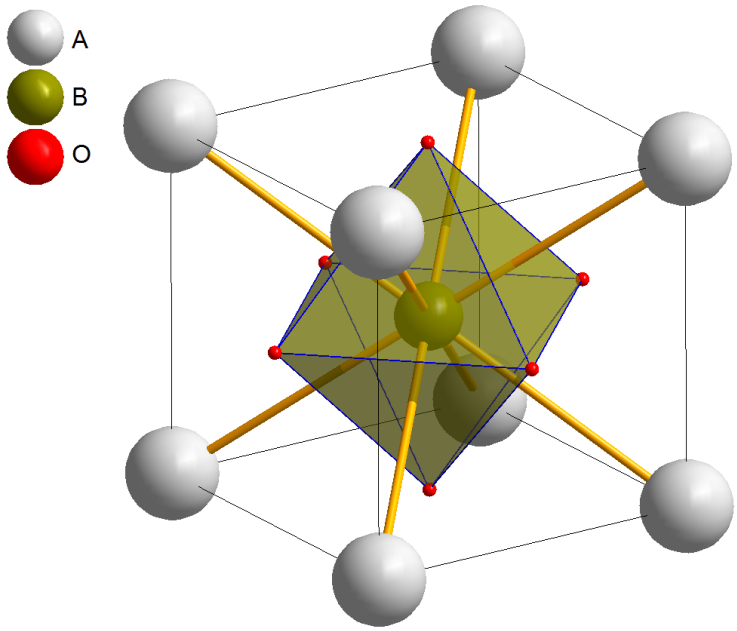

Figure 1.1: An idealised $Pm\bar{3}m$ cubic perovskite cell. The B-site is in the centre of the octahedron formed by the O-sites, and the A-sites are at the vertices of the cell.

structures, such as $R3c$, $P1m1$ or $P4mm$ cells, which will be seen later in this thesis, in Chapter 3 and Chapter 4.

1.2 Piezoelectricity

All crystals can be classified as being one of the 32 crystal classes, which are subsets of the crystal systems dscussed in Table 1.1; this corresponds to the 32 crystal point groups, defined by symmetry operations. Of these crystal classes, 21 are noncentrosymmetric, meaning that they do not have inversion symmetry. Of those noncentrosymmetric classes, 20 are piezoelectric; in crystals of these classes an electrical charge is produced in response to a mechanical deformation, and inversely, when under the influence of an electric field the crystal will undergo a mechanical deformation [3]. The piezoelectric effect and the inverse piezoelectric effect are important properties for device applications, with a larger deformation per unit charge being preferable.

1.2.1 Ferroelectrics

Of the piezoelectric classes, 10 are pyroelectric, meaning that they are spontaneously polarised when varied with temperature. Of those pyroelectric materials, some are

ferroelectric, meaning that the polarisation can be reversed through the application of an electric field. Ferroelectrics are thus a subset of pyroelectric materials, which are a subset of piezoelectric materials, so all ferroelectrics show both piezoelectric and pyroelectric properties, but the converse is not necessarily true [4].

At high temperature, room temperature ferroelectric perovskites are all of centrosymmetric cubic structure and thus paraelectric (so are no longer ferroelectric). However, as the temperature is decreased, many of these materials will undergo a distortion to a lower symmetry structure, such as rhombohedral $R3c$ or tetragonal $P4mm$. The temperature at which this transition occurs is known as the Curie temperature, T_C. It is below this temperature that ferroelectric properties manifest, as the lower symmetry structure can be reversibly spontaneously polarised. In addition, the dielectric and piezoelectric properties of the material are enhanced in the region of T_C [5].

1.2.1.1 Relaxors

Relaxor ferroelectrics (often just called 'relaxors') were discovered in the 1950's [6] and display interesting properties for a ferroelectric material, notably an extremely broad distribution of relaxation times. In the radiofrequency range, the dielectric response in a relaxor is significantly wider than that of a traditional ferroelectric. These result from the nano-structure of the relaxor, which consists of polar nanoclusters in a highly polarisable neutral matrix [7]. Thus, relaxation times are distributed widely as a result of the nano-structure. The nanoclusters are smaller than the domains found in traditional ferroelectrics (no larger than 500Å, so unable to be discerned by x-ray powder diffraction or x-ray single crystal diffraction experiments), and their sizes are roughly equal to one another at any given temperature. As these nanoclusters grow with decreasing temperature, they are able to coalesce and form true ferroelectric domains [8]. The local, nanometre-scale structure of a relaxor is quite different from the long range, or even the micrometre-scale range structure, which are essentially an average of the nanostructure. This means that relaxors generally appear to be cubic, or near cubic, in terms of long range order.

At high temperatures, as in normal ferroelectrics, relaxors form a non-polar paraelectric phase. At a temperature, known as the Burns temperature (T_B), they begin to exhibit relaxor properties, entering an ergodic state (i.e. all possible microstates are equally probable) in which polar regions of randomly orientated and distributed directions of dipole moments appear.

For a relaxor to form, there must exist a highly polarisable neutral matrix;

in other words, it is not currently polarised but easily can be. This neutral matrix must have a high dielectric constant, such as is found in perovskite structures. The neutral matrix determines whether the mobile nanodomains will coalesce into a true ferroelectric (known as percolation, occurring at a temperature T_p) at some non-zero temperature, or whether the relaxor will show relaxor properties down to T = 0K. The percolation temperature, T_p is significantly lower than the Burns temperature. Relaxors do not show a macroscopic change in structure at the transition temperatures as normal ferroelectrics do at the Curie temperature (T_C); in relaxors, this phenomenom does not constitute a structural phase transition [7, 9].

Relaxors have been found to exhibit giant electromechanical properties such as piezoelectricity when compared with regular ferroelectrics, which have often been linked with the morphotropic phase boundary found in the perovskite solid solutions that many relaxors are comprised of [7]. Morphotropic phase boundaries are discussed further in Section 1.3.

1.3 Morphotropic Phase Boundaries

In order to understand the idea of a morphotropic phase boundary, it is helpful to first introduce the idea of phase transitions, specifically with respect to temperature and with composition.

1.3.1 Phase Transitions

A phase transition is the way in which one phase becomes another, and is applied in a wide variety of situations; for example, when a material is heated from a solid to a liquid, or when a material is heated from a ferroelectric state to a paraelectric state, which occurs at T_C. Phase transitions take multiple forms, which are described by Landau Theory [10] and others.

In Landau theory an order parameter η is used to describe the breaking of the symmetry present at high temperature. At high temperature, $\eta = 0$, but becomes finite at T_C, increasing from that point as the temperature is further lowered. The nature of the change in η at T_C defines what order of phase transition is present. Figure 1.4 shows a comparison of an idealised first order phase transition (Figure 1.2a) and second order phase transition (Figure 1.2b), showing the way in which η changes with increasing temperature. A discontinuity at T_C, demonstrated in Figure 1.2a, indicates a first order phase transition. In such a transition, both states are present at once, i.e. there is coexistence of the state expected at temperatures $>T_C$ and $<T_C$ at the same time, with the mixing decreasing the further from T_C

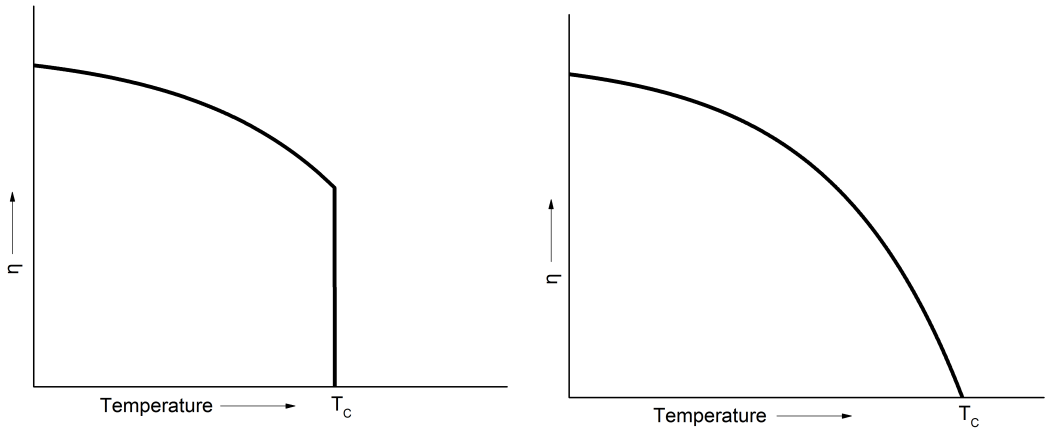

(a) First Order Phase Transition **(b)** Second Order Phase Transition

Figure 1.2: First order phase transition (Figure 1.2a and second order phase transition (Figure 1.2b). The graphs show η vs a parameter with which the system changes.

the material gets. A continuous change, demonstrated in Figure 1.2b, indicates a second order phase transition. In a second order phase transition, there is no mixing of states.

1.3.1.1 Compositionally Driven Phase Boundaries

While phase transitions are often considered in terms of temperature, it is also possible to form materials with phase transitions that are relative to the composition. Perovskites are of particular note here, as mixing multiple perovskite structures together in a solid solution will generally result in a perovskite structure with fractionally occupied A-site and B-site positions based on the composition of the material. This can give rise to Morphotropic Phase Boundaries, which require that a material have phase transitions as a function of temperature and composition.

1.3.1.2 Morphotropic Phase Boundary

A Morphotropic Phase Boundary (MPB) may exist in materials with both a compositionally driven phase transition and a temperature driven phase transition. The term is mostly used to refer to perovskite solid solutions with a tetragonal end member and a rhombohedral end member [11]. In order to be considered an MPB, the compositionally driven phase boundary must be nearly vertical with respect to temperature, meaning that until a further phase transition to a more ordered system, the material will display phase transition properties at this composition irrespective of temperature [12]. The phase transition itself is an abrupt one. Since

the dielectric properties and the piezoelectric properties of the material are enhanced at the MPB [13], this provides a very attractive option for device applications such as electrostrictive actuators, where getting the most efficient dielectric and piezoelectric properties possible is important and such a phase transition will mean that the properties are maintained even at high temperatures. While the change in structure across an MPB is abrupt [14], measurements of the local atomic structure by Egami *et al.* [15] have shown signs of smooth local changes across the transition, similar to those found in lead zirconate titanate [16].

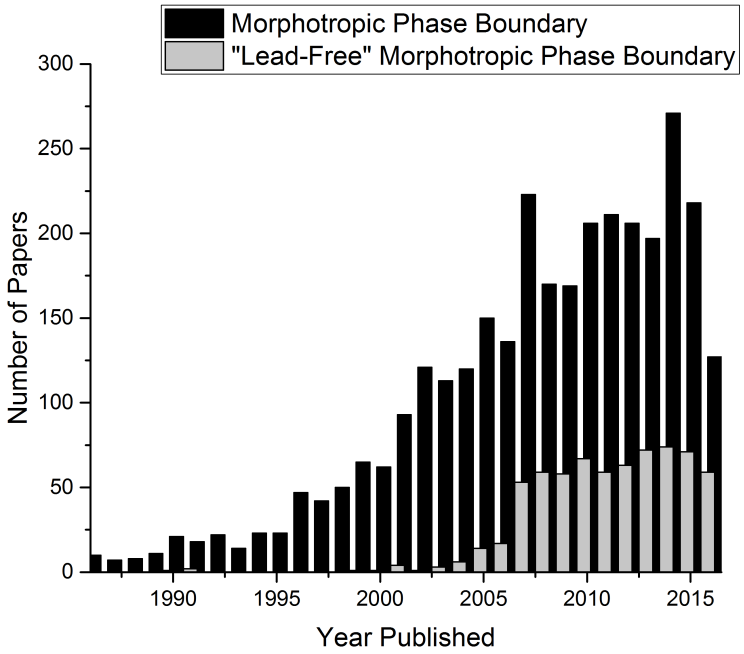

Figure 1.3: Number of papers published by year with the stated words existing in the title, abstract or keywords (as searched on Web of Science in Sept. 2016).

Figure 1.3 shows the rate of papers being published on the subject of Morphotropic Phase Boundaries and Lead Free Morphotropic Phase Boundaries over the last 30 years. From this, it can be seen that the interest in MPBs is increasing steadily, and that interest in lead-free materials containing MPBs is still an area of much interest,as discussed in more detail in Section 1.3.2.1.

MPBs found so far have exhibited a second order phase transition [17], though a first order phase transition is possible. A Polymorphic Phase Boundary (PPB) can appear similar to an MPB, but unlike MPBs, PPBs have a significant variance in phase transition temperature with respect to composition, i.e. the phase transition lines are not vertical on a composition-temperature graph [18].

1.3.2 Lead Zirconate Titanate

Lead Zirconate Titanate ($Pb(Zr_xTi_{1-x})O_3$, PZT) is considered to be the archtype MPB material, the phase diagram first investigated by Shirane and Takeda [19]. Jaffe [20] discovered the increase in piezoelectric properties at the MPB, and as such analysis of a material exhibiting an MPB tends to include comparison with PZT. PZT is widely used in piezoelectric devices because of its extremely good piezoelectric properties around the MPB.

Early phase diagrams, such as Figure 1.4a showed a direct transition from $R3m$ to $P4mm$ at the MPB [21], but it was found that an intermediate monoclinic phase existed in a narrow compositional range at the MPB [22], confirmed with alternative methodologies such as infrared spectroscopy [23], as shown in Figure 1.4b. Since then, more analysis has been conducted on the exact nature of the MPB in PZT, with discussions about the difference between local and average order in the material, especially around the MPB [24], and investigations into changes in tilt to determine the specific structure of the material around the MPB [16, 25, 26] also reported.

In PZT, the rhombohedral end member is $R3c$, but closer to the MPB the rhombohedral phase is reported as $R3m$. The tetragonal phase is $P4mm$ and the monoclinic phase is $C1m1$ [26].

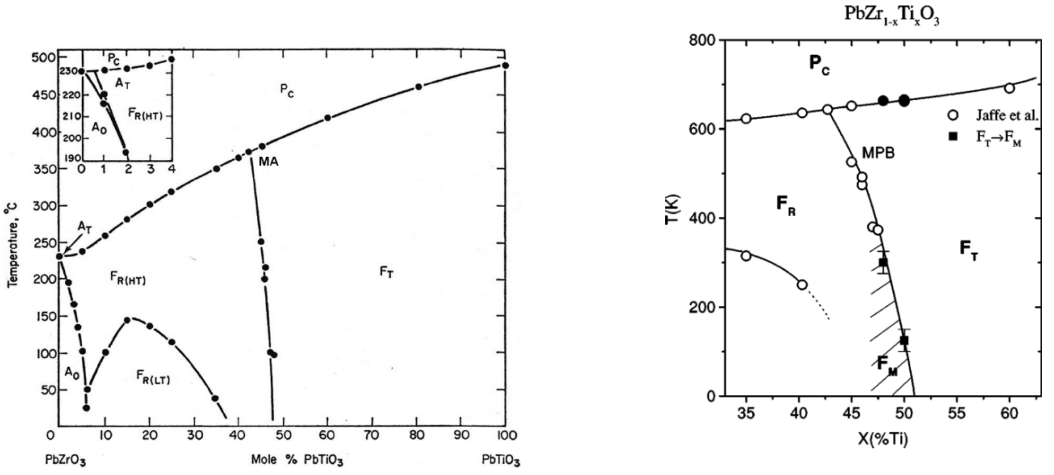

(a) Jaffe *et al.* original phase diagram

(b) Updated diagram by Noheda *et al.*

Figure 1.4: A comparison of the original PZT MPB phase diagram by Jaffe *et al.* [21] and a contemporary PZT phase diagram focussed on the region around the MPB, showing the monoclinic phase (shaded), reported by Noheda *et al.* [27].

1.3.2.1 Lead Free PZT Replacements MPBs

While PZT is widely used, it is necessary to find a suitable, lead-free replacement due to concerns over the toxicity of lead lost in the synthesis of the material as well as the lead concentration in used items. During synthesis, this can be lost in the extraction of lead-based ores. These concerns resulted in legislation designed to restrict its use in 2003 [28]. In Figure 1.3 it is clear that this is where the search for a "Lead-Free" material with an MPB really began. Any replacement material for PZT will need to replicate its functionality, which will require a high piezoelectric response across a wide range of temperatures, meaning that a material with a MPB would be most likely to be suitable.

With this in mind, much research over the past decade has been focussed on the synthesis and characterisation of a range of lead-free ferroelectric piezoelectric materials, with the body of work to this end progressing at a steady rate over the past decade. Thus this research into the MPB of lead-free BFO-KBT fits well into the context of the current body of work being produced in this field, whilst providing a novel examination of the system to produce a phase diagram.

Some examples of other materials being studied in a similar vein are
$(1-x)(BaTiO_3)$ $(x)(Bi(Mg_{0.5}Zr_{0.5})O_3)$ (BT-BMZ) [29];
$(1-x)((Bi_{0.5}Na_{0.5})TiO_3)$ $(x)(BaTiO_3)$ (NBT-BT); [30] and
$(1-x)((Na_{0.5}Bi_{0.5})TiO_3)$ $(x)((K_{0.5}Bi_{0.5})TiO_3)$ (NBT-KBT) [31].
$(1-x)((K_{0.5}Na_{0.5})NbO_3)(x)((Bi_{0.5}Na_{0.5})TiO_3)$ (KNN-NBT) [32] was also investigated in this way, but was discovered to be a PPB.

1.4 Introduction to Bismuth Ferrite ($BiFeO_3$, BFO)

The synthesis of $BiFeO_3$ (BFO) was first reported by Smolenskii *et al.* in 1958. It was found to have high conductivity so was thought to be of limited usefulness as a material in terms of its piezoelectric properties [33]. BFO is a perovskite with a rhombohedral distortion [34]. It has a space group of $R3c$ [35] at room temperature. It is a room temperature multiferroic material, showing ferroelectric ordering coupled weakly to a long range magnetic ordering [36, 37] (in the form of antiferromagnetism) [38].

While it has a high remnant polarisation of 100 μCcm^{-2} [39], the high conductivity as a result of the iron component gives rise to higher dielectric losses when compared with the archetype material, PZT, as discussed in Section 1.3.2. Interest in BFO was renewed in 2003 when it was found that thin films of the material displayed higher than expected residual polarisation [40]. This was also

found to be true in single crystals [41], and thus the material was seen to have device applications.

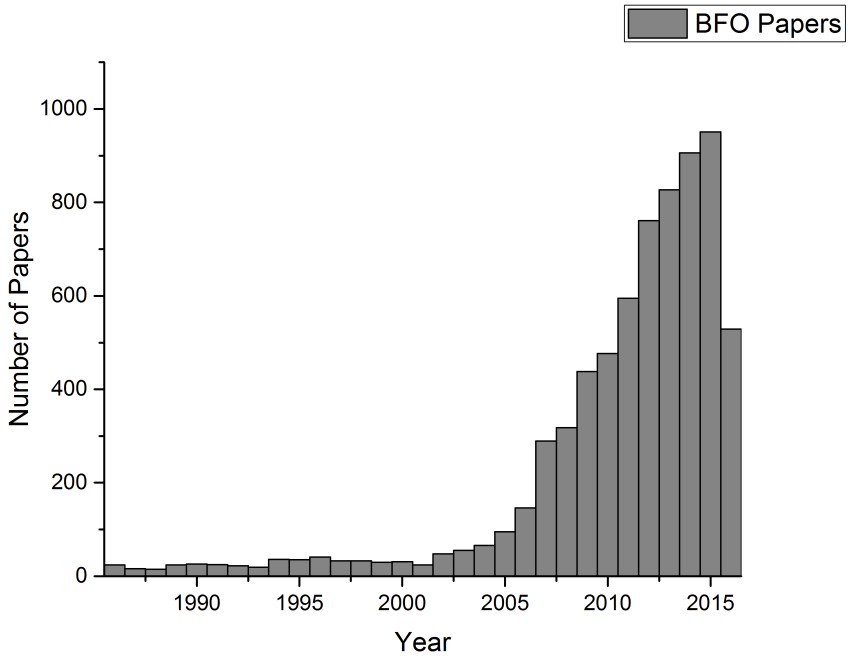

Figure 1.5: Number of papers published by year with BFO, BiFeO3 or Bismuth Ferrite existing in the title, abstract or keywords (as searched on Web of Science in Sept. 2016).

Figure 1.5 shows the number of papers published on the subject of BFO by year over the past 30 years; from this it can be seen that the interest in BFO is growing year by year, and has been since the early 2000s; in 2003 high remnant polarisations were first reported in BFO thin films [40], which have since been repeated in single crystals meaning that the effect is not dependent on strain but inherent to the system, reported in 2007 [41]. This has sparked a great deal of interest in the material, its physics and its potential device applications. Figure 1.5 shows that novel work on BFO and BFO-containing materials is relevant to current research.

This timing also coincided with the necessity of finding a lead-free alternative to PZT, as discussed in Section 1.3.2, which has spurred further interest in the material, including as a component in a mixed state material, such as BFO-KBT, which is expanded upon in Section 1.6 as it is the main focus of this thesis.

BFO undergoes a first order phase transition at 825°C. The structure of this phase was uncertain for many years, with orthorhombic, rhombohedral, tetragonal and monoclinic models put forth; the insensitivity of x-rays to the precise location of oxygen atoms has been cited as a likely source for this uncertainty [39]. It has

since been shown by neutron diffraction [42] to be orthorhombic with a *Pbnm* space group. Since *Pbnm* is centrosymmetric, this transition would also be T_C for BFO. From this phase, it then undergoes a further phase transition (second order) at 931°C, where it becomes cubic.

1.5 Introduction to Potassium Bismuth Titante ($(K_{0.5}Bi_{0.5})TiO_3$, KBT)

The synthesis of $(K_{0.5}Bi_{0.5})TiO_3$ (KBT) was first reported in 1958 by Smolenskii *et al.* [43], where it was synthesised as a test of theoretical compounds. KBT is a lead-free ferroelectric reported to have a *P*4*mm* tetragonal space group at room temperature [44] and has a relatively high T_c of 380°C [45]. It has a complex A-site [46], with a mix of bismuth and potassium atoms.

KBT is reported to become cubic around 450°C, and is reported to show a mixed phase of pseudocubic and tetragonal phases between 280°C and 450°C of cubic and tetragonal phases [47]. Due to reported issues of volatility of Bi_2O_3, it is difficult to synthesise dense KBT ceramics [48], which may also have lead to some inconsistency in reported results [49]. There are further issues with K_2CO_3 volatility, as reported by König *et al.* [50]. Between these two, it is possible that no stoichiometric KBT samples have been produced, with EDX measurements on KBT powders showing an imbalance between the potassium and bismuth atoms [50, 51].

KBT is commonly used as a tetragonal end member in solid solutions intended to produce morphotropic phase boundaries (See Section 1.3), such as $(K_{0.5}Na_{0.5})NbO_3$ - $(Bi_{0.5}K_{0.5})TiO_3$ [45] (KNN-KBT), $(Na_{0.5}Bi_{0.5})TiO_3$ - $(K_{0.5}\ Bi_{0.5})\ TiO_3$ [44, 51, 52, 53, 54] (NBT-KBT) and $(Bi_{0.5}Na_{0.5})ZrO_3$ - $(Bi_{0.5}K_{0.5})TiO_3$ [55] (BNZ-KBT). KNN is orthorhombic at room temperature, NBT is rhombohedral at room temperature and BNZ is cubic at room temperature, so KBT has been found to form MPBs with a variety of end member structures, making it a good candidate for the production of an MPB in solid solution with BFO.

Most work on KBT has been conducted on ceramic samples and powders, but there are examples of thin film experiments in the literature [56]. There are no examples of single crystal XRD experiments with KBT in the literature, meaning that the single crystal KBT measurements in this thesis are novel.

1.6 Introduction to (1-x) $BiFeO_3$-(x) ($K_{0.5}Bi_{0.5}$) TiO_3 (BFO-KBT) Solid Solutions

The (1-x) $BiFeO_3$-(x) ($K_{0.5}Bi_{0.5}$)TiO_3 (BFO-KBT) system is a solid solution of BFO and KBT. The (1-x)BFO-(x)KBT system is of interest for multiple reasons. The first is that by doping BFO with KBT, the reduction in iron content due to the inclusion of the titanium on the B-site should serve to lower the conductivity of the material, which would then potentially give the mixed material superior piezoelectric properties. This has been investigated by Wefring et. al. [57], Morozov *et al.* [58] and Hussain *et al.* [59]. It has been found that the BFO-KBT system could be suitable for high temperature piezoelectric applications [60]. Given the fact that BFO is rhombohedral and KBT is reported to be tetragonal at room temperature, the mixed material is also a good candidate in which to find a morphotropic phase boundary [61], as found in PZT. Since BFO-KBT is lead free, it would provide another alternative material for functions currently undertaken by PZT.

BFO-KBT synthesis was first reported in 2010 by Kim et al [61]. Most of the experiments conducted on the BFO-KBT system so far have been on powders or ceramic samples, though some recent experiments have been conducted on thin films [62]. Experimentation on single crystals is completely absent in the literature, so the crystals in this thesis (flux grown, received from Noguchi in Japan) present a unique and novel area for study.

Fisher *et al.* investigated calcine temperatures and times in 2016, and sintering temperatures and times for ceramics. They concluded that the overall results are quite stable, with similar densities, all samples still had impurity phase, and all were found to have similar structures, based on the BFO rhombohedral cell [63]. Wefring *et al.* investigated the electrical properties in 2015, and high temperature structure of some selected BFO-KBT samples [64].

1.6.1 BFO-KBT Phase Diagram

Since it is reported that BFO is rhombohedral and KBT is reported as tetragonal at room temperature, then in the solid solution there must necessarily be a point at which the structure changes. Analysis of the data obtained by other groups shows that the nature of these changes are still an area of active discussion, which this thesis aims to settle. The papers discussed here are summarised in Table 1.2

It was found by Kim *et al.* in 2010 [61] that sample melting was a possibility at a sintering temperature of 1050°C for samples with $x \leq 0.8$. Kim *et al.* found that the BFO-KBT system was tetragonal for $x \geq 0.9$, with the lower mol% region

claimed to be rhombohedral. They noted that the material was piezoelectric, and that the peak in the piezoelectricity in the range studied was at x = 0.94, with the d_{33} value changing from 31pC/N in the KBT end member to 64 pC/N at 94% KBT. From dielectric measurements, they claimed that the material would become pseudocubic in the region of 270°C to 340°C, varying based on composition with higher mol% KBT materials transitioning at lower temperature, consistent with measurements on KBT [47].

It was found by Matsuo *et al.* in 2010 [65] that $x = 0.36$ was rhombohedral, while $x = 0.4$ was found to be cubic. However, neutron diffraction measurements on the samples found that an $R3c$ tilt peak was still present in the $x = 0.4$ sample, so it was reported that $x = 0.43$ was the start of the pseudocubic region. A possible MPB around $x = 0.4$ was investigated. This revealed that the best piezoelectric properties in the studied range were found at $x = 0.4$, with a large remnant polarisation of $52\,\mu C/cm^2$. It was also found that the dielectric properties of the material at $x = 0.4$ showed relaxor properties; these were investigated further through transmission electron microscopy (TEM) selected area electron diffraction (SAED) measurements, which found polar rhombohedral nanoregions, consistent with other relaxor materials [55].

Ozaki *et al.* [66] reported that the material was rhombohedral up to $x = 0.3$ in 2010. Ferroelectric domains of the order of 200 nm were observed in the $x = 0.3$ material. They stated that at $x = 0.4$, the material should be considered as being comprised of polar rhombohedral and non-polar cubic nanoregions, which are of the order of 10 nm.

Pushkarev *et al.* [67] reported that in the region $x \leq 0.4$ the structure was rhombohedral, like the BFO end member in 2011. In the region $0.4 \leq x \leq 0.9$, it was reported that the diffraction peaks showed no clear signs of splitting, making characterisation difficult. This region was reported to be orthorhombic and found to have properties consistent with a relaxor material. The region $0.9 \leq x$ was reported as having tetragonal diffraction peak splitting, consistent with the KBT end member. It was found that when considering the pseudocubic lattice parameters, all three compositional regions had a different gradient, though in each case as the mol% KBT was increased, this pseudocubic lattice parameter decreased.

Morozov *et al.* [68] reported that the peak broadening and strain in the sample reportedly made characterisation harder in 2012. A maximum in piezoelectric and ferroelectric performance were reported at $x = 0.75$, which was explained as a possible phase boundary between the region of rhombohedral and cubic mixed phase and a proposed tetragonal and cubic mixed phase.

Bennett *et al.* [60] found that the system was $R3c$ rhombohedral in the region $0.2 \leq x \leq 0.4$ in 2013. They found that the material was antiferromagnetic and that the oxygen tilt angle was decreased with increasing KBT content. This is the only example of Rietveld refinements reported on the BFO-KBT system in the literature prior to this thesis.

In addition to these, in 2015, Bennett *et al.* [69] constructed a phase diagram for the BFO-KBT system, though the high temperature observations used were not diffraction based, but rather based on permittivity plots as a function of temperature, meaning that a diffraction-based phase diagram of the BFO-KBT system has still not been compiled.

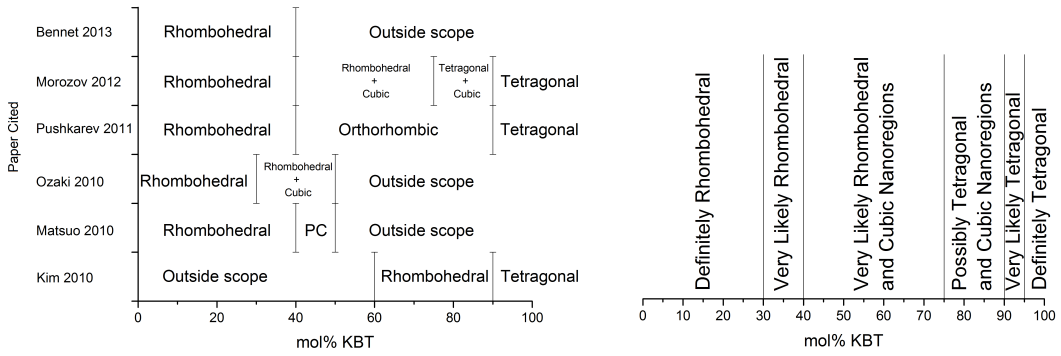

(a) Per paper **(b)** Overall

Figure 1.6: Phase diagrams constructed from the existing literature regarding the structure of the BFO-KBT system at room temperature. Figure 1.6a shows the contributions from individual papers, from oldest paper (Kim) to newest structural paper (Bennett). Figure 1.6b shows the overall expected structure from these papers [60, 61, 65, 66, 67, 68].

In summary of this, Figure 1.6 shows a preliminary room temperature phase diagram for the BFO-KBT system, constructed from the transition compositions stated in the literature discussed [60, 61, 65, 66, 67, 68]. Possible MPBs have been reported at 40 mol% KBT, 75 mol% KBT and 94 mol% KBT. There is still some disagreement about the exact nature of the phase diagram, especially for the high mol% KBT region of the phase diagram, with tetragonal and cubic nanoregions proposed by Morozov *et al.*

Additionally, there are very few data regarding non-room temperature structural characterisation of the (1-x)BFO-(x)KBT system, which is important for the classification of the phase boundaries as morphotropic. This thesis thoroughly explores the structure of the (1-x)BFO-(x)KBT system at high temperature to produce a reliable phase diagram with respect to composition and temperature.

Table 1.2: Diffraction-based studies of the BFO-KBT system. It should be noted that there have been no reported single crystal studies prior to this thesis.

Paper	Synthesis Methodology	Compositional Range mol% KBT	Observation Methodology	Calcine Temperature (°C)	Calcine Time (Hours)	Sinter Temperature (°C)	Sinter Time (Hours)
Kim (2010) [61]	solid-state reaction method	60-100	SEM, powder x-ray diffraction	750, 800	2, 2	1050-1060	2-6
Matsuo (2010) [65]	Flash-Creation method	20-50	powder neutron diffraction powder x-ray diffraction TEM, SAED	-	-	1000	4
Ozaki (2010) [66]	Flash-Creation method	20-50	TEM, SAED	-	-	1000	4
Pushkarev (2011) [67]	mixed oxide	0-100	powder x-ray diffraction	867	0.2-1.5	997-1097	2-4
Morozov (2012) [68]	solid-state reaction method	10-90	powder x-ray diffraction	800	5	1070-1080	2
Bennett (2013) [60]	conventional mixed oxide processing method	20-40	powder neutron diffraction Rietveld Refinement	-	-	980-1025	2
Bennett (2015) [69]	cold isostatic pressing	0-100	powder x-ray diffraction	-	-	975-1070	-

1.7 Project Overview

A brief overview of the motivations for the project as well as the aims are presented here. The former describes why this was considered an interesting research area, while the latter describes the approach taken to investigating these areas.

1.7.1 Motivations for the Project

The (1-x) $BiFeO_3$-(x) $(K_{0.5}Bi_{0.5})TiO_3$ (BFO-KBT) system is a relaxor ferroelectric with potential piezoelectric applications based in part around the MPB reported in the material [65]. Both of its constituent parts are of major interest for their potential technological applications, both as a replacement for lead-based piezoelectric materials, and in their own rights.

BFO is both ferroelectric and antiferromagnetic; with the coupling of the two factors, it has been reported [37] that it may be possible to manipulate an MPB through magnetic means. BFO is of interest in mixed systems because of this possibility for a tuneable MPB. In addition, by mixing the system the conductivity in BFO can potentially be reduced, since the iron would be diluted, for example by titanium in the case of BFO-KBT, which would emphasise other properties, such as the piezoelectric response.

Prior research shows some disagreement in the nature of the BFO-KBT system (discussed at length in Section 1.6), especially between the phase transition regions from rhombohedral and tetragonal to some mixed system in the middle of the compositional range. As a potentially very interesting material for device applications, it is important to have a reliable phase diagram for both composition and temperature, especially since this is related with the MPB in the material.

In addition, some rare single crystals of BFO-KBT have been obtained from the group of Noguchi at Tokyo University, allowing for novel single crystal XRD experiments to be undertaken in the BFO-KBT system, which is used as an independent verification for the structure refined from the powder XRD data.

1.7.2 Aims of this Project

Section 1.6.1 discussed the interest in the structure of the BFO-KBT system. However, it must be noted that there are many open questions regarding the BFO-KBT system which are yet to be answered because the measurements taken so far have been analysed mostly through visual inspection; there are no Rietveld refinements reported so far in the literature with XRD, and only one reported

Rietveld refinement at all. This means that the exact nature of the system is currently not fully known. In this thesis, Rietveld analysis is used systematically in order to provide quantitative analysis of the whole system. An investigation culminating in a full room temperature phase diagram is presented in Chapter 3.

From the phase diagram constructed in Figure 1.6 it can be seen that the general outline of the room temperature phase diagram is in place, but questions still remain; it is reported that there is a transition from rhombohedral to pseudocubic to tetragonal at room temperature, but there is currently little analysis of how this occurs, and no quantitative studies regarding this reported. In this thesis, Rietveld analysis of powder XRD investigating the evolution of the lattice parameters, the displacements, the long range order and the mixed phases with respect to composition, and also with respect to temperature is presented. In order to do so, high resolution XRD patterns are needed, which have been used in this thesis. The tilts have also been investigated with respect to composition where possible.

A deeper understanding of the material, especially around the reported MPBs with enhanced piezoeelctric and dielectric properties will be beneficial for researchers intending to further improve the properties of the material; for example, it has been found that doping the BFO-KBT system with lead titanate can provide exceptional piezoelectric properties [70]. This means that BFO-KBT will be an extremely useful functional material, and further knowledge of the crystal structures and transitions will help explain the regions with enhanced piezoelectric properties and enable further research to develop the system and further improve those properties.

In addition, there is currently very little high-temperature structural analysis of the BFO-KBT system, which is an important consideration for the designation of morphotropic phase boundaries, such as those proposed at 40% KBT. To this end, an investigation of the phase diagram with respect to temperature and composition in and around the rhombohedral-pseudocubic-mixed-phase is presented in Chapter 4. This comprises the first diffraction-based phase diagram of BFO-KBT.

The KBT end member has been reported [71] to display relaxor properties, which is inconsistent with its reported tetragonal long range order, since relaxor properties come from nanoregions, which will generally tend towards a pseudocubic form. An entirely novel investigation into single crystal BFO-KBT is presented in Chapter 5, with the aim of confirming the data obtained in Chapter 3 for the compositions available. In addition, a single crystal of KBT was analysed through single crystal XRD techniques, which has also not been previously reported.

1.8 References

Bibliography

[1] Tilley, R. J. D., in 'Perovskites: Structure-Property Relationships,' , (Wiley, Chichester2016), 1 edn.

[2] Ferraris, G., Makovicky, E., Merlino, S., *Crystallography of Modular Materials*, (Oxford University Press, Oxford2008).

[3] Vijaya, M. S., in 'Piezoelectric Materials and Devices,' (1–17) (2012).

[4] Känzig, W., *Ferroelectrics and Antiferroelectrics*, (Academic Press, New York1957).

[5] Lines, M. E., Glass, A. M., *Principles and Applications of Ferroelectrics and Related Materials*, (Oxford University Press, Oxford1997).

[6] Cowley, R. a., Gvasaliya, S. N., Lushnikov, S. G., Roessli, B., Rotaru, G. M., *Advances in Physics*, **60**:229 (2011).

[7] Blinc, R., *Advanced Ferroelectrics*, (Oxford Science Publications, Oxford2011).

[8] Burns, G., Dacol, F. H., *Solid State Communications*, **48**:853 (1983).

[9] Bokov, A. A., Ye, Z. G., *Journal of Materials Science*, **41**:31 (2006).

[10] Rabe, K. M., Ahn, C. H., Triscone, J. M. M., Dawber, M., Lichtensteiger, C., *Physics of Ferroelectrics*, vol. 105 (2007).

[11] Ahart, M., Somayazulu, M., Cohen, R. E., Ganesh, P., Dera, P., Mao, H.-k., Hemley, R. J., Ren, Y., Liermann, P., Wu, Z., *Nature*, **451**:545 (2008).

[12] Jo, W., Daniels, J. E., Jones, J. L., Tan, X., Thomas, P. a., Damjanovic, D., Rodel, J., *Journal of Applied Physics*, **109**:014110 (2011).

[13] Bokov, A., Ye, Z.-G., in Guo, R., Nair, K., Wong-Ng, W., Bhalla, A., Viehland, D., Suvorov, D., Wu, C., Hirano, S.-I. (Eds.), 'Symposium on Dielectric Materials and Multilayer Electronic Devices and the Symposium on Morphotropic Phase Boundary Phenomena and Perovskite Materials,' , (Indianapolis2003).

[14] Alberta, E. F., Guo, R., Bhalla, A. S., in Guo, R., Nair, K., Wong-Ng, W., Bhalla, A., Viehland, D., Suvorov, D., Wu, C., Hirano, S.-I. (Eds.), 'Symposium on Dielectric Materials and Multilayer Electronic Devices and the Symposium on Morphotropic Phase Boundary Phenomena and Perovskite Materials,' , (Indianapolis2003).

[15] Egami, T., Dmowski, W., in Guo, R., Nair, K., Wong-Ng, W., Bhalla, A., Viehland, D., Suvorov, D., Wu, C., Hirano, S.-I. (Eds.), 'Symposium on Dielectric Materials and Multilayer Electronic Devices and the Symposium on Morphotropic Phase Boundary Phenomena and Perovskite Materials,' , (Indianapolis2003).

[16] Glazer, A. M., Thomas, P. A., Baba-Kishi, K. Z., Pang, G. K. H., Tai, C. W., *Physical Review B - Condensed Matter and Materials Physics*, **70**:1 (2004).

[17] Ibrahim, A., Murgan, R., Rahman, M., Osman, J., in 'Ferroelectrics - Physical Effects,' (1–26) (2011).

[18] Yang, S. A., Kim, B. H., Lee, M. K., Bu, S. D., Lee, G. J., *Current Applied Physics*, **16**:593 (2016).

[19] Shirane, G., Takeda, A., 'Phase Transitions in Solid Solutions of PbZrO 3 and PbTiO 3 (I) Small Concentrations of PbTiO 3,' (1952).

[20] Jaffe, B., Cook, W. R., Jaffe, H. L., *Piezoelectric Ceramics*, (Academic Press, London; New York1971).

[21] Jaffe, B., Cook, W. R., Jaffe, H. L., in 'Piezoelectric Ceramics,' (136), (Academic Press, London; New York1971).

[22] Noheda, B., Cox, D. E., Shirane, G., Gonzalo, J. A., Cross, L. E., Park, S.-E., *Applied Physics Letters*, **2059**:6 (1999).

[23] Araújo, E., Yukimitu, K., Moraes, J. C. S., Pelaio, L. H. Z., Eiras, J. A., *Journal of Physics: Condensed Matter*, **14**:5195 (2002).

[24] Baldwin, A., Thomas, P. A., Dupree, R., *Journal of Physics: Condensed Matter*, **17**:7159 (2005).

[25] Corker, D. L., Glazer, A. M., Whatmore, R. W., Stallard, A., Fauth, F., *Physical Review B*, **80**:104109 (2009).

[26] Cordero, F., Trequattrini, F., Craciun, F., Galassi, C., *Journal of physics. Condensed matter : an Institute of Physics journal*, **23**:415901 (2011).

[27] Noheda, B., Gonzalo, J., Cross, L., Guo, R., *Physical Review B*, **61**:8687 (2000).

[28] 'DIRECTIVE 2002/95/EC OF THE EUROPEAN PARLIAMENT AND OF THE COUNCIL of 27 January 2003 on the restriction of the use of certain hazardous substances in electrical and electronic equipment,' (2003).

[29] Anand, S., Pandey, R., Shankar, U., Singh, A. K., *Journal of the American Ceramic Society*, **8**:1 (2016).

[30] Xu, Q., Chen, S., Chen, W., Wu, S., Lee, J., Zhou, J., Sun, H., Li, Y., *Journal of Alloys and Compounds*, **381**:221 (2004).

[31] Liu, J., Vanderbilt, D., *Physical Review B*, **88**:224202 (2013).

[32] Liu, L., Knapp, M., Ehrenberg, H., Fang, L., Schmitt, L. A., Fuess, H., Hoelzel, M., Hinterstein, M., *Journal of Applied Crystallography*, **49**:574 (2016).

[33] Rojac, T., Kosec, M., Budic, B., Setter, N., Damjanovic, D., *Journal of Applied Physics*, **108**:0 (2010).

[34] Jacobson, A. J., Fender, B. E. F., *J. Phys. C: Solid State Phys.*, **8**:844 (1975).

[35] Fischer, P., Polomska, M., Sosnowska, I., Szymanski, M., *Journal of Physics C: Solid State Physics*, **13**:1931 (1980).

[36] Palewicz, a., Sosnowska, I., Przeniosło, R., Hewat, a. W., *Acta Physica Polonica A*, **117**:296 (2010).

[37] Pradhan, a. K., Zhang, K., Hunter, D., Dadson, J. B., Loiutts, G. B., Bhattacharya, P., Katiyar, R., Zhang, J., Sellmyer, D. J., Roy, U. N., Cui, Y., Burger, a., *Journal of Applied Physics*, **97**:093903 (2005).

[38] Fu, C., Long, X., Cai, W., Chen, G., Deng, X., *Ferroelectrics*, **445**:114 (2013).

[39] Catalan, G., Scott, J. F., *Advanced Materials*, **21**:2463 (2009).

[40] Wang, J., Neaton, J. B., Zheng, H., Nagarajan, V., Ogale, S. B., Liu, B., Viehland, D., Vaithyanathan, V., Schlom, D. G., Waghmare, U. V., Spaldin, N. a., Rabe, K. M., Wuttig, M., Ramesh, R., *Science (New York, N.Y.)*, **299**:1719 (2003).

[41] Lebeugle, D., Colson, D., Forget, A., Viret, M., *Applied Physics Letters*, **91**:89 (2007).

[42] Arnold, D. C., Knight, K. S., Morrison, F. D., Lightfoot, P., **027602**:1 (2009).

[43] Smolenskii, G. A., Agranovskaya, A. I., *Soviet Physics Solid State1*, **1**:1429 (1960).

[44] Jones, G. O., Kreisel, J., Thomas, P. A., *Powder Diffraction*, **17** (2002).

[45] Du, H., Zhou, W., Luo, F., Zhu, D., Qu, S., Li, Y., Pei, Z., *Journal of Physics D: Applied Physics*, **41**:085416 (2008).

[46] Hagiwara, M., Fujihara, S., *Journal of Applied Crystallography*, **54** (2015).

[47] Otoničar, M., Škapin, S. D., Jančar, B., Ubic, R., Suvorov, D., *Journal of the American Ceramic Society*, **93**:4168 (2010).

[48] Zhu, M., Hou, L., Hou, Y., Liu, J., Wang, H., Yan, H., *Materials Chemistry and Physics*, **99**:329 (2006).

[49] König, J., Suvorov, D., *Journal of the European Ceramic Society*, **35**:2791 (2015).

[50] König, J., Spreitzer, M., Jančar, B., Suvorov, D., Samardžija, Z., Popovič, A., *Journal of the European Ceramic Society*, **29**:1695 (2009).

[51] Jones, G. O., *Investigation of the Structure and Phase Transitions in the Novel A-site Substituted Perovskite Series (Na1-xKx)0.5Bi0.5TiO3.*, Ph.D. thesis, University of Warwick (2001).

[52] Isupov, V. A., *Ferroelectrics*, **315**:123 (2005).

[53] O'Brien, A., *Investigation of the Structure of the Perovskite Series (Na1-xKx)1/2Bi1/2TiO3*, Ph.D. thesis (2013).

[54] Xie, H., Jin, L., Shen, D., Wang, X., Shen, G., *Journal of Crystal Growth*, **311**:3626 (2009).

[55] Wefring, E. T., Morozov, M. I., Einarsrud, M. A., Grande, T., *Journal of the American Ceramic Society*, **97**:2928 (2014).

[56] Jing, X., Huang, B., Zhang, X., Qin, X., Wei, J., Wang, X., Yao, S., Xu, Z., Wang, Z., Wang, P., *Journal of Physics D: Applied Physics*, **42**:045421 (2009).

[57] Wefring, E. T., Schader, F. H., Webber, K. G., Einarsrud, M.-a., **36**:497 (2016).

[58] Morozov, M. I., Einarsrud, M. A., Grande, T., *Applied Physics Letters*, **104**:0 (2014).

[59] Hussain, A., Zheng, P., Xu, X., Chen, X., Li, T., Wang, Y., Yuan, G., Yin, J., Liu, Z., *Journal of Alloys and Compounds*, **678**:228 (2016).

[60] Bennett, J., Bell, A., Stevenson, T., Smith, R., Sterianou, I., Reaney, I., Comyn, T., *Materials Letters*, **94**:172 (2013).

[61] Kim, J. M., Sung, Y. S., Cho, J. H., Song, T. K., Kim, M. H., Chong, H. H., Park, T. G., Do, D., Kim, S. S., *Ferroelectrics*, **404**:88 (2010).

[62] Choi, J. H., Yoshimura, T., Norifumi, F., *Japanese Journal of Applied Physics*, **54** (2015).

[63] Fisher, J. G., Park, H.-Y., Song, Y.-O., Baek, S.-J., Vu, H., Kim, J.-H., Kim, Y.-H., Lee, J. S., *Journal of the Korean Physical Society*, **68**:59 (2016).

[64] Wefring, E. T., Einarsrud, M.-a., Grande, T., *Phys. Chem. Chem. Phys.*, **17**:9420 (2015).

[65] Matsuo, H., Noguchi, Y., Miyayama, M., Suzuki, M., Watanabe, A., Sasabe, S., Mori, S., Torii, S., Kamiyama, T., **104103**:1 (2011).

[66] Ozaki, T., Matsuo, H., Noguchi, Y., Miyayama, M., Mori, S., *Japanese Journal of Applied Physics*, **49**:09MC05 (2010).

[67] Pushkarev, A. V., Olekhnovich, N. M., Radyush, Y. V., *Inorganic Materials*, **47**:774 (2011).

[68] Morozov, M. I., Einarsrud, M.-A., Grande, T., *Applied Physics Letters*, **101**:252904 (2012).

[69] Bennett, J., Shrout, T. R., Zhang, S., Owston, H. E., Stevenson, T. J., Esat, F., Bell, A. J., Comyn, T. P., *IEEE transactions on ultrasonics, ferroelectrics, and frequency control*, **62**:33 (2015).

[70] Bennett, J., Bell, a. J., Stevenson, T. J., Comyn, T. P., *Scripta Materialia*, **68**:491 (2013).

[71] Hagiwara, M., Fujihara, S., *Applied Physics Letters*, **107** (2015).

Chapter 2

Experimental Methods

2.1 Powder X-ray Diffraction

The basic operation of diffraction is well known to solid-state scientists and so is not discussed here but good descriptions are given by Giacovazzo [1] and Hammond [2].

Powder x-ray diffraction (powder XRD) is a powerful crystallographic technique which, along with structural refinement, is able to determine the lattice parameters, atomic positions and atomic displacement parameters (ADPs) for a material. In a powder XRD profile, the phases can be identified by comparison with a standard database, since the phases will exhibit a unique diffraction pattern. As such, powder XRD is an excellent methodology for determining the phases present in a sample (such as impurity phases, or for multiple structural phases of the same material present simultaneously) which made its use vital for this thesis.

In a powder XRD experiment, the large number of individual, randomly orientated grains means that all orientations are represented. Consequently, unlike in single crystal x-ray diffraction, individual Bragg reflections are not observed; instead reflections are distributed in 2θ by d-spacing, forming a one dimensional intensity plot, with all {hkl}s not subject to systematic absence present and merged, with any symmetry constrained or coincidentally identical peaks (such as two phases with the same atoms) overlapping exactly. Peaks with very similar d-spacing can be difficult to separate in low resolution measurements. In a multiphase material, all phases exist in the same peak profile, and the relative intensities of those phases can be calculated from the profile, allowing a measure of the relative quantities of the phases present.

Powder XRD is a convenient technique for materials with high absorption, since Bragg-Brentano geometry, the geometry used in this thesis, is reflection based,

meaning that the absorption is not a major issue. Powder XRD is also a suitable methodology for measurements with respect to temperature, such as the observation of phase transitions and thermal expansion of the lattice [3]. A further advantage of powder XRD is that it is generally simpler to produce a high quality powder sample than a high quality crystal of suitable size for diffraction techniques [2].

The powder diffractometer used to collect the data presented in this thesis was a *Panalytical X-Pert Pro MPD* $K_{\alpha 1}$ equipped with a curved Johansen Ge monochromator giving pure focussed Cu $K_{\alpha 1}$ radiation. The focussed x-rays give less instrumental broadening, so this is considered a high-resolution powder diffraction instrument, which uses a solid state *PiXcel* detector. In addition an *Anton Paar HTK1200N* spinner chamber, capable of achieving temperatures up to 1200°C was used to collect the high temperature data used. The use of this high resolution diffractometer allowed features usually obscured by resolution to be discerned.

2.1.1 Rietveld Refinement

Rietveld refinement was first introduced by Hugo Rietveld in his seminal papers on the subject in 1967 and 1969 respectively [4, 5]. The technique employs a least-squares fitting algorithm to act as a whole pattern fitting program [6], where the least squares refinements are carried out until the best fit between the entire observed pattern and the entire calculated pattern are obtained, with feedback between the improving knowledge of the system with each iteration and the assignment of intensity to given, overlapping Bragg reflections. Least-squares refinements are discussed in Section 2.1.2.

The refinement contains significant data about the crystallographic system. From the peak positions in 2θ, the lattice parameters can be accurately determined. From the peak heights the atomic positions within the cell can be determined. In addition, the refinement also contains background terms, ADPs which are used to model the thermal motion of the atoms, and a peak-profile shape function, discussed in Section 2.1.3.1, used to refine the model.

Figure 2.1 shows that an offset in height can greatly effect the angular information gathered, introducing an offset to all 2θ measurements taken. In addition, it also changes the focal length, which means that the diffraction optics are not optimised to observe the data, which will systematically change the intensities of the peaks. Because of these issues, it is important to accurately determine the offset correction that the measurements are taken at. To this end, the equipment is regularly recalibrated with a standard material (National Institute Science Technology standard reference material, CeO_2) with a well characterised

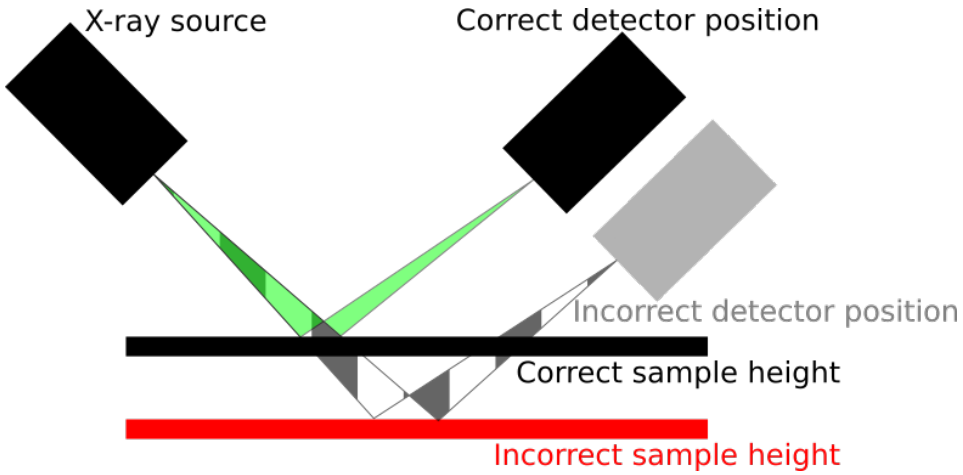

Figure 2.1: Diagram of height offset and its importance for Rietveld.

diffraction pattern and little instrument broadening leading to sharp peaks, to determine the mechanical offsets to the height by any differences between the obtained pattern and the standard pattern. From this, the sample-dependant offset to height can be calculated as a part of the Rietveld analysis of the sample, which will then account for the systematic changes in 2θ and intensity. The offset in 2θ is given by:

$$2\theta_{offset} = \frac{-2rad\,(H)\,cos\,(\theta)}{R} \tag{2.1}$$

where H is the height offset in mm and R is the secondary radius of the diffractometer (mm). [7].

2.1.2 Least-Squares Refinement

Rietveld analysis requires a type of algorithm known as a 'least-squares' refinement. In a least-squares refinement, the refinement is iterated until the residual factor (S_y) is found to have been minimised to its lowest point:

$$S_y = \sum_i w_i\,(y_{oi} - y_{ci})^2 \tag{2.2}$$

where w_i is the weighting factor of the i^{th} observation($w_i = 1/y_{oi}$), y_{oi} is the observed value for the i^{th} observation and y_{ci} is the calculated value for the i^{th} observation. In other words, S_y is relative to the sum of the disagreement across the entire 2θ range in a powder diffraction experiment. When this is minimised, the differences between the calculated model and the observed data will have reached a minimum. It

is important to note that the model must begin close to the correct model, otherwise it is possible for the refinement to refine to a 'false minimum', a point at which there exists a local minimum in the residual factor that is not the true minimum.

The calculated intensity, y_{ci} is given by:

$$y_{ci} = f \sum_h L_h |F_h|^2 \phi \left(2\theta_i - 2\theta_h\right) A + y_{bi} \tag{2.3}$$

where f is the scale factor, h represents the Miller indices h, k, l for a Bragg reflection, L_h is the Lorentz polarisation and multiplicity factors, F_h is the structure factor for the h^{th} Bragg reflection, $\phi\left(2\theta_i - 2\theta_h\right)$ is the reflection profile function, A is the absorption factor and y_{bi} is the background of the i^{th} step. [6]

The minimisation of the residual factor is achieved through the refinement of various parameters of the model. A set of normal equations relating the derivatives of the calculated intensities with respect to each of these parameters is produced, which is solved by the inversion of a matrix:

$$M_{jk} = -\sum_i 2w_i \left[\left(y_{oi} - y_{ci}\right) \frac{\delta^2 y_{ci}}{\delta x_j \delta x_k} - \left(\frac{\delta y_{ci}}{\delta x_j}\right)\left(\frac{\delta y_{ci}}{\delta x_k}\right) \right] \tag{2.4}$$

where j, k are the set of m refining parameters (i.e. the matrix has dimensions $m \times m$). The change in a parameter is not constant for each iteration, and the change in some parameter, x_k, is given by:

$$\Delta x_k = \sum M_{jk}^{-1} \frac{\delta S_y}{\delta x_k} \tag{2.5}$$

This change is added to the initial value after each iteration, then the next iteration begins until a minimum value for S_y is reached. This is the basic form of all least squares refinements, such as Rietveld refinements, and a version of this is utilised in TOPAS ACADEMIC and SHELXL. From this, calculations for how well the model fits the observed data can be calculated, shown in Section 2.1.3.4.

2.1.3 Refineable Parameters

For these Rietveld refinements, many parameters of the data can be refined to obtain a better model, resulting in a peak profile that better matches the observed data. These can be broadly split into two groups: those due to the instrumentation, and those due to the material itself.

Those due to the instrument itself should be well known and accounted for since they will systematically effect all samples measured. These include effects

due to the diffractometer geometry, the incident beam settings and detector effects, corrected with an axial divergence correction. These result in peaks best described by a Gaussian peak shape.

Those due to the sample have become more apparent as detector resolution has improved and include strain effects, thermal vibrations, structure factors (discussed in Section 2.2.2.1) and crystallite size effects. These result in peaks best described by a Lorentzian peak shape.

The most important parameters to determine prior to measurement are the zero offset and the sample height error, as discussed in Section 2.1.1. The zero offset is determined by measurements performed regularly on a well characterised sample.

2.1.3.1 Peak Shape

Given that in modern experiments, both instrument-based and sample-based parameters are present, it is therefore important to be able to model a peak as both Gaussian and Lorentzian. To this end, there are several ways of mixing these, known as a convolution. The convolution equation generally used throughout this thesis is the TCHZ methodology [8], which is a pseudo-Voight function. The only exception to this is in Section 4.5 which uses a Split Pearson VII methodology [9]. Both the TCHZ and Split Pearson VII functions are described here, with a description of the Gaussian and Lorentzian peak profiles and the pseudo-Voight function for the convolution, with details for the individual functions described in Table 2.2 (TCHZ function) and Table 2.3 (Pearson VII function). In Table 2.1, w is the Full Width at Half of the Maximum height of the peak (FWHM). η is the mixing factor between the Gaussian and Lorentzian peaks. Table 2.2 contains multiple constants: $A = 2.69269$, $B = 2.42843$, $C = 4.47163$, $D = 0.07842$, $E = 1.33603$, $F = 0.47719$, $G = 0.1116$ (which were obtained through a series of computer generated convolutions and here are taken directly from the paper in which the methodology was introduced [8]). U, V, W, X, Y, Z are parameters refined in TOPAS ACADEMIC. Γ_a and ζ are described in Section 2.1.3.3. The values from the TCHZ function are directly applied to the pseudo-Voight function. In Table 2.3, x is the angle 2θ and $2\theta_0$ is the peak position, m indicates the level to which the peak is described by a Lorentzian or a Gaussian peak, with $m = 1$ giving a pure Lorentzian fit and $m \to \infty$ giving a pure Gaussian fit. The subscript L or R gives the left or right contribution to this respectively to both w and m variables. $P_{PVII}(x)$ shows the standard Pearson VII equation. The equation is split as shown in the $P_{SplitPVII}(x)$ equation, depending on whether the current 2θ value is above or below the centre of the peak, i.e. left (L) or right (R) of the centre. The split plots have to meet in the centre, so are

Table 2.1: Peak Profile Fitting Functions

Peak Type	Equation
Lorentzian	$L(x) = \left(\frac{2/\pi}{w}\right) / \left(\frac{1+4x^2}{w^2}\right)$
Gaussian	$G(x) = \left(\frac{2\sqrt{ln(2)/\pi}}{w}\right) exp\left(\frac{-4ln(2)x^2}{w^2}\right)$
Pseudo-Voight	$F(x) = \eta L(x) + (1-\eta)\, G(x)$

subject to a constant scaling factor, shown in the c_R equation for the right side and the c_L equation for the left side. While the Pearson VII function acts as a pseudo-Voight function, it is calculated as shown in Table 2.3, rather than being used in the pseudo-Voight function shown in Table 2.1. In a split Peason VII function, w_L, w_R, m_L and m_R are refineable parameters. Γ is the gamma function. c_L and c_R are the constant scaling factors to ensure that the left and right halves meet at the centre point.

2.1.3.2 Atomic Displacement Parameters

The atomic positions calculated for a structure actually represent the average positions of those atoms. There are two effects that lead to this; dynamic effects such as thermal effects, which mean that an individual atom is vibrating around this average position, and static effects such as structural disorder often found in mixed-site materials, where the fact that the cell obtained is an average over many individual unit cells means that local distortions will be lost to the average position. It is generally not possible to determine from the displacement itself whether it is produced by static or dynamic means. These deviations create deviations in electron density, thus changing the ability of the atom to scatter x-rays. This results in a weakening of the Bragg intensities [1].

Atomic Displacement Parameters (ADPs) represent these effects. At one point they were known as thermal parameters, but in order to describe effects from other sources, such as structural disorder, the more general ADP nomenclature is used in modern writing [10]. ADPs can be calculated in two forms. Where the displacement can be modelled by a sphere, isotropic parameters can be used:

Table 2.2: TCHZ Refinement Parameters

Parameter	Equation
w	$\left(\Gamma_G^5 + A\Gamma_G^4\Gamma_L + B\Gamma_G^3\Gamma_L^2 + C\Gamma_G^2\Gamma_L^3 + D\Gamma_G\Gamma_L^4 + \Gamma_L^5\right)$
Γ_L	$Xtan\theta + Y/cos\theta + \zeta\Gamma_a$
Γ_G	$\left[Utan^2\theta + Vtan\theta + W + Z/cos^2\theta + (1-\zeta)\,\Gamma_a^2\right]^{0.5}$
η	$E\left(\frac{\Gamma_L}{w}\right) - F\left(\frac{\Gamma_L}{w}\right)^2 + G\left(\frac{\Gamma_L}{w}\right)^3$

Table 2.3: Split Pearson VII Refinement Parameters

Parameter	Equation
$P_{P_{VII}}(x)$	$\frac{2}{w}\left(\frac{2^{1/m}-1}{\pi}\right)^{1/2}\frac{\Gamma(m)}{\Gamma(m-1/2)}\left[1+4\left(2^{1/m}-1\right)\left(\frac{x}{w}\right)^2\right]^{-m}$
$P_{SplitP_{VII}}(x)$	$\begin{cases} c_L P_{P_{VII}}(x;2\theta_0;w_L;m_L) & \text{if } 2\theta < 2\theta_0 \\ c_R P_{P_{VII}}(x;2\theta_0;w_R;m_R) & \text{if } 2\theta \geq 2\theta_0 \end{cases}$
c_R	$2 - c_L$
c_L	$2\left[1+\frac{w_R}{w_L}\left(\frac{2^{1/m_L}-1}{2^{1/m_R}-1}\right)^{1/2}\frac{\Gamma(m_L)}{\Gamma(m_R)}\frac{\Gamma(m_R-1/2)}{\Gamma(m_L-1/2)}\right]^{-1}$

Table 2.4: Stephens parameters [11] necessary for different structures.

Structure	S_{HKL}
Trigonal (Hexagonal indices)	$S_{400} = S_{040} = S_{310}/2 = S_{130}/2 = S_{220}/3$ $S_{202} = S_{022} = S_{112}$ S_{004} $S_{301}/2 = -S_{031}/2 = S_{211}/3 = -S_{121}/3$
Tetragonal	$S_{400} = S_{040}$ $S_{202} = S_{022}$ S_{004}, S_{220}
Monoclinic	$S_{400}, S_{301}, S_{220}, S_{202}$ $S_{121}, S_{103}, S_{040}$ $S_{022},\ S_{004}$
Cubic	$S_{400} = S_{040} = S_{004}$ $S_{220} = S_{202} = S_{022}$

$$B = 8\pi^2 U \left(\mathring{A}^2\right) \tag{2.6}$$

where B is the atomic displacement factor, $U = \langle r'^2 \rangle$ and r' is the displacement of the atom from its mean position, so U is the squared mean displacement of the atom with respect to its equilibrium position.

If the displacement can not be modelled by a sphere, anisotropic (or harmonic) parameters are used. Here, a three-dimensional Gaussian distribution of the probability is applied, forming ellipsoids around the equilibrium position:

$$q\left(\boldsymbol{r^*}\right) = exp\left[-2\pi^2\left(U_{11}^* x^* + U_{22}^* y^* + U_{33}^* z^* + 2U_{12}^* x^* y^* + 2U_{13}^* x^* z^* + 2U_{23}^* y^* z^*\right)\right] \tag{2.7}$$

where U_{ij}^* are the unique U parameters necessary to characterise the anisotropic displacement, forming an ellipsoid in reciprocal space, $\boldsymbol{r^*}$ represents the atomic position in reciprocal space.

2.1.3.3 Anisotropic Peak Broadening

Many of the peaks observed required an extra term to properly fit the peak shape, as it was found that the broadening was not a smooth function with respect to d-spacing. Specifically, the methodology of Stephens [11] was necessary to properly fit the anisotropically broadened peaks, since this anisotropy causes problems with

whole pattern fitting functions, such as those found in Rietveld refinement.

Stephens parameters model strain in a sample, which results in anisotropically broadened peaks. With the mismatch in lattice parameters between the BFO and KBT components of the mixed system, some amount of strain was expected.

In this methodology, a matrix $M_{hkl} = 1/d^2$ is used to model the effects of the distribution of the anisotropy in the peaks. This distribution is assumed to be Gaussian, such that:

$$\sigma^2 (M_{hkl}) = \sum_{HKL} S_{HKL} h^H k^K l^L \tag{2.8}$$

where the terms for S_{HKL} are defined for $H + K + L = 4$. For a triclinic system, all 15 possible values of S_{HKL} are allowed, whereas for more symmetric structures, the values are constrained by symmetry, with the relevant symmetries for this thesis shown in Table 2.4. In Table 2.4, any missing $S_{HKL} = 0$.

The equation for M_{hkl} can be rearranged to $sin\theta = \lambda M_{hkl}^{1/2}/2$ via the Bragg equation, meaning that the contribution to the FWHM from anisotropic peak broadening Γ_A is given by:

$$\Gamma_A = \left[\sigma^2 M_{hkl}\right]^{1/2} tan\theta / M_{hkl} \tag{2.9}$$

The effects of this anisotropic term have already been added to the TCHZ profiles in Table 2.2, related with ζ and Γ_A.

2.1.3.4 Model Quality

While the residual factor being minimised in Equation 2.2 was S_y, other statistical measures to determine how well the refined model matches the observed data are simultaneously calculated. These residual factors, known generally as R-factors, provide a numerical metric by which to measure the fitting of the model profile to the observed data, such that two fits that seem to be in similar agreement can be probed statistically.

Table 2.5 shows the R-factors used for Rietveld refinements undertaken in TOPAS ACADEMIC, where Y_{om} is the observed data at data point m, Y_{cm} is the calculated data at data point m, B_m is the background at data point m, N_M is the number of data points, N_P is the number of parameters, I_{ok} is the intensity observed for the k^{th} reflection, I_{ck} is the intensity calculated for the k^{th} reflection, w_m is the weighting parameter given to point m. $w_m = 1/\sigma (Y_{om})^2$ where $\sigma (Y_{om})$ is the error

Table 2.5: R-factors (TOPAS ACADEMIC Rietveld refinement).

Value	R	R'
R_p	$R_p = \left(\frac{\sum \lvert Y_{om} - Y_{cm} \rvert}{\sum \lvert Y_{om} \rvert} \right)^{1/2}$	$R_p{}' = \left(\frac{\sum \lvert Y_{om} - Y_{cm} \rvert}{\sum \lvert Y_{om} - B_m \rvert} \right)^{1/2}$
R_{wp}	$R_{wp} = \left(\frac{\sum w_m \left(Y_{om} - Y_{cm} \right)^2}{\sum w_m {Y_{om}}^2} \right)^{1/2}$	$R_{wp}{}' = \left(\frac{\sum w_m \left(Y_{om} - Y_{cm} \right)^2}{\sum w_m \left(Y_{om} - B_m \right)^2} \right)^{1/2}$
R_{exp}	$R_{exp} = \left(\frac{N_M - N_P}{\sum w_m {Y_{om}}^2} \right)^{1/2}$	$R_{exp}{}' = \left(\frac{N_M - N_P}{\sum w_m \left(Y_{om} - B_m \right)^2} \right)^{1/2}$
GoF	$GOF = \chi = \frac{R_{wp}}{R_{exp}} = \left(\frac{\sum w_m \left(Y_{om} - Y_{cm} \right)^2}{N_M - N_P} \right)^{1/2}$	
Durbin-Watson (d) [7]	$d = \frac{\sum_{m=2}^{M} \left(\Delta Y_m - \Delta Y_{m-1} \right)^2}{\sum_{m=1}^{M} \left(\Delta Y_m \right)^2} \; ; \quad \Delta Y_m = Y_{om} - Y_{cm}$	
R_{Bragg}	$R_{Bragg} = \frac{\sum \lvert I_{ok} - I_{ck} \rvert}{\sum I_{ok}}$	

in Y_{om}.

The values in Table 2.5 on the right (showing the R' R-factors) include a background correction (B_m), which has been used for the final tabulated outputs, though during the refinements the uncorrected versions were used.

Of these, the refined parameter (Rwp), the goodness of fit (GoF) and the R_{Bragg} are the parameters which were most used during refinement to define improvements between one form of the model and another; the refined parameter because it was the minimised function, the GoF because it takes some account of the number of parameters refined and thus provides a better comparison between different models, and the R_{Bragg} because it allowed for the influence of each of the phases in the mixed phase systems investigated to be observed independently.

From the GoF equation in Table 2.5, it can be seen that as the number of independent reflections increases, and/or as the number of refined parameters decreases, the GoF will converge to a minimum. This is helpful, because the number of refined parameters should ideally be as low as possible, and the higher the number of independent reflections the better the data set for refinement.

2.2 Single Crystal X-ray Diffraction

Single crystal x-ray diffraction (single crystal XRD) is another form of x-ray diffraction in which a single crystal is exposed to monochromatic x-rays, the pattern of diffracted spots from which correspond to the individual Bragg peaks. As the individual Bragg peaks are separated, it can be used to determine structural effects that powder XRD can not discern, such as centrosymmetry. A Laue check is also possible in single crystal XRD, used to test the Laue class to which the crystal belongs and thus the symmetry. In order to interpret the data thus obtained, it is necessary to collect data from a sufficient proportion of the Ewald sphere; the lower the symmetry of the system, the higher this proportion should be (with a cubic system, a quadrant is sufficient, with a triclinic system the whole sphere should be collected). CRYSALIS PRO is a data collection and reduction software produced by Rigaku Oxford Diffraction [12]. In CRYSALIS PRO, a pre-experiment can be taken to optimise the data collection process.

In a pre-experiment, a number of frames (15 is the standard for the Mo source which was used in these experiments) are collected, from which a preliminary set of unit cell parameters and diffraction symmetries are calculated, which then informs the experimental set up, with lower symmetries requiring a more complete Ewald sphere and larger lattice parameters generally requiring smaller step sizes between

frames.

In this thesis, single crystal data has been collected using three sources. Most of the data has been collected on the lab-based diffractometers:

Rigaku Oxford Diffraction *Gemini R*, a Kappa geometry goniometer equipped with fine focus Cu and Mo x-ray sources, graphite monocromators, and a *Ruby* CCD area detector. On this machine, the generator was set to a lower power than usual (specifically, it was set to 33kV 30mA) to remove $\lambda/2$ reflections, which can otherwise be mistaken for tilt peaks.

Rigaku Oxford Diffraction *SuperNova*, a Kappa geometry goniometer with microfocus Cu and Mo x-ray sources and an *Atlas S2* CCD area detector. On this machine, $\lambda/2$ reflections are not a concern. This machine was only added to the department in the final year of this thesis, so the bulk of the single crystal experiments were conducted on the other machine.

In addition to these, there was also an experiment undertaken at beamline I15, Diamond Light Source, Harwell Campus, Oxfordshire, UK, utilising 0.2772Å wavelength radiation, a six-circle diffractometer with an Oxford Diffraction *Atlas* detector.

2.2.1 Data Integration

To get from the individual frames with different angles that are collected in data collection to a single dataset with defined HKL values, the data must be integrated. During this process, a crystal structure is chosen by the operator of the program, using the data from the Ewald sphere to determine the symmetries and then using these to use the Laue symmetry to reject any outlying reflections. The data rejection can be skipped if it is important to output the entire dataset (such as when trying to determine multiple phases from one dataset). The unit cell parameters are calculated from the data during the data integration step by selecting peaks and constructing the lattice based on the integration considerations.

A given Bragg peak will be collected in multiple frames (the redundancy) and these are integrated to give a single set of data when all the individual data frames are integrated. The degree to which these data sets agree is given by:

$$R_{int} = \frac{\sum_{hkl} |F^2_{hkl(o)} - \langle F^2_{hkl(o)} \rangle|}{\sum_{hkl} F^2_{hkl(o)}} \tag{2.10}$$

which means that the intensities of a given peak, $F^2_{hkl(o)}$, is related to all instances of the same peak via an average. Since $R_{int} \propto |F^2_{hkl(o)} - \langle F^2_{hkl(o)} \rangle|$, a perfect data integration would result in $R_{int} = 0$, so the lower R_{int} the better. R_{int} gives a

measure of the consistency of the data set.

All single crystal data integration in this thesis was conducted using the program CRYSALIS PRO from *Rigaku Oxford Diffraction*. This process is also known as data reduction.

2.2.1.1 Absorption Correction

Single crystal diffraction requires a sufficient diffracting volume to extract high enough scattering intensity, which pushes the ideal crystal size up. At the same time, however, the absorption of the crystal means that the maximum size is strongly limited by the chemical composition of the crystal; the higher the absorption of the materials in the crystal, the smaller the crystal has to be. Because of these two competing requirements for crystal size, there exists an ideal size for a crystal, maximising the diffraction volume while minimising the effects of absorption.

Beer's Law [13] states that:

$$\frac{I}{I_0} = e^{-\mu x} \tag{2.11}$$

where I_0 is the incident intensity, I is the diffracted intensity, μ is the linear absorption coefficient and x is the total linear distance travelled through the crystal (both incident and diffracted distance).

Assuming a roughly spherical crystal, to ignore the effects of anisotropic size, then $I_0 \propto x^3$, and thus $I \propto x^3 e^{-\mu x}$. The maximum intensity for I can be found by setting its first derivative equal to 0:

$$\frac{dI}{dx} = 3x^2 e^{-\mu x} - x^3 \mu e^{-\mu x} = x^2 e^{-\mu x} (3 - \mu x) \tag{2.12}$$

therefore, a minimum is found when $x = 0$ or when $x = 3/\mu$. Given that the crystal is going to be of non-zero size, this means that the ideal size scale of the crystal will be $x = 3/\mu$. The materials discussed in this thesis are all based on at least a partially bismuth A-site, with the highest amount being 100% bismuth, and the lowest being 50% bismuth, therefore the absorption in all samples is very high, limiting single crystal sizes to the range 20 µm - 100 µm. This is a small size for single crystals, making preparation more challenging.

As mentioned, this does neglect size anisotropy, which needs to be accounted for in any absorption corrections carried out on a non-spherical sample. The anisotropic path length in a crystal results in a reflection dependant absorption, hence measured intensities, resulting in inaccurate data integration ; the higher μ, the larger an effect the size anisotropy would otherwise have. To this end, these

differences in the transmission factor were calculated in this thesis by the analystical method of Clark and Reid [14].

The analytical method for calculating the transmission factor involves splitting the crystal into Howell's Polyhedra [15], ensuring that for each polyhedra only one face is illuminated and that the x-ray intensity is either absorbed or diffracted out of another face.

This method, unlike some of the others available such as the Empirical method, provides an exact solution. The limiting factor on this method was originally computing factor, but with improvements to the algorithm for identifying the Howell's polyhedra [16] and increases in analytical computer power, these limitations have been overcome. The method in CRYSALIS PRO is applied mostly automatically, but still requires that the faces of the crystal be drawn on to a sequence of still images of the crystal as it is rotated, resulting in a 3D representation of the crystal.

With the absorption in mind, one of the advantages of synchrotron single crystal XRD measurements is that the energy of the beam is tunable, meaning that absorption edges in the material can be avoided. In the BFO-KBT crystals, the absorption in the laboratory was calculated to be $\mu = 62.90$ mm^{-1}, while the absorption at the synchrtron was $\mu = 5.52$ mm^{-1}. The absorption corrections are completed as part of the data integration step.

2.2.2 SHELXL Refinements

The structures of perovskite materials are well known, so for the materials in this thesis, the next step after the data integration was to refine the structure. The lattice parameters are not refined after the data integration step; instead it is the atomic positions within those parameters which are constructed from the rules of reflection for those space groups from the International Tables of Crystallography [17]; specifically, the structures used in this thesis were rhombohedral (trigonal) $R3c$, tetragonal $P4mm$, monoclinic $P1m1$ and cubic $Pm\bar{3}m$.

From these initial starting conditions, SHELXL [18], a least-squares refinement program for single crystal diffraction data, can be employed to refine the preliminary model applied to the observed data. The general operation of a least-squares refinement is described in Section 2.1.2.

2.2.2.1 Structure Factor and Electron Density Maps

Electron density provides a numerical measure for the probability of an electron being in a particular position. A map of these shows the projected distribution of electrons throughout a volume of crystal. Electron density should be high in the vicinity of atoms and low elsewhere. Since the diffracted x-ray beam in an x-ray diffraction experiment is made up of the constructive interactions between the x-rays and electrons, the electron density of the crystal that causes a given diffraction pattern can be calculated. This requires the structure factor, which is essentially the amplitude scattered by the atoms in the unit cell divided by the amplitude scattered by a single electron [2].

The structure factor of a diffraction pattern represents amplitude and phase of the x-ray radiation scattered by one unit cell of a structure [19]. The structure factor is given by:

$$F(hkl) = \sum_j f_{j\theta} exp\left(i2\pi\left[hx_j + ky_j + lz_j\right]\right) \tag{2.13}$$

where $F(hkl)$ is the structure factor (which is dimensionless), hx_j is the fractional distance along the h direction that the j^{th} atom is found at, likewise for ky_j and lz_j. $f_{j\theta}$ is the scattering factor for the j^{th} atom and is implicitly related to the angle θ, [20]. $[hx_j + ky_j + lz_j]$ can also be written as $\boldsymbol{S} \cdot \boldsymbol{r}_j$, where $\boldsymbol{r}_j = x_j\boldsymbol{a} + y_j\boldsymbol{b} + z_j\boldsymbol{c}$ and $\boldsymbol{S} = h\boldsymbol{a}^* + k\boldsymbol{b}^* + l\boldsymbol{c}^*$.

This equation technically consists of a sum across j atoms; relatively simple to calculate for a small molecule, but since larger, more complicated molecular crystals also exist it is useful to have an integral form of Equation 2.13, by summing across all electrons in the cell:

$$F(hkl) = \int_{cell} \rho\left(\boldsymbol{r}\right) exp\left(i2\pi\boldsymbol{S} \cdot \boldsymbol{r}_j\right) dv \tag{2.14}$$

where $\boldsymbol{r} = x\boldsymbol{a} + y\boldsymbol{b} + z\boldsymbol{c}$, $\rho\left(\boldsymbol{r}\right)$ is the electron density at position $\boldsymbol{r}$ in the cell, with higher electron densities corresponding with atoms, and $dv = V \cdot dx\,dy\,dz$ [21], where V is the cell volume. This integral version of Equation 2.13 is in fact a Fourier transform of the electron density. As such, it is possible to calculate the electron density by taking the Fourier transform of the structure factor [22]:

$$\rho\left(\boldsymbol{r}\right) = \frac{1}{V} \sum_h \sum_k \sum_l F(hkl) exp\left(-i2\pi\boldsymbol{S} \cdot \boldsymbol{r}_j\right) \tag{2.15}$$

Since dv was multiplied by V, this needs to be taken into account in the calculation of

Table 2.6: R-factors for a single crystal refinement in SHELXL. [23]

Value	Equation
R1	$\frac{\sum \big\lvert \lvert F_o \rvert - \lvert F_c \rvert \big\rvert}{\sum \lvert F_o \rvert}$
wR2	$\left(\frac{\sum w(F_o^2 - F_c^2)^2}{\sum w F_o^2} \right)^{1/2}$
GoF	$\left(\frac{\sum w(F_o^2 - F_c^2)^2}{\sum (N_R - N_P)} \right)^{1/2}$

the electron density. From this, the difference in the observed and calculated electron densities can be obtained, which can then be mapped in two or three dimensions to probe the disagreements between the model and the observed data. Using this difference Fourier method, it is possible to find missing atoms, displaced atoms, and atoms incorrectly assigned an isotropic atomic displacement parameter which should have an anisotropic atomic displacement parameter [1].

2.2.2.2 Model Quality

Table 2.6 shows the R-factors for SHELXL, where: F_o is the structure factor of the observed data, F_c is the structure factor from the calculated structure, GoF is the Goodness of Fit, w is the weighting factor, N_R is the number of independent reflections and N_P is the number of refined parameters. The simplest R-Factor is given in Table 2.6 as R1, which compares the structure factors directly. However, it is now more common to use the F^2 factors, as these utilise the data better, with negative comparisons possible. The weighted R factor is commonly used, given in Table 2.6 as wR2, which can be seen to be dependent on F^2 as well as being moderated by a weighting factor. In these refinements, the factor R was the most commonly used to determine whether a model was increasingly describing the data or not as it was refined. In addition to these, the residual electron density maps discussed in Section 2.2.2.1 also provide a measure for how well the calculated model and observed data agree.

Table 2.7: Megaw Parameters for an $R3c$ crystal.

	x	y	z
A	0	0	$\left(\frac{1}{4}+s\right)$
B	0	0	t
O	$\left(\frac{1}{6}-2e-2d\right)$	$\left(\frac{1}{3}-4d\right)$	$\frac{1}{12}$

2.2.2.3 Tilt Parameters

There are multiple ways of parameterising a rhombohedral cell with hexagonal axes. The most commonly used one has the A-site taken to occur at the vertex of the a, b and c lattice parameters, so would be found at $A_x = 0$, $A_y = 0$, $A_z \approx 0$. However, to use the description of the tilt in the system known as Megaw parameters [24], the B-site needs to occupy this position, resulting in $A_x = 0$, $A_y = 0$, $A_z \approx 0.28$ and $B_x = 0$, $B_y = 0$, $B_z \approx 0$ for BFO.

With this orientation, the Megaw parameters in Table 2.7 can be calculated, where s is the displacement of the A-site, t is displacement of the B-site from the centre of the octahedron, d is the distortion. i.e. the difference between the size of the upper and lower faces of the octahedron and e is the displacement of an octahedral face from its ideal position, resulting in a rotation, or tilt, of the whole octahedron in that direction. This tilt angle of the oxygen octahedron, ω, can be calculated:

$$tan(\omega) = 4\sqrt{3}e \tag{2.16}$$

These tilts have an effect on the size of the lattice parameters required to describe the cell [25]. The Megaw orientation is the standard orientation used by this group, and the values s , t , d, e and ω provide a compact way of discussing the atomic positions in an $R3c$ rhombohedral cell. In an $R3m$ rhombohedral cell, $e = 0$.

2.2.3 JANA2006 Refinements

JANA2006 [26] is a program that also uses a least-squares fitting to minimise the difference between the observed and modelled data. JANA2006 was created to solve and refine regular, modulated and composite structures from single crystal diffraction data, but its use in this thesis is due to its ability to model anharmonic atomic displacement parameters (discussed in Section 2.2.3.2 and its ability to model multiple crystal structure phases simultaneously.

Table 2.8: JANA2006 Parameters. Since JANA2006 offers the option to refine with respect to F or F^2 both sets of R-factors are included.

Value	Equation (F based)	Equation (F^2 based)
Weighting	$w = \frac{1}{\sigma^2(\lvert F_o \rvert) - (uF_o)^2}$	$w' = \frac{w}{4{F_o}^2}$
P	$\sum w(\lvert F_c \rvert - \lvert F_o \rvert)^2$	$w'({F_o}^2 - {F_c}^2)^2$

2.2.3.1 Model quality

Table 2.8 gives the residual factors for JANA2006, in addition to those defined for SHELXL in Table 2.6 which are also used in JANA2006, where σ is the estimated standard deviation (ESD), u is the instability factor, which is set by the user and is not refined; it should be consistent across all measurements on the same diffractometer and P is the minimised function.

In JANA2006, these are further subdivided by 'all' and 'observed'. A reflection is considered 'observed' if the intensity I $>k\sigma(I)$, where k is user defined. Generally, all data should be used, including the weaker 'unobserved' reflections, and in the work included in this thesis all data has been included. The R-factor is based on F_o and F_c, irrespective of whether the refinement is based on F or F^2 [27].

2.2.3.2 Anharmonic Atomic Displacement Parameters

One of the advantages to using JANA2006 over other refinement programs such as SHELXL is its ability to describe anharmonic atomic displacement parameters. Atomic displacement Debye-Waller factors are normally modelled as a harmonic function representing a Gaussian probability distribution in real space for an atom around the location it is modelled as occupying (discussed in Section 2.1.3.2). While most measurements do have some level of anharmonicity to them, this is not normally strong enough that another model is required to adequately model the data [10].

There are some exceptions to this; ionic conducting materials may also be best fitted with anharmonic ADPs, as may materials near a phase transition. The most interesting exception for this thesis though is for materials in which the short range order does not match the long range order, such as in relaxors [28].

Anharmonic ADPs are described in terms of the Gram-Charlier series. In this thesis, terms up to the 4th order tensor have been used, but terms up to the 6th order have been used elsewhere [29]. The Fourier transform of the Gram-Charlier series gives:

$$P(u) = P^{harm}(u)\left[1 + \frac{1}{3!}C^{jkl}H_{jkl}(u) + \frac{1}{4!}D^{jklm}H_{jklm}(u) + ...\right] \tag{2.17}$$

where P is the probability distribution function, P^{harm} is the harmonic probability distribution function , u is the atomic displacement, C^{jkl} and D^{jklm} are sets of coefficients (10 in C^{jkl} and 15 in D^{jklm}), and $H_{jk...}$ are the Hermite polynomials. In a cubic function, all of $C^{jkl} = 0$. D^{jjjj} all have the same non-zero value, and D^{jjkk} all have the same non-zero value. All other $D^{jklm} = 0$ [30]. It should be noted that there is no direct physical meaning for any given parameter of C^{jkl} or D^{jklm} outside of the equation; they are not directly related to any spacial arrangement in the same way as the parameters of the harmonic displacement parameters.

2.3 Methods Complimentary to X-ray Diffraction

In addition to the x-ray diffraction methodologies described so far, there were also some other analysis methodologies used to determine other parameters of the material or to confirm those found in the x-ray diffraction experiments.

2.3.1 Scanning Electron Microscopy

A scanning electron microscope (SEM) allows analysis of a material at the micrometre to nanometre scale. In this thesis, a magnification of the order of 13,000x was used. The area to be analysed is irradiated with a finely focussed beam of electrons, generated by the heating of an element such as tungsten. In this thesis, a tungsten hairpin filament is used. This beam can either be swept across the surface in a raster, forming an image, or focussed on one single point to analyse that point specifically, depending on the mode of analysis undertaken. The interaction of the beam with the material produces a number of physical phenomena, most interestingly for the analysis undertaken in this thesis, backscattered electrons, secondary electrons and characteristic x-rays [31]. Backscattered electrons and secondary electrons allow an image of the surface topography to be generated, and due to the large depth of field, this image has a three-dimensional effect to it, with different heights and shadows visible, making it easier to understand the nature

of the topography [32]. The characteristic x-rays allow analysis of the chemical composition of the material to be conducted.

2.3.1.1 Energy-Dispersive X-Ray Spectrometry (EDX)

Energy-Dispersive X-Ray Spectrometry (known as EDS or EDX; the latter will be used in this thesis) is a method for determining the chemical composition of a material analysed through SEM methods. It can be used both qualitatively and quantitatively. Electrons from the electron beam can eject inner shell electrons from atoms in the material under analysis, which leaves the atom in an excited state. Outer orbital electrons release discrete energies in the form of photons in order to fill the inner shell vacancy, resulting in a discrete set of x-ray frequencies being emitted. By measuring the x-ray frequencies emitted by this process, and their relative intensities, it is possible to build a model for the atoms making up the sample [32].

Since these x-rays will often have to pass through the material in order to be detected, some corrections are necessary to ensure the correct interpretation of the data is achieved. In this thesis, ZAF corrections (corrections due to the atomic number (Z), the absorption (A) and the fluorescence (F)) have been applied automatically by the software used to analyse the EDX data through an *EDAX* system; a thorough description of ZAF corrections is given by Dekker [33].

By observing the characteristic x-rays as a function of position, as in a raster SEM image, elemental maps can be constructed, which mean that areas with higher or lower concentrations of a given element can be observed, which can allow the characterisation of structures within the sample.

2.3.2 Thermal Analysis

Thermal analysis is a blanket term for various measurements taken as a function of temperature. In this thesis, combined Thermogravimetric Analysis (TGA) and Mass Spectrometry (MS) were used, using a *Mettler Toledo DSC1-Star* system.

TGA is a technique where the mass is measured as a function of time. The temperature is either changed at a constant rate, or held at a given temperature, while the measurements are taken [34]. This allows a measure of the change in mass with temperature, or if the sample is heated and then cooled, a measurement of the change in temperature as a result of the whole heating process.

MS is a varied technique, but there are some broad steps followed in all cases: A material is ionized. The ionized material is then analysed by mass, often separated

by mass-to-charge ratio by utilising a magnetic or electric field. This distribution is then detected, usually both by this ratio and their relative abundance. All of this is operated under high vacuum conditions [35]. From this, the materials can be identified. In the case of MS in the context of thermal analysis, this can be combined with TGA to observe the temperature at which a material is given off from the material, at which point the vapour is ionised, to determine its composition through MS.

2.3.3 Birefringence

Transparent crystals are rarely optically isotropic; in other words, the refractive index varies depending on the direction through which the light is propagating through the crystal. These differences in refractive index with respect to propagation direction are represented by a surface, which generally forms an ellipsoid. This is generally known as an optical indicatrix [36] (though is also known as an index ellipsoid [37]). The major and minor radii of this ellipsoid give the refractive indices experienced by waves propagating in those directions; for any general direction of travel in such an anisotropic material, an elliptical cross section of the optical indicatrix is observed. The difference between the axes gives the linear birefringence.

The symmetry of a system defines the form of optical anisotropy possible (uniaxial or biaxial) and also the orientation of the optical indicatrix with respect to the crystal axes; as such, from observing the optical indicatrix, it is possible to derive the crystal system and symmetry to which a material belongs [38].

2.4 References

Bibliography

[1] Giacovazzo, C., Monaco, H. L., Viterbo, D., Scordari, F., Gilli, G., Zanotti, G., Catti, M., *Fundamentals of Crystallography*, (Oxford University Press, Oxford1992), 2 edn.

[2] Hammond, C., *The Basics of Crystallography and Diffraction*, (Oxford University Press, Oxford2009).

[3] Azároff, L. V., Kaplow, R., Kato, N., Weiss, R. J., Wilson, A. J. C., Young, R. A., *X-Ray Diffraction*, (McGraw-Hill, Inc.1974).

[4] Rietveld, H. M., *Acta Crystallographica*, **22**:151 (1967).

[5] Rietveld, H. M., *Journal of Applied Crystallography*, **2**:65 (1969).

[6] Young, R. A., *The Rietveld Method*, (Oxford University Press, Oxford1993).

[7] Coelho, A. A., 'Topas-Academic Version 6 Technical Reference,' Tech. rep., Bruker-AXS (2016).

[8] Thompson, P., Cox, D. E., Hastings, J. B., *Journal of Applied Crystallography*, **20**:79 (1987).

[9] Krill, C., Haberkorn, R., Birringer, R., *Specification of microstructure and characterization by scattering techniques*, vol. 2 (2000).

[10] Kuhs, W. F., *Acta Crystallographica Section A*, **48**:80 (1992).

[11] Stephens, P. W., *Journal of Applied Crystallography*, **32**:281 (1999).

[12] {Agilent Technologies Ltd, Yarnton, Oxfordshire, England}, 'CrysAlis PRO,' (2014).

[13] Luger, P., *Modern X-ray analysis on single crystals : a practical guide*, (Berlin, Germany : De Gruyter2014).

[14] Clark, R. C., Reid, J. S., 'The Analytical Calculation fo Absorption in Multifaceted Crystals,' .

[15] Howells, R. G., *Acta Crystallographica*, **3**:366 (1950).

[16] Clark, R. C., *Acta Crystallographica Section A*, **49**:692 (1993).

[17] Hahn, T. (Ed.), *International tables for crystallography volume A: space-group symmetry*, (The International Union of Crystallography2005), fifth edn.

[18] Sheldrick, G. M., *ACTA CRYSTALLOGRAPHICA SECTION A*, **64**:112 (2008).

[19] Glusker, J. P., Trueblood, K. N., *Crystal Structure Analysis*, (Oxford University Press, Oxford1985), 2 edn.

[20] Ladd, M., Palmer, R., *Structure determination by X-ray crystallography* (2006).

[21] Drenth, J., *Principles of Protein X-Ray Crystallography*, (Springer-Verlag New York, New York1999), 2 edn.

[22] Sherwood, D., J. Cooper, *Crystals, X-rays and Proteins*, (Oxford University Press, Oxford2011).

[23] Müller, P., Herbst-Irmer, R., Spek, A. L., Schneider, T. R., Sawaya, M. R., *Crystal Structure Refinement: A Crystallographer's Guide to SHELXL* (2010).

[24] Megaw, H. D., Darlington, C. N. W., *Acta Crystallographica Section A*, **31**:161 (1975).

[25] Glazer, A. M., *Acta Crystallographica Section B Structural Crystallography and Crystal Chemistry*, **28**:3384 (1972).

[26] Petíček, V., Dušek, M., Palatinus, L., *ZEITSCHRIFT FUR KRISTALLOGRAPHIE*, **229**:345 (2014).

[27] Petíček, V., Dušek, M., Palatinus, L., *Institute of Physics, Academy of Sciences of the Czech Republic*, **162**:53 (2006).

[28] Kiat, J.-m., Baldinozzi, G., Dunlop, M., Masson, O., **8411** (2000).

[29] Boysen, H., in 'Accuracy in Powder Diffraction II,' (165–175) (1992).

[30] Yamanaka, T., Ahart, M., Nakamoto, Y., Ye, Z.-g., Gramsch, S. A., Mao, H.-k., Hemley, R. J., **174108**:1 (2012).

[31] Krinsley, D. H., Pye, K., Boggs, S., Tovey, N. K., in 'Backscattered Scanning Electron Microscopy and Image Analysis of Sediments and Sedimentary Rocks,' chap. 2, (4–24) (2010).

[32] Goldstein, J. I., Lyman, C. E., Newbury, D. E., Lifshin, E., Echlin, P., Sawyer, L., Joy, D. C., Michael, J. R., *Scanning Electron Microscopy and X-Ray Microanalysis*, (Springer, New York2007), 6 edn.

[33] Dekker, M., *Handbook of X-ray Spectrometry*, (Marcel Dekker Inc., New York1993).

[34] Bottom, R., in 'Principles and Applications of Thermal Analysis,' (87–118) (2007).

[35] Yates, J. R., *Mass spectrometry - A Textbook*, vol. 16, (Springer2000), 2 edn.

[36] Glazer, A. M., Lewis, J. G., Kaminsky, W., **452**:2751 (2012).

[37] Scharf, T., in 'POLARIZED LIGHT IN LIQUID CRYSTALS AND POLYMERS,' (19–36) (2007).

[38] Gorfman, S., Glazer, A. M., Noguchi, Y., Miyayama, M., Luo, H., Thomas, P. A., *Journal of Applied Crystallography*, **45**:444 (2012).

Chapter 3

Room Temperature Powder Investigation

3.1 Introduction

This chapter describes the work done to investigate the
(1-x) $BiFeO_3$-(x) $(K_{0.5}Bi_{0.5})TiO_3$ (BFO-KBT) system through the preparation of powder samples, culminating in a room temperature phase diagram of the system. The investigation covered the full x = 0 to x = 1 range, although more focus was initially put on the region from x = 0 to x = 0.5. Powder samples were investigated through x-ray powder diffraction methodology, with the collected data interpreted by Rietveld analysis. The results are displayed and discussed in this chapter.

When discussing the BFO-KBT system, it is useful to be able to discuss the mol% of KBT. If a '% KBT' is mentioned here, this shall refer to the 'mol% KBT' value. When discussing the end members of 0% KBT, i.e. BFO and 100% KBT, these will be referred to simply as end members.

3.2 Sample Preparation

The BFO-KBT powders were synthesised from the following powders:
Bi_2O_3 (Alfa Aesar, 99.99%);
Fe_2O_3 (Alfa Aesar, 99.99%);
K_2CO_3 (Alfa Aesar, 99.997%);
TiO_2 (Sigma Aldrich, 99.9%).

The BFO-KBT powders were prepared by first calculating the amount of each of the powders mentioned necessary for the x value chosen. This was calculated by

molar mass where the mass of the total powder required and the percentage of BFO and KBT was used to determine the number of moles of BFO and KBT required for that final output. From there, the chemical formulae for making BFO and KBT were used to calculate how much of each reagent was necessary, shown in the equations 3.1 and 3.2:

$$Bi_2O_3 + Fe_2O_3 => 2BiFeO_3 \tag{3.1}$$

$$Bi_2O_3 + K_2CO_3 + 4TiO_2 => 4(0.5K0.5Bi)TiO_3 + CO_2 \tag{3.2}$$

The powders were dried for 2 hours at 200°C at a ramp rate of 5°C per minute, both heating and cooling, to ensure that powders weighed for the next section would be the dry weight. This was especially important for the potassium carbonate because it tended to absorb significantly more water than the other raw powders, which would then adversely affect the stoichiometry.

Once dried, the masses were more reliable, so the calculated weight of each powder was weighed out utilising a weighing balance, accurate to ± 0.001g. The samples were ball milled with zirconia-stabilised (ZiO_2) ceramic beads for 20 hours in isopropanol in plastic milling vessels.

Once milled, the sample was emptied into an evaporation dish, with more isopropanol used to ensure that all of the powder was extracted and left to dry in an oven at 70°C, taking at least 48 hours. The residue was collected and crushed into a fine powder using a pestle and mortar, ensuring that the powder was thoroughly mixed and homogeneous.

3.2.1 Calcining/Sintering Investigation

It was important to have a reliable basis for the synthesis of samples, so an investigation was undertaken to find the optimum calcination and sintering methodologies. To this end, samples were synthesised with different calcining and sintering times in order to determine which produced the least impurity phase, as has been reported in the literature [1].

Initial calcine times were obtained from references [2, 3], and these were then modified to give the results with least impurity phase. The ramp rates were all a uniform 3°C per minute, both for heating and cooling. This was also the ramp rate used for sintering the samples. Once calcined, the samples were crushed into a fine powder using a pestle and mortar. It was found that the calcined powder was not phase pure, which can be seen in Figure 3.1, showing an example calcined

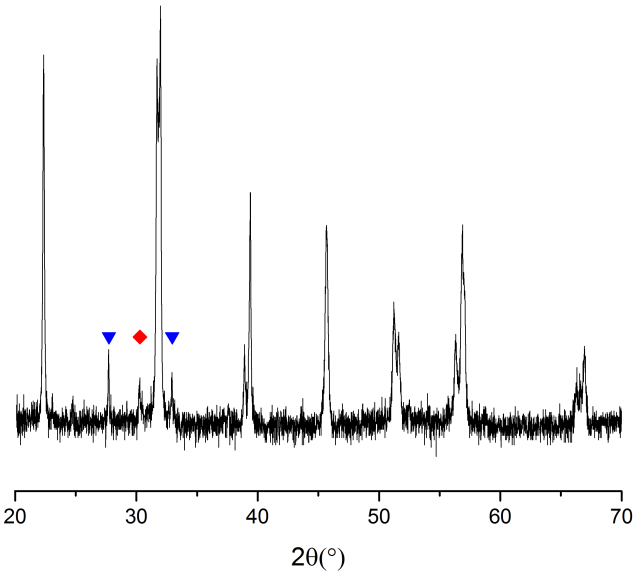

Figure 3.1: 45 minute x-ray diffraction measurement of 20% KBT calcined powder. The blue triangles correspond to $Bi_{12}TiO_{20}$ and the red diamond corresponds to $Bi_5Ti_3FeO_{15}$.

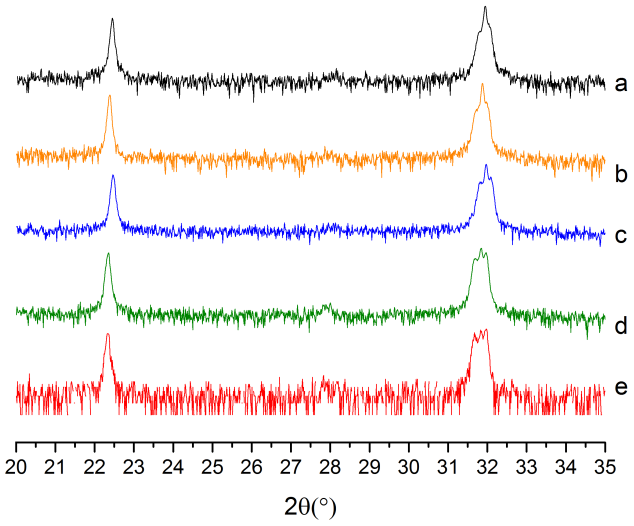

Figure 3.2: A comparison of sintering times and temperatures in 20 mol% KBT BFO-KBT presented as a stacked plot of logarithmic values. These were taken over 45 minutes. From top to bottom, these were sintered at 1000°C for 4 hours, 1000°C for 3 hours, 1000°C for 2 hours, 950°C for 2 hours and 900°C for 2 hours.

powder of 20% KBT. Extra phases can be seen highlighted around 27.5° 2θ,and 33° 2θ in blue corresponding to $Bi_{12}TiO_{20}$ and around 31° 2θ corresponding to $Bi_5Ti_3FeO_{15}$ in red. Impurity phases like these were found in all calcined powders; it proved impossible to find a phase pure calcined powder. Well defined impurity peaks can be resolved in Rietveld refinement, so do not have a significant impact on the quality of a refinement, but it is better to start with as close to a phase pure sample as possible.

A batch of the calcined powders were then sintered. Since it was possible to generate almost phase pure powders by sintering, more emphasis was put on ensuring good sintering values. In Figure 3.2, five examples of sintered powders can be seen with varying sintering temperature and time. It was found from c, d and e that the impurity phase was decreased with increasing temperature, but it was already known that sintering at 1050°C would result in the sample melting, meaning that 1000°C was the optimum temperature reached for 20 mol% KBT. For higher KBT content samples, a higher temperature was possible and thus was used.

Different lengths of time for sintering were investigated. Between 2 and 3 hours, impurity phase around 27° 2θ was decreased slightly. However it then increased slightly by sintering for 4 hours, so the final decision was to use the 1000°C 3 hour sintered sample. The impurity phase around 27° 2θ the samples was found to be Bi_2O_3, despite bismuth being reported in the literature as the element most commonly lost upon heating from other sources due to volatility [4, 5, 6, 7]. In addition, in KBT it was known that potassium volatility causes problems in synthesis [8]. As such, a selection of samples were weighed before and after calcining, and before and after sintering. It was found that the majority of mass loss was moisture, with dry mass loss around 0.3% found for calcining and mass loss around 0.3% found for sintering. The samples were synthesised from a stoichiometric mix of reagents. This would be unlikely to result in a stoichiometric final sample because of the volatility issues discussed, but the SEM EDX measurements from Section 3.2.2 did not observe any large systematic variations from a stoichiometric sample.

Once sintered, the powders were then re-crushed into a fine powder with a pestle and mortar. These initial experiments made clear that there was a danger of the samples melting, which would result in an unusable sample. Because of this, some samples required a lower calcine and sintering temperature, which was offset by calcining or sintering for longer. Table 3.1 lists the calcine temperatures and times, and the sintering temperatures and times.

The heating processes were conducted in alumina crucibles. These crucibles were necessary to ensure a sealed environment for the reaction, preventing the loss

Table 3.1: BFO-KBT sample table with calcine time/temperature and sintering time/temperature for each sample. Different sintering times and temperatures were experimented with to produce the best samples possible. It was found that 1050°C was an acceptable temperature away from the end members, allowing samples with little impurity phase to be produced and not resulting in melted samples, but closer to the end members was likely to result in melting. The samples indicated with * were synthesised by project students, K. Zahra and S. M. Johari, using the same equipment, powders and methodology.

Composition (%KBT)	Calcine Temperature (°C)	Calcine Time (Hours)	Sinter Temperature (°C)	Sinter Time (Hours)
0	790	2	800	5
10*	850	4	900	2
15	900	2	950	5
20	900	2	1000	3
25	900	2	1050	2
30	900	2	1050	2
33	900	2	1050	2
40	900	2	1050	2
50	900	2	1050	2
60*	900	4	1050	2
70*	900	4	1050	2
80*	850	4	1050	2
90*	850	4	1075	2
100	850	12	1030	20

of any volatile compounds. In order to prevent the reaction with the crucibles which was found at high temperature, all samples were placed on a platinum plate inside the alumina crucibles. This prevented any contact with the alumina crucibles, ensuring the purity of the sintered powders. Over time, it was found that the alumina crucibles would become stained with BFO-KBT. Multiple crucibles were used to prevent contamination of the samples. In order to ensure they were completely clean between samples, the platinum plates were cleaned with hydrochloric acid.

3.2.2 Scanning Electron Microscopy

A representative selection of the final sintered powders were examined with scanning electron microscopy (SEM) to check the stoichiometry through Energy-Dispersive X-Ray Spectrometry (EDX) using an *EDAX* system. The selection of samples studied provided a baseline for the expectations for the final composition compared to the nominal composition of the synthesised samples.

Gold coating of the samples was required to attain meaningful results from the SEM equipment because the powder was found to charge quickly which made measurements unreliable. Since BFO is known to be a good conductor, this could be an effect of the possible non-stoichiometry of the samples. The gold coating allowed the charging to be circumvented as long as the electron beam was not focussed on any single point for longer than 30s; sufficient time for long scans, as long as a wide enough area was scanned. The samples were mounted on a carbon pad stuck on an aluminium base, which meant that powders investigated would generally also show gold, carbon and aluminium peaks.

To determine the composition of the powders, several methods were used in tandem. The first and simplest was to compare the ratios of the A site atoms and B site atoms to see how well that ratio matches the predicted amount. In other words, the ratio of Bi:K and Fe:Ti, which would be expected to vary by composition.

For a 30% powder, as an example, the ratio of Fe:Ti should be 70:30, and for Bi:K 85:15. These ratios provided a quick check that the powders were approximately correct, and could easily be calculated while data were being collected.

A more sophisticated method was also used, looking at each atomic quantity in isolation and comparing this with a known quantity of that atom which should exist in the whole. Examples of this can be seen in Table 3.2. Here, the compositional percentage from the EDX measurements are compared with a look up table calculated for the expected compositional percentages for each element for each mol% KBT composition. The observed mol% KBT compositions from these

Table 3.2: Two examples for the 30% KBT powders. The left hand table shows the results from a powder which was formed as a part of a pellet, while the right hand table shows results from a loose powder. In both cases, they can be seen to be close to the nominal compositions of 30% (errors calculated as 1 standard deviation of a reliable selection of data)

Pellet			Powder		
Element	Composition %	KBT %	Element	Composition %	KBT %
Bi	42.7(4)	30	Bi	41.4(4)	34
K	8.4(4)	34	K	7.3(4)	30
Ti	15.6(8)	31	Ti	14.7(8)	29
Fe	33.3(9)	33	Fe	36.6(9)	27

tables are then listed. For example, at 100% KBT, there would be 25% Bi, 25% K, 50% Ti. At 0% KBT, there would be 50% Bi, 0% K, 0% Ti, 50% Fe. So if the compositional percentage obtained from the EDX measurements for Bi was 50%, this would correspond to a mol% KBT of 0%.

Comparing each atom's percentage in the EDX measurements with the known values for that particular atom in a given mol% KBT, it is possible to discern the mol% KBT that the measured atomic percentage corresponds to, meaning that a mol% KBT was calculated individually for each atom. Once these were completed for each of the four atoms observed, they were compared with one another and the nominal composition expected.

So, drawing both of these methods together, the example on the left of Table 3.2 would be in the range 30-34% KBT, with a nominal composition of 30%. The ratios given from the other method for this powder give approximately 33% by Bi:K and 32% by Fe:Ti, so this powder is around 32% $\pm$ 2%.

For the example on the right of the table, the range is from 27% to 34%. Bi:K gives a composition around 30%, Fe:Ti gives a composition around 29%, so this was considered to be 30% $\pm$ 4%.

While the errors on the calculations were generally in the range of 2% - 5%, the average values for the powders investigated in this way (15%, 20%, 30%) were within 2% of the nominal compositional values. From this, the methodology for generating the powders was considered to produce good enough results that the nominal compositions could be used in calculations and occupancies when analysing the data.

In addition, to investigate whether the sintered powder was made up of a single mixed material or grains of BFO and grains of KBT, elemental mapping was employed to search for differences in composition; if there were individual grains, then some regions of the map would have been found to be potassium and titanium

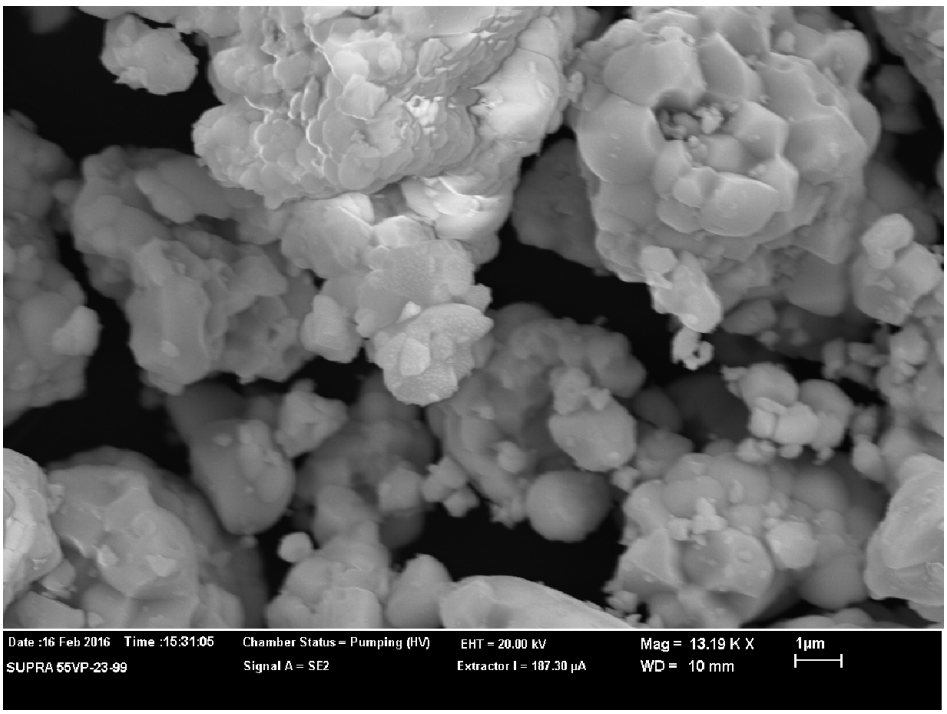

(a) SEM image of the 15% KBT powder, looking at individual grains.

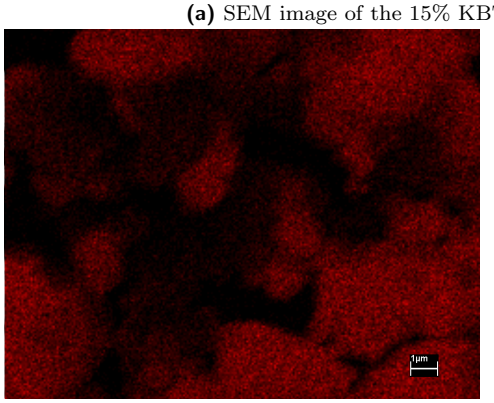

(b) Bismuth elemental map

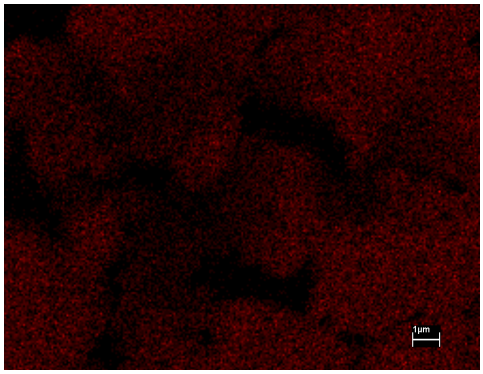

(c) Iron elemental map

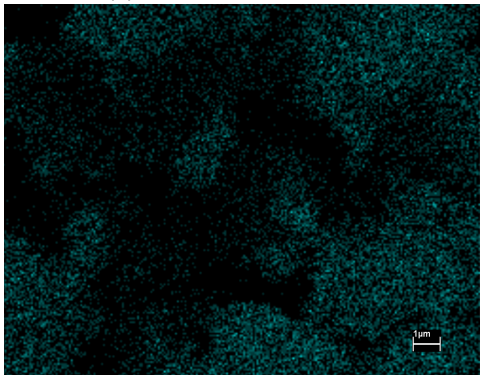

(d) Titanium elemental map

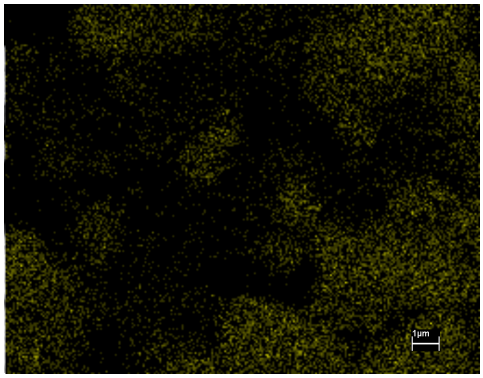

(e) Potassium elemental map

Figure 3.3: Elemental maps of the constituent parts of the 15% BFO-KBT and the raw SEM image of the scanned area for comparison. Note that all elements appear to coexist homogeneously through the sample. The scale bar on each is 1 µm.

rich and iron deficient, while others would have been found to be iron rich and deficient in titanium and potassium. Figure 3.3 shows an example of one of these SEM measurements, conducted on 15% KBT. Figure 3.3a shows that the sample range chosen was made up of multiple individual grains, the majority of which would be expected to be BFO with the remainder KBT in a mixed powder rather than a mixed material. Figure 3.3b shows the bismuth elemental map. Since bismuth is present in both BFO and KBT, this provides a useful baseline for the other graphs, showing the areas that would be expected to be picked up by the system. Figure 3.3c shows the iron elemental map, which can be seen to cover the same areas as the bismuth map, though since bismuth has the strongest response by being the heaviest element present, the other graphs are slightly less well defined. However, it is still clear that they cover the same area. Figure 3.3d shows the titanium elemental map, which is completely analogous to the iron map. As confirmation, the potassium map is included as Figure 3.3e, which is also completely analogous to the other maps. From these it can be concluded that the BFO-KBT powder is not a mix of BFO and KBT powder grains.

Focussing on any single grain was impractical, so elemental maps of single grains were not obtained. This was due to the effects of charging; a result of low conductivity in the material: an encouraging sign for the piezoelectric properties of the material, but a complicating factor for SEM measurements.

3.3 Room Temperature X-Ray Diffraction

As discussed in Section 3.2, the sintered powders were analysed by powder diffraction. These experiments used the spinner stage of a *Panalytical X-Pert Pro MPD* $K_{\alpha 1}$ diffractometer in Bragg-Brentano geometry.

First the powders were finely ground and packed carefully into the sample holders, ensuring a flat surface to ensure reliable data for later refinement. Measurements were generally taken between 20° 2θ and 90°, though for consistency the region from 20°2θ and 70°2θ is the region presented in the later Rietveld refinement presentations. This 2θ range was chosen as these were the areas of interest for refinement, with the strongest peaks. All measurements had the same step size, 0.0131° in 2θ and so the length of scan was varied only by the amount of time per step, with a longer time resulting in better counting statistics, or by altering the range in 2θ. Those powders found to be of good quality (i.e. showing little sign of impurity phases) in the initial scans, which took under an hour, were then measured again; these new measurements were in the range from 15 to 20 hours for better

counting statistics.

3.3.0.1 BFO and KBT End Members

A BFO end member sample and a KBT end member sample powder were both made, for comparison to the BFO-KBT powders. A sample of KBT was able to be synthesised without large amounts of impurity phase. BFO is notoriously difficult to synthesise as a phase pure powder [7], and while multiple attempts were made, large amounts of impurity phase were present in each of them. The best of these samples was chosen for this comparison.

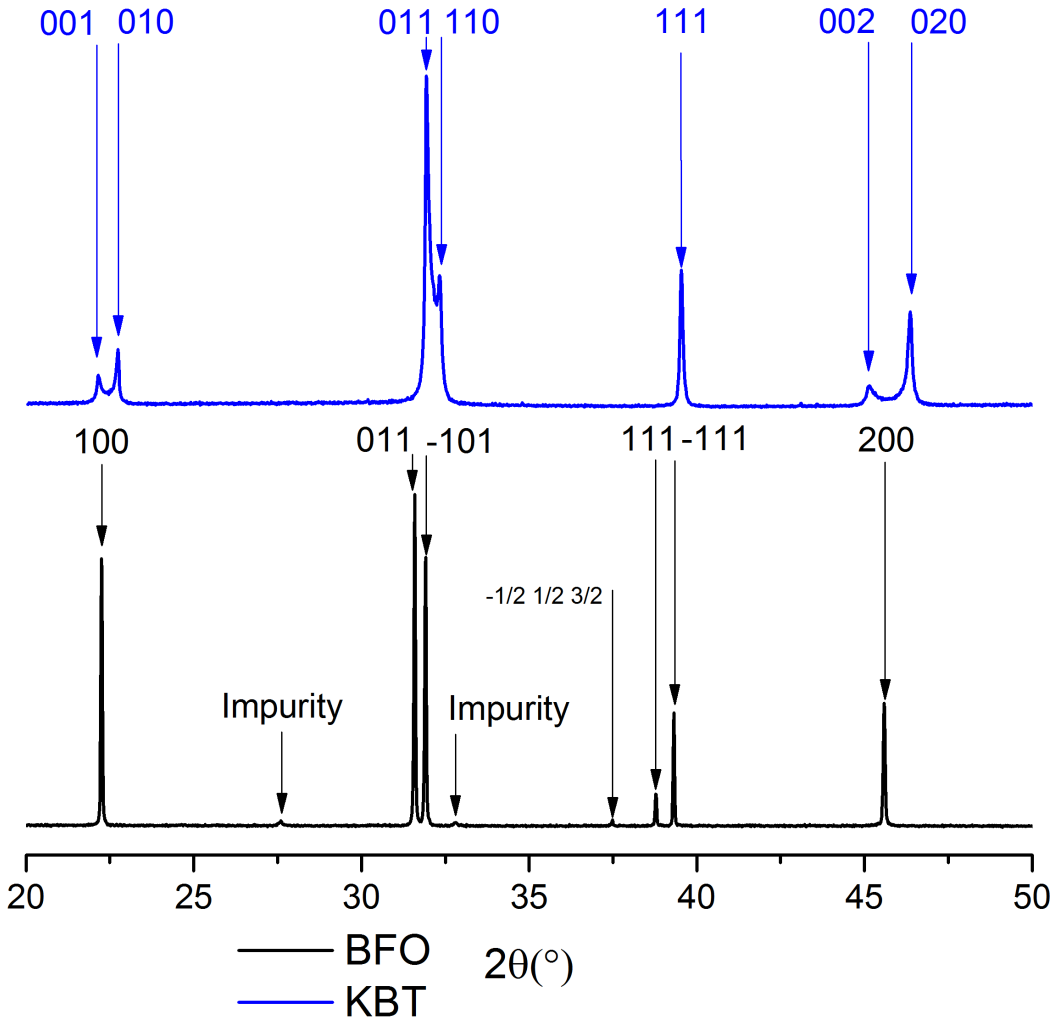

Figure 3.4: Comparison of the end members, with KBT above in blue and BFO below in black, showing the {100}, {110}, $\{\frac{1}{2}\frac{1}{2}\frac{3}{2}\}$ tilt peak,{111} and {200} peaks in cubic notation.

Figure 3.4 focuses on the area between 20° 2θ and 50° 2θ which allows a

clearer view of the {100}, {110}, {111} and {200} peaks (as well as the $\{\frac{1}{2}\frac{1}{2}\frac{3}{2}$ tilt peak) in cubic notation. It is clear to see that the KBT shows tetragonal peak splitting on the {100} and {110} peaks, but not the {111}, while the BFO shows rhombohedral peak splitting on the {110} and {111} peaks. From this, it would be expected that across the range of the mixing, the diffraction patterns would switch from one crystal system to the other, as they approach the other end member.

While the KBT powder shows little sign of impurity phase, the BFO shows several additional peaks between 25° 2θ and 35° 2θ, corresponding to a Bi_2O_3 impurity. Even with the impurity phases in the BFO, the differences between the main diffraction patterns are clear; BFO is consistent with an $R3c$ rhombohedral structure, while the KBT pattern is consistent with a $P4mm$ tetragonal structure.

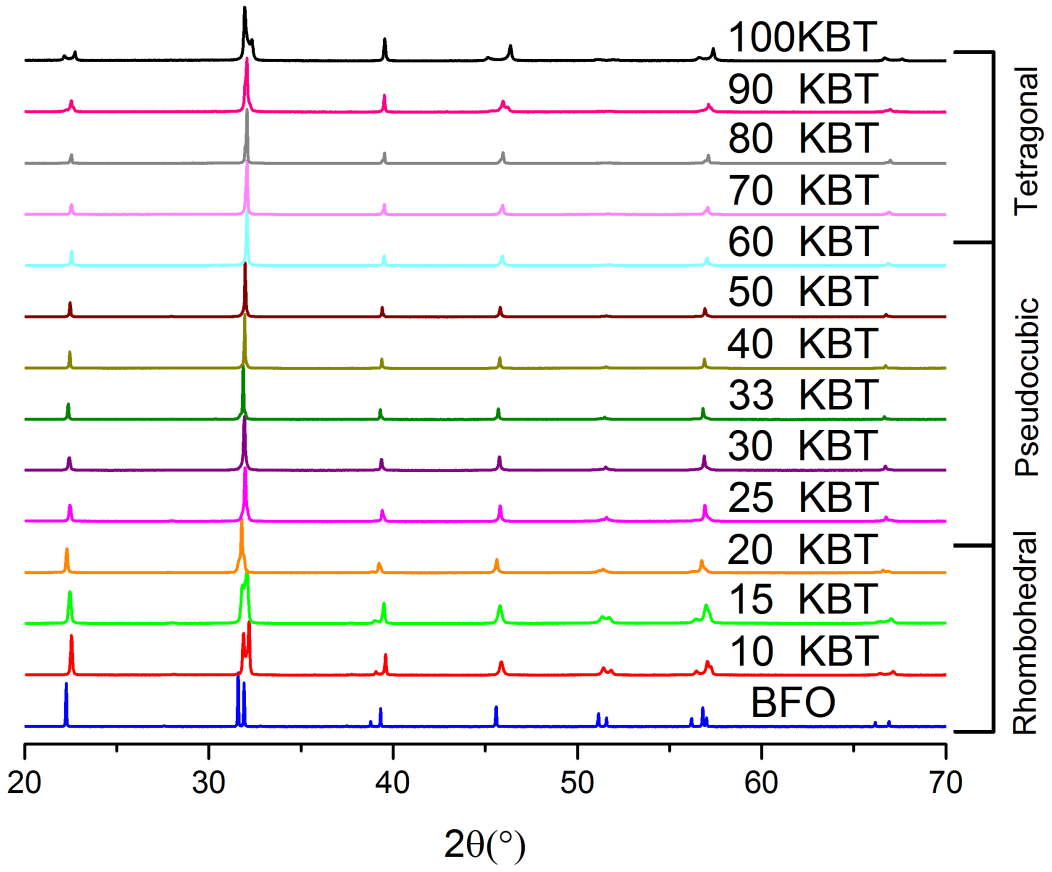

Figure 3.5: Comparison of the long (>6 hours) powder diffraction results in a stacked plot. Compositional regions have been identified through visual inspection as near-tetragonal, near-cubic and near-rhombohedral.

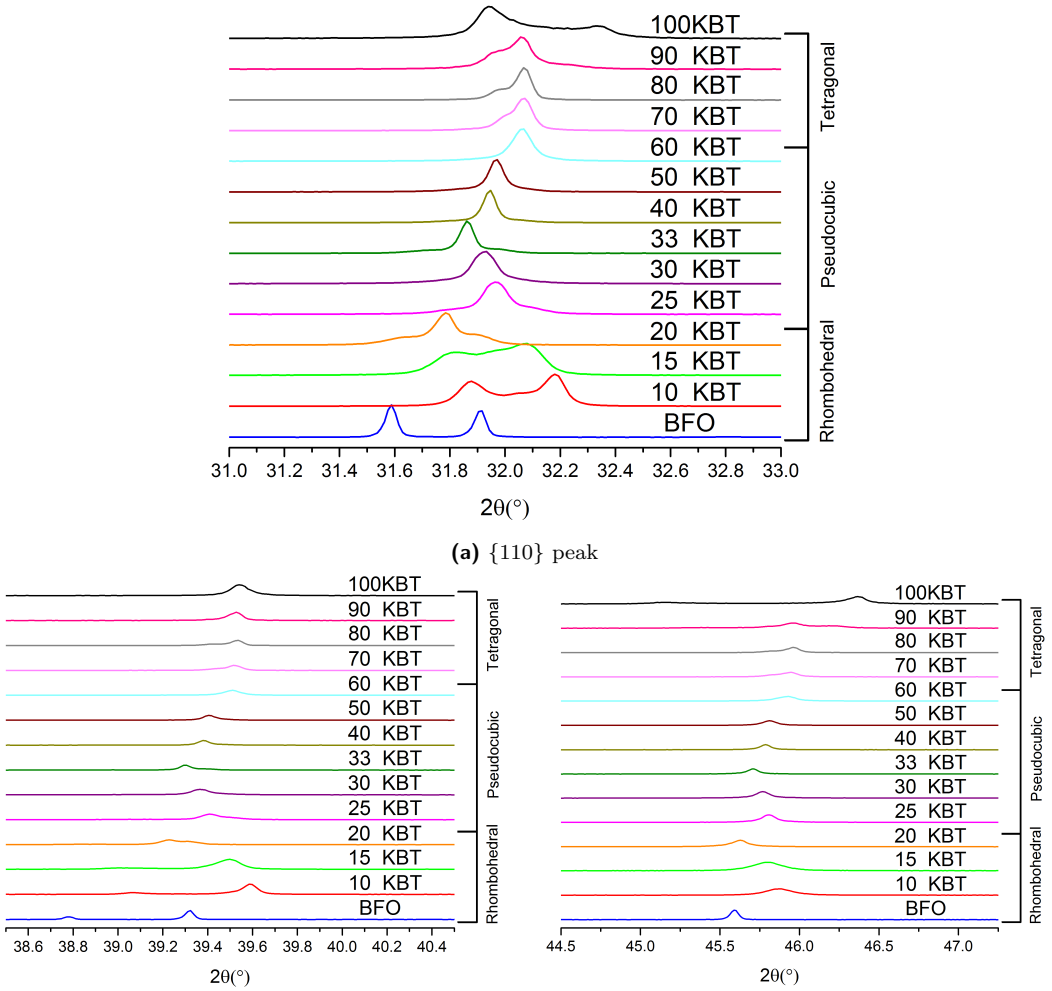

(a) {110} peak

(b) {111} peak

(c) {200} peak

Figure 3.6: Closer examination of Figure 3.5 powder diffraction 111 reflection. Each graph shows from high %mol KBT at the top to low %mol KBT at the bottom.

3.3.0.2 Mixed BFO-KBT

It is seen from the change in the peak shape in Figure 3.5 that as the KBT ratio is increased, the rhombohedral peak splitting intensities decrease while the intensity at the centre of those split peaks increase. This indicates that the system becomes less rhombohedral and more pseudocubic, appearing to be almost entirely pseudocubic by 50-60% KBT.

For further clarity, the {111}, {110} and {200} peaks have been highlighted in Figures 3.6b, 3.6a and 3.6c respectively. In a cubic system, none of these are split. In a rhombohedral system like the BFO end member, the {111} and {110} are both split, but the {200} is not. In a tetragonal system, like the KBT end member, the

{200} peak would be split. Figures 3.6b and 3.6a show from the peak splittings that as the KBT% is increased to around 60%, the system becomes more cubic, the rhombohedral intensity first shrinking and then diminishing to the point of being broader shoulders on the otherwise cubic looking peaks around 30% KBT. From 60% to 100% KBT, the peak splittings are consistent with the material becoming more tetragonal, first widening and then splitting. These observations provided a starting point for modelling the data by Rietveld refinement. The drift in the {110} peak with respect to composition is not a result of changes in sample height as these have been corrected, but is instead due to the phase coexistence in the material.

3.4 Rietveld Analysis

Rietveld refinement of the x-ray diffraction data was conducted to determine the structure of the material with respect to composition at room temperature. A Rietveld refinement requires a starting structural model; from the observation of the peak splitting in the diffraction data, the most likely candidates were thought to be a cubic system at mol% KBT between 30 and 60, with either rhombohedral or monoclinic at lower mol% KBT, and a tetragonal or monoclinic system most likely at higher mol% KBT. While the final systems proved to be more complicated than this, each requiring a multiphase model to fit the data, these different broad areas still provide a useful categorisation of the general appearance of the patterns at room temperature.

At high mol% KBT, an additional mixed phase structure was found to be necessary, splitting the high mol% KBT region further. An example of each of these multiphase refinements have been highlighted in this section, arranged in order of increasing mol% KBT and with the 'main' phase listed first and the 'mixed' phase listed second: rhombohedral mixed with cubic, cubic mixed with rhombohedral, cubic mixed with monoclinic and tetragonal mixed with monoclinic. While these four compositions have been highlighted, they are representative of the Rietveld refinement data gathered from each of the samples.

A difference plot has been included on all graphs below the plots. From the {110}, {111} and {200} peak figures, it is clear that the actual agreement between the model and observed data in all cases is very high.

At low mol% KBT, it was found that the BFO-KBT showed distinctly rhombohedral peak splitting, though the intensity between the peaks was found to be more intense than a simple, single phase rhombohedral was able to account for. A cubic $Pm\bar{3}m$ phase was added in addition to the rhombohedral $R3c$ phase. Both

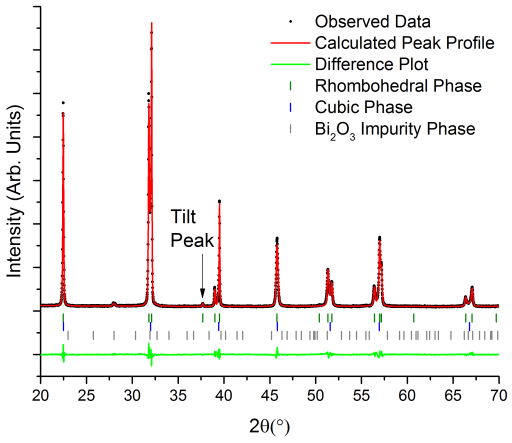

(a) 10% KBT powder, showing the cubic $Pm\bar{3}m$ and rhombohedra $R3c$ Rietveld peak profile for the full profile from 20° 2θ to 70° 2θ.

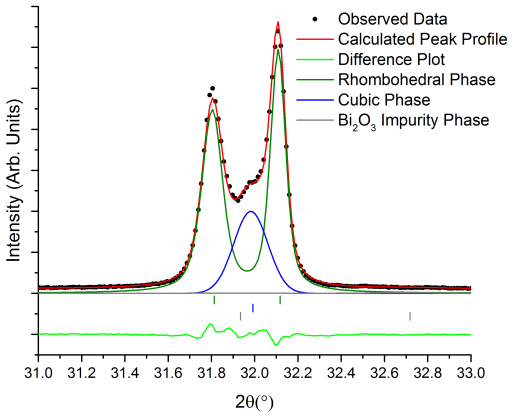

(b) 10% KBT powder, showing the cubic $Pm\bar{3}m$ and rhombohedral $R3c$ Rietveld peak profile for the {110} peak.

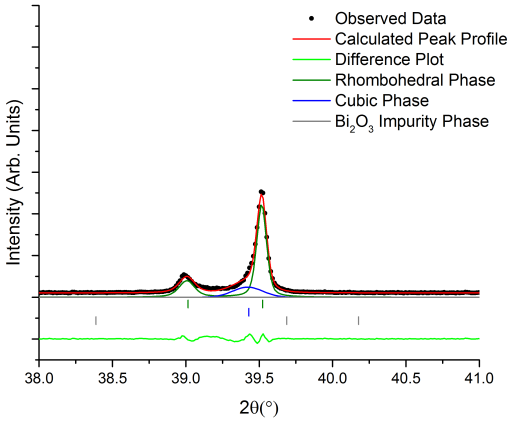

(c) 10% KBT powder, showing the cubic $Pm\bar{3}m$ and rhombohedral $R3c$ Rietveld peak profile for the {111} peak.

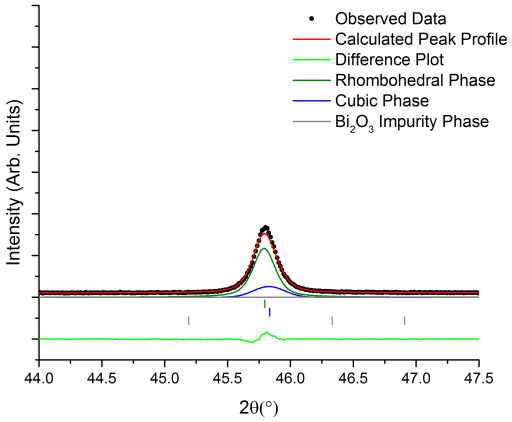

(d) 10% KBT powder, showing the cubic $Pm\bar{3}m$ and rhombohedral $R3c$ Rietveld peak profile for the {200} peak.

Figure 3.7: Plot of the cubic $Pm\bar{3}m$ and rhombohedral $R3c$ mixed phase Rietveld peak profile fitting for the data plots. The vertical lines below denote the peak locations. The difference plot shows the difference between the calculated and observed values. Cubic phase: 25.0(8)%, $R_{Bragg} = 1.020$. Rhombohedral phase: 73.9(8)%, $R_{Bragg} = 1.130$.

10% KBT and 15% KBT were found to be fitted well by this majority $R3c$, minority $Pm\bar{3}m$ phase structure.

Figure 3.7 shows the region between 20° 2θ and 70° 2θ for the 10% KBT sample. From the figure, the tilt peak can be seen to be present, confirming the rhombohedral component to be $R3c$ rather than $R3m$. The difference plot shows that there are no significant divergences between the observed data and the proposed model. Figure 3.7b shows the {110} peak, split in a rhombohedral system but not in a cubic one. The peak is seen to be split, but the intensity between the split peaks is higher than would be expected. The observed data is overlaid with the total model and the individual components, seen to compliment each other well, with the cubic phase providing intensity at the centre of the peak, while the rhombohedral phase provides the split peaks either side of the central intensity. The {111} peak, shown in Figure 3.7c is also split in rhombohedral systems but not in cubic systems. This peak was not fit as well by the model, but it is clear that it still requires both the rhombohedral contribution and some additional intensity in the centre. The {200} peak shown in Figure 3.7d is not split in cubic or rhombohedral systems, and is a clear single peak in the observed data.

In Figure 3.7b, the cubic peak is observed to have a large Full Width at Half Maximum (FWHM). This could result from disorder in the system, either static based on the mixed sites or dynamic as a thermal effect, or else could be a result of the grain size of the particles investigated (which can be calculated through the Scherrer equation).

An impurity phase was present in all BFO-KBT samples except for the 40% KBT sample. In low mol% KBT samples, this was identified in HIGHSCORE PLUS as Bi_2O_3, and was refined with the other present phases. In higher mol% KBT samples, this was identified as $Bi_5Ti_3FeO_{15}$. This impurity phase fraction was generally around 1%, with more detail included in the tabulated results in Tables 3.6 - 3.10 in Section 3.4.2.

As the mol% KBT was increased, it was found that the cubic phase was increased, while the rhombohedral phase diminished. A point where a single, unmixed cubic phase could be used to satisfactorily describe the peak profile was not found, so this is instead the compositional region where the rhombohedral phase is dominated by the cubic phase.

Figure 3.8a shows the Rietveld refinement of the 40% KBT sample, chosen as the best sample to include here since it is a stable region of mostly cubic BFO-KBT, with both 50% and 60% KBT showing little change to the phase proportions between cubic and rhombohedral phases, and the range of 20% to 40% increasing

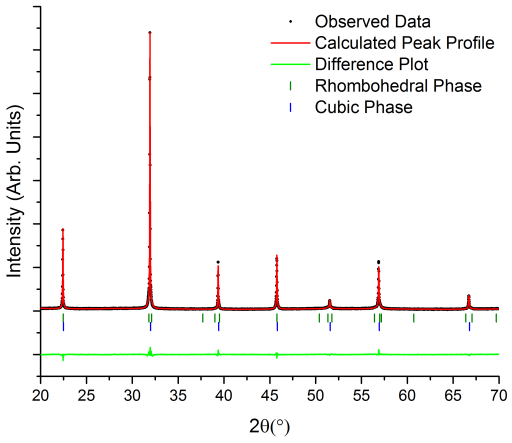

(a) 40% KBT powder, showing the cubic $Pm\bar{3}m$ and rhombohedral $R3c$ Rietveld peak profile for the full profile from 20° 2θ to 70° 2θ.

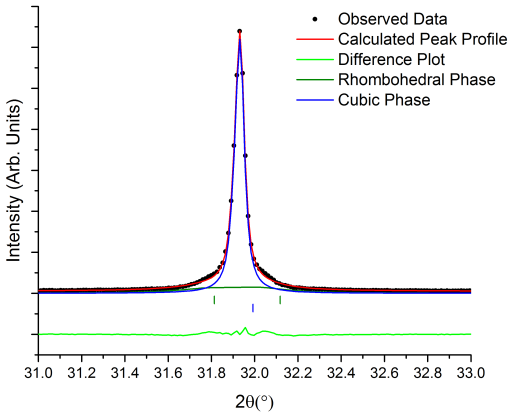

(b) 40% KBT powder, showing the cubic $Pm\bar{3}m$ and rhombohedral $R3c$ Rietveld peak profile for the {110} peak.

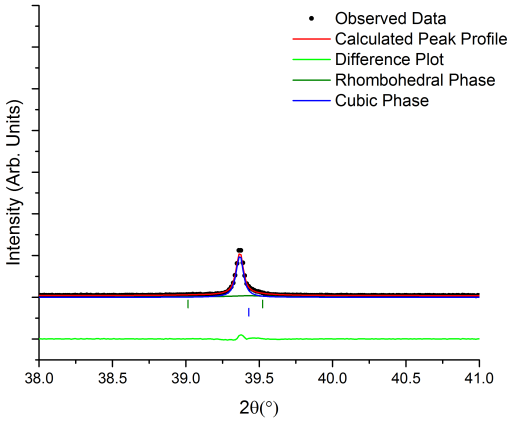

(c) 40% KBT powder, showing the cubic $Pm\bar{3}m$ and rhombohedral $R3c$ Rietveld peak profile for the {111} peak.

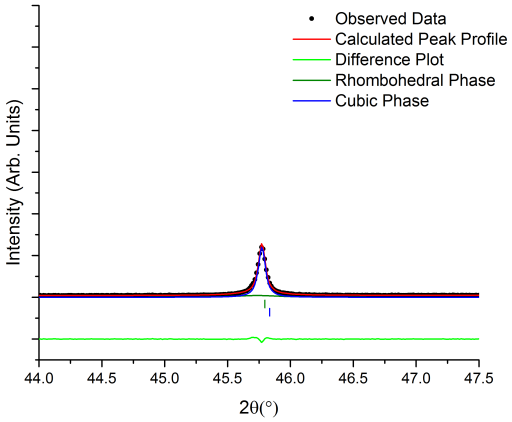

(d) 40% KBT powder, showing the cubic $Pm\bar{3}m$ and rhombohedral $R3c$ Rietveld peak profile for the {200} peak.

Figure 3.8: Plot showing the cubic $Pm\bar{3}m$ and rhombohedral $R3c$ mixed phase Rietveld peak profile fitting for the data plots of the 40% KBT powder. The vertical lines below denote the peak locations. Cubic phase: 83.6(5)%, $R_{Bragg} = 2.567$. Rhombohedral phase: 16.4(5)%, $R_{Bragg} = 1.704$

steadily in cubic phase. The 40% sample is also of great interest because there has been an MPB reported around 40 mol% KBT, so it shows enhanced piezoelectric properties making it an attractive material for device applications. In addition, the 40% sample is also the only phase pure sample produced. As such, the 40% KBT provides the best example of the cubic-rhombohedral mixed phase diffraction pattern with a larger cubic than rhombohedral phase. The difference plot shows very little deviation, indicative of good agreement between the model and the observed data. Figure 3.8b shows the {110} peak of this 40% KBT data, from which can be seen how the phases interact, with the cubic phase corresponding to the central intensity and the rhombohedral phase providing a wider base than the cubic phase would be able to alone, making it continue to be a necessary component of the model. Figure 3.8c shows the {111} peak, which can be seen to be slightly split, meaning that like the {110} peak it could not be fitted with a simple cubic model, but a cubic and rhombohedral mixed phase model does fit the peak splitting observed well. The {200} peak shown in Figure 3.8d is once again seen to be a single peak.

While both of these models consist of a cubic and rhombohedral component, there are some differences between the two. The most obvious is which of the phases is the dominant one, with the cubic phase becoming the dominant phase by 20% KBT and continuing to increase as the % KBT is increased. With the diminishing proportion of the rhombohedral phase, the tilt peak becomes less visible in the powder XRD data with increasing mol% KBT. In addition the splitting of the rhombohedral peaks, rhombohedralicity, decreases with increasing mol% KBT.

As the % KBT is increased still further (70% KBT - 80% KBT), the central peaks themselves begin to show signs of deviation from a cubic structure, with deviations on the side of some of the peaks, including the {100} peak which can not be accounted for by a rhombohedral system. At this point, the model which was found to best fit the observed data was a mix of cubic and monoclinic phases, though other models were able to fit the observed data, notably two cubic phases together and a mix of cubic and tetragonal phases. The monoclinic and cubic mixed phase provided a slightly better fit to the data than these, and was consistent with literature descriptions of transitions from a mostly tetragonal phase to a mostly cubic one, so was accepted as the best model for the data.

Figure 3.9a shows the Rietveld refinement of the 70% KBT sample, chosen as the best sample to include as a representative of the 70% KBT and 80% KBT samples. The difference plot between the observed data and the calculated model shows more deviation in this sample than for the cubic-rhombohedral mixed systems, and this was found to be systematically true of all of the models containing

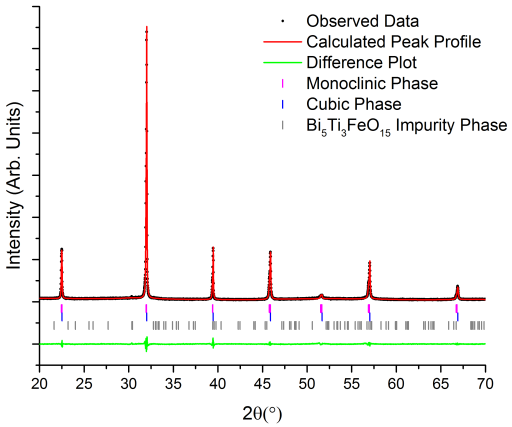

(a) The $P1m1$+$Pm\bar{3}m$ phase Rietveld fitting for 70% KBT powder, for the full profile from 20° 2θ to 70° 2θ.

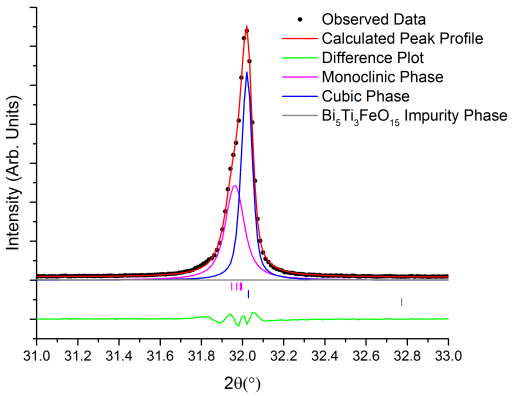

(b) The $P1m1$+$Pm\bar{3}m$ phase Rietveld fitting for 70% KBT powder, for the {110} peak.

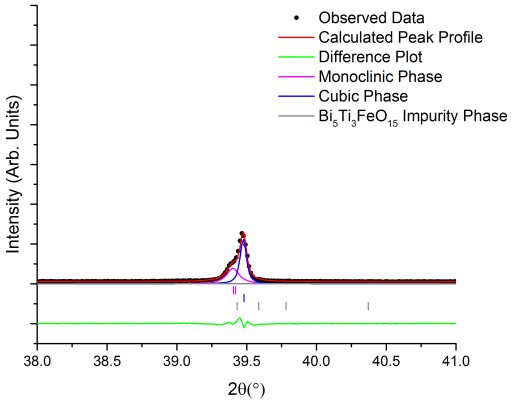

(c) The $P1m1$+$Pm\bar{3}m$ phase Rietveld fitting for 70% KBT powder, for the {111} peak.

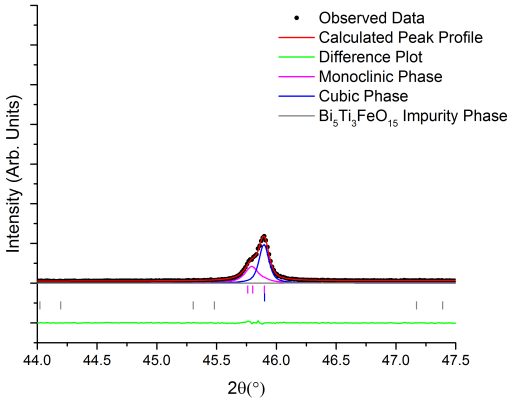

(d) The $P1m1$+$Pm\bar{3}m$ phase Rietveld fitting for 70% KBT powder, for the {200} peak.

Figure 3.9: Plot showing the cubic $Pm\bar{3}m$ and monoclinic $P1m1$ mixed phase Rietveld peak profile fitting for the data plots of the 70% KBT powder. The vertical lines below denote the peak locations. Cubic phase: 40(5)%, R_{Bragg} = 0.471. Monoclinic phase: 58(5)%, R_{Bragg} = 0.424

a monoclinic phase. Figure 3.9b shows the {110} peak, which has a clear shoulder on the low angle side, confirming that the peak can not be represented by a cubic model. The monoclinic model here is seen to fit the low angle split as well as provide additional intensity to the most intense peak. Figure 3.9c shows that the {111} peak is split, and thus the model can not be purely tetragonal or orthorhombic in nature. Figure 3.9d shows splitting in the {200} peak, meaning that a purely rhombohedral model could not be used to fit this model well. In addition, a monoclinic model alone was found to fit the data only slightly better than a cubic model was able to, unable to account for both the peak splitting and the high intensity peaks well.

A mixed phase model was once again used, where it was found that the peaks were split into a lower and higher 2θ angle, with the monoclinic phase systematically the lower of the two. This meant that the monoclinic phase corresponded to a higher set of average pseudocubic lattice parameters/volume than the cubic phase did, thus represented a larger unit cell.

When the mol% KBT was increased further (towards the KBT end member, 90% and 100% KBT), there was another change in the way in which the diffraction pattern was fitted. Specifically, it was found that the cubic component of the phases was replaced with a tetragonal phase, leaving a mix of tetragonal and monoclinic phases. The change from a (mostly) cubic phase through to a tetragonal-monoclinic mixed phase via a cubic-monoclinic mixed phase with $Pm\bar{3}m$, $P4mm$ and $C1m1$ space groups is known to occur in $(1x)(BaTiO_3)(x)(Bi\ (Mg_{0.5}Zr_{0.5})O_3)$ (BT-BMZ) [9], but with the lack of superstructure reflections present in this sample it was decided that a primitive $P1m1$ lattice would be more suitable, so the presence of such phase mixing in BFO-KBT is consistent with this known material system. In addition, it was found that as the mol% KBT was increased, the tetragonal splitting, the c/a parameter, increased, meaning the tetragonality (the split in the tetragonal c and a parameters) of the material increased with increasing KBT content.

Figure 3.10a shows the Rietveld refinement for the 100% KBT sample. This was chosen as the best sample of the high mol% KBT samples to include here since the divergences from the literature found during the Rietveld refinement of the material were found to be extremely interesting, and have been expanded on and discussed in depth in Section 3.4.1.

Figure 3.10b shows the {110} peak, split in both the tetragonal and monoclinic systems, which is somewhat analogous to the rhombohedral-cubic mixed systems, though in this case the tetragonal phase is fitting the shoulders of the peaks, while the monoclinic phase was found to fit the central intensity. It was expected that as the % KBT was increased, the monoclinic intensity would diminish as the

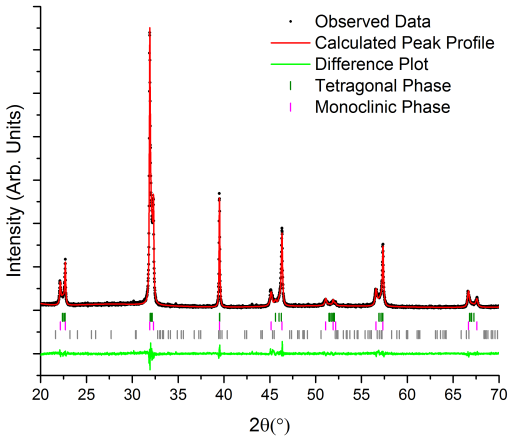

(a) The $P1m1$+$Pm\bar{3}m$ phase Rietveld fitting for 100% KBT powder, for the full profile from 20° 2θ to 70° 2θ.

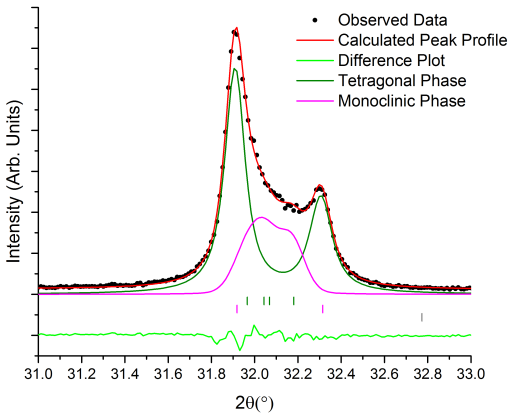

(b) The $P1m1$+$Pm\bar{3}m$ phase Rietveld fitting for 100% KBT powder, for the {110} peak.

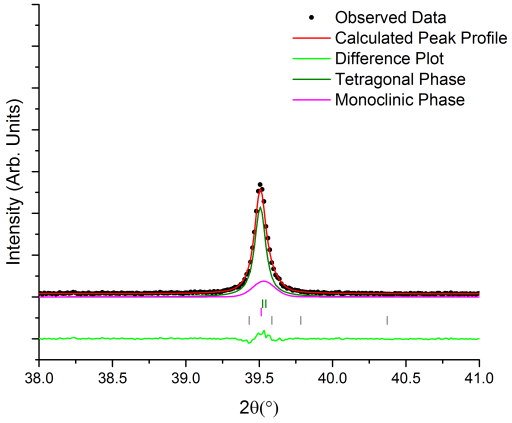

(c) The $P1m1$+$Pm\bar{3}m$ phase Rietveld fitting for 100% KBT powder, for the {111} peak.

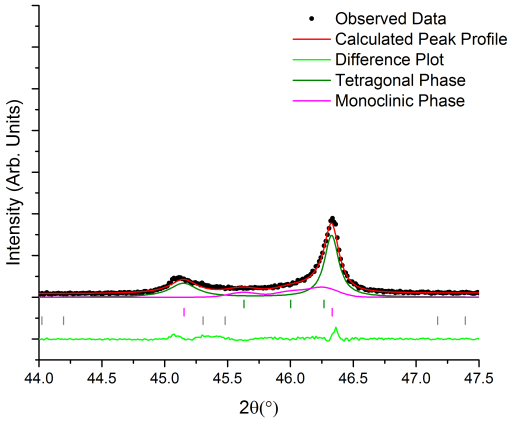

(d) The $P1m1$+$Pm\bar{3}m$ phase Rietveld fitting for 100% KBT powder, for the {200} peak.

Figure 3.10: Plot showing the tetragonal $P4mm$ and monoclinic $P1m1$ mixed phase Rietveld peak profile fitting for the data plots of the 100% KBT end member powder. The vertical lines below denote the peak locations. Tetragonal phase: 69(1)%, $R_{Bragg} = 1.877$. Monoclinic phase: 31(1)%, $R_{Bragg} = 1.305$

tetragonal intensity increased, which was observed. It was also expected that at 100% KBT the structure would be fully tetragonal, but in the samples produced as a part of this thesis this was not found to be the case. Figure 3.10c shows the {111} peak, which is not split in the tetragonal system, and can be seen in the data to be unsplit, though extra peak width is provided by the monoclinic phase. Figure 3.10d shows the {200} peak, where the tetragonal phase is seen to show splitting as expected, with the central intensity covered by the monoclinic phase.

In summary, this means that the structure of the BFO-KBT system changes from rhombohedral at the fully BFO compositions through to a rhombohedral-cubic mix, through to a cubic-rhombohedral mix, to a cubic-monoclinic mix, to a monoclinic-tetragonal mix at high KBT compositions. This would mean that there could be multiple morphotropic phase boundaries, between each of these regions. The system is investigated with respect to temperature in Chapter 4, to investigate how stable it is with respect to temperature, given that to be considered an MPB it should be temperature-independent.

The multiphase models provided significantly better agreement with the observed data than any single phase was able to, which can be seen summarised in Table 3.3, which compares the single-phase models for tetragonal $P4mm$, monoclinic $P1m1$, rhombohedral $R3c$ and cubic $Pm\bar{3}m$ with the mixed phase models for those compositions. The comparisons are made using the goodness of fit (GoF) value which takes into account changes in expected value and the number of parameters refined, described in Section 2.1.3.4. The phase percentages are also listed.

In addition, a mix of cubic and monoclinic was investigated for the 60% KBT diffraction pattern, given that this was found to be the transition from the rhombohedral mixed model to the monoclinic mixed model, but the cubic-rhombohedral multiphase model was found to significantly better fit the data.

Table 3.3: Values of GoF from TOPAS ACADEMIC refinements of the powders with different crystal systems, followed by the percentage of the mixed phases given by the refinements. The mixed phases can be seen to consistently provide the best GoF value.

mol% KBT	Tetragonal	Monoclinic	Rhombohedral	Cubic	Mixed Phase	Cubic percentage	Rhombohedral percentage	Monoclinic percentage	Tetragonal percentage
10	10.668	4.933	3.914	9.844	1.686	25.0(8)	73.9(8)	0	0
15	7.656	1.754	2.414	5.595	1.764	29(1)	70(1)	0	0
20	5.967	3.688	2.992	3.758	1.620	61.5(8)	37.8(8)	0	0
25	3.227	2.234	2.774	2.368	1.504	64(1)	34(1)	0	0
30	5.724	3.257	2.463	2.558	1.270	74.1(5)	25.2(4)	0	0
33	2.069	2.258	2.293	1.859	1.152	78.3(6)	21.1(6)	0	0
40	3.931	5.131	7.397	3.324	1.491	83.6(5)	16.4(5)	0	0
50	6.670	3.126	2.284	2.351	1.408	82.1(4)	17.1(4)	0	0
60	2.284	1.989	4.466	2.018	1.465	83.2(7)	15.9(7)	0	0
70	3.623	1.750	5.649	5.788	1.506	40(5)	0	58(5)	0
80	4.987	3.660	6.275	4.057	1.440	45(2)	0	54(2)	0
90	2.649	2.559	3.447	2.780	1.485	0	0	60(2)	40(2)
100	2.910	4.227	4.497	6.382	1.226	0	0	31(1)	69(1)

3.4.1 KBT Analysis

The results from the 100% KBT sample are extremely interesting, and provoke further questions. In the literature, it is claimed that KBT is a tetragonal material, but looking in more depth there is cause for some degree of uncertainty, and the data obtained as a part of this thesis certainly does not support a simple tetragonal conclusion.

Table 3.4 and Table 3.5 give an overview of published papers describing the structure of KBT through diffraction, while Figure 3.11 shows some examples from the papers mentioned here, compared with the data obtained as a part of this thesis (along with the mixed phase Rietveld refinement used to model it) in Figure 3.11c. Most recent structural analysis of the structure of KBT seems to be focussed on grain size and impurity phase, while very little investigation has been made utilising Rietveld refinement techniques.

In this thesis, the method of powder synthesis was a solid state reaction method, which has been investigated by other groups before. These are shown in Table 3.4, though few of those investigations have involved Rietveld refinements of the data. Observing the data obtained by x-ray powder diffraction on these samples, it becomes increasingly clear that the diffraction pattern obtained in the course of this thesis is a standard diffraction pattern for the material. All samples generated by a solid-state reaction method show very similar x-ray powder diffraction patterns; The tetragonally split peaks are filled in in the middle. This means that the intensity between the split peaks may not necessarily be fully accounted for by a tetragonal model. In the case of the data obtained in this thesis, this filling in is seen to not be able to be modelled with a fully tetragonal system, but instead it was necessary to introduce a second, monoclinic phase to increase the intensity between the peaks on the split {110}, {200} etc. peaks. Other models were used as a second phase, but the monoclinic second phase fits significantly better. Since the published papers using the solid-state reaction method show very similar powder x-ray diffraction patterns but few have been analysed by Rietveld refinement, it is possible that they all exhibit this mixed phase state.

Jones, Kriesel and Thomas [12] produced the data that the currently accepted KBT cif file is based on, along with cif files for other materials of the NBT-KBT series. Through powder XRD and neutron diffraction, they were able to utilise Rietveld analysis techniques to determine a $P4mm$ tetragonal structure for KBT. However, it must be noted that in this paper, it is stated that the final R-factors obtained through Rietveld analysis for the KBT data was worse than those obtained for the other members of the NBT-KBT series studied, which means that there is

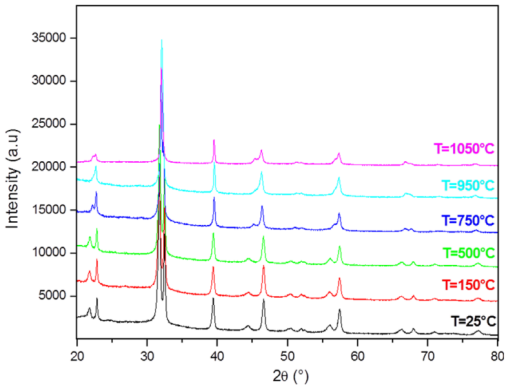

(a) Krad *et al.* (2016). Comparison of sintering temperatures on hydrothermal KBT. [10]

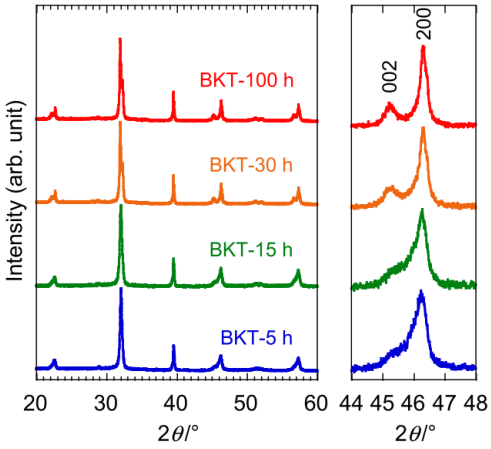

(b) Hagiwara *et al.* (2015). Comparison of different sintering times, with focus on {200} peak. [11]

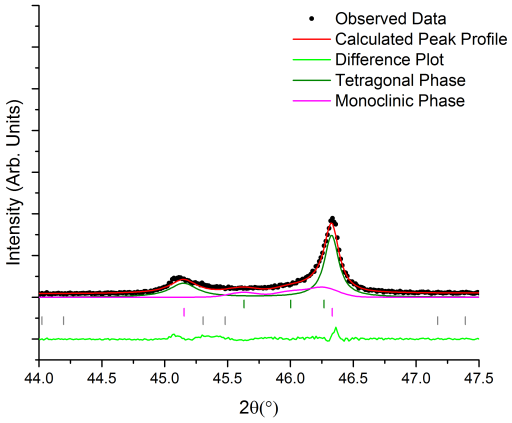

(c) {200} Data obtained in this project, fitted with Rietveld analysis. The pink line is the monoclinic contribution, the dark green line is the tetragonal contribution, and the light green line at the bottom is the difference plot.

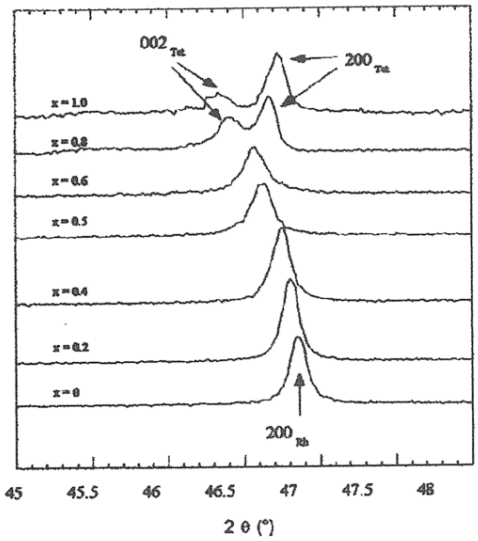

(d) Jones *et al.* (2002). {200} reflections of $_{(x)}$KBT$_{(1-x)}$NBT system. [12]

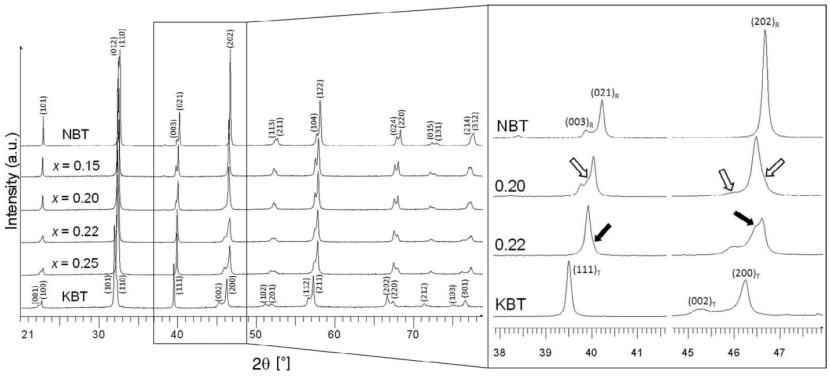

(e) Otoničar *et al.* (2011). KBT-NBT system with {200} focus. [13]

Figure 3.11: Comparisons between KBT powder x-ray diffraction profiles obtained as a part of this project and those found in the literature.

still the possibility for a better fit to the data than that proposed in the paper. Since this paper, there has been little further Rietveld analysis of 100% KBT published to date. The {200} peak from their paper is seen in Figure 3.11d. In the 100% KBT sample, the {200} peak can be seen split into the (200) and (002) peaks, and the intensity between the two does not reach the background intensity. It is also important to note that the resolution of the neutron diffraction was lower than that of the x-ray diffraction used here.

With respect to the solid-state reaction method itself, the paper from König *et al.* in 2009 [8] investigated the stoichiometry of KBT produced by this method, and found that the resultant powder was K-deficient and Bi-rich, due to the loss of K_2CO_3 during the calcining and sintering processes. They investigated this through EDS and WDS methods to quantise the loss that they found through the Knudsen Effusion Mass Spectrometry (KEMS) method, which was also seen to change the x-ray diffraction pattern obtained. This was found to be linked to sintering time by the fact that sintering for longer gives more opportunity for volatilisation. Their results showed significant volatilisation of bismuth and potassium components when synthesising KBT ceramics. They concluded that the resultant composition would not be stoichiometric KBT, but instead through WDS they found that the resulting material was deficient in K and rich in Bi, essentially meaning that KBT synthesised from stoichiometric powder ratios is unlikely to have formed stoichiometric KBT.

Sung *et al.* [14] investigated the effects of varying the stoichiometry with a variable potassium component. They found that in the range of $\pm$ 1 mol% potassium that a standard KBT powder x-ray diffraction pattern was reproduced. As the potassium component was decreased further, bismuth heavy impurity phases started forming, specifically $Bi_4Ti_3O_{12}$ was reported. A potassium deficiency around 5-6 mol% was found to represent a minimum in the c/a parameter and a maximum in the piezoelectric d_{33} parameters.

Wicheanrat *et al.* [15] investigated the response of the KBT system to excess amounts of BiO_2 and K_2CO_3 in a 1:1 ratio. From their results, they concluded that the lattice parameters a, c and c/a decreased with an increase in bismuth and potassium content. They found that the average grain size decreased with increased bismuth and potassium content. The resulting powder x-ray diffraction profiles show that as excess reagents are introduced, the tetragonal splitting appears to first increase between 0 and 1% excess, and then decrease as the excess is increased up to 10%, through the c/a parameter.

Liu *et al.* [16] investigated KBT as an end member through synchrotron x-ray diffraction and used Rietveld refinement on the data. It must be noted that

in order to compensate for the loss of potassium, they added 10%-15% K_2CO_3 and sintered for longer at a lower temperature; a significantly larger excess of reagents than was found to be beneficial by Wicheanrat *et al.*, though the latter did also add BiO_2. No specific checks with regards to the stoichiometry of the sample were reported. Liu *et al.* did not publish any form of quality factors for the Rietveld refinements of their data, so it is not possible to compare the refinements directly with those in this thesis. They reported KBT as being fit well with a tetragonal $P4mm$ structure when the strain was allowed for; refinements of the KBT in this thesis also allowed for strain, in the form of Stephens' parameters on the tetragonal phase.

Table 3.4: Literature structural studies of KBT system. (ceramic/solid state/combustion methods)

Paper	Synthesis Methodology	Observation Methodology	Calcine Temperature (°C)	Calcine Time (Hours)	Sinter Temperature (°C)	Sinter Time (Hours)
Jones (2002) [12]	solid-state reaction method	powder neutron diffraction, powder x-ray diffraction	800/800	12/12	1100	6
Hiruma (2005) [17]	conventional ceramic fabrication process	powder x-ray diffraction, SEM	800/950	4/2	1030-1080	2-3
König (2009) [8]	solid-state reaction method	powder x-ray diffraction, SEM, EDS, WDS	750/850	10/10	1030	5-80
Xie (2009) [18]	solid-state reaction method	powder x-ray diffraction, SEM	800	24	1000	2
Otoničar (2010) [19]	solid-state reaction method	powder x-ray diffraction, SAED	750/850	10/10	1030	20
Sung (2010) [14]	solid-state reaction method	powder x-ray diffraction, SEM	780/800	2/2	1050-1070	2-10
Wicheanrat (2013) [15]	solid-state reaction method	powder x-ray diffraction, SEM	650-900	2	1000-1040	2
Tabuchi (2013) [20]	conventional ceramic fabrication process	powder x-ray diffraction, SEM	200/600/950	4/5/4	1000-1060	2-20
Tabuchi (2013) [21]	conventional ceramic fabrication process	powder x-ray diffraction, SEM	200/600/950	4/5/4	1000-1060	20
Thongtha (2013) [22]	combustion technique	powder x-ray diffraction, SEM	850	2	975-1025	2
Wefring (2014) [23]	conventional solid-state synthesis method	powder x-ray diffraction, SEM	700	3	1060	3
König (2015) [24]	solid-state reaction method	powder x-ray diffraction, SEM	750/850	10/10	1030	5-40
Pan (2015) [25]	conventional solid-state synthesis method	powder x-ray diffraction, SEM	800	3	1070	2
Liu (2015) [16]	conventional solid-state synthesis method	Synchrotron x-ray diffraction, XANES	750	8	950	72

Table 3.5: Literature structural studies of KBT system produced by sol-gel or hydrothermal methods.

Paper	Synthesis Methodology	Observation Methodology	Calcine Temperature (°C)	Calcine Time (Hours)	Sinter Temperature (°C)	Sinter Time (Hours)
Kreisel (2000) [26]	spontaneous flux crystallisation then ground to powder	powder x-ray diffraction, Raman	800	12	-	-
Li (2003) [27]	sol-gel method	powder x-ray diffraction	700	4	1070	2
Hou (2006) [28]	hydrothermal and sol-gel fabrication processes	powder x-ray diffraction, SEM, TEM	400-800	2	1000-1050	2
Zhu (2006) [29]	sol-gel method	powder x-ray diffraction, Raman	700-900	2	1000-1100	2
Wang (2011) [30]	hydrothermal fabrication process	powder x-ray diffraction, SEM	-	-	1050	2
O'Brien (2013) [31]	hydrothermal fabrication process	powder x-ray diffraction, SEM	25-900	1	-	-
Hagiwara (2015) [32]	hydrothermal fabrication process	powder x-ray diffraction, SEM, EDX	600	1	1020-1060	2
Hagiwara (2015) [11]	hydrothermal fabrication process	powder x-ray diffraction, SEM	700	not mentioned	1050	5-100
Krad (2016) [10]	stirring hydrothermal method	powder x-ray diffraction, SEM, Raman	25-1050	not mentioned	1050	2

Comparing these results with the results of a hydrothermally produced sample by Hagiwara *et al.* [11], whose conclusions were that a longer sintering time results in a tetragonal material with larger peak splittings due to larger grain size, it seems that there could be alternative explanations for some of the effects noted. They noted that longer sintering times lead to larger grains and larger c/a parameters, which could also be consistent with data seen by Wichenrat *et al.* [15] where an excess of BiO_2 and K_2CO_3 produces the opposite result. Hagiwara *et al.* noted that less than 1% mass loss was seen during sintering, however this could still be enough to modify the stoichiometry in a large way, especially since most of the material lost is likely to be the relatively light potassium, which was seen by König *et al.* [8]. Thus, their results are still consistent with a claim that a close to stoichiometric KBT powder will result in a powder x-ray diffraction profile similar to that seen in this project. In that case, the split peaks are seen overlapping slightly, with the area between them still filled in by an additional phase, seen in Figure 3.11b. The longer sintering time powders show a larger split between the {200} peaks.

Some hydrothermally synthesised powder, such as that of O'Brien [31] forms a tetragonal structure with fully separated peaks, and significantly higher c/a parameters prior to heat treating. However, Krad *et al.* [10] investigated the composition of KBT formed hydrothermally with respect to treatment temperature, and hydroxyl groups in the structure. They utilised Raman spectroscopy to investigate the existence of the hydroxyl groups in the KBT, and found that they were removed entirely by 750°C. When treated at 750°C, the powder x-ray diffraction profile of the hydrothermally synthesised KBT powder appears identical to the solid-state synthesised powder, with the split peaks close together with a relatively large intensity between them. These results can be seen in Figure 3.11a; 750°C is the point at which the hydroxyl groups were found to be absent in Raman studies, and also the point at which the peak profile matches well with other KBT samples, including the one synthesised in this project in Figure 3.11c.

Sol-gel produced samples, such as those of Zhu *et al.* [29] and Li *et al.* [27] show the same overlapped tetragonal splitting, with a filled central area that the solid state and hydrothermally synthesised powders do, making the resultant powder x-ray diffraction profile consistent.

From TEM studies into the material, such as those produced by Otoničar *et al.* [13, 19], a tetragonal structure is reported. In both of these studies, the KBT was seen to be tetragonally twinned. However, with respect to the $P4mm$-$C1m1$ phase in PZT, a very similar system in this respect, Schierholz and Fuess [33] stated

that the monoclinic $C1m1$ domains could not be distinguished from the tetragonal $P4mm$ domains simply by the splitting of reflections in the SAED patterns alone. Thus it is possible that the twinning seen in the work of Otoničar *et al.* could potentially be from a $P1m1$ monoclinic phase. An example of one of the peak profiles from the x-ray powder diffraction experiments is included in Figure 3.11e, which again, shows the same profile as found in this project.

From these investigations it can be concluded that the synthesis of KBT is a challenging exercise, and it is possible that the exact composition of each KBT sample synthesised may be different. As such, with the differences in stoichiometry clearly having such a large effect, it is possible that both the differences between literature results, and differences between the literature and this study, could be explained by different stoichiometry. It is also possible that the structures seen in the literature are also a mix of tetragonal and monoclinic, which would then explain why the R-factors for Jones *et al.* [12] were larger than for other structures they investigated, and few other Rietveld results for KBT have been published since.

3.4.2 Rietveld Results Tabulated

Results from all of the room temperature Rietveld refinements are tabulated here, listed in order of increasing mol% KBT. The rhombohedral and cubic mixed phase refinements are given first in Table 3.6, Table 3.7 and Table 3.8, followed by the monoclinic and cubic mixed phase refinements in Table 3.9, and the tetragonal and monoclinic mixed phase refinements in Table 3.10. The refined impurity phase composition and percentage are included; these can be seen to be very low aside from the 70% KBT powder, which also has the largest errors in phase percentage refinement.

Table 3.6: Summary of refinement of mixed rhombohedral and cubic phases from 10% KBT to 20% KBT.

Composition	10% KBT		15% KBT		20% KBT	
Crystal System	Cubic	Rhombohedral	Cubic	Rhombohedral	Cubic	Rhombohedral
Space Group	$Pm\bar{3}m$	$R3c$	$Pm\bar{3}m$	$R3c$	$Pm\bar{3}m$	$R3c$
Phase Percentage	25.0(8)	73.9(8)	29(1)	70(1)	61.5(8)	37.8(8)
Lattice Parameters						
a (Å)	3.96197(9)	5.58163(8)	3.9612(1)	5.5827(1)	3.96422(5)	5.5858(1)
c (Å)	3.96197(9)	13.8652(2)	3.9612(1)	13.8527(4)	3.96422(5)	13.8519(5)
α (°)	90	90	90	90	90	90
γ (°)	90	120	90	120	90	120
Pseudocubic Volume (Å^3)	62.192(4)	62.348(2)	62.154(5)	62.317(4)	62.298(2)	62.382(4)
R'_{Exp}	5.480		6.477		8.319	
R'_p	9.568		11.970		14.717	
R'_{wp}	9.237		11.423		13.475	
Durbin-Watson	0.756		0.664		0.842	
GoF	1.686		1.764		1.620	
Impurity Phase %	Bi_2O_3: 1.1(1)		Bi_2O_3: 0.8(1)		Bi_2O_3: 0.6(1)	
R_{Bragg}	1.020	1.130	2.753	2.822	0.927	2.756
Atomic Positions						
A						
$x = y = 0, z =$	0	0.2930(4)	0	0.2898(6)	0	0.293(1)
Beq (Å^2)	4.4(3)	0.81(6)	4.0(4)	0.1(1)	4.9(1)	0.0(1)
B						
$x = y =$	0.5	0	0.5	0	0.5	0
z	0.5	0.0146(5)	0.5	0.0149(7)	0.5	0.016(1)
Beq (Å^2)	2.0(3)	0.1(1)	0.0(4)	0.0(2)	1.6(2)	0.0(2)
O						
x	0.5	0.235(1)	0.5	0.225(2)	0.5	0.248(3)
y	0	0.338(1)	0	0.332(2)	0	0.338(3)
z	0.5	0.0833	0.5	0.0833	0.5	0.0833
Beq (Å^2)	14(1)	0.0(3)	10(1)	0.0(4)	5.7(3)	0.0(6)

Table 3.7: Summary of refinement of mixed rhombohedral and cubic phases from 25% KBT to 33% KBT.

Composition	25% KBT		30% KBT		33% KBT	
Crystal System	Cubic	Rhombohedral	Cubic	Rhombohedral	Cubic	Rhombohedral
Space Group	$Pm\bar{3}m$	$R3c$	$Pm\bar{3}m$	$R3c$	$Pm\bar{3}m$	$R3c$
Phase Percentage	64(1)	34(1)	74.1(5)	25.2(4)	78.3(6)	21.1(6)
Lattice Parameters						
a (Å)	3.96286(9)	5.5849(2)	3.96389(3)	5.5890(3)	3.96351(5)	5.5852(2)
c (Å)	3.96286(9)	13.839(1)	3.96389(3)	13.825(1)	3.96351(5)	13.8507(9)
α (°)	90	90	90	90	90	90
γ (°)	90	120	90	120	90	120
Pseudocubic Volume (Å^3)	62.234(4)	62.302(7)	62.282(2)	62.334(8)	62.264(2)	62.362(6)
R'_{Exp}	10.941		8.603		16.289	
R'_p	18.464		13.440		19.520	
R'_{wp}	16.452		10.925		18.769	
Durbin-Watson	1.045		1.287		1.464	
GoF	1.504		1.270		1.152	
Impurity Phase %	Bi_2O_3: 1.1(1)		Bi_2O_3: 0.6(1)		Bi_2O_3: 0.5(0.2)	
R_{Bragg}	2.675	4.456	1.118	1.151	1.567	2.024
Atomic Positions						
A						
$x = y = 0, z =$	0	0.288(2)	0	0.292(2)	0	0.295(2)
Beq (Å^2)	3.3(1)	0.0(2)	6.18(8)	0.0(1)	5.6(1)	0.0(2)
B						
$x = y =$	0.5	0	0.5	0	0.5	0
z	0.5	0.011(2)	0.5	0.018(2)	0.5	0.016(2)
Beq (Å^2)	0.0(2)	0.0(4)	1.28(9)	0.0(4)	1.1(1)	0.0(5)
O						
x	0.5	0.231(5)	0.5	0.248(4)	0.5	0.252(6)
y	0	0.336(5)	0	0.340(4)	0	0.344(6)
z	0.5	0.0833	0.5	0.0833	0.5	0.0833
Beq (Å^2)	3.3(4)	0.0(9)	4.5(2)	0.0(8)	5.1(3)	0(1)

Table 3.8: Summary of refinement of mixed rhombohedral and cubic phases from 40% KBT to 60% KBT.

Composition	40% KBT		50% KBT		60% KBT	
Crystal System	Cubic	Rhombohedral	Cubic	Rhombohedral	Cubic	Rhombohedral
Space Group	$Pm\bar{3}m$	$R3c$	$Pm\bar{3}m$	$R3c$	$Pm\bar{3}m$	$R3c$
Phase Percentage	83.6(5)	16.4(5)	82.1(4)	17.1(4)	83.2(7)	15.9(7)
Lattice Parameters						
a (Å)	3.96321(3)	5.5894(7)	3.96235(4)	5.5896(2)	3.95851(5)	5.5919(3)
c (Å)	3.96321(3)	13.836(4)	3.96235(4)	13.829(1)	3.95851(5)	13.813(2)
α (°)	90	90	90	90	90	90
γ (°)	90	120	90	120	90	120
Pseudocubic Volume (Å^3)	62.250(1)	62.39(2)	62.210(2)	62.362(7)	62.029(2)	62.34(1)
R'_{Exp}	9.380		8.205		6.740	
R'_p	15.813		14.303		12.081	
R'_{wp}	13.988		11.550		9.877	
Durbin-Watson	1.005		1.087		0.965	
GoF	1.491		1.408		1.465	
Impurity Phase %	-		Bi_2O_3: 0.75(6)		$Bi_5Ti_3FeO_{15}$: 0.9(1)	
R_{Bragg}	2.567	1.704	0.935	0.895	1.077	0.991
Atomic Positions						
A						
$x = y = 0, z =$	0	0.294(3)	0	0.291(2)	0	0.292(2)
Beq (Å^2)	6.12(8)	0.0(2)	7.23(9)	1.0(2)	7.2(1)	2.0(3)
B						
$x = y =$	0.5	0	0.5	0	0.5	0
z	0.5	0.013(4)	0.5	0.018(2)	0.5	0.029(9)
Beq (Å^2)	0.11(9)	0.3(8)	1.3(1)	0.9(4)	0.4(2)	10(2)
O						
x	0.5	0.245(9)	0.5	0.236(5)	0.5	0.264(7)
y	0	0.329(7)	0	0.347(4)	0	0.374(6)
z	0.5	0.0833	0.5	0.0833	0.5	0.0833
Beq (Å^2)	2.4(2)	0(2)	3.2(2)	0.0(9)	2.9(2)	0(1)

3.4.2.1 Data Comparison

Table 3.11 shows the data obtained by Bennett *et al.* [34] through neutron powder diffraction. The Megaw atomic positions have been calculated through symmetry from the standard atomic positions [35], and the tilt angles generated from them are in agreement with the paper. These values can be compared with the values obtained in this thesis, shown in Table 3.6, Table 3.7 and Table 3.8. In the paper by Bennett *et al.*, the 20% KBT, 30% KBT and 40% KBT samples have been fitted with a single rhombohedral phase.

Differences can be seen in the lattice parameters, with the a lattice parameter systematically smaller in the data presented in this thesis than the data of Bennett *et al.*, while the c parameters presented in this thesis are systematically larger.

The lattice distortions, shown in Table 3.12, show that the rhombohedral distortions in this thesis are systematically larger; this is a result of fitting the shoulder peaks rather than the central intensity of the peaks with the rhombohedral phase.

In terms of the atomic positions, the data of Bennett *et al.* is broadly similar to the data presented in this thesis, with the exception of a large difference in the oxygen x component; as it is systematically quite different, this may not simply be a result of the better resolution of oxygen atoms provided by neutron diffraction, but could instead be related to the difference in the models used, single phase rhombohedral vs. mixed phase rhombohedral and cubic.

The ADP data obtained by Bennett *et al.* is more accurate than the data obtained in this thesis, which were often found to be 0 within the errors, but in both cases it can be seen that the atomic displacement parameters are very small.

3.4.2.2 Discussion of Parameters from Rietveld Tables

From the data displayed in these tables, some analysis of the system as a whole was undertaken, better to understand the way in which the system evolves with respect to composition.

Figure 3.12 shows the way in which the average lattice parameter (calculated as the cube root of the cubic volume) of the mixed phases evolves with respect to composition. This shows that the average lattice parameters of the rhombohedral phase are stable across the compositional range with a small peak around the 20% KBT composition, despite the fact that as mol% KBT is increased the phase presence of the rhombohedral phase is reduced. In contrast, the cubic parameters can be seen to decrease from 40% to the point where the cubic phase disappears

Table 3.9: Summary of refinement of mixed cubic and monoclinic phases (70% KBT and 80% KBT).

Composition	70% KBT		80% KBT	
Crystal System	Cubic	Monoclinic	Cubic	Monoclinic
Space Group	$Pm\bar{3}m$	$P1m1$	$Pm\bar{3}m$	$P1m1$
Phase Percentage	40(5)	58(5)	45(2)	54(2)
Lattice Parameters				
a (Å)	3.95485(8)	3.9663(6)	3.95100(5)	3.9636(2)
b (Å)	3.95485(8)	3.9629(3)	3.95100(5)	3.9592(3)
c (Å)	3.95485(8)	3.9550(5)	3.95100(5)	3.9509(3)
α (°)	90	90	90	90
β (°)	90	89.97(2)	90	90.164(6)
γ (°)	90	90	90	90
Volume (Å^3)	61.857(4)	62.16(1)	61.677(2)	62.000(7)
R'_{Exp}	8.271		8.205	
R'_p	13.702		13.826	
R'_{wp}	12.455		11.817	
Durbin-Watson	1.041		1.061	
GoF	1.506		1.440	
Impurity Phase %	$Bi_5Ti_3FeO_{15}$: 2.4(6)%		$Bi_5Ti_3FeO_{15}$: 0.60(4)%	
R_{Bragg}	0.471	0.424	1.334	0.684
Atomic Positions				
A $x = y = 0, z = 0$				
ADP (Å^2)	Beq = 7.7(3)		Beq = 6.7(3)	
U_{11}		0.5(2)		0.053(9)
U_{22}		0.06(4)		0.09(2)
U_{33}		0.3(1)		0.08(1)
$U_{12} = U_{23} = 0$, U_{13} =		-0.4(1)		-0.002(8)
B				
x	0.5	0.547(4)	0.5	0.474(5)
y	0.5	0.5	0.5	0.5
z	0.5	0.037(6)	0.5	0.520(4)
ADP (Å^2)	Beq = 1.1(2)		Beq = 0.0(3)	
U_{11}		0.3(5)		0.05(2)
U_{22}		0.00(5)		0.00(2)
U_{33}		0.3(1)		0.00(2)
$U_{12} = U_{23} = 0$, U_{13} =		-0.20(7)		0.03(2)
O1				
x	0.5	0.48(2)	0.5	0.61(2)
y	0	0.5	0	0.5
z	0.5	0.037(6)	0.5	0.027(6)
Beq (Å^2)	0.7(3)	0(2)	0.5(3)	0(3)
O2				
x	-	0.60(2)	-	0.38(2)
y	-	0	-	0
z	-	0.55(2)	-	0.49(2)
Beq (Å^2)	-	9(10)	-	0(3)
O3				
x	-	0.068(4)	-	-0.032(6)
y	-	0.5	-	0.5
z	-	0.63(2)	-	0.48(3)
Beq (Å^2)	-	7(13)	-	0(1)

Table 3.10: Summary of refinement of mixed tetragonal and monoclinic phases (90% KBT and KBT end member).

Composition	90% KBT		100% KBT	
Crystal System	Tetragonal	Monoclinic	Tetragonal	Monoclinic
Space Group	$P4mm$	$P1m1$	$P4mm$	$P1m1$
Phase Percentage	40(2)	60(2)	69(1)	31(1)
Lattice Parameters				
a (Å)	3.9326(3)	3.9652(3)	3.9186(1)	3.9756(5)
b (Å)	3.9326(3)	3.9534(2)	3.9186(1)	3.9453(4)
c (Å)	3.9916(5)	3.9469(2)	4.0154(2)	3.9239(4)
α (°)	90	90	90	90
β (°)	90	90.215(6)	90	90.04(3)
γ (°)	90	90	90	90
Volume (Å^3)	61.73(1)	61.872(7)	61.658(5)	61.55(1)
R'_{Exp}	13.738		13.103	
R'_p	21.577		15.326	
R'_{wp}	20.398		16.061	
Durbin-Watson	1.018		1.384	
GoF	1.485		1.226	
Impurity Phase %	Bi_2O_3: 0.28(3)%		-	
R_{Bragg}	4.772	4.511	1.877	1.305
Atomic Positions				
A				
$x = y = 0, z =$	-0.041(4)	0	-0.057(2)	0.012(6)
ADP (Å^2)				
U_{11}	0.056(5)	0.46(2)	0.057(3)	0.13(1)
U_{22}	0.056(5)	0.10(2)	0.057(3)	0.12(2)
U_{33}	0.13(1)	0.12(1)	0.046(5)	0.023(8)
$U_{12} = U_{23} = 0$, $U_{13} =$	0	-0.18(1)	0	-0.02(2)
B				
x	0.5	0.460(4)	0.5	0.462(2)
y	0.5	0.5	0.5	0.5
z	0.5	0.522(3)	0.5	0.49(1)
ADP (Å^2)				
U_{11}	0.000(7)	0.10(2)	0.005(4)	0.01(2)
U_{22}	0.000(7)	0.03(2)	0.005(4)	0.02(2)
U_{33}	0.00(2)	0.00(2)	0.01(1)	0.00(2)
$U_{12} = U_{23} = 0$, $U_{13} =$	0	0.019(9)	0	0.07(2)
O1				
x	0.5	0.44(2)	0.5	0.45(1)
y	0.5	0.5	0.5	0.5
z	0.024(5)	0.008(6)	0.036(2)	-0.01(7)
Beq (Å^2)	0(1)	0(1)	0.0(7)	20(6)
O2				
x	0.5	0.42(1)	0.5	0.41(1)
y	0	0	0	0
z	0.583(6)	0.62(2)	0.543(2)	0.52(2)
Beq (Å^2)	0.0(9)	0(2)	0.0(3)	0(2)
O3				
x	-	-0.021(6)	-	-0.043(7)
y	-	0.5	-	0.5
z	-	0.59(2)	-	0.47(2)
Beq (Å^2)	-	0(2)	-	9(3)

Table 3.11: Bennett *et al.* data on BFO-KBT [34] with Megaw atomic positions added, for comparison with data obtained as a part of this thesis (shown in the preceding tables).

Parameter	20% KBT	30% KBT	40% KBT
a (Å)	5.5956(2)	5.5982(3)	5.5936(3)
c (Å)	13.8076(9)	13.781(2)	13.782(2)
A_z	0	0	0
B_z	0.2270(2)	0.2289(3)	0.2294(3)
O_x	0.4532(3)	0.4592(4)	0.4679(3)
O_y	0.0110(4)	0.0074(4)	0.0073(3)
O_z	0.9618(2)	0.9654(3)	0.9650(2)
Beq_A	0.0208(7)	0.025(1)	0.0249(9)
Beq_B	0.0028(3)	0.0008(4)	0.0054(7)
Beq_O	0.0147(1)	0.0172(5)	0.0199(5)
Megaw:			
A_z	0.2882	0.2846	0.2850
B_z	0.0152	0.0135	0.0144
O_x	0.1199	0.1259	0.1346
O_y	0.3443	0.3411	0.3406
O_z	$\frac{1}{12}$	$\frac{1}{12}$	$\frac{1}{12}$
$\omega(^\circ)$	10.26	8.84	7.07

Table 3.12: Bennett *et al.* lattice distortions compared with the distortions calculated in this thesis.

Composition	Bennett [34]	This thesis
20% KBT	1.007	1.012
30% KBT	1.004	1.010
40% KBT	1.006	1.011

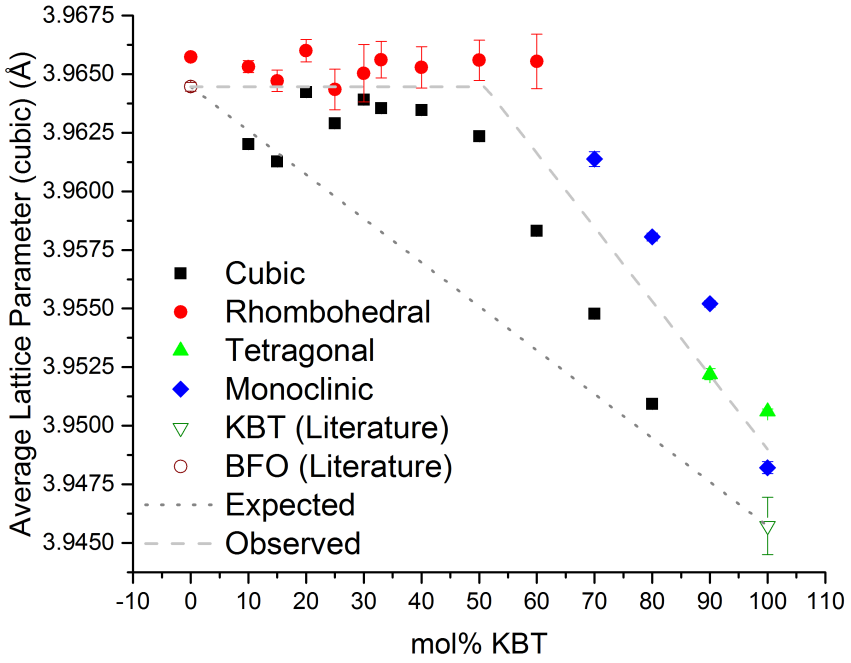

Figure 3.12: A plot showing the average lattice parameters for the phases used in the peak profiles of the Rietveld refinements [19, 23, 36, 37].

around 80% KBT. The cubic parameters also show a small peak around the 20% KBT composition. The tetragonal parameters are of a similar size to the lowest cubic parameters. This is consistent with the cubic parameters changing with increasing mol% KBT to better fit the tetragonal parameters, while the monoclinic lattice parameters bridge the gap between the larger rhombohedral parameters and the lower tetragonal parameters. There is a discrepancy at 100% KBT sample, which is reported in the literature as being fully tetragonal [19], but (as discussed in detail in Section 3.4.1) was found in this investigation to be best fitted with a mixed phase of tetragonal and monoclinic phases.

KBT end member lattice parameters were taken from the literature as $a = 3.9247(0)$ and $c = 3.9844(3)$ [19] or $a = 3.933(3)$ and $c = 3.975(4)$ [23], which results in an average lattice parameter of 3.946(1). BFO end member lattice parameters were taken from the literature as $a = 5.57874(16)$, $c = 13.8688(3)$ [36], $a = 5.5799(3)$ and $c = 13.8670(5)$ [37], which results in an average lattice parameter of 3.9645(2). Comparing these with the data obtained, the BFO lattice parameter was found to be consistent with that of the rhombohedral lattice parameters found from 10% KBT to 60% KBT, though the cubic parameters were generally lower over this range. By comparison, the KBT lattice parameter was found to be below the lattice parameter obtained here of 3.9503(1). The discussions in Section 3.4.1 are consistent with high

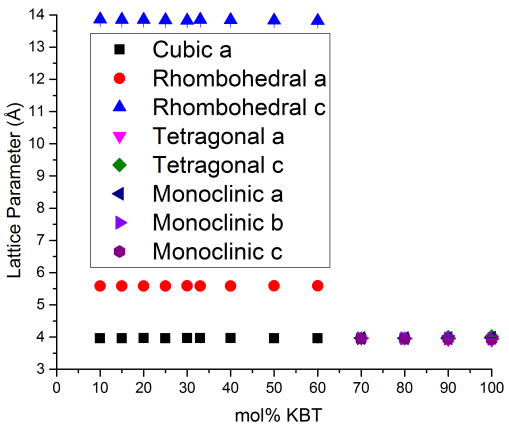

(a) All room temperature lattice parameters.

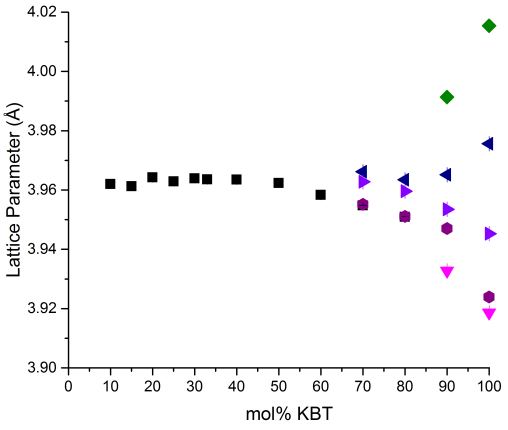

(b) Cubic, tetragonal a, tetragonal c, monoclinic a, monoclinic b and monoclinic c lattice parameters.

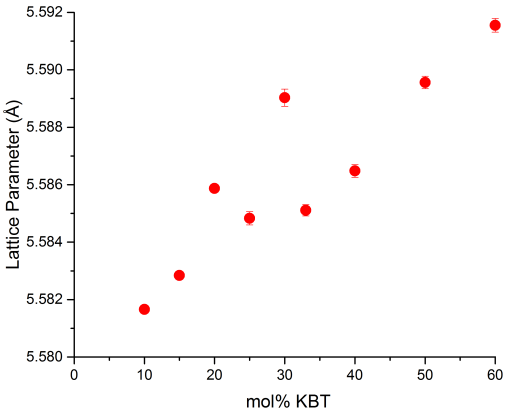

(c) Rhombohedral a lattice parameters.

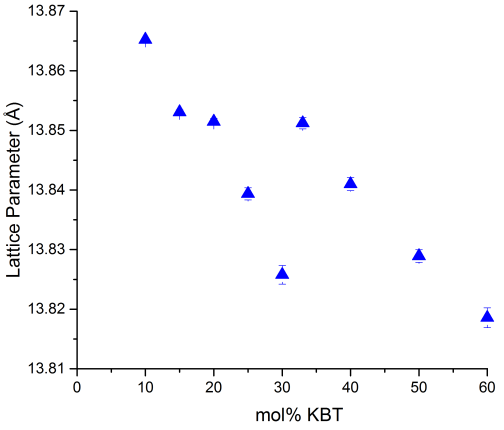

(d) Rhombohedral c lattice parameters.

Figure 3.13: Evolution of lattice parameters with respect to %mol KBT.

uncertainty in the exact KBT lattice parameters.

It is noted that the system does not fully follow Vegard's law [38], represented by the 'Expected' line. Instead, the system maintains a stable average lattice parameter until above 40% KBT. At this point, it follows a delayed version of Vegard's law, varying near-linearly with composition.

Figure 3.13 shows the cubic (black squares), rhombohedral a (red circles), rhombohedral c (blue upwards triangle), tetragonal a (pink downwards triangle), tetragonal c (green diamond), monoclinic a (dark blue leftwards triangle), monoclinic b (light purple rightwards triangle) and monoclinic c (dark purple hexagon) lattice parameters as they evolve with increasing mol% KBT. Figure 3.13a shows all of the room temperature lattice parameter data.

Figure 3.13b shows the lattice parameters close to the cubic lattice parameters. With an increase in mol% KBT, the monoclinic and then the tetragonal

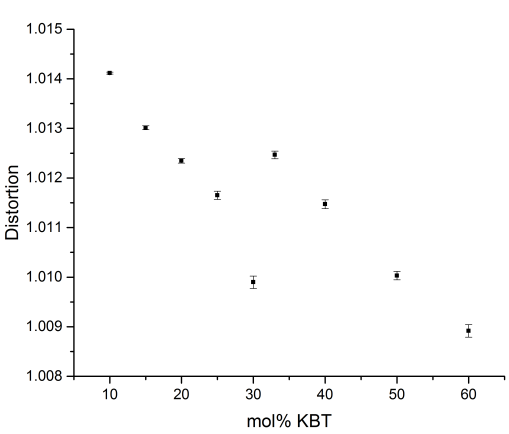

(a) Rhombohedral distortion with respect to composition.

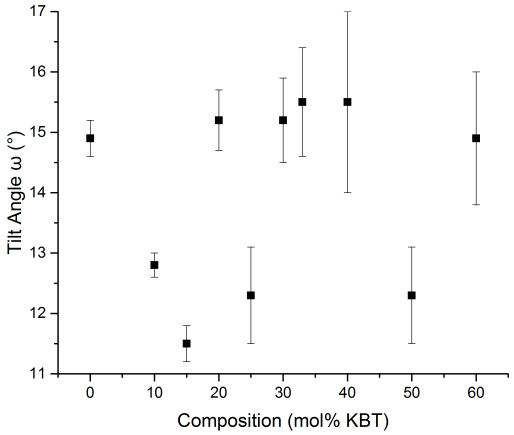

(b) Octahedral tilt angle, ω

Figure 3.14: Evolution of rhombohedral distortion and octahedral tilt [35] with respect to composition.

lattice parameters are found to occur. The splitting in the tetragonal and monoclinic lattice parameters were found to increase with increasing KBT content. From this graph, it can be seen that the tetragonal phase had a higher level of splitting than the monoclinic phase.

Figure 3.13c shows the rhombohedral a/b parameters with respect to the composition. These are seen to increase slightly across the compositional range with increasing mol% KBT.

Figure 3.13d shows the rhombohedral c lattice parameter with respect to the composition. These seem to show a discontinuity between 30% KBT and 33% KBT which is not replicated in the average lattice parameters, calculated from the volume, nor in the cubic parameter. There is a discontinuity at the same composition in the rhombohedral a/b lattice parameter. The rhombohedral c lattice parameter decreased with increasing mol% KBT. This combined with the increase in the a/b parameter shows the rhombohedral splitting decreasing with increasing composition, in addition to the decrease in intensity of the rhombohedral phase.

Figure 3.14a shows the lattice distortion for the rhombohedral lattice, calculated as $\left(\frac{c}{a}\right)/\sqrt{6}$. It can be seen that the discontinuity noted at 30% KBT is repeated here, meaning that the differences in the a and c parameter do not average out here, despite doing so in the volume plot.

Utilising the method of Megaw and Darlington [35] the evolution of the octahedral tilting angle, ω, with respect to composition was investigated. Figure 3.14b shows the large increase in uncertainty as the composition was increased. In

the 20% KBT sample, the rhombohedral phase percentage is still high, but is no longer the dominant phase; this measurement showed an increase in error, but was still below the errors from the larger mol% KBT samples. The higher mol% KBT samples have such a small rhombohedral phase percentage that, with the already poor resolution for oxygen atoms through x-ray means, result in very large errors and unreliable data for values based on the oxygen atom positions. The octahedral strain was also investigated in the same way, but had the same issue with large errors.

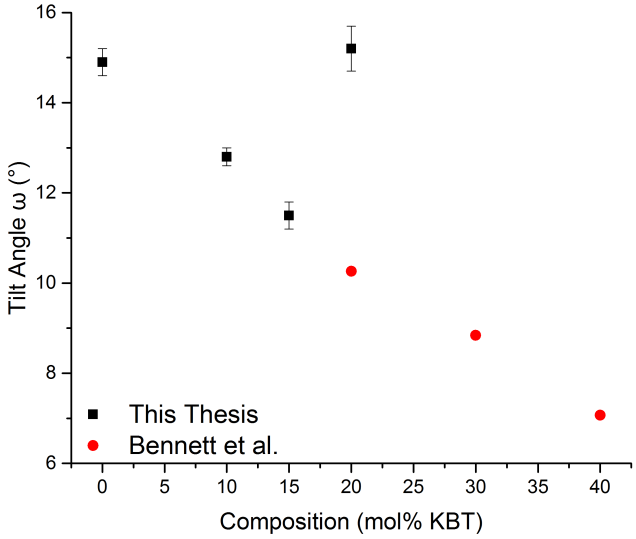

Figure 3.15: Comparison of the low mol% KBT tilt peaks obtained in this thesis and the tilt peaks obtained by Bennett *et al.* [34].

Comparing the tilt peak values obtained by Bennett *et al.* [34] (shown in Table 3.11) with the data obtained in this thesis, the low mol% KBT samples can be seen to fit a similar trend in Figure 3.15, while the 20% KBT and higher does not, corresponding with the change from the rhombohedral phase being the dominant phase to the cubic phase being the dominant phase.

3.5 Conclusions and Room Temperature Phase Diagram

Figure 3.16 describes the change in the percentages of rhombohedral phase, cubic phase, monoclinic phase and tetragonal phase with respect to the changes in the mol% of KBT in the powder, a visual representation of percentage data in Table 3.3. The 'cubic' phase in the figure is actually the result of averaging of short range order, not a true cubic phase.

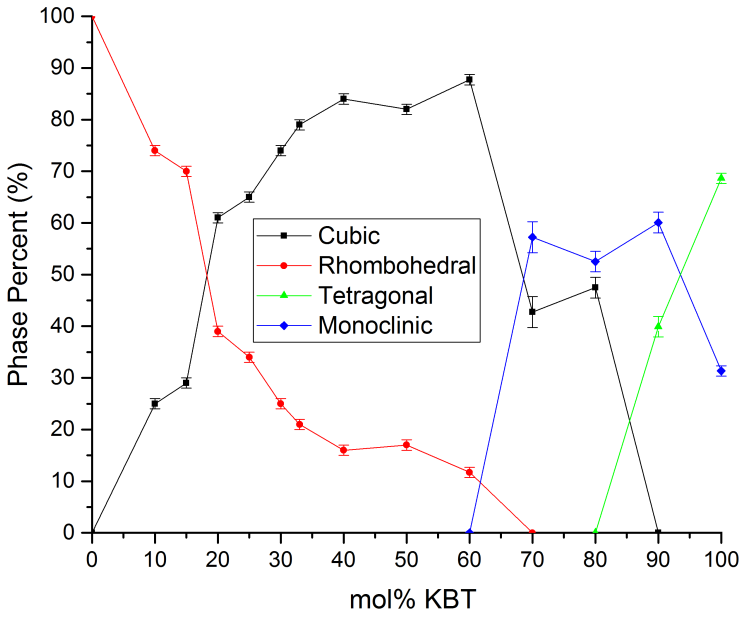

Figure 3.16: Phase percentages for the samples at room temperature. The cubic phase is represented by the black line with square points, the rhombohedral phase is represented by the red line with circles, the monoclinic phase is represented by the blue line with diamonds, and the tetragonal phase is represented by the green line with triangles.

Comparing Figure 3.16 to the earlier phase diagram constructed in the literature review, Figure 1.6 in Section 1.6.1 where the transition to pseudocubic was around 40% KBT, it can be seen that this is the region where the rhombohedral influences reach a stable minimum, but are still present. In the region between 15% KBT and 20% KBT, the system switches from a rhombohedrally dominated structure to a cubically dominated structure, so it is possible that there may be some enhanced properties around this region. At the higher mol% KBT end of the graph, it can be seen that there is a transition from the rhombohedral-cubic model to a mixed model of monoclinic and cubic, then monoclinic and tetragonal. From the data in Figure 3.12 these transitions can be seen to coincide with discontinuities in the average lattice parameters; from the rhombohedral component to a monoclinic component which allows a smaller average lattice parameter, and from a cubic component to direct influence from the tetragonal end member. Additionally, the data obtained at 90% KBT and 100% KBT shows a transition away from the cubic phase to a tetragonal mixed phase, meaning that the results of the experiments undertaken give the KBT end member as a mixed phase material between tetragonal and monoclinic, with the majority of the intensity coming from the tetragonal peaks. This means that not only does the phase diagram

presented here add an additional monoclinic phase into the phase diagram, the KBT end of the diagram is presented as not simply being tetragonal but rather a mixed phase, as discussed in Section 3.4.1. The mixed phases in each composition may also be fitting some amount of background noise in addition to the peak intensities they are included to model.

From Section 3.2.2 it was shown that the KBT-BFO powder is one single, powder with homogeneous composition (though it is still possible for structural nanoregions to exist within the powder, such as those proposed by Matsuo *et al.* [1]). As a result, the multiphase structures proposed must necessarily be multiple phases in the same material rather than two disparate materials with a phase associated with each.

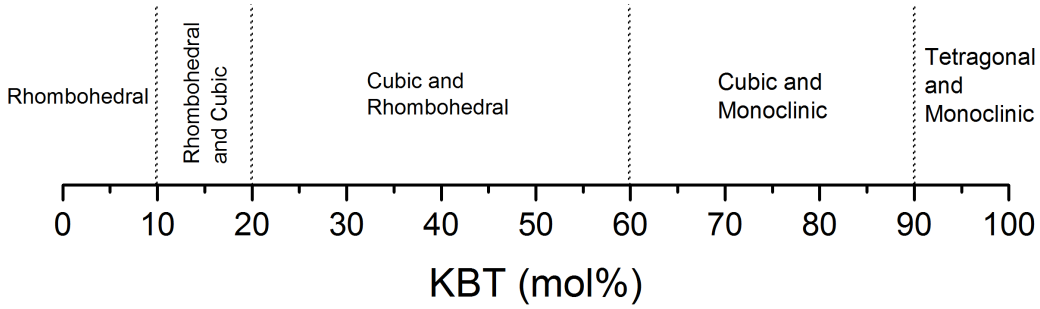

Figure 3.17: Simplified phase diagram from the information in Figure 3.16. The difference between 'Rhombohedral and Cubic' and 'Cubic and Rhombohedral' is that in the former the rhombohedral phase is dominant, whereas in the latter the cubic phase is dominant. The dotted lines do not represent sharp phase transitions but rather the point at which the optimum model for discussing the structure has moved from one mixed phase to the next.

Figure 3.17 is another representation of the data displayed in Figure 3.16. It must be noted that there have been no sharp transitions or distinctions across the compositional range, and the noted boundaries should not be considered definite phase transitions; they are a representation of where the model presented in that section was found to be the best representation of the data. The cubic and monoclinic region especially is vague in terms of its optimum representation; two-cubic and cubic-tetragonal models are also viable, but the cubic and monoclinic model is slightly better and also matches with the transition noted from a highly cubic to a majority tetragonal model in the literature [9]. From the elemental maps compiled in Section 3.2.2 it is clear that the samples were homogeneous and could not then be explained by a simple mix of end member powders, thus requiring the mixed phase models proposed.

Comparing the simplified phase diagram in Figure 3.17 with Figure 1.6 in Section 1.6.1, good agreement can be seen with the general trend, with additional

nuance introduced from the experiments conducted in this chapter with the addition of a monoclinic element at high mol% KBT and the mixing of the rhombohedral phase with cubic phase even at low mol% KBT compositions.

Other similar relaxor materials such as $(1-x)(Bi_{1/2}K_{1/2})TiO_3$-$(x)Bi(Mg_{2/3}Nb_{1/3})O_3$ (KBT-BMN) [25] show similar cubic-like phases of long range order, but the BFO-KBT system is rare in the range over which the transitions from the end members to this cubic phase take place; in $(1-x)$KBT-(x)BMN for example, another material with a rhombohedral end member and KBT as the other end member, the cubic phase is produced by $x = 0.05$, whereas in $(1-x)$BFO-(x)KBT the most cubic phase is not obtained until the range $0.3 \leq x \leq 0.6$, and even in that case there is still a remnant rhombohedral phase present in the material. In all mixed samples of BFO-KBT investigated, a mixed phase provided the optimum model for the data obtained.

Further comparing these results to other perovskite materials known to have morphotropic phase boundaries, such as the archetype material PZT (the MPB of which is less than 5 mol% $PbTiO_3$ across) it is clear that having the mixed phases observed across so wide a range of measured compositions is unusual. Aksel [39] reviews several other known MPBs for perovskite materials, such as NBT-KBT, with an MPB between 16 and 22 mol% KBT; NBT-KNN, with an MPB between 6 and 7 mol% KNN and also between 2 and 3 mol% NBT; NBT-BT, with an MPB between 6 and 7 mol% BT; KNN-BT with MPBs at 6 and 20 mol% BT. As can be seen from the list, none of these are as wide as the mixed phase region found in BFO-KBT, which, from the data obtained, extends between at least 10 and 100 mol% KBT, making the BFO-KBT system one with a very large mixed phase region, which contains multiple MPBs, since MPBs have been reported at 40% KBT [1], 75% KBT [7] and 94% KBT [2].

Overall, comparing the phase diagram in Figure 3.16 or Figure 3.17 with the one constructed from the literature in Section 1.6.1, an advancement in the model of the system is presented, with almost the entire phase diagram (everything but the BFO end member) being best represented by a mixed phase, which have been presented quantitatively. The evolution of these phases with respect to composition are shown. In addition, a $P1m1$ monoclinic phase is proposed as a phase component at high % KBT values, which has not been reported before. In addition to this, the 100% KBT end member is presented as being a mixed phase of tetragonal and monoclinic, discussed in detail in Section 3.4.1.

3.6 References

Bibliography

[1] Matsuo, H., Noguchi, Y., Miyayama, M., Suzuki, M., Watanabe, A., Sasabe, S., Mori, S., Torii, S., Kamiyama, T., **104103**:1 (2011).

[2] Kim, J. M., Sung, Y. S., Cho, J. H., Song, T. K., Kim, M. H., Chong, H. H., Park, T. G., Do, D., Kim, S. S., *Ferroelectrics*, **404**:88 (2010).

[3] Morozov, M. I., Einarsrud, M., Grande, T., Damjanovic, D., *Ferroelectrics*, **439**:88 (2012).

[4] Zurbuchen, M. A., Lettieri, J., Fulk, S. J., Jia, Y., Carim, A. H., Schlom, D. G., *Applied Physics Letters*, **82**:4711 (2003).

[5] Barz, R., Neumayer, D., Majhi, P., Wang, C., Dey, S., *Integrated Ferroelectrics*, **39**:61 (2001).

[6] Mubarak, T. H., Azhdar, B., Hassan, K. H., Kareem, C. H., *International Journal of Innovative Research in Science, Engineering and Technology*, **03**:17034 (2014).

[7] Morozov, M. I., Einarsrud, M.-A., Grande, T., *Applied Physics Letters*, **101**:252904 (2012).

[8] König, J., Spreitzer, M., Jančar, B., Suvorov, D., Samardžija, Z., Popovič, A., *Journal of the European Ceramic Society*, **29**:1695 (2009).

[9] Anand, S., Pandey, R., Shankar, U., Singh, A. K., *Journal of the American Ceramic Society*, **8**:1 (2016).

[10] Krad, I., Bidault, O., Geoffroy, N., Maaoui, M. E., *Ceramics International*, **42**:3751 (2016).

[11] Hagiwara, M., Fujihara, S., *Journal of Applied Crystallography*, **54** (2015).

[12] Jones, G. O., Kreisel, J., Thomas, P. A., *Powder Diffraction*, **17** (2002).

[13] Otoničar, M., Škapin, D., Jan, B., **58**:1928 (2011).

[14] Sung, Y. S., Kim, J. M., Cho, J. H., Song, T. K., Kim, M. H., Chong, H. H., Park, T. G., Do, D., Kim, S. S., *Integrated Ferroelectrics*, **114**:92 (2010).

[15] Wicheanrat, C., Laowanidwatana, A., Bongkarn, T., *Integrated Ferroelectrics*, **149**:9 (2013).

[16] Liu, S., Blanchard, P. E. R., Zhang, Z., Kennedy, B. J., Ling, C. D., *Dalton Transactions*, **44**:10681 (2015).

[17] Hiruma, Y., Aoyagi, R., Nagata, H., Takenaka, T., *Japanese Journal of Applied Physics*, **44**:5040 (2005).

[18] Xie, H., Jin, L., Shen, D., Wang, X., Shen, G., *Journal of Crystal Growth*, **311**:3626 (2009).

[19] Otoničar, M., Škapin, S. D., Jančar, B., Ubic, R., Suvorov, D., *Journal of the American Ceramic Society*, **93**:4168 (2010).

[20] Tabuchi, K., Inoue, Y., Nagata, H., Takenaka, T., *Ferroelectrics*, **457**:124 (2013).

[21] TABUCHI, K., NAGATA, H., TAKENAKA, T., *Journal of the Ceramic Society of Japan*, **121**:623 (2013).

[22] Thongtha, A., Laowanidwatana, A., Bongkarn, T., *Integrated Ferroelectrics*, **149**:32 (2013).

[23] Wefring, E. T., Morozov, M. I., Einarsrud, M. A., Grande, T., *Journal of the American Ceramic Society*, **97**:2928 (2014).

[24] König, J., Suvorov, D., *Journal of the European Ceramic Society*, **35**:2791 (2015).

[25] Pan, Z., Wang, Q., Chen, J., Liu, C., Fan, L., Liu, L., Fang, L., Xing, X., *Journal of the American Ceramic Society*, **98**:104 (2015).

[26] Kreisel, J., Glazer, A. M., Jones, G., Thomas, P. A., Abello, L., Lucazeau, G., *Journal of Physics: Condensed Matter*, **12**:3267 (2000).

[27] Li, Z. F., Wang, C. L., Zhong, W. L., Li, J. C., Zhao, M. L., *Journal of Applied Physics*, **94**:2548 (2003).

[28] Hou, Y. D., Hou, L., Huang, S. Y., Zhu, M. K., Wang, H., Yan, H., *Solid State Communications*, **137**:658 (2006).

[29] Zhu, M., Hou, L., Hou, Y., Liu, J., Wang, H., Yan, H., *Materials Chemistry and Physics*, **99**:329 (2006).

[30] F Wang, XF Qin, YF Meng, ZL Guo, LX Yang, Y. M., Chen, D., Jiao, X., Zhang, M., *Materials Research Bulletin*, **35**:2101 (2011).

[31] O'Brien, A., *Investigation of the Structure of the Perovskite Series (Na1-xKx)1/2Bi1/2TiO3*, Ph.D. thesis (2013).

[32] Hagiwara, M., Fujihara, S., *Journal of Materials Science*, **50**:5970 (2015).

[33] Schierholz, R., Fuess, H., *Journal of Applied Crystallography*, **45**:766 (2012).

[34] Bennett, J., Bell, A., Stevenson, T., Smith, R., Sterianou, I., Reaney, I., Comyn, T., *Materials Letters*, **94**:172 (2013).

[35] Megaw, H. D., Darlington, C. N. W., *Acta Crystallographica Section A*, **31**:161 (1975).

[36] Kubel, F., Schmid, H., *ACTA CRYSTALLOGRAPHICA SECTION B-STRUCTURAL SCIENCE*, **46**:698 (1990).

[37] Bucci, J., Robertson, B. K., James, W. J., *JOURNAL OF APPLIED CRYSTALLOGRAPHY*, **5**:187 (1971).

[38] Denton, A. R., Ashcroft, N. W., *Physical Review A*, **43**:3161 (1991).

[39] Aksel, E., Jones, J. L., *Sensors*, **10**:1935 (2010).

Chapter 4

High Temperature Powder Investigation

4.1 Introduction

This chapter describes the investigation of the (1-x) $BiFeO_3$-(x) $(K_{0.5}Bi_{0.5})TiO_3$ (BFO-KBT) system using non-ambient powder diffraction. As discussed in Chapter 3, in the range of $0.1 \geq x \leq 0.5$ there is strong evidence of a mixed rhombohedral and cubic phase. High temperature powder x-ray diffraction measurements have been taken to characterise the rhombohedral-cubic phase boundary with respect to temperature. It is known that at high temperature, both BFO and KBT form cubic structures [1, 2]. An investigation was carried out to determine the way in which this mixed phase evolved with temperature; since both BFO and KBT are known to become cubic at high temperature, it was expected that the mixed samples would also become cubic at high temperature. This, along with the in depth analysis at room temperature of the BFO-KBT system, allowed a phase diagram of the system to be constructed. When discussing the BFO-KBT system, where a '% KBT' value is mentioned, this refers to the mol% of KBT.

4.2 Experimental Details

The high temperature measurements used the same sintered powders as were described in Chapter 3. The experiments were conducted on a *Panalytical X-Pert Pro MPD* $K_{\alpha 1}$ diffractometer, equipped with an *Anton Paar HTK1200N* furnace stage.

The powders were carefully packed and flattened into the ceramic furnace

stage mounting, and inserted into the *HTK1200N* stage. Thermal expansion alters the stage height, therefore the stage height needs to be able to move to compensate. Before the experiment, the stage height was set at room temperature for each sample by checking for the point at which the sample was half-cutting the straight-through beam. Once this point was obtained, it could then be calculated automatically through the use of a look-up table through AP STAGE MOVER as the system changed in temperature. The table related known components to their thermal expansion, allowing the changes in height due to temperature to be negated.

Two types of measurement were taken:

(a) 6 hour measurements, in the range 20° 2θ to 90° 2θ with step size of 0.013° 2θ and a counting time of 1050s per step. The range in 2θ allowed full Rietveld refinements to be conducted on these measurements, shown in Section 4.4. Experimental time constraints limited the number of these measurements during a run.

(b) The second type of measurement were 30 minute measurements. These allowed more scans to be completed in any given time for an experiment, which in turn allowed a more finely graduated set of temperature data to be obtained than would have been possible with just the longer scans. This meant that a better model for the temperature range at which the data could be fitted with a purely cubic model was able to be found. These measurements were taken between 30° 2θ and 33° 2θ, and like the 6 hour measurements, also used a step size of 0.013° 2θ, with a counting time of 1000s per step. This covered the area of the {110} peak, chosen as a representative of the whole measurement because it was the most intense peak and showed the greatest change (along with the {111} peak) between low and high temperatures from preliminary 6 hour measurements. While these were not able to be analysed through Rietveld refinement, alternative methods of analysing them were employed, discussed in Section 4.5.

4.3 Powder X-ray Diffraction Data Across Wide 2θ Range

In this section, the x-ray diffraction was used to probe the structure of the BFO-KBT system as a function of temperature. This was to determine the point at which the ratio between the rhombohedral and cubic phase components of the overall structure had shifted to such a point as the structure could be considered cubic. The measurements included here were chosen to best represent the system, the lowest two temperatures showing the stable region from room temperature up to the temperature at which this stable region was found to destabilise and larger

Table 4.1: Compositions and the temperatures at which changes were noticed from visual inspection of the data in Figure 4.1, Figure 4.2, Figure 4.3, and Figure 4.4. The blank cubic entries indicate that the sample did not appear to form a single cubic phase at high temperature.

Composition (mol% KBT)	Rapid Cubic Phase Increase (°C)	Cubic After (°C)
15	350	-
20	650	850
30	500	800
40	650	800
50	600	800
60	300	-
70	500	-
80	300	-
90	300	-
100	270	500

changes in the ratio between the cubic and rhombohedral phases were found to begin, with all the measurements above this temperature included. In all cases, the graphs are presented as a stacked plot.

Figure 4.1 and Figure 4.2 show a representative sample of the changes observed when heating a BFOKBT powder sample as stacked plots. The largest changes observed were often found to be in the {110} peak, which are then expanded in Figure 4.3 and Figure 4.4. It was found that few changes were observed until some given temperature, at which point the patterns would begin to look more cubic, and then at some higher temperature would often become indistinguishable from cubic; these temperatures are summarised in Table 4.1 for all samples.

The BFO-KBT powders were found to become more cubic with increasing temperature. Both BFO and KBT are known to become cubic at high temperatures (931 °C [1] and 410-450°C [2, 3, 4] respectively), and so it was thought that the mixed state would also do so. In the case of BFO, it has been reported that the material undergoes an initial transition to orthorhombic between 820°C and 830°C [5]. In the case of KBT, the transition is reported to begin at 280°, with a mixed cubic and tetragonal phase existing between 280°C and 450°C [2]. In this respect, it seems that the BFO-KBT material experiences a high temperature transition more like that found in KBT than that found in BFO, given that from Chapter 3 it was found that the material exists in a mixed phase at room temperature, and in addition there is no evidence to support the transition from this mixed phase to an orthorhombic phase before the transition to a cubic phase occurs.

At low mol% KBT compositions, the high temperature state visually resembled a single cubic phase, whereas at higher mol% KBT compositions a single cubic phase would not be able to represent the data, despite both end members

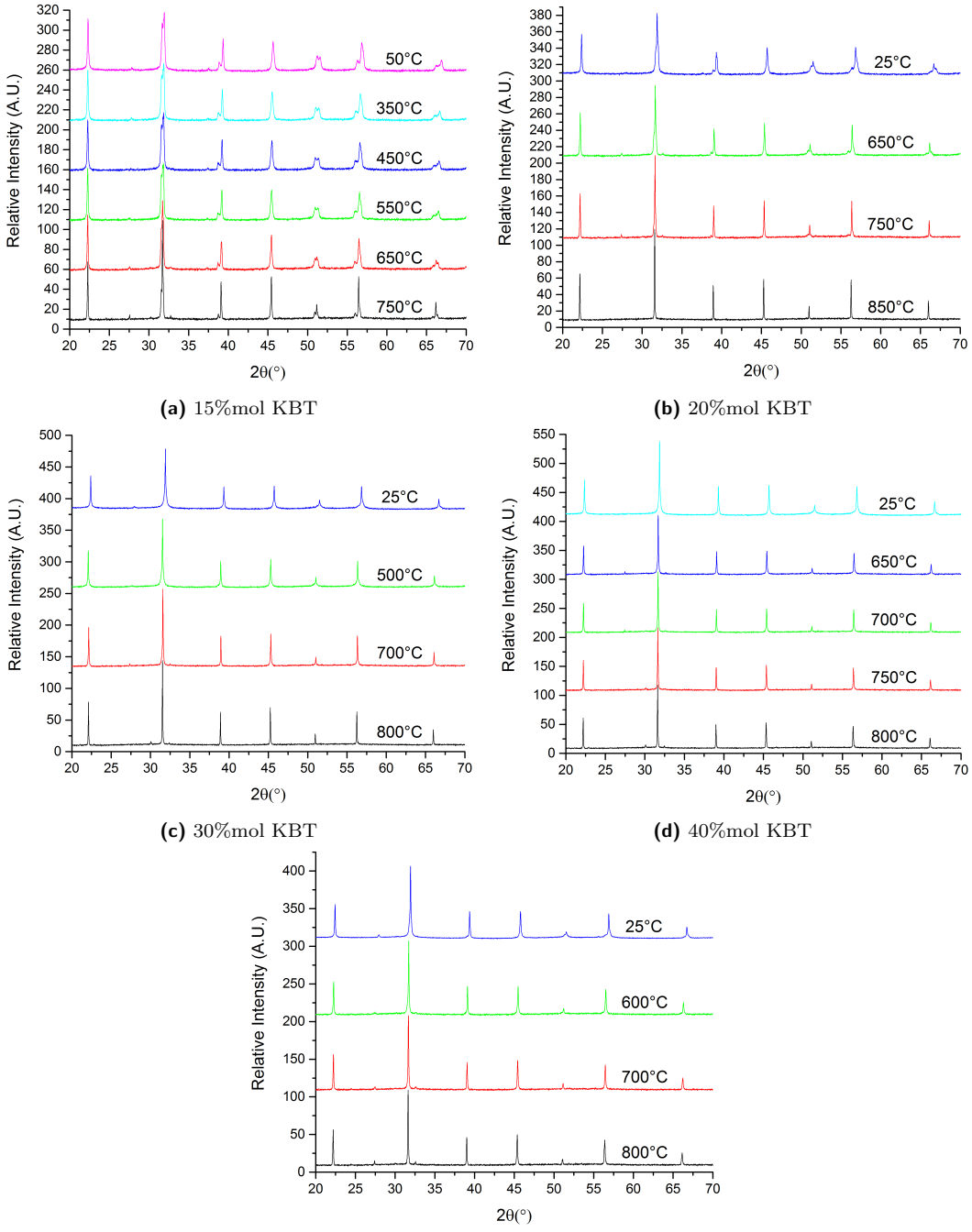

(a) 15%mol KBT

(b) 20%mol KBT

(c) 30%mol KBT

(d) 40%mol KBT

(e) 50%mol KBT

Figure 4.1: Stacked plots of the different temperature measurements for the different compositions of BFO-KBT investigated with respect to temperature. Of particular note are the {110} peaks around 31-32 ° 2θ, which show the clearest change from the stable lower temperature measurements and the higher temperature measurements. The values included have been square rooted to allow for easier comparison between the different plots without losing the relevant details.

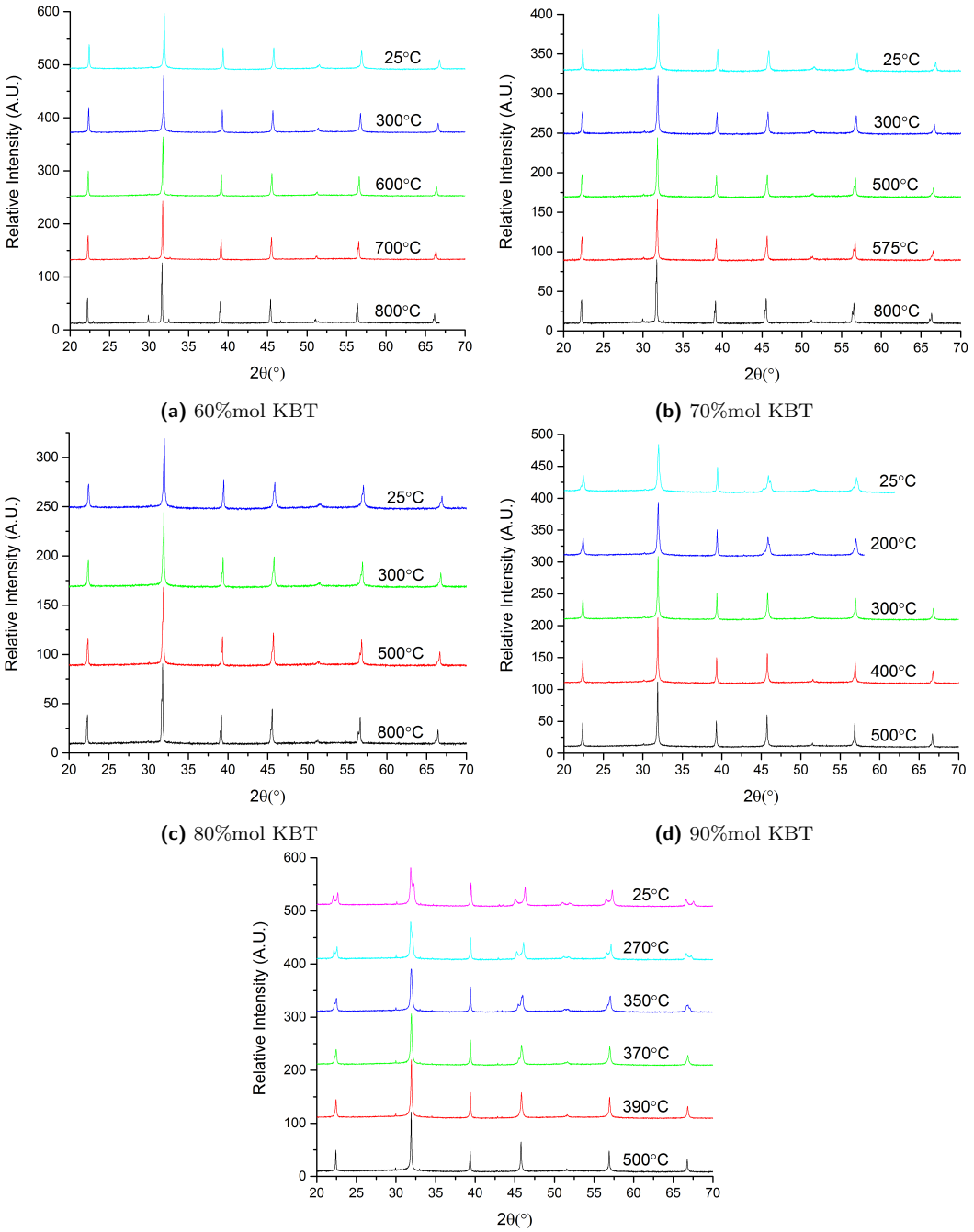

(a) 60%mol KBT

(b) 70%mol KBT

(c) 80%mol KBT

(d) 90%mol KBT

(e) 100%mol KBT

Figure 4.2: Stacked plots of the different temperature measurements for the different compositions of BFO-KBT investigated with respect to temperature. Of particular note are the {110} peaks around 31-32 ° 2θ for lower mol% KBT, and the {200} peaks around 45-48 ° 2θ for higher mol% KBT. The values included have been square rooted to allow for easier comparison between the different plots without losing the relevant details. Some minor mechanical issues resulted in some scans being cut short.

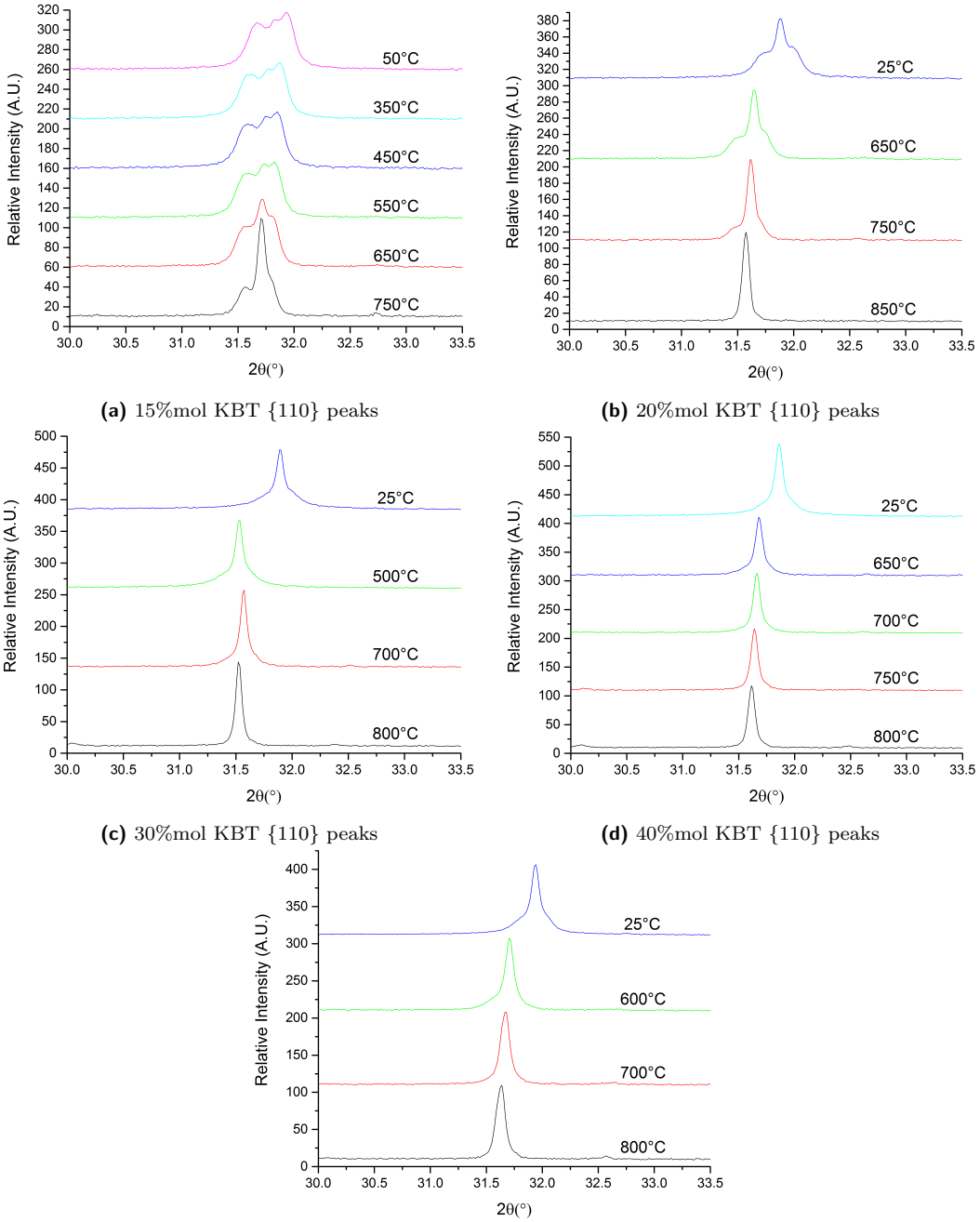

(a) 15%mol KBT {110} peaks

(b) 20%mol KBT {110} peaks

(c) 30%mol KBT {110} peaks

(d) 40%mol KBT {110} peaks

(e) 50%mol KBT {110} peaks

Figure 4.3: Stacked plots of the {110} peaks at different temperatures for the different compositions of BFO-KBT investigated with respect to temperature, presented with square rooted data. These peaks show the greatest difference with respect to temperature.

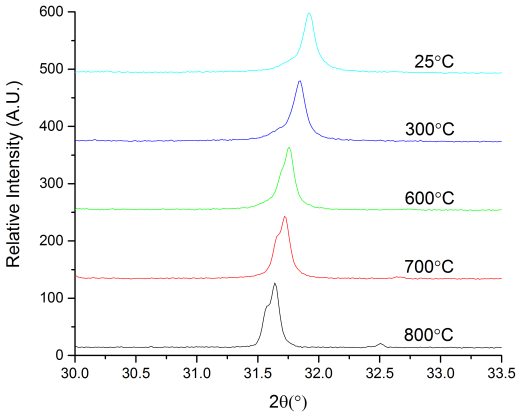

(a) 60%mol KBT {110} peaks

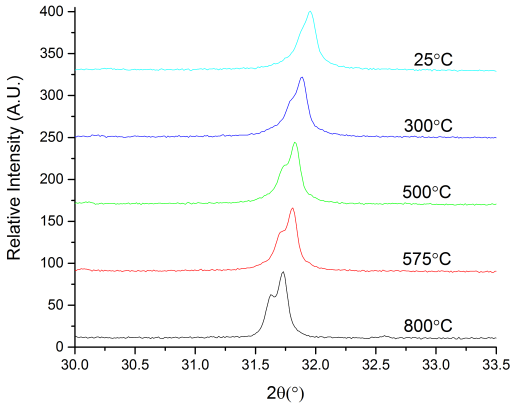

(b) 70%mol KBT {110} peaks

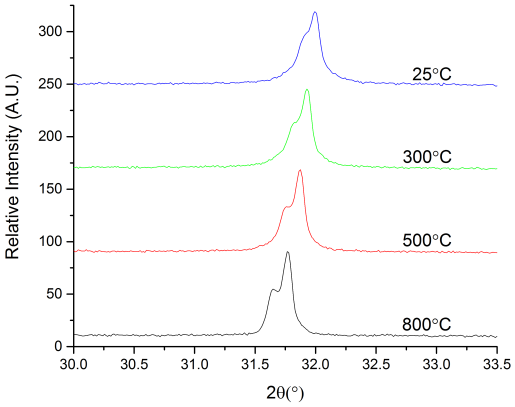

(c) 80%mol KBT {110} peaks

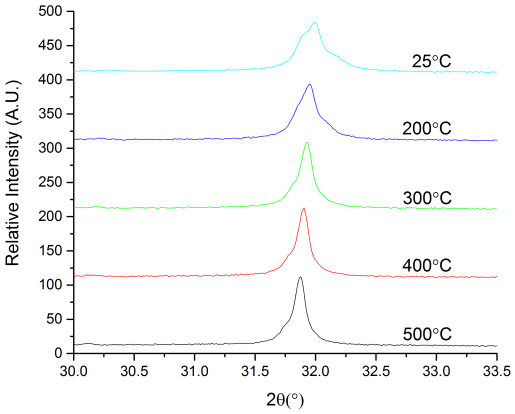

(d) 90%mol KBT {110} peaks

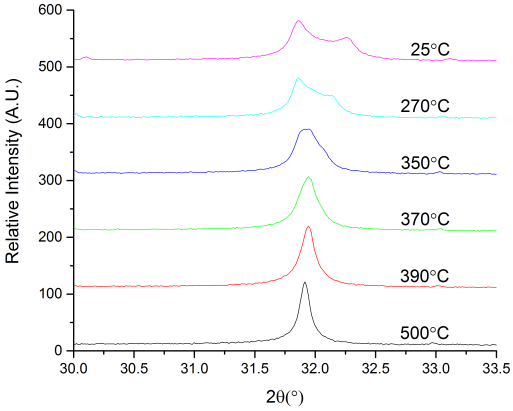

(e) 100%mol KBT {110} peaks

Figure 4.4: Stacked plots of the {110} peaks at different temperatures for the different compositions of BFO-KBT investigated with respect to temperature, presented with square rooted data. These peaks show the greatest difference with respect to temperature.

forming a cubic phase at high temperature.In addition, given the lower temperature of the cubic transition in KBT, it was expected that the higher KBT % material would become cubic at lower temperatures than the lower KBT % material, and even before Rietveld refinement in Section 4.4 it appears that this is the case. It was also observed that at high temperature, the secondary phases within the material changed, even in 40% KBT samples which originally had no impurity phase which formed a Bi_2O_3 phase when returned to room temperature, the same phase present in other low mol% KBT samples. This is discussed in more detail in section 4.6.

4.4 Rietveld Refinements

As in the room temperature analysis of the diffraction data, Rietveld refinement was used to characterise the structure and phase composition of the BFO-KBT powder samples. These were conducted on samples of 15% KBT, 20% KBT, 30% KBT, 40% KBT, 50% KBT, 60% KBT, 70% KBT, 80% KBT, 90% KBT and 100% KBT. As many of the samples are very similar to other samples of similar composition, only the 15% KBT, 20% KBT, 40% KBT, 70% KBT and 100% KBT samples are examined here in detail, with notes included regarding similar compositions and any deviations from the presented samples. These refinements were conducted in the same way as described in the room temperature powder chapter, Chapter 3; the expected 'main' phase was refined first and the 'additional' phase added in second (So rhombohedral first for the lower % KBT samples at low temperature, and cubic first at higher % KBT and higher temperatures for example) and the impurity phase was added in last in all cases. The refined room temperature structures were used as a basis for the refinements.

Figure 4.5 shows the plot of the diffraction data for a sample of 15% KBT at 25°C which was compared with the multiphase model. The diffraction data also includes error bars, calculated as the square root of the intensity. It can be seen that the model compares with the data well within the errors. Below these, the difference plot can be seen in green, with the largest divergence between the observed and calculated data in the difference plot corresponding to the largest errors; these divergences are at most of approximately the same magnitude as the errors. This shows that the mixed phase 25°C, originally used in the room temperature powder chapter, Chapter 3 also works well with the data taken from the 25°C measurements of the variable temperature experiments. This allows for the comparison of the difference plot with other temperatures to determine whether the model provides a successful fit to the data observed.

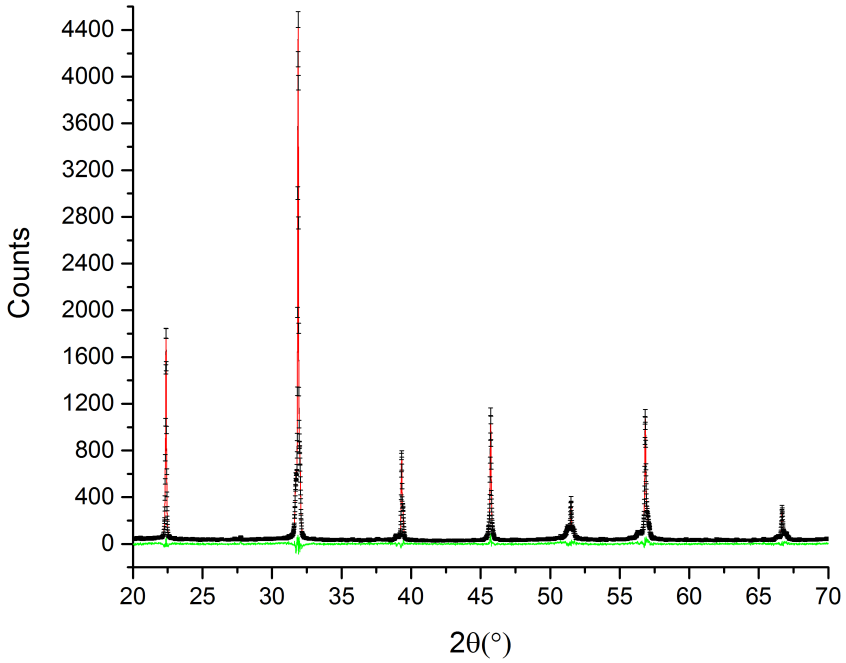

Figure 4.5: Plot of 15% KBT between 20° 2θ and 70° 2θ at 25°C, compared to the intensity in counts. In black with error bars is the observed data, with the calculated model in red. The green line at the bottom is the difference plot between these.

4.4.1 15% KBT High Temperature Rietveld Refinements

Figure 4.6 shows the Rietveld model for a mixed phase state for 15% KBT at 25°C in the range between 20° 2θ and 70° 2θ, with the observed and calculated data. Below this is a difference plot between the observed and calculated values. This difference plot shows that there are no large discrepancies between the observed data and calculated model, consistent with measurements of this sample in Chapter 3. However, it should be noted that this room temperature measurement was taken after the sample had been heated and cooled, which as Section 4.6 will explain, is relevant. Due to this, this measurement was not used as the baseline of these measurements in 15% KBT, but rather the 50°C measurement was. All room temperature graphs will be noted as being taken prior to high temperature measurements (pre) of after the high temperature measurements have been taken and the system cooled (post).

Figure 4.7 shows the {110} peak from the data in Figure 4.6, between 30° 2θ and 33.5° 2θ and includes the cubic phase percentage and the goodness of fit (GoF). In this diagram, it is clearer how the individual contributions from the rhombohedral and cubic phases contribute to the model, fitting a complicated observed peak extremely well. It is clear from this figure that the peak can be

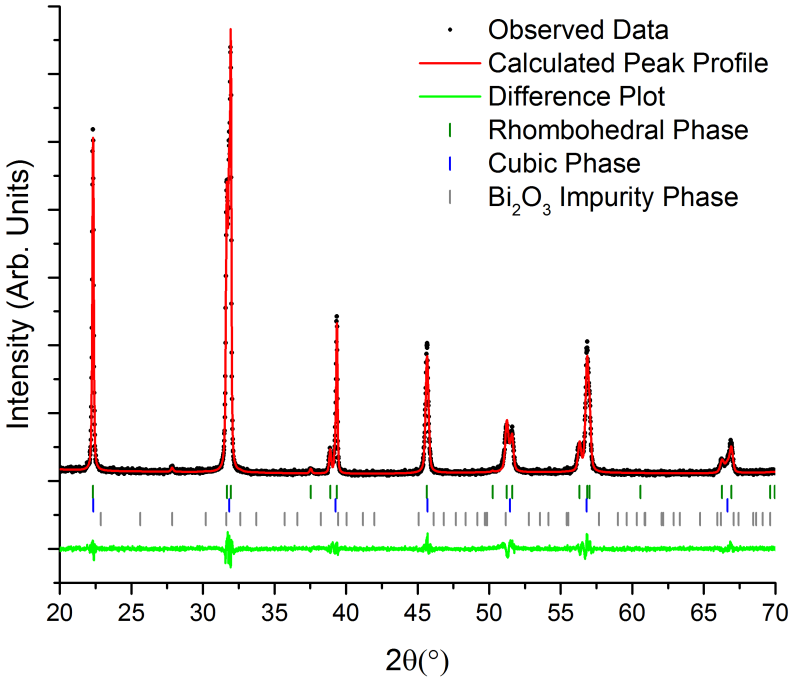

Figure 4.6: Plot of 15% KBT at 25°C, post heating. The observed data is compared with the calculated model, the difference between the two shown as the difference plot. The lines below are the peak positions, with the dark green corresponding to the rhombohedral peaks and the blue corresponding to the cubic peaks.

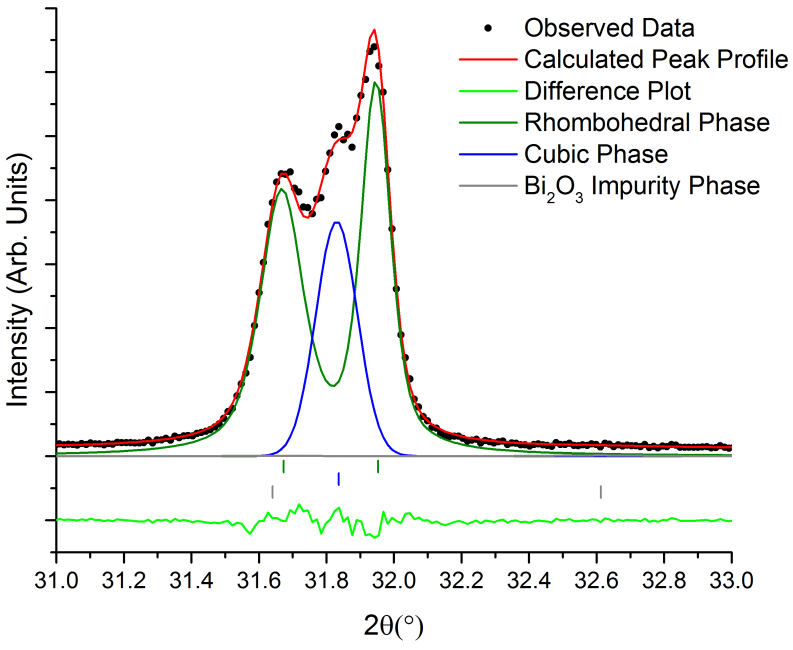

Figure 4.7: Plot of the {110} peak of 15% KBT at 25°C. The GoF from the Rietveld refinement was 1.185, and the cubic percentage was 29(1)%

modelled as a mix of a central cubic peak, with outer rhombohedral peaks. From the difference plot at the bottom and a visual inspection of the peak, it is clear that the mixed model fits this data as well as expected from Chapter 3.

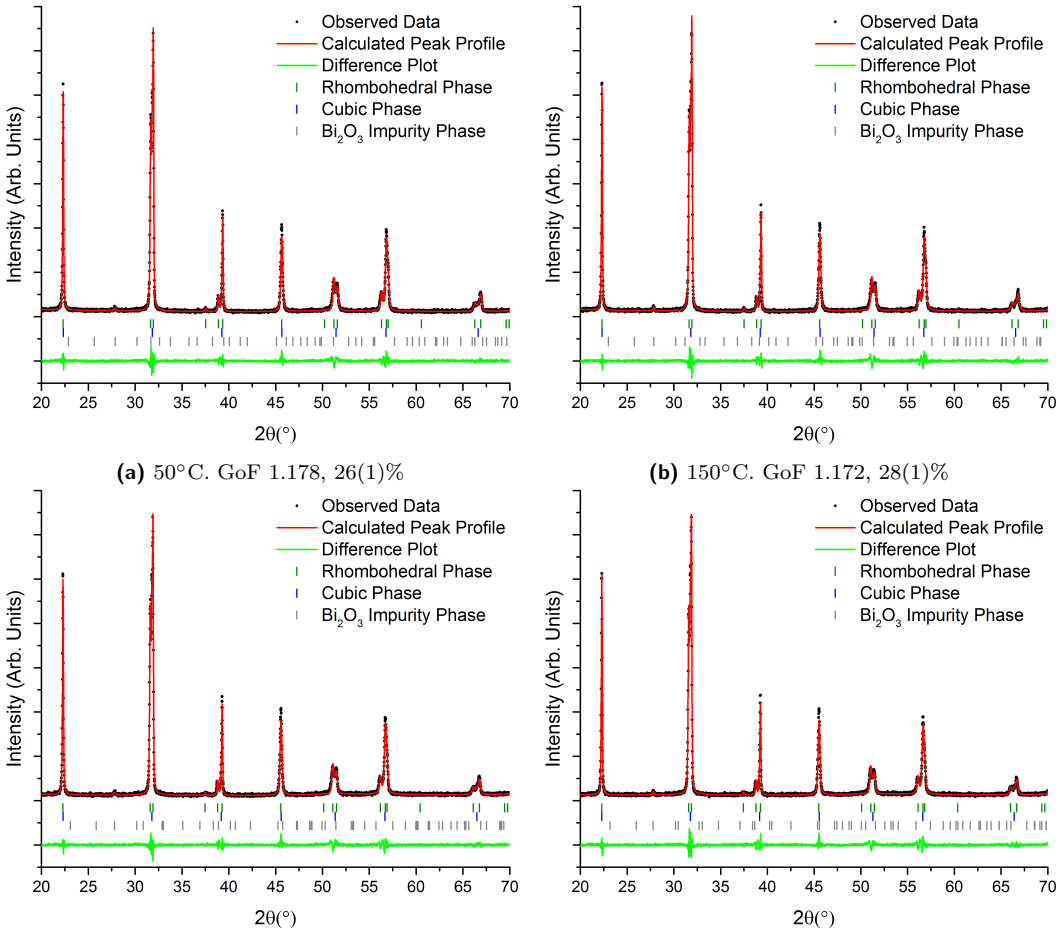

(a) 50°C. GoF 1.178, 26(1)%

(b) 150°C. GoF 1.172, 28(1)%

(c) 250°C. GoF 1.195, 31(2)%

(d) 350°C. GoF 1.199, 31(2)%

Figure 4.8: Plots of the 15% KBT powder with respect to temperature. The listed percentages are the percentage of cubic phase present.

Figure 4.8 and Figure 4.9 show the Rietveld models for 15% KBT samples between 50°C and 350°C and between 450°C and 750°C respectively. These again show the observed and calculated data like Figure 4.6. A closer examination of the {110} peaks are available in Figure 4.10 and Figure 4.11, from which it is clear the way in which the rhombohedral and cubic models intersect to provide the complicated peak shape, with the cubic peak at the centre with a rhombohedral peak either side of it, and the way in which this model evolves with respect to temperature. It can also be seen that the impurity phase is well fitted by the impurity model used.

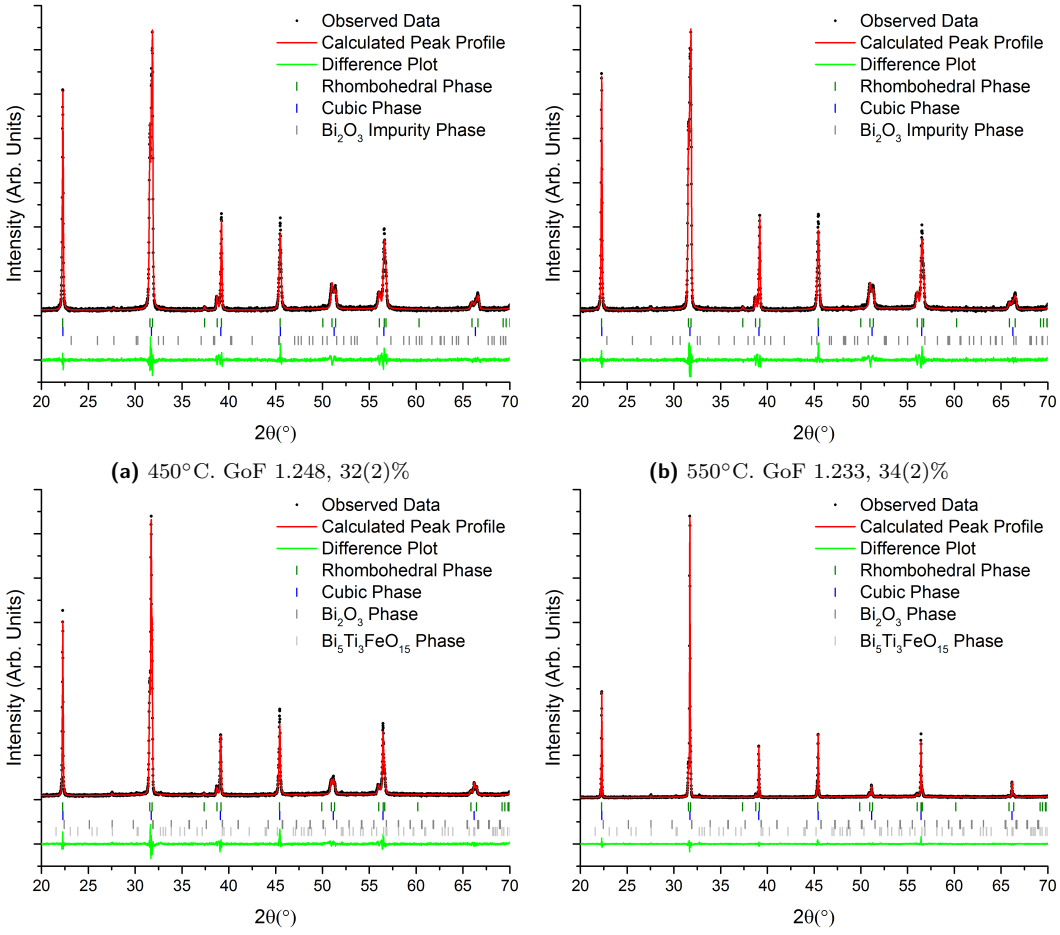

(a) 450°C. GoF 1.248, 32(2)%

(b) 550°C. GoF 1.233, 34(2)%

(c) 650°C. GoF 1.224, 51(1)%

(d) 750°C. GoF 1.112, 70.3(8)%

Figure 4.9: Plots of the 15% KBT powder with respect to temperature. The listed percentages are the percentage of cubic phase present.

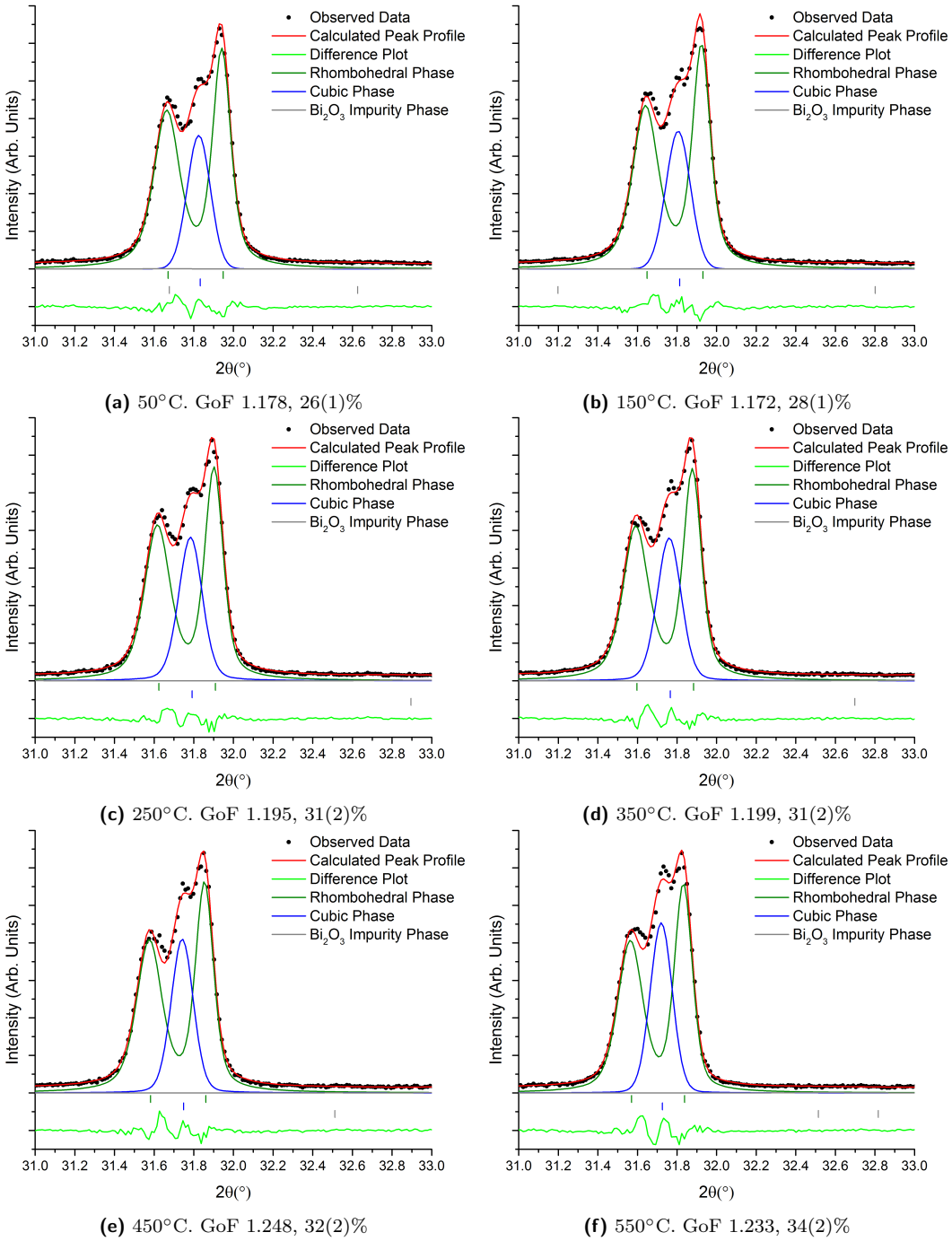

(a) 50°C. GoF 1.178, 26(1)%

(b) 150°C. GoF 1.172, 28(1)%

(c) 250°C. GoF 1.195, 31(2)%

(d) 350°C. GoF 1.199, 31(2)%

(e) 450°C. GoF 1.248, 32(2)%

(f) 550°C. GoF 1.233, 34(2)%

Figure 4.10: 15% KBT {110} graphs with respect to temperature, from 50°C to 550°C. The goodness of fit is included. The listed percentages are the cubic fraction.

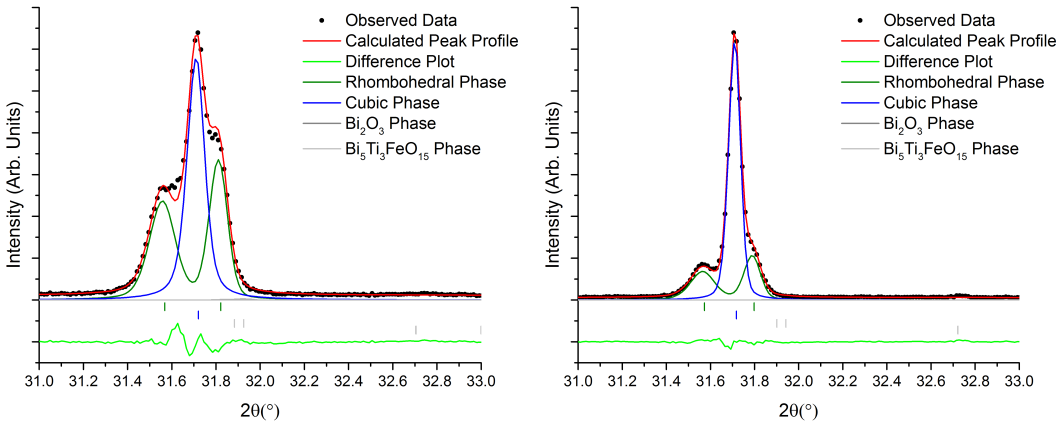

(a) 650°C. GoF 1.224, 51(1)%

(b) 750°C. GoF 1.112, 70.3(8)%

Figure 4.11: 15% KBT {110} graphs with respect to temperature at 650°C and 750°C. The goodness of fit is included. The listed percentages are the cubic fraction.

Figure 4.8a shows the Rietveld model for a mixed phase state for 15% KBT at 50°C, comparable to the room temperature model used in Chapter 3. A closer examination of the {110} peak is provided in Figure 4.10a, showing how the two phases form the more complicated peak, with the cubic peak at the centre with a rhombohedral peak either side of it. In this case, the cubic peak can be seen to have a lower intensity than either of the rhombohedral peaks. This cubic peak fills out the area between the rhombohedral peaks, making the splitting between the peak less apparent.

Figure 4.8b and Figure 4.10b show Rietveld model for a mixed phase state for 15% KBT at 150°C, which can be seen to be virtually unchanged from the model at 50°C. This is also true at 250 °C (Figure 4.8c and Figure 4.10c), 350°(Figure 4.8d and Figure 4.10d) and 450°C (Figure 4.9a and Figure 4.10e); the only marginal differences across this range is a slight increase in the cubic peak intensities relative to the rhombohedral peak intensities, most clearly seen in the {110} images in Figure 4.10.

Figure 4.9b and Figure 4.10f show the Rietveld model for a mixed phase state for 15% KBT at 550°C. Here a slight change can be observed, with the cubic peak in the {110} graph increasing further relative to the rhombohedral peaks, now becoming nearly level, the central peak of the three now comparable with the higher of the split peaks. In addition, a different impurity phase can be seen to be forming around 25°2θ, another form of Bi_2O_3.

Figure 4.9c and Figure 4.11a show the Rietveld model for a mixed phase state for 15% KBT at 650°C, where it can be seen that the diffraction pattern is

becoming significantly more cubic. This is especially clear in the {110} peak, where the central cubic peak is now more intense than the rhombohedral split peaks, now more like a central peak with rhombohedral shoulders. This is extended further at 750°C, shown in Figure 4.9d and Figure 4.11b, which now resembles the peaks observed at room temperature for higher KBT% samples. While it is likely that higher temperature measurements would result in a cubic diffraction pattern, it was not possible to obtain these due to concerns about damaging the equipment.

As in the room temperature refinements, an impurity phase was identified in the samples and refined with the other phases. In the case of the 15% KBT, it was found to be Bi_2O_3, and was found to increase as the temperature was increased, but remained below 1%. At high temperature, an additional impurity phase, $Bi_5Ti_3FeO_{15}$ was found to form. Like the Bi_2O_3 this was a small fraction of the overall intensity, around 1%. A room temperature measurement was taken after the sample had been cooled, and the Bi_2O_3 was found to have increased relative to the pre-heating low temperature measurements. The $Bi_5Ti_3FeO_{15}$ phase was not found to be present.

Table 4.2: Summary of Rietveld refinement of 15% KBT with respect to temperature. 25°C to 150°C measurements are included; the 25°C (Post) refinement is post heating.

Temperature (°C)	25 (Post)		50		150	
Crystal System	Cubic	Rhombohedral	Cubic	Rhombohedral	Cubic	Rhombohedral
Space Group	$Pm\bar{3}m$	$R3c$	$Pm\bar{3}m$	$R3c$	$Pm\bar{3}m$	$R3c$
Phase Percentage	29(1)	71(1)	26(1)	73(1)	28(1)	71(1)
Lattice Parameters						
a (Å)	3.9616(2)	5.5827(3)	3.9628(2)	5.5845(2)	3.9671(2)	5.5903(2)
c (Å)	3.9616(2)	13.8517(7)	3.9628(2)	13.8552(6)	3.9671(2)	13.8732(6)
α (°)	90	90	90	90	90	90
γ (°)	90	120	90	120	90	120
Pseudocubic Volume (Å^3)	62.174(9)	62.313(6)	62.231(8)	62.368(6)	62.435(8)	62.579(6)
R'_{Exp}	13.064		12.932		12.979	
R'_p	14.873		14.903		14.833	
R'_{wp}	15.482		15.235		15.212	
Durbin-Watson	1.469		1.461		1.427	
GoF	1.185		1.178		1.172	
Impurity Phase %	Bi_2O_3: 0.6(1)		Bi_2O_3: 0.46(8)		Bi_2O_3: 0.5(1)	
R_{Bragg}	0.877	1.464	1.106	1.320	1.071	1.616
Atomic Positions						
A						
$x = y = 0, z =$	0	0.2916(8)	0	0.2909(7)	0	0.2923(7)
Beq (Å^2)	5.2(5)	0.6(1)	5.1(5)	1.0(1)	5.7(5)	1.1(1)
B						
$x = y =$	0.5	0	0.5	0	0.5	0
z	0.5	0.0156(8)	0.5	0.0145(8)	0.5	0.0168(8)
Beq (Å^2)	0.6(5)	0.2(2)	0.4(5)	0.3(2)	0.6(5)	0.8(2)
O						
x	0.5	0.238(2)	0.5	0.235(2)	0.5	0.232(2)
y	0	0.342(2)	0	0.340(2)	0	0.339(2)
z	0.5	0.0833	0.5	0.0833	0.5	0.0833
Beq (Å^2)	10(1)	0.0(5)	10(1)	0.0(4)	9(1)	0.0(4)

Table 4.3: Summary of Rietveld refinement of 15% KBT with respect to temperature. 250°C to 450°C measurements are included.

Temperature (°C)	250		350		450	
Crystal System	Cubic	Rhombohedral	Cubic	Rhombohedral	Cubic	Rhombohedral
Space Group	$Pm\bar{3}m$	$R3c$	$Pm\bar{3}m$	$R3c$	$Pm\bar{3}m$	$R3c$
Phase Percentage	31(2)	69(2)	31(2)	69(2)	32(2)	68(2)
Lattice Parameters						
a (Å)	3.9717(2)	5.5966(2)	3.9767(2)	5.6038(3)	3.9811(2)	5.6109(3)
c (Å)	3.9717(2)	13.8907(7)	3.9767(2)	13.9091(7)	3.9811(2)	13.9221(7)
α (°)	90	90	90	90	90	90
γ (°)	90	120	90	120	90	120
Pseudocubic Volume (Å^3)	62.653(8)	62.799(6)	62.887(9)	63.044(7)	63.099(9)	63.262(7)
R'_{Exp}	13.161		13.365		13.524	
R'_p	15.651		16.036		16.840	
R'_{wp}	15.732		16.026		16.884	
Durbin-Watson	1.516		1.388		1.366	
GoF	1.195		1.199		1.248	
Impurity Phase %	Bi_2O_3: 0.6(1)		Bi_2O_3: 0.54(9)		Bi_2O_3: 0.24(5)	
R_{Bragg}	1.048	1.414	0.939	1.195	1.102	1.537
Atomic Positions						
A						
$x = y = 0, z =$	0	0.2908(8)	0	0.2892(8)	0	0.2893(8)
Beq (Å^2)	5.2(6)	1.3(2)	5.9(7)	1.6(2)	6.2(7)	1.9(2)
B						
$x = y =$	0.5	0	0.5	0	0.5	0
z	0.5	0.0155(9)	0.5	0.0152(9)	0.5	0.0160(9)
Beq (Å^2)	0.9(6)	0.4(2)	1.4(7)	0.6(2)	1.5(7)	0.4(2)
O						
x	0.5	0.231(2)	0.5	0.231(2)	0.5	0.234(2)
y	0	0.337(2)	0	0.337(2)	0	0.341(2)
z	0.5	0.0833	0.5	0.0833	0.5	0.0833
Beq (Å^2)	13(1)	0.4(2)	12(1)	0.0(5)	11(1)	0.4(2)

Table 4.4: Summary of Rietveld refinement of 15% KBT with respect to temperature. 550°C to 750°C measurements are included.

Temperature (°C)	550		650		750	
Crystal System	Cubic	Rhombohedral	Cubic	Rhombohedral	Cubic	Rhombohedral
Space Group	$Pm\bar{3}m$	$R3c$	$Pm\bar{3}m$	$R3c$	$Pm\bar{3}m$	$R3c$
Phase Percentage	34(2)	66(2)	51(1)	48(1)	70.3(8)	28.5(8)
Lattice Parameters						
a (Å)	3.9864(2)	5.6183(2)	3.99098(9)	5.6266(2)	3.99335(4)	5.6336(1)
c (Å)	3.9864(2)	13.9342(7)	3.99098(9)	13.9447(6)	3.99335(4)	13.9438(7)
α (°)	90	90	90	90	90	90
γ (°)	90	120	90	120	90	120
Pseudocubic Volume (Å^3)	63.351(8)	63.486(6)	63.568(4)	63.721(4)	63.681(2)	63.874(4)
R'_{Exp}	13.829		14.224		15.356	
R'_p	17.504		18.811		18.934	
R'_{wp}	17.055		17.407		17.074	
Durbin-Watson	1.373		1.391		1.649	
GoF	1.233		1.224		1.112	
Impurity Phase(s) %	Bi_2O_3: 0.4(1)		$Bi_5Ti_3FeO_{15}$: 1.3(3) Bi_2O_3: 0.25(5)		$Bi_5Ti_3FeO_{15}$: 0.8(2) Bi_2O_3: 0.27(5)	
R_{Bragg}	1.436	1.464	2.108	2.366	1.659	1.852
Atomic Positions						
A						
$x = y = 0, z =$	0	0.2894(8)	0	0.292(1)	0	0.286(1)
Beq (Å^2)	6.3(6)	2.3(2)	6.1(3)	2.7(2)	6.8(1)	3.5(2)
B						
$x = y =$	0.5	0	0.5	0	0.5	0
z	0.5	0.0162(9)	0.5	0.017(1)	0.5	0.014(2)
Beq (Å^2)	1.3(6)	0.8(3)	1.4(3)	0.9(3)	1.1(1)	1.3(4)
O						
x	0.5	0.230(2)	0.5	0.233(3)	0.5	0.247(4)
y	0	0.336(2)	0	0.332(3)	0	0.354(5)
z	0.5	0.0833	0.5	0.0833	0.5	0.0833
Beq (Å^2)	10(1)	0.0(5)	6.9(6)	0.0(6)	4.8(3)	0.7(8)

4.4.2 20% KBT High Temperature Rietveld Refinements

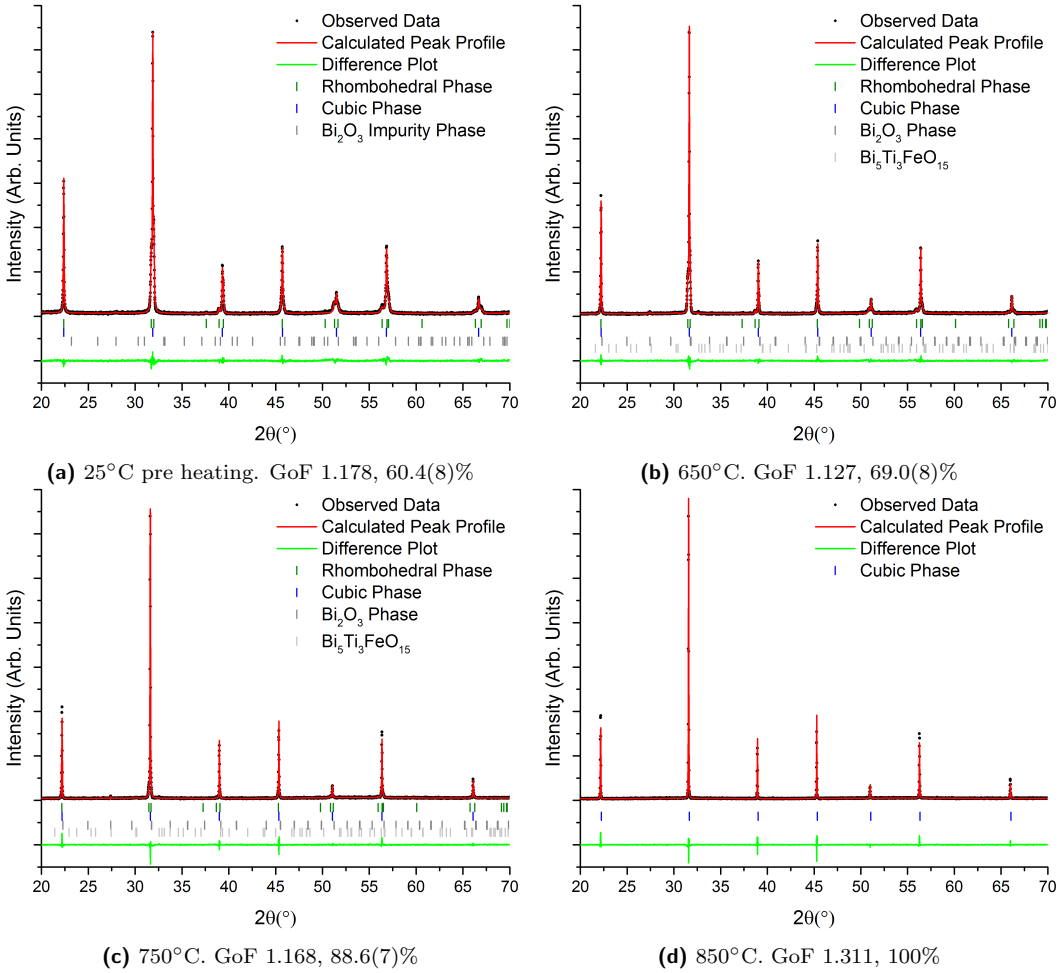

(a) 25°C pre heating. GoF 1.178, 60.4(8)%

(b) 650°C. GoF 1.127, 69.0(8)%

(c) 750°C. GoF 1.168, 88.6(7)%

(d) 850°C. GoF 1.311, 100%

Figure 4.12: Plots of the 20% KBT powder with respect to temperature. The goodness of fit is included, and the listed percentage is the cubic phase percentage.

Figure 4.12 shows the Rietveld model for a mixed phase state for 20% KBT. The difference plots again show good agreement between the observed data and the models applied. Though the cubic only model in Figure 4.12d shows deeper troughs than the other models, this was not found to be improved with a mixed model for the data. As in the 15% KBT powder, the {110} peaks are also available for separate viewing, seen in Figure 4.13.

Figure 4.12a shows the Rietveld model for a mixed phase state for 20% KBT at 25°C. Looking at the {110} peak specifically in Figure 4.13a, it can be seen that the peak shape here is more comparable with the high temperature 15% KBT sample than the room temperature 15% KBT sample, with Figure 4.13a showing

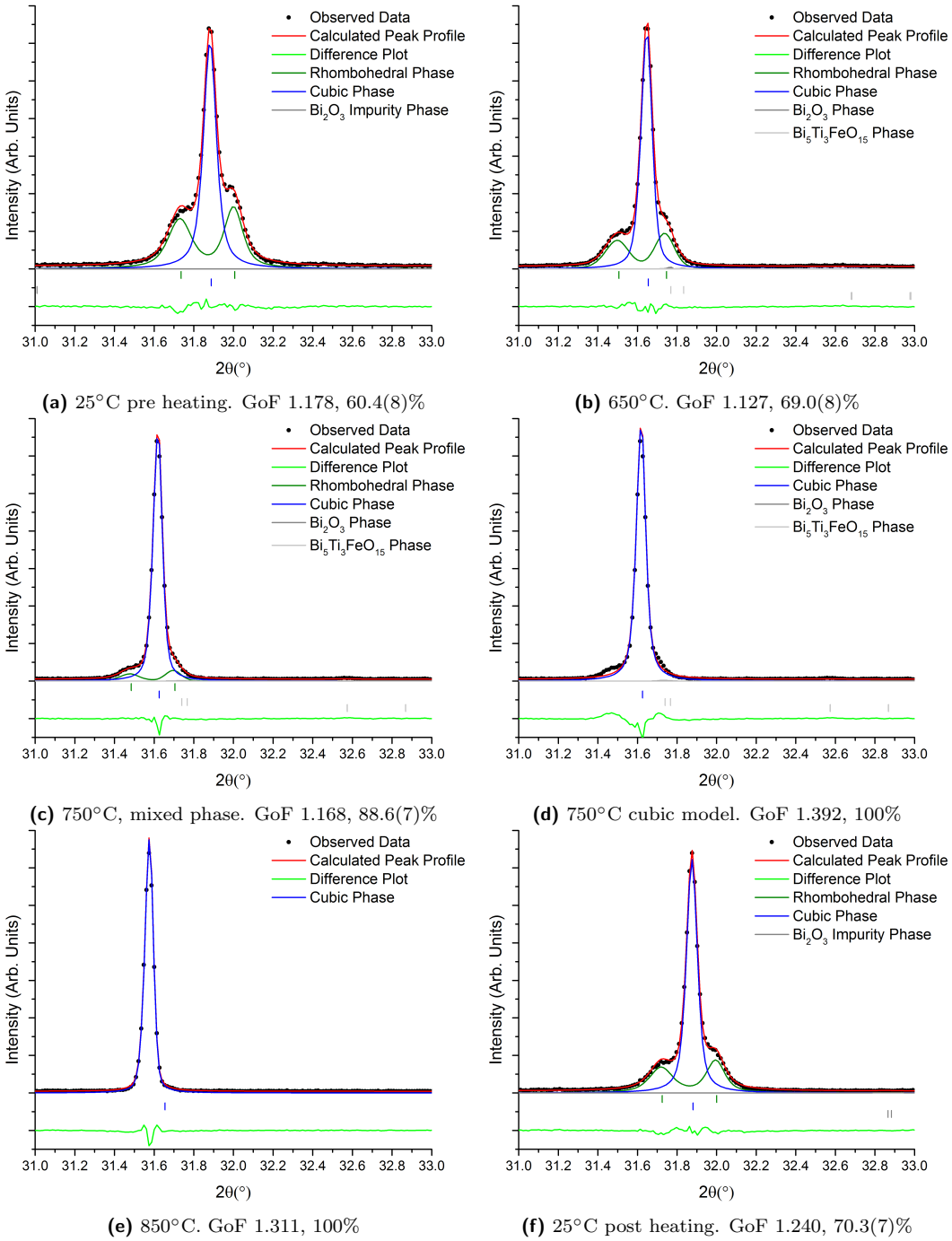

(a) 25°C pre heating. GoF 1.178, 60.4(8)%

(b) 650°C. GoF 1.127, 69.0(8)%

(c) 750°C, mixed phase. GoF 1.168, 88.6(7)%

(d) 750°C cubic model. GoF 1.392, 100%

(e) 850°C. GoF 1.311, 100%

(f) 25°C post heating. GoF 1.240, 70.3(7)%

Figure 4.13: 20% KBT {110} graphs with changing temperature, showing the mixed cubic and rhombohedral model compared to the observed data. The goodness of fit is included. The listed percentages are the cubic phase fraction.

the central cubic peak as being more intense than the outer rhombohedral peaks, which act as shoulders around the peak.

Figure 4.12b and Figure 4.13b show the Rietveld model for 20% KBT at 650°C. This can be seen to be largely the same as the measurement at room temperature, aside from a slight change in the impurity phase with peaks at around 27.5° 2θ and 32.5° 2θ, and for an increase in the cubic intensity relative to the rhombohedral intensity. Measurements taken at 225°C 425°C, 500°C and 600°C also showed this trend, so only the highest temperature model for this has been included.

Figure 4.12c, Figure 4.13c and Figure 4.13d show the Rietveld model for 20% KBT at 750°C. At this temperature, the contribution from the rhombohedral phase is only slight, but as can be seen in the difference between Figure 4.13c and Figure 4.13d, it is still an important component of the model and as such it can not be said that 20% KBT is cubic at 750°C. By comparison, at 850°C, shown in Figure 4.12d and Figure 4.13e, when refined with both cubic and rhombohedral phases, there was not sufficient data to resolve the rhombohedral phase, so it is modelled as being cubic.

After the sample was cooled, a second room temperature measurement was taken. Comparing the pre heating Figure 4.13a with the post heating Figure 4.13f, it can be seen that after heating, the central cubic peak is sharper, with smaller rhombohedral shoulders; thus the system has become more cubic by heating. This will be discussed further in Section 4.6.

As in the 15% KBT powder, a Bi_2O_3 impurity phase was found and refined, remaining under 1% throughout the refinement. Again, a $Bi_5Ti_3FeO_{15}$ phase was found around 650°C, which was not present in the subsequent room temperature measurement.

4.4.3 40% KBT High Temperature Rietveld Refinements

While the 20% KBT refinements provide a good model for all of the cubically dominated cubic-rhombohedral mixed model refinements, the importance of the 40% KBT sample with respect to temperature with the reported MPBs around this region [6] make it a useful and informative dataset to include with the other refinements. As such, Figure 4.14 provides an overview of the 40% KBT refinements at high temperature.

Figure 4.14 shows the Rietveld model for a mixed phase state for 40% KBT between 25°C and 850°C in the range between 20° 2θ and 70° 2θ, showing the observed data, the calculated model and a difference plot between the observed and

Table 4.5: Summary of Rietveld refinement of 20% KBT at room temperature, pre and post heating.

Temperature (°C)	25 (Pre)		25 (Post)	
Crystal System	Cubic	Rhombohedral	Cubic	Rhombohedral
Space Group	$Pm\bar{3}m$	$R3c$	$Pm\bar{3}m$	$R3c$
Phase Percentage	60.4(8)	39.1(8)	70.3(7)	29.4(7)
Lattice Parameters				
a (Å)	3.96268(9)	5.5838(2)	3.96281(6)	5.5839(2)
c (Å)	3.96268(9)	13.8490(8)	3.96281(6)	13.8519(8)
α (°)	90	90	90	90
γ (°)	90	120	90	120
Pseudocubic Volume (Å^3)	62.225(4)	62.324(5)	62.231(3)	62.339(5)
R'_{Exp}	14.830		14.979	
R'_p	17.064		17.934	
R'_{wp}	17.477		18.581	
Durbin-Watson	1.465		1.341	
GoF	1.178		1.240	
Impurity Phase %	Bi_2O_3: 0.53(8)		Bi_2O_3: 0.24(7)	
R_{Bragg}	1.426	3.014	1.632	3.982
Atomic Positions				
A				
$x = y = 0, z =$	0	0.296(1)	0	0.296(2)
Beq (Å^2)	4.3(2)	0.0(1)	3.7(1)	0.0(2)
B				
$x = y =$	0.5	0	0.5	0
z	0.5	0.017(1)	0.5	0.016(2)
Beq (Å^2)	0.6(2)	0.0(3)	0.7(1)	0.0(4)
O				
x	0.5	0.238(4)	0.5	0.260(5)
y	0	0.346(4)	0	0.361(5)
z	0.5	0.0833	0.5	0.0833
Beq (Å^2)	7.3(5)	0.0(7)	7.0(4)	0.0(9)

Table 4.6: Summary of Rietveld refinement of 20% KBT with respect to temperature. 650°C to 850°C measurements are included.

Temperature (°C)	650		750		850
Crystal System	Cubic	Rhombohedral	Cubic	Rhombohedral	Cubic
Space Group	$Pm\bar{3}m$	$R3c$	$Pm\bar{3}m$	$R3c$	$Pm\bar{3}m$
Phase Percentage	69.0(8)	28.8(8)	88.6(7)	10.2(7)	100
Lattice Parameters					
a (Å)	3.99016(5)	5.6271(2)	3.99349(4)	5.6340(3)	3.99852(3)
c (Å)	3.99016(5)	13.9377(8)	3.99349(4)	13.942(1)	3.99852(3)
α (°)	90	90	90	90	90
γ (°)	90	120	90	120	90
Pseudocubic Volume (Å^3)	63.529(2)	63.700(5)	63.688(2)	63.876(9)	63.929(2)
R'_{Exp}	16.210		17.407		17.911
R'_p	19.690		24.254		29.088
R'_{wp}	18.270		20.323		23.477
Durbin-Watson	1.632		1.521		1.427
GoF	1.127		1.168		1.311
Impurity Phase %	$Bi_5Ti_3FeO_{15}$: 1.8(4) Bi_2O_3: 0.39(5)		$Bi_5Ti_3FeO_{15}$: 0.8(2) Bi_2O_3: 0.33(6)		-
R_{Bragg}	1.589	1.555	3.040	1.907	4.299
Atomic Positions					
A					
$x = y = 0, z =$	0	0.289(2)	0	0.288(4)	0
Beq (Å^2)	5.8(1)	2.5(2)	5.8(1)	3.2(6)	6.42(7)
B					
$x = y =$	0.5	0	0.5	0	0.5
z	0.5	0.015(2)	0.5	0.011(5)	0.5
Beq (Å^2)	1.0(1)	0.7(4)	1.0(1)	4(1)	1.16(9)
O					
x	0.5	0.245(5)	0.5	0.26(1)	0.5
y	0	0.360(5)	0	0.39(1)	0
z	0.5	0.0833	0.5	0.0833	0.5
Beq (Å^2)	5.1(3)	0.0(9)	5.1(3)	0(2)	6.2(3)

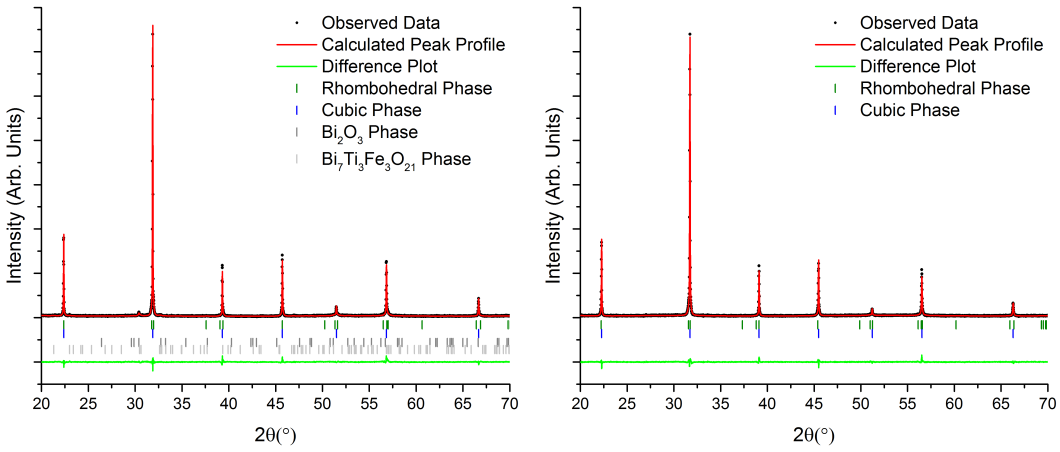

(a) 25°C post heating. GoF 1.226, 85.1(8)%

(b) 550°C. GoF 1.136, 91.5(9)%

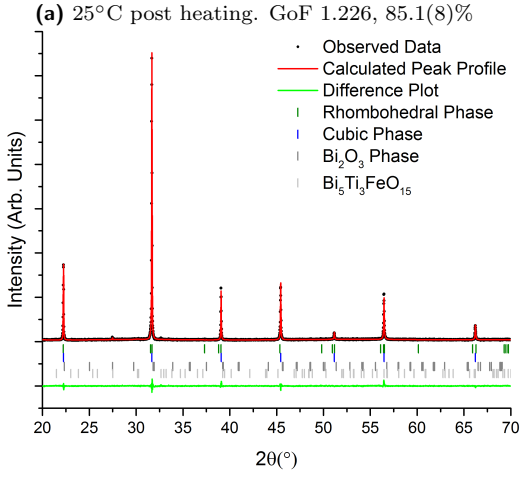

(c) 650°C mixed model. GoF 1.113, 94(1)%

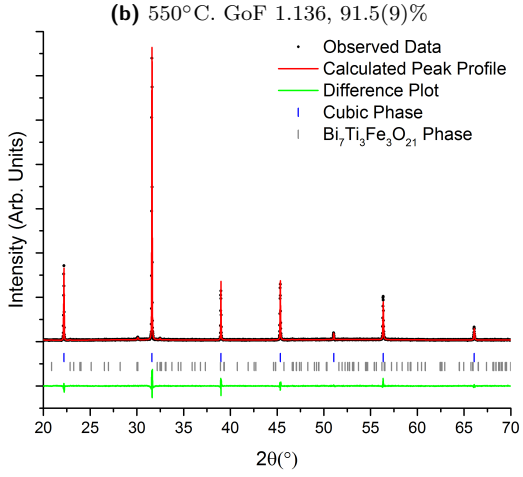

(d) 800°C cubic model. GoF 1.293, 100%

Figure 4.14: Plots of the 40% KBT powder with respect to temperature.

calculated values.

At 800°C, in Figure 4.14d, the peaks are sharper than even the cubic model was able to accurately model, so it can be seen that there is some minor disagreement with the model in the difference peaks. The post heating measurement, Figure 4.14a also showed higher disagreement between the calculated model and the observed data than in the measurements taken while heating, which may be partly a result of the changes at high temperature discussed in Section 4.6.

The 40% sample was also the only sample synthesised without any impurity phase detectably present at room temperature prior to heating. There is still no impurity phase present at 550°C in Figure 4.14b, but an impurity phase can be seen to be present in the 650°C measurements in Figure 4.14c, found to be Bi_2O_3 and $Bi_5Ti_3FeO_{15}$. A different impurity phase is also seen in the 800°C measurement in Figure 4.14d, $Bi_7Ti_3Fe_3O_{21}$ which was found to fit the impurity phase better than the more commonly used (in this thesis) Bi_2O_3 and $Bi_5Ti_3FeO_{15}$ phases. As can be seen from Figure 4.14a, there are impurity phases present in the material once cooled after heating; both Bi_2O_3 as in the other samples and also the $Bi_7Ti_3Fe_3O_{21}$ phase found at high temperatures.

Table 4.7: Summary of Rietveld refinement of 40% KBT with respect to temperature. 25°C to 850°C measurements are included; the 25°C refinement is post heating. It should be noted that the oxygen atom positions in the 650°C rhombohedral refinement are not defined, due to the very small rombohedral phase percentage and the difficulty of refining oxygen atoms from x-ray diffraction measurements.

Temperature (°C)	25 (Post)		550		650		850
Crystal System	Cubic	Rhombohedral	Cubic	Rhombohedral	Cubic	Rhombohedral	Cubic
Space Group	$Pm\bar{3}m$	$R3c$	$Pm\bar{3}m$	$R3c$	$Pm\bar{3}m$	$R3c$	$Pm\bar{3}m$
Phase Percentage	85.1(8)	11.4(8)	91.5(9)	8.5(9)	94(1)	5(1)	97.9(2)
Lattice Parameters							
a (Å)	3.96299(4)	5.5886(6)	3.98320(4)	5.628(1)	3.98688(4)	5.6340(8)	3.99376(4)
c (Å)	3.96299(4)	13.817(5)	3.98320(4)	13.901(6)	3.98688(4)	13.904(4)	3.99376(4)
α (°)	90	90	90	90	90	90	90
γ (°)	90	120	90	120	90	120	90
Pseudocubic Volume (Å^3)	62.240(2)	62.29(2)	63.197(2)	63.55(4)	63.372(2)	63.70(3)	63.701(2)
R'_{Exp}	17.243		17.591		18.075		18.523
R'_p	22.064		22.501		23.120		28.843
R'_{wp}	21.143		19.989		20.127		23.953
Durbin-Watson	1.348		1.611		1.627		1.390
GoF	1.226		1.136		1.113		1.293
Impurity Phase(s) %	$Bi_7Ti_3Fe_3O_{21}$: 2.7(2) Bi_2O_3: 0.74(9)		-		$Bi_5Ti_3FeO_{15}$: 1.4(3) Bi_2O_3: 0.28(6)		$Bi_7Ti_3Fe_3O_{21}$: 2.12
R_{Bragg}	2.704	3.554	2.266	1.222	2.340	0.877	3.705
Atomic Positions							
A							
$x = y = 0, z =$	0	0.295(6)	0	0.29(2)	0	0.31(9)	0
Beq (Å^2)	5.80(9)	0.0(4)	7.3(1)	1.3(8)	7.3(1)	3(3)	7.41(9)
B							
$x = y =$	0.5	0	0.5	0	0.5	0	0.5
z	0.5	0.004(6)	0.5	0.00(1)	0.5	0.00(7)	0.5
Beq (Å^2)	0.0(1)	0(1)	0.7(1)	0(3)	0.7(1)	0(9)	0.7(1)
O							
x	0.5	0.21(2)	0.5	0.17(6)	0.5	0(51)	0.5
y	0	0.27(1)	0	0.18(5)	0	0(96)	0
z	0.5	0.0833	0.5	0.0833	0.5	0.0833	0.5
Beq (Å^2)	1.4(2)	0(3)	2.2(2)	9(14)	1.8(2)	10(62)	2.8(2)

4.4.3.0.1 Summary of 15-40% KBT

As in Chapter 3, the best solution for the structure of the 15-40% KBT mixed powder was found to be a mixed phase of $R3c$ and $Pm\bar{3}m$ at room temperature. As the temperature was increased, the proportions of these phases was altered, with the rhombohedral phase diminishing with increasing temperature, and the pseudocubic phase increasing. The pseudocubic $Pm\bar{3}m$ is modelling the local disorder in the system, and so should properly be called pseudocubic rather than cubic, though at high temperatures it is possible that the phase actually is cubic in nature.

It should be noted that while the 50% KBT and 60% KBT would be expected to fit in with these refinements from the room temperature measurements, it was found that with respect to temperature they were a cross between this low mol% KBT compositional region and the higher mol% KBT compositional region. An example of this crossing can be seen in Section 4.4.4.2.

4.4.4 70% KBT High Temperature Rietveld Refinements

Figure 4.15 shows the Rietveld model 70% KBT between 25°C and 800°C. The difference plots again show good agreement between the observed data and the models applied. The {110} peaks are also available for separate viewing, seen in Figure 4.16.

Figure 4.15a shows the Rietveld model for 70% KBT at 25°C prior to heating. As with the other room temperature measurements, an initial model utilising the earlier room temperature models was used as a starting point for these refinements, so a good agreement between the model and the observed data was expected. Like the prior room temperature refinement, it was found that two peaks were needed to fit the data, a cubic peak and a monoclinic peak; a cubic and tetragonal and two cubic peaks were also tried, but it was found that the cubic and monoclinic peaks fitted the data best, and made most sense with respect to later measurements. The {110} peak in Figure 4.16a reinforces the quality of this fit.

Figure 4.15b and Figure 4.16b show the peak profile at 500°C. It can be seen that the nature of the two peaks has changed slightly; the cubic peak has become more intense, while the monoclinic peak has become wider, This makes it clearer that there are two separate peaks present in the peak profile. The peaks in this graph can also be fited with two cubic peaks instead, which makes discerning the point at which the cubic and monoclinic model gives way to a two-cubic model extremely difficult, resulting in a large uncertainty for the point at which the high temperature model is used. The difference plot is consistently good at this point.

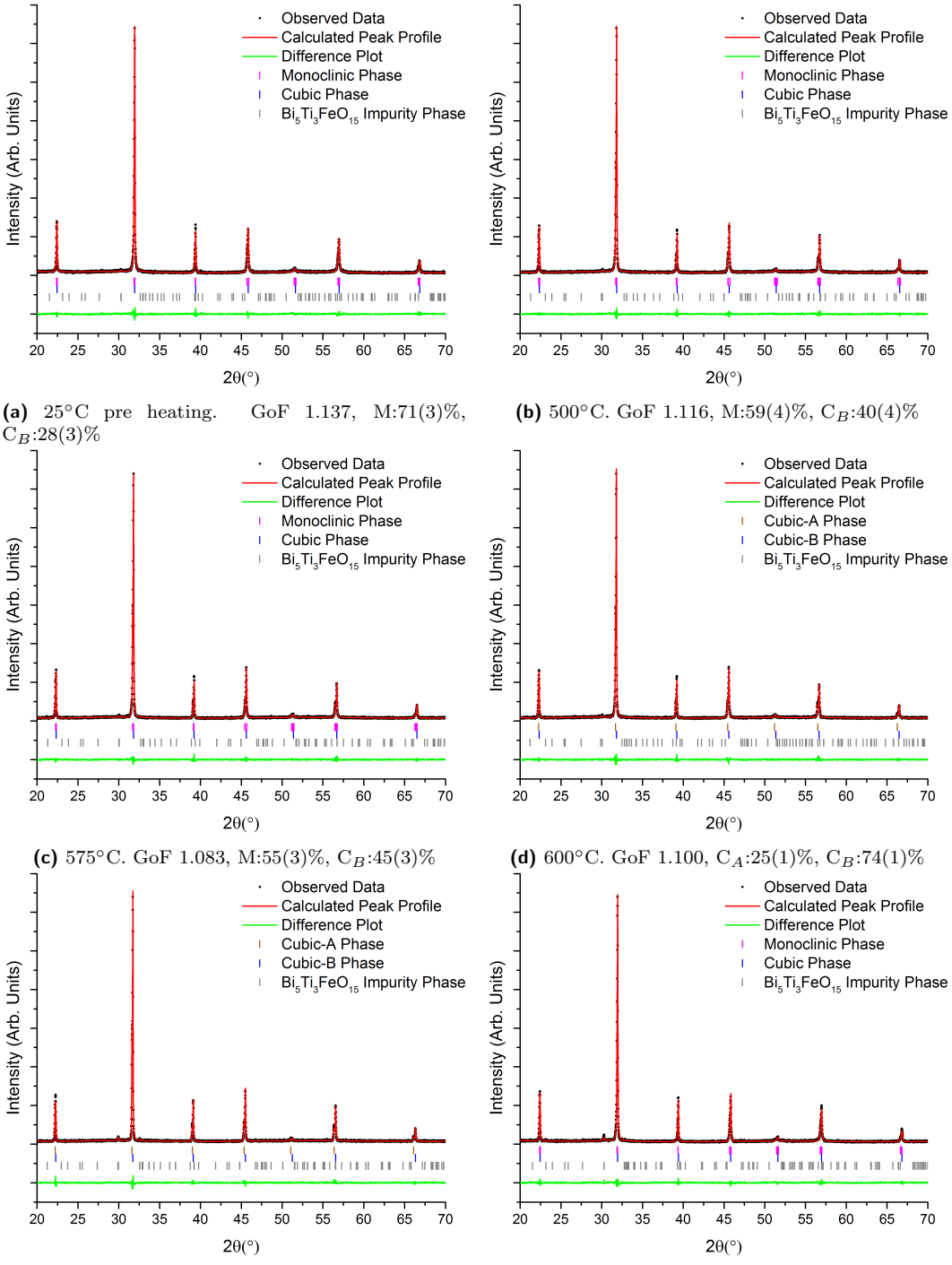

(a) 25°C pre heating. GoF 1.137, M:71(3)%, C_B:28(3)%

(b) 500°C. GoF 1.116, M:59(4)%, C_B:40(4)%

(c) 575°C. GoF 1.083, M:55(3)%, C_B:45(3)%

(d) 600°C. GoF 1.100, C_A:25(1)%, C_B:74(1)%

(e) 800°C. GoF 1.107, C_A:22(1)%, C_B:77(1)%

(f) 25°C post heating. GoF 1.149, M:77(3)%, C_B:21(3)%

Figure 4.15: Plots of the 70% KBT powder with respect to temperature. M: Monoclinic percentage, C_A: Cubic-A percentage, C_B: Cubic-B percentage.

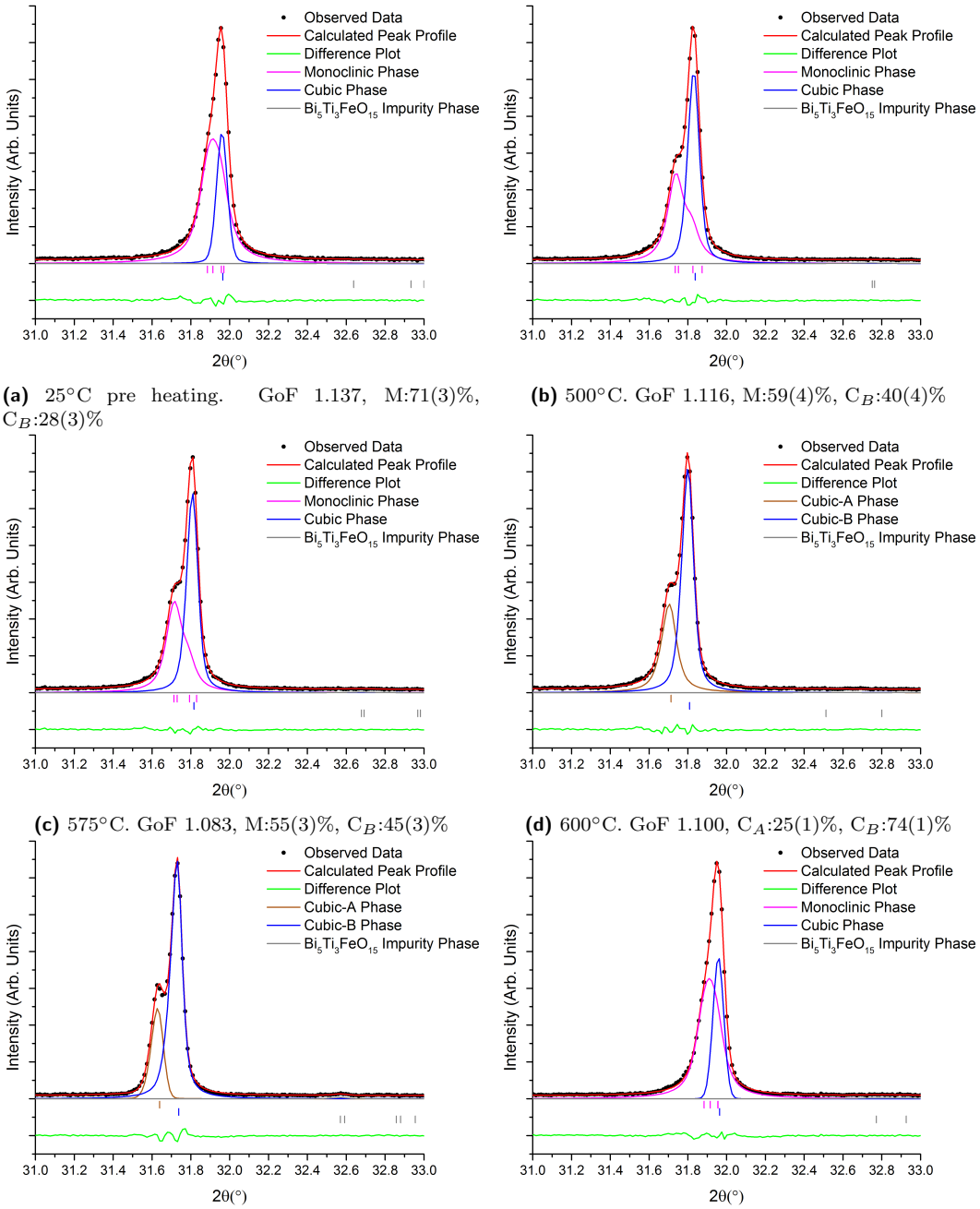

(a) 25°C pre heating. GoF 1.137, M:71(3)%, C_B:28(3)%

(b) 500°C. GoF 1.116, M:59(4)%, C_B:40(4)%

(c) 575°C. GoF 1.083, M:55(3)%, C_B:45(3)%

(d) 600°C. GoF 1.100, C_A:25(1)%, C_B:74(1)%

(e) 800°C. GoF 1.107, C_A:22(1)%, C_B:77(1)%

(f) 25°C post heating. GoF 1.149, M:77(3)%, C_B:21(3)%

Figure 4.16: Plots of the {110} peaks for a 70% KBT powder with respect to temperature. M: Monoclinic percentage, , C_A: Cubic-A percentage, C_B: Cubic-B percentage.

In Figure 4.15c at 575°C, the monoclinic peak has become sharper and more cubic than it was at 500°C. This is clearer in Figure 4.16c. Again, these could be replaced by two cubic phases. In Figure 4.15d at 600°C, the model is replaced with a two-cubic mixed phase, with the individual phases termed 'Cubic-A' and 'Cubic-B', resulting in a commensurate difference plot between the 575°C refinement and the 600°C refinement. Comparing Figure 4.16c with Figure 4.16d for a closer look at the {110} peak, it's clearer still that these two models can be used interchangeably at this temperature.

At higher temperatures, it becomes clearer that the 'two-cubic mixed phase' model of Cubic-A and Cubic-B is the best fit to the data, with Figure 4.15e showing excellent agreement between the model and the observed data at 800°C and Figure 4.16e showing the {110} peak specifically. The sharp, narrow and clearly split peak in the observed data is here fit better with two cubic phases than it was with a cubic and monoclinic model.

The post heating room temperature peak profile is especially important in this composition, since it was possible that the phase separation found at high temperature could be irreversible. However, as Figure 4.15f shows, a very similar peak profile is recovered on cooling the system; as in all other samples, there is additional impurity phase, but the main peaks themselves have recovered their prior room temperature forms, with the {110} peak in Figure 4.16 only showing a small deviation from a cubic peak, just as Figure 4.16a does. This means that the phase separation seen at high temperature is a reversible process.

The impurity phase was also refined. The impurity phase was determined to be $Bi_5Ti_3FeO_{15}$. The impurity phase percentage increased from 0.58(7)% pre heating to 1.4(2)% after heating.

4.4.4.1 Cubic-A and Cubic-B Two-Cubic Mixed Phase Model

Two cubic peaks are necessary for the refinement of high temperature diffraction patterns of the compositional range from 50 mol% KBT to 90 mol% KBT. They were found to appear with increasing temperature, and are a result of phase separation between BFO-rich regions and KBT-rich regions, which is discussed in more detail in Section 4.4.6.4. Since in all cases where they were found to exist, the left and right cubic peaks exhibited similar properties irrespective of composition, it was decided that it was useful to be able to discuss the peaks as a group, so they were termed 'Cubic-A' and 'Cubic-B'. In other words, the 50% KBT Cubic-A peak is similar to the 90% KBT Cubic-A peak. This model with two cubic phases is referred to as the 'two-cubic' mixed phase model.

Table 4.8: Summary of Rietveld refinement of 70% KBT both pre heating and post heating.

Temperature (°C)	25 (Pre)		25 (Post)	
Crystal System	Cubic	Monoclinic	Cubic	Monoclinic
Space Group	$Pm\bar{3}m$	$P1m1$	$Pm\bar{3}m$	$P1m1$
Phase Percentage	28(3)	71(3)	21(3)	77(3)
Lattice Parameters				
a (Å)	3.9540(2)	3.9654(6)	3.9547(2)	3.9667(8)
b (Å)	3.9540(2)	3.9617(3)	3.9547(2)	3.9620(3)
c (Å)	3.9540(2)	3.9481(4)	3.9547(2)	3.9494(6)
α (°)	90	90	90	90
β (°)	90	89.90(2)	90	89.93(2)
γ (°)	90	90	90	90
Volume (Å^3)	61.819(8)	62.02(1)	61.848(9)	62.07(2)
R'_{Exp}	18.349		18.258	
R'_p	22.462		22.220	
R'_{wp}	20.855		20.981	
Durbin-Watson	1.540		1.572	
GoF	1.137		1.149	
Impurity Phase %	$Bi_5Ti_3FeO_{15}$: 0.58(7)		$Bi_5Ti_3FeO_{15}$: 1.4(1)	
R_{Bragg}	0.990	0.681	1.186	0.575
Atomic Positions				
A $x = y = 0, z = 0$				
ADP (Å^2)	Beq = 9.4(8)		Beq = 6.0(9)	
U_{11}		0.37(5)		0.43(7)
U_{22}		0.039(9)		0.05(1)
U_{33}		0.24(2)		0.37(4)
$U_{12} = U_{23} = 0$, U_{13} =		-0.26(3)		-0.34(4)
B				
x	0.5	0.594(4)	0.5	0.597(4)
y	0.5	0.5	0.5	0.5
z	0.5	0.449(4)	0.5	0.448(4)
ADP (Å^2)	Beq = 6.3(7)		Beq = 1.1(5)	
U_{11}		0.19(6)		0.12(6)
U_{22}		0.01(2)		0.00(2)
U_{33}		0.00(1)		0.03(2)
$U_{12} = U_{23} = 0$, U_{13} =		-0.16(3)		-0.14(4)
O1				
x	0.5	0.56(2)	0.5	0.56(3)
y	0	0.5	0	0.5
z	0.5	-0.062(6)	0.5	-0.062(9)
Beq (Å^2)	0.1(9)	0(1)	0.0(7)	3(2)
O2				
x	-	0.64(2)	-	0.60(2)
y	-	0	-	0
z	-	0.47(3)	-	0.48(3)
Beq (Å^2)	-	5(4)	-	3(3)
O3				
x	-	0.103(5)	-	0.110(5)
y	-	0.5	-	0.5
z	-	0.52(3)	-	0.51(3)
Beq (Å^2)	-	15(8)	-	9(5)

Table 4.9: Summary of Rietveld refinement of 70% KBT with respect to temperature. 500°C and 575°C measurements.

Temperature (°C)	500		575	
Crystal System	Cubic	Monoclinic	Cubic	Monoclinic
Space Group	$Pm\bar{3}m$	$P1m1$	$Pm\bar{3}m$	$P1m1$
Phase Percentage	40(4)	59(4)	45(3)	55(3)
Lattice Parameters				
a (Å)	3.96914(9)	3.9833(7)	3.97199(8)	3.9863(5)
b (Å)	3.96914(9)	3.9799(2)	3.97199(8)	3.9829(2)
c (Å)	3.96914(9)	3.9613(8)	3.97199(8)	3.9667(8)
α (°)	90	90	90	90
β (°)	90	89.79(2)	90	89.82(2)
γ (°)	90	90	90	90
Volume (Å^3)	62.530(4)	62.80(2)	62.665(4)	62.98(2)
R'_{Exp}	18.224		18.165	
R'_p	22.781		22.345	
R'_{wp}	20.344		19.669	
Durbin-Watson	1.767		1.727	
GoF	1.116		1.083	
Impurity Phase %	$Bi_5Ti_3FeO_{15}$: 0.54(9)		$Bi_5Ti_3FeO_{15}$: 0.46(7)	
R_{Bragg}	0.492	0.508	0.722	0.465
Atomic Positions				
A $x = y = 0, z = 0$				
ADP (Å^2)	Beq = 7.3(4)		Beq = 7.3(3)	
U_{11}		0.55(9)		0.41(8)
U_{22}		0.06(1)		0.07(1)
U_{33}		0.47(5)		0.48(6)
$U_{12} = U_{23} = 0$, U_{13} =		-0.46(6)		-0.38(6)
B				
x	0.5	0.590(5)	0.5	0.580(5)
y	0.5	0.5	0.5	0.5
z	0.5	0.440(6)	0.5	0.446(5)
ADP (Å^2)	Beq = 2.5(3)		Beq = 1.9(3)	
U_{11}		0.20(9)		0.11(5)
U_{22}		0.00(2)		0.00(2)
U_{33}		0.13(3)		0.13(3)
$U_{12} = U_{23} = 0$, U_{13} =		-0.23(5)		-0.17(4)
O1				
x	0.5	0.55(3)	0.5	0.58(3)
y	0	0.5	0	0.5
z	0.5	-0.05(1)	0.5	-0.05(1)
Beq (Å^2)	2.0(6)	1(2)	2.5(5)	0(2)
O2				
x	-	0.66(3)	-	0.63(3)
y	-	0	-	0
z	-	0.47(2)	-	0.45(2)
Beq (Å^2)	-	6(5)	-	4(5)
O3				
x	-	0.101(6)	-	0.086(7)
y	-	0.5	-	0.5
z	-	0.53(4)	-	0.47(2)
Beq (Å^2)	-	19(11)	-	20(9)

Table 4.10: Summary of Rietveld refinement of 70% KBT with respect to temperature for the 600 °C and 800°C measurements, both of which have been refined with a two-cubic mixed phase model.

Temperature (°C)	600		800	
Crystal System	Cubic-A	Cubic-B	Cubic-A	Cubic-B
Space Group	$Pm\bar{3}m$	$Pm\bar{3}m$	$Pm\bar{3}m$	$Pm\bar{3}m$
Phase Percentage	25(1)	74(1)	22(1)	77(1)
Lattice Parameters				
a (Å)	3.9850(1)	3.97332(9)	3.99361(9)	3.98152(7)
α (°)	90	90	90	90
Volume (Å^3)	63.282(5)	62.728(4)	63.694(4)	63.117(3)
R'_{Exp}	18.047		18.038	
R'_p	22.777		23.494	
R'_{wp}	19.847		19.968	
Durbin-Watson	1.751		1.752	
GoF	1.100		1.107	
Impurity Phase %	$Bi_5Ti_3FeO_{15}$: 0.8(1)		$Bi_5Ti_3FeO_{15}$: 0.91(7)	
R_{Bragg}	0.851	0.904	1.847	0.712
Atomic Positions				
A $x = y = z = 0$				
Beq (Å^2)	7.4(3)	7.5(2)	6.9(4)	8.2(1)
B $x = y = z = 0.5$				
Beq (Å^2)	1.3(3)	2.3(2)	2.6(4)	1.8(2)
O $x = z = 0.5, y = 0$				
Beq (Å^2)	4.8(7)	3.3(3)	4.7(6)	3.6(3)

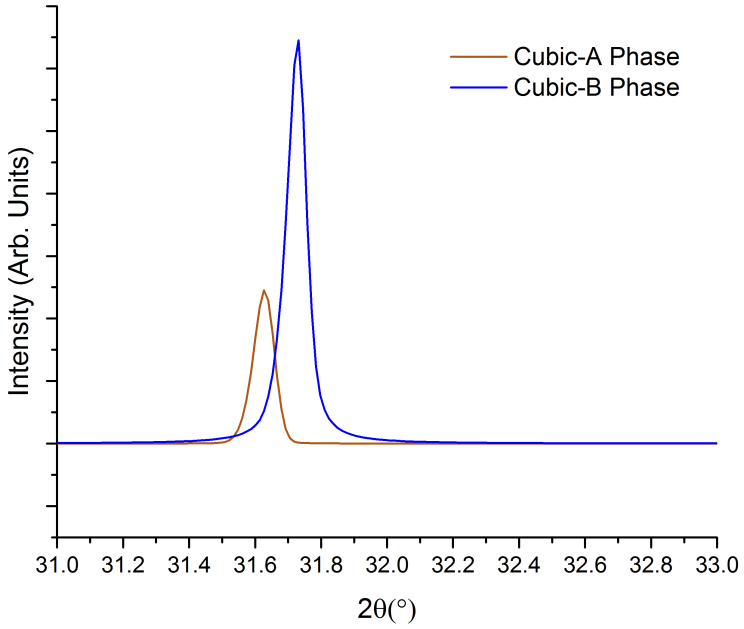

Figure 4.17: Illustrative example of standard Cubic-A and Cubic-B peak relation.

Figure 4.17 shows an example Cubic-A and Cubic-B phase, taken from the {110} peak of the 70 mol% KBT data at 800°C, and is presented as a representative of the Cubic-A and Cubic-B two-cubic mixed phase state of the high KBT compositional powders at high temperature. This can be seen with the observed peak profile in Figure 4.16e.

Cubic-A has larger lattice parameters, closer to those found in the BFO end member, so can also be thought of as the BFO-like cubic peak, while Cubic-B has smaller lattice parameters, closer to the KBT end member, so can be thought of as the KBT-like cubic peak.

It was found that when a cubic phase was present at room temperature this cubic phase would have lattice parameters and show expansion that match well with the high temperature Cubic-B peak. As such, the cubic peaks present at room temperature in the high KBT compositional region can be considered commensurate with Cubic-B peaks.

4.4.4.2 50% and 60% KBT Triple Phase Region

50% KBT and 60% KBT behaved like the lower mol% KBT samples at low temperature, but at high temperature the central cubic peaks in each was found to split into a Cubic-A and Cubic-B phase, as in 70% KBT and 80% KBT. Between the high temperature two-cubic mixed phases and the lower temperature cubic and rhombohedral mixed phases, there was a crossover region in which the central peaks were not a single cubic phase, thus requiring the two-cubic mixed phase model, but there were still rhombohedral shoulders on the peak, meaning that both the two-cubic model and the cubic and rhombohedral mixed phase model were unable to account for their structures. A model replacing the rhombohedral phase with a monoclinic phase was tested, but this was found to produce an unreasonably distorted monoclinic structure. Given that the end states of the structure were known, it was decided to test mixing them together; Cubic-A, Cubic-B and rhombohedral mixed phases. While this allows for more refinement parameters than would be considered ideal, the results shown in Figure 4.18 show that this model was successful in modelling the observed data, and the peak figures, Figure 4.18b, Figure 4.18c and Figure 4.18d, show that the model fits the data in the expected way; with the two cubic phases fitting the central intensity, while the rhombohedral phase intensity surrounds one of the peaks.

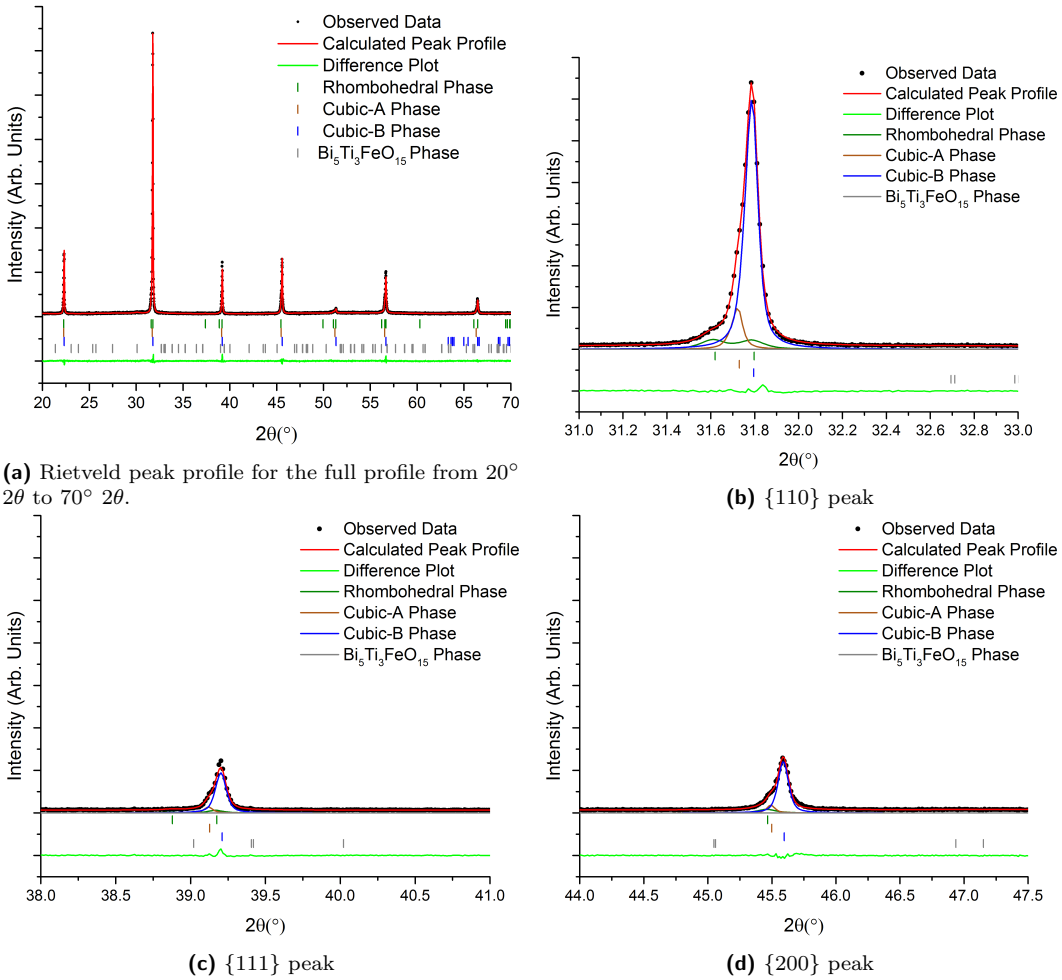

(a) Rietveld peak profile for the full profile from 20° 2θ to 70° 2θ.

(b) {110} peak

(c) {111} peak

(d) {200} peak

Figure 4.18: 60 mol% KBT at 500°C, showing the three mixed phases. Cubic$_A$: 10(1)% $R_{Bragg} = 0.691$; Cubic$_B$: 80(1)% $R_{Bragg} = 1.151$; Rhombohedral: 8.6(9)%, $R_{Bragg} = 0.946$. The {110} (Figure 4.18b), {111} (Figure 4.18c) and {200} (Figure 4.18d) peaks are shown for clarity.

Table 4.11: 60% KBT 500°C Rietveld refinement, showing the two-cubic mixed phase model with the remnant rhombohedral phase.

Crystal System	Cubic-A	Cubic-B	Rhombohedral
Space Group	$Pm\bar{3}m$	$Pm\bar{3}m$	$R3c$
Phase Percentage	10(1)	80(1)	8.6(9)
Lattice Parameters			
a (Å)	3.9822(1)	3.97416(6)	5.620(1)
c (Å)	3.9822(1)	3.97416(6)	13.880(3)
α (°)	90	90	90
γ (°)	90	90	120
Pseudocubic Volume (Å^3)	63.149(6)	62.768(3)	63.27(3)
R'_{Exp}	13.771		
R'_p	18.962		
R'_{wp}	15.997		
Durbin-Watson	1.614		
GoF	1.162		
Impurity Phase %	$Bi_5Ti_3FeO_{15}$: 1.5(2)		
R_{Bragg}	0.691	1.151	0.946
Atomic Positions			
A			
$x = y = 0, z =$	0	0	0.291(4)
Beq (Å^2)	5.2(7)	7.7(1)	3.0(8)
B			
$x = y =$	0.5	0.5	0
z	0.5	0.5	0.018(6)
Beq (Å^2)	0.8(8)	1.6(2)	0(3)
O			
x	0.5	0.5	0.25(1)
y	0	0	0.35(1)
z	0.5	0.5	0.0833
Beq (Å^2)	7(2)	2.5(2)	0(3)

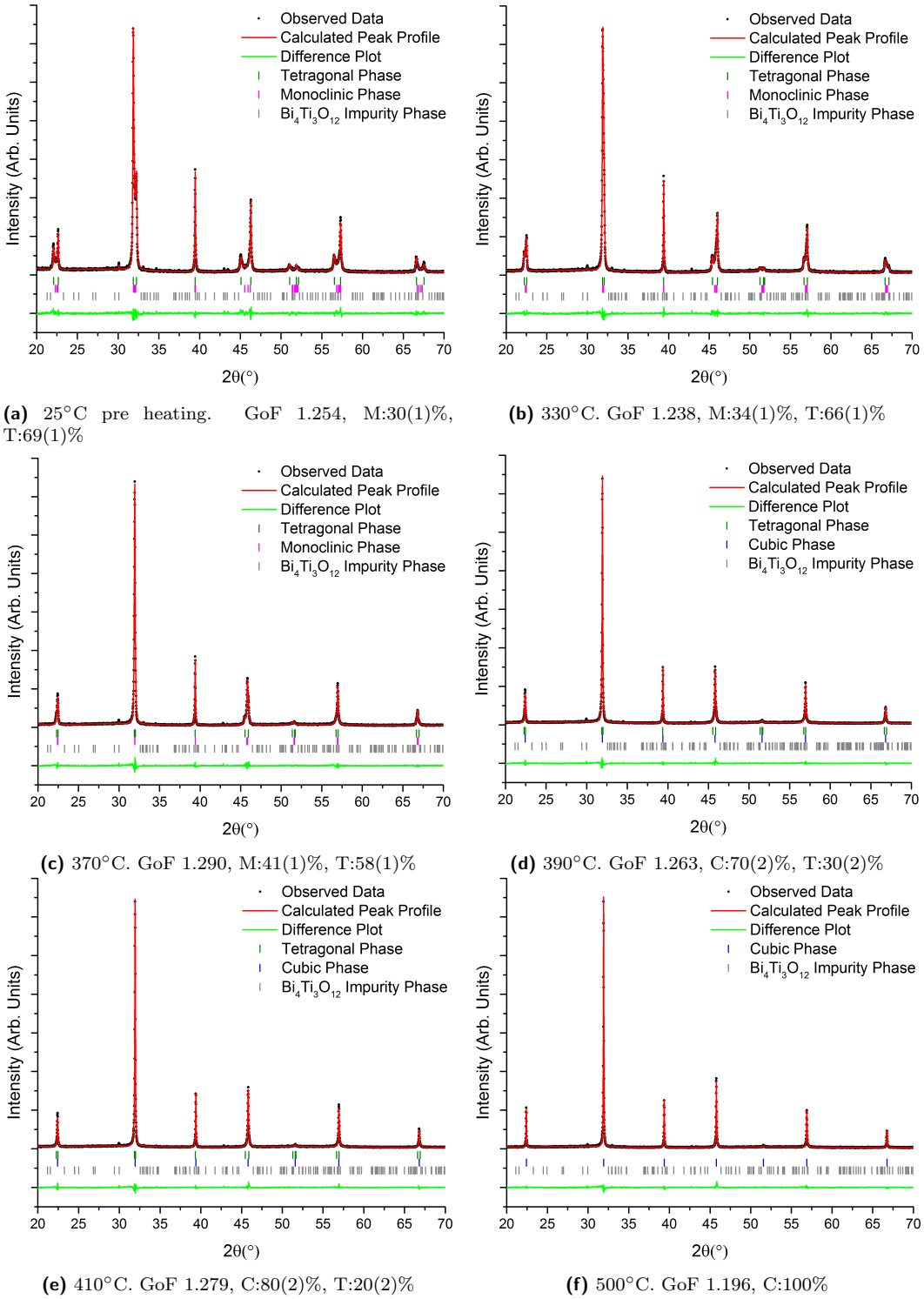

(a) 25°C pre heating. GoF 1.254, M:30(1)%, T:69(1)%

(b) 330°C. GoF 1.238, M:34(1)%, T:66(1)%

(c) 370°C. GoF 1.290, M:41(1)%, T:58(1)%

(d) 390°C. GoF 1.263, C:70(2)%, T:30(2)%

(e) 410°C. GoF 1.279, C:80(2)%, T:20(2)%

(f) 500°C. GoF 1.196, C:100%

Figure 4.19: Plots of the 100% KBT powder with respect to temperature. M: Monoclinic percentage, T: Tetragonal percentage, C: Cubic percentage.

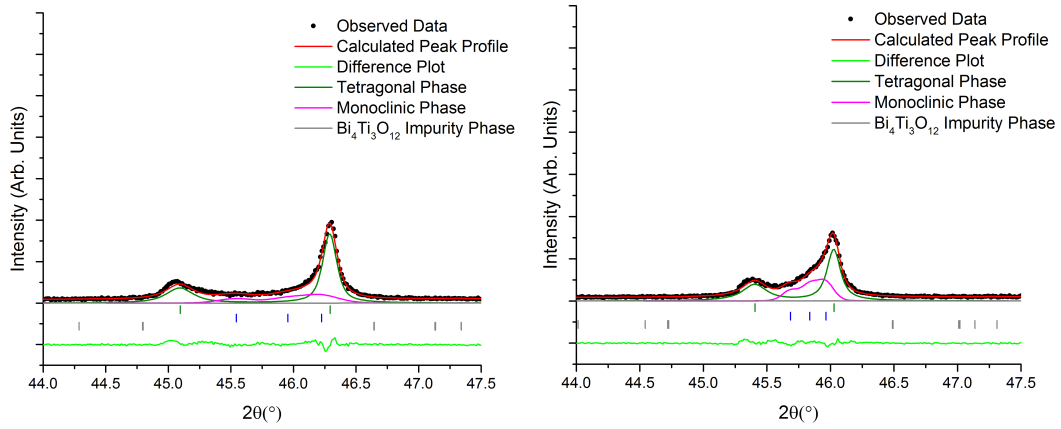

(a) 25°C pre heating. GoF 1.254, M:30(1)%, T:69(1)%

(b) 330°C. GoF 1.238, M:34(1)%, T:66(1)%

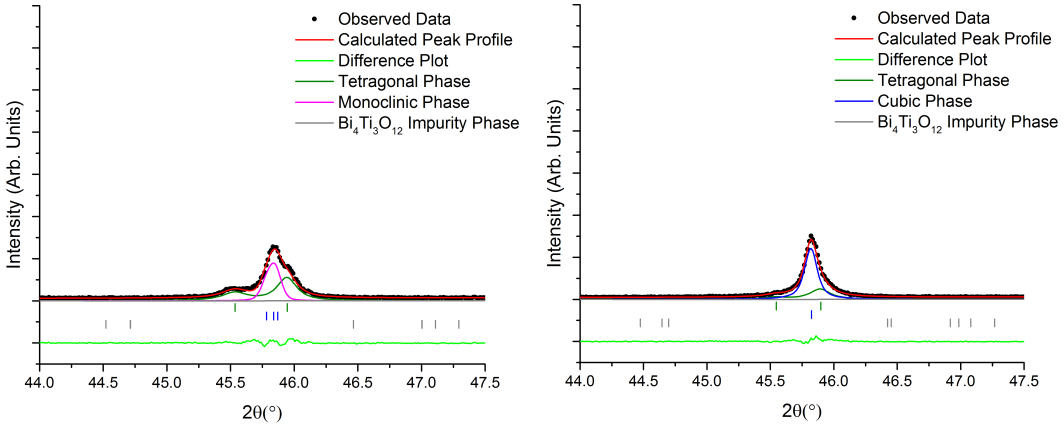

(c) 370°C. GoF 1.290, M:41(1)%, T:58(1)%

(d) 390°C. GoF 1.263, C:70(2)%, T:30(2)%

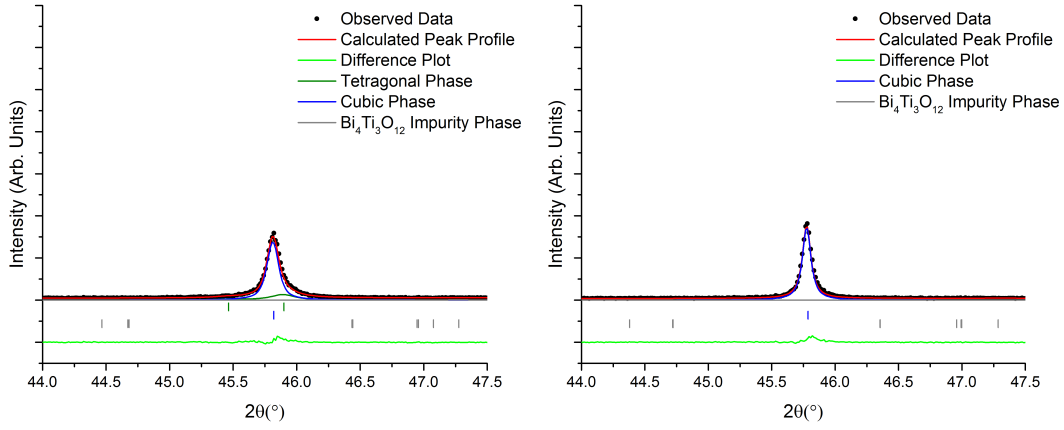

(e) 410°C. GoF 1.279, C:80(2)%, T:20(2)%

(f) 500°C. GoF 1.196, C:100%

Figure 4.20: Plots of the {200} peaks for a 100% KBT powder with respect to temperature. M: Monoclinic percentage, T: Tetragonal percentage, C: Cubic percentage.

4.4.5 100% KBT High Temperature Rietveld Refinements

100% KBT samples have been experimented with with respect to temperature before [2], but with the difference in room temperature model discussed in Section 3.4.1, it was decided that an investigation into the evolution of KBT structure with respect to temperature would be beneficial.

At high temperature, KBT is reported to become cubic. Between the room temperature and high temperature structures, it has been reported that KBT undergoes a mixed phase of cubic and tetragonal. Since the room temperature structure was found to include a monoclinic phase, both mixed tetragonal and cubic as in the literature, and mixed tetragonal and monoclinic were investigated, to find whether there was a point at which the monoclinic contribution could be represented just as well as a cubic phase, before the whole structure was cubic [2].

Figure 4.19f shows the Rietveld model for a mixed phase state for 100% KBT between 25°C and 500°C. The {200} peaks are also available for separate viewing, seen in Figure 4.20.

It can be seen from the figures that in the range from 25°C in Figure 4.19a to 330°in Figure 4.19b that the tetragonal and monoclinic peak splitting decreases. This is clearer in Figure 4.20a and Figure 4.20b, where it can be seen that the monoclinic peak is now sharper and the tetragonality has decreased.

This continues as the temperature is increased to 370°C in Figure 4.19c, where the monoclinic peak is now very close to cubic in nature and is now visible in the full pattern above the tetragonal peaks in Figure 4.20d, which are now acting as shoulders to the central peak in the same way as the rhombohedral peaks do to the cubic peak in the region from 20% KBT to 60% KBT at room temperature.

As the temperature is increased by another 20°C to 390°C, it is possible to see in Figure 4.19d and in Figure 4.20d that the monoclinic phase has been replaced with a cubic phase, but the tetragonal phase still persists, widening the base of the cubic peak. Increasing the temperature further increases the intensity of the cubic peak, while the tetragonal peaks diminish in both intensity and tetragonality, seen in Figure 4.19e and in Figure 4.20e. By 500°C, in Figure 4.19f and in Figure 4.20f the diffraction pattern can be seen to be fully cubic, in agreement with the literature.

The impurity phase in the KBT powders was found to be $Bi_4Ti_3O_{12}$, and it was found to increase slightly in phase percentage with temperature, but was not found to significantly increase between pre heating measurements and post heating experiments.

Table 4.12: Summary of Rietveld refinement of the KBT end member with respect to temperature. 25°C measurement was taken prior to heating.

Temperature (°C)	25 Pre		330	
Crystal System	Tetragonal	Monoclinic	Tetragonal	Monoclinic
Space Group	$P4mm$	$P1m1$	$P4mm$	$P1m1$
Phase Percentage	69(1)	30(1)	66(1)	34(1)
Lattice Parameters				
a (Å)	3.9178(1)	3.9233(5)	3.9383(2)	3.9434(3)
b (Å)	3.9178(1)	3.9787(6)	3.9383(2)	3.9661(4)
c (Å)	4.0162(2)	3.9451(6)	3.9892(2)	3.9537(4)
α (°)	90	90	90	90
β (°)	90	90.12(1)	90	90.02(3)
γ (°)	90	90	90	90
Volume (Å^3)	61.645(5)	61.58(2)	61.872(6)	61.836(9)
R'_{Exp}	12.521		12.569	
R'_p	15.128		15.243	
R'_{wp}	15.701		15.560	
Durbin-Watson	1.292		1.324	
GoF	1.254		1.238	
Impurity Phase %	$Bi_4Ti_3O_{12}$: 0.36(5)		$Bi_4Ti_3O_{12}$: 0.41(6)	
R_{Bragg}	2.195	1.608	1.340	1.066
Atomic Positions				
A				
$x = y = 0, z =$	-0.061(2)	0.12(2)	-0.038(3)	0
ADP (Å^2)				
U_{11}	0.064(3)	0.03(1)	0.122(4)	0.051(8)
U_{22}	0.064(3)	0.104(8)	0.064(3)	0.23(1)
U_{33}	0.050(5)	0.11(2)	0.045(3)	0.056(9)
$U_{12} = U_{23} = 0$, $U_{13} =$	0	-0.02(1)	0	0.02(3)
B				
x	0.5	0.600(4)	0.5	0.482(4)
y	0.5	0.5	0.5	0.5
z	0.5	0.489(9)	0.5	0.484(3)
ADP (Å^2)				
U_{11}	0.000(4)	0.00(3)	0.003(4)	0.00(2)
U_{22}	0.000(4)	0.01(2)	0.003(4)	0.000(9)
U_{33}	0.00(1)	0.02(2)	0.00(1)	0.03(1)
$U_{12} = U_{23} = 0$, $U_{13} =$	0	0.09(2)	0	0.03(3)
O1				
x	0.5	0.61(2)	0.5	0.57(1)
y	0.5	0.5	0.5	0.5
z	0.033(2)	0.00(2)	0.028(3)	0.00(1)
Beq (Å^2)	1.3(6)	2(2)	0.0(8)	0(2)
O2				
x	0.5	0.57(1)	0.5	0.53(2)
y	0	0	0	0
z	0.543(2)	0.46(1)	0.546(3)	0.45(1)
Beq (Å^2)	0.0(3)	4(2)	0.2(8)	3(2)
O3				
x	-	0.12(3)	-	0.00(2)
y	-	0.5	-	0.5
z	-	0.45(1)	-	0.38(1)
Beq (Å^2)	-	20(6)	-	1(2)

Table 4.13: Summary of Rietveld refinement of the KBT end member with respect to temperature.

Temperature (°C)	370		390	
Crystal System	Tetragonal	Monoclinic	Tetragonal	Cubic
Space Group	$P4mm$	$P1m1$	$P4mm$	$Pm\bar{3}m$
Phase Percentage	58(1)	41(1)	30(2)	70(2)
Lattice Parameters				
a (Å)	3.9451(2)	3.9512(4)	3.9496(3)	3.95553(8)
b (Å)	3.9451(2)	3.9584(2)	3.9496(3)	3.95553(8)
c (Å)	3.9786(3)	3.9538(3)	3.9784(7)	3.95553(8)
α (°)	90	90	90	90
β (°)	90	90.01(2)	90	90
γ (°)	90	90	90	90
Volume (Å^3)	61.924(8)	61.838(9)	62.06(1)	61.889(4)
R'_{Exp}	12.654		12.675	
R'_p	16.456		16.408	
R'_{wp}	16.328		16.005	
Durbin-Watson	1.266		1.300	
GoF	1.290		1.263	
Impurity Phase %	$Bi_4Ti_3O_{12}$: 0.43(7)		$Bi_4Ti_3O_{12}$: 0.45(7)	
R_{Bragg}	1.302	0.727	1.715	1.281
Atomic Positions				
A				
$x = y = 0, z =$	-0.0425(3)	0	-0.068(4)	0
ADP (Å^2)				Beq = 7.6(3)
U_{11}	0.107(5)	0.08(3)	0.047(7)	
U_{22}	0.107(5)	0.12(2)	0.047(7)	
U_{33}	0.077(7)	0.07(3)	0.20(2)	
$U_{12} = U_{23} = 0$, $U_{13} =$	0	0.02(6)	0	
B				
x	0.5	0.491(5)	0.5	0.5
y	0.5	0.5	0.5	0.5
z	0.5	0.502(6)	0.5	0.5
ADP (Å^2)				Beq = 1.5(2)
U_{11}	0.000(6)	0.05(3)	0.003(9)	
U_{22}	0.000(6)	0.02(2)	0.003(9)	
U_{33}	0.02(1)	0.00(3)	0.01(1)	
$U_{12} = U_{23} = 0$, $U_{13} =$	0	0.03(6)	0	
O1				
x	0.5	0.60(2)	0.5	0.5
y	0.5	0.5	0.5	0
z	0.0295(3)	0.00(2)	0.025(6)	0.5
Beq (Å^2)	0.2(9)	0(4)	8(2)	1.0(3)
O2				
x	0.5	0.54(2)	0.5	-
y	0	0	0	-
z	0.549(4)	0.47(2)	0.538(6)	-
Beq (Å^2)	0.0(5)	2(2)	0(1)	-
O3				
x	-	-0.01(1)	-	-
y	-	0.5	-	-
z	-	0.42(2)	-	-
Beq (Å^2)	-	0(4)	-	-

Table 4.14: Summary of Rietveld refinement of the KBT end member with respect to temperature.

Temperature (°C)	410		500
Crystal System	Tetragonal	Cubic	Cubic
Space Group	$P4mm$	$Pm\overline{3}m$	$Pm\overline{3}m$
Phase Percentage	20(2)	80(2)	99.5(1)
Lattice Parameters			
a (Å)	3.9498(4)	3.95628(7)	3.95898(6)
c (Å)	3.986(1)	3.95628(7)	3.95898(6)
α (°)	90	90	90
Volume (Å^3)	62.18(2)	61.924(3)	62.051(3)
R'_{Exp}	12.759		17.161
R'_p	16.782		20.413
R'_{wp}	16.316		20.524
Durbin-Watson	1.303		1.433
GoF	1.279		1.196
Impurity Phase %	$Bi_4Ti_3O_{12}$: 0.44(8)		$Bi_4Ti_3O_{12}$: 0.4(1)
R_{Bragg}	1.779	1.707	2.166
Atomic Positions			
A			
$x = y = 0, z =$	-0.076(5)	0	0
ADP (Å^2)		Beq = 7.5(2)	Beq = 8.06(9)
$U_{11} = U_{22} =$	0.035(8)		
U_{33}	0.20(2)		
$U_{12} = U_{23} = 0$, $U_{13} =$	0		
B $x = y = z = 0.5$			
ADP (Å^2)		Beq = 1.3(2)	Beq = 1.68(8)
$U_{11} = U_{22} =$	0.01(1)		
U_{33}	0.00(2)		
$U_{12} = U_{23} = 0$, $U_{13} =$	0		
O1			
$x = y = 0.5, z =$	0.029(8)	0	0
Beq (Å^2)	7(3)	1.3(2)	1.6(1)
O2			
x	0.5	-	-
y	0	-	-
z	0.546(8)	-	-
Beq (Å^2)	0(2)	-	-

4.4.6 High Temperature Analysis from Rietveld Refinements

From the tabulated Rietveld refinements, it was possible to directly compare how structural parameters evolved with respect to temperature and composition. The results of these are presented here.

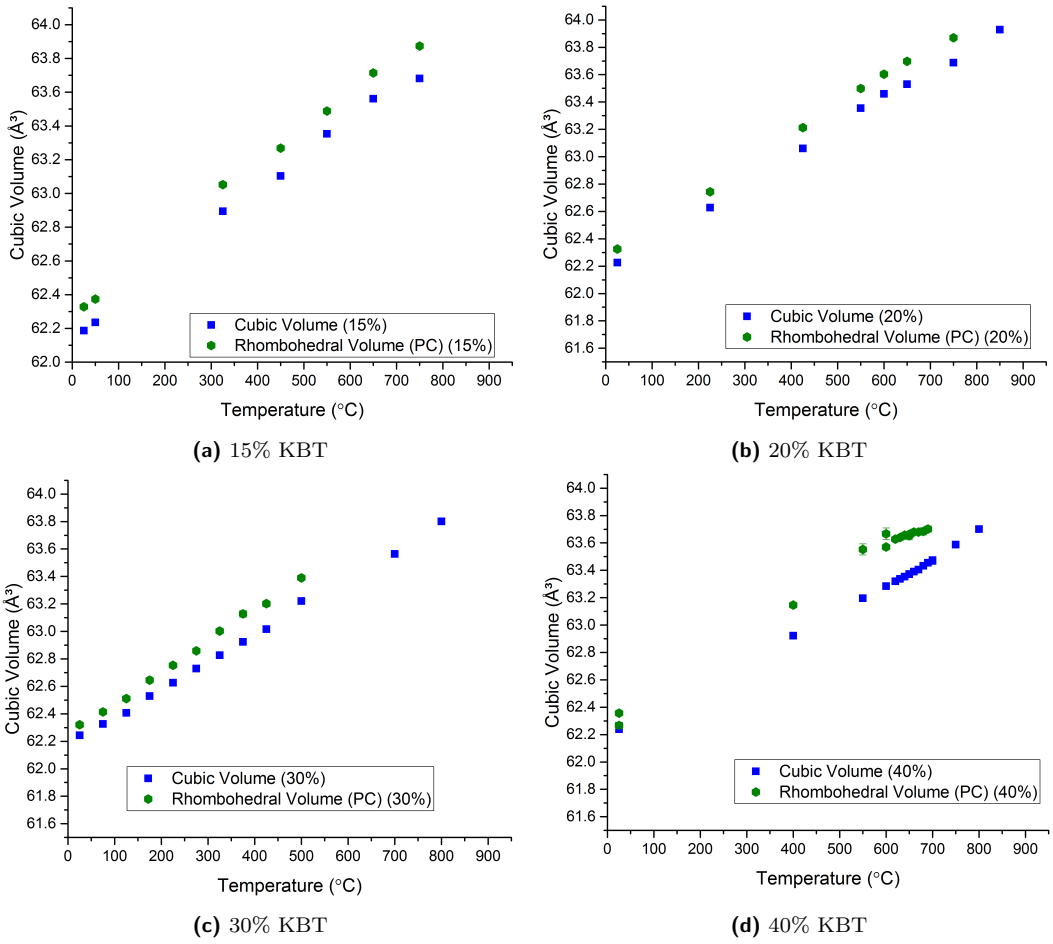

(a) 15% KBT

(b) 20% KBT

(c) 30% KBT

(d) 40% KBT

Figure 4.21: Volume with respect to temperature for the noted compositions. The different phase volumes are presented. The axes are the same to allow for easy direct comparison. The rhombohedral volume is presented as a pseudocubic volume.

4.4.6.1 Volume Analysis

Figure 4.21 and Figure 4.22 display the volume with respect to temperature for the compositions. The rhombohedral volumes are displayed in pseudocubic notation to facilitate easier comparison between the values, dividing the volume by the Z factor of the rhombohedral cell; in the case of $R3c$ this means $Volume_{PC} = \frac{Volume_{Rh}}{6}$. All graphs use the same axes, to enable direct comparison between graphs.

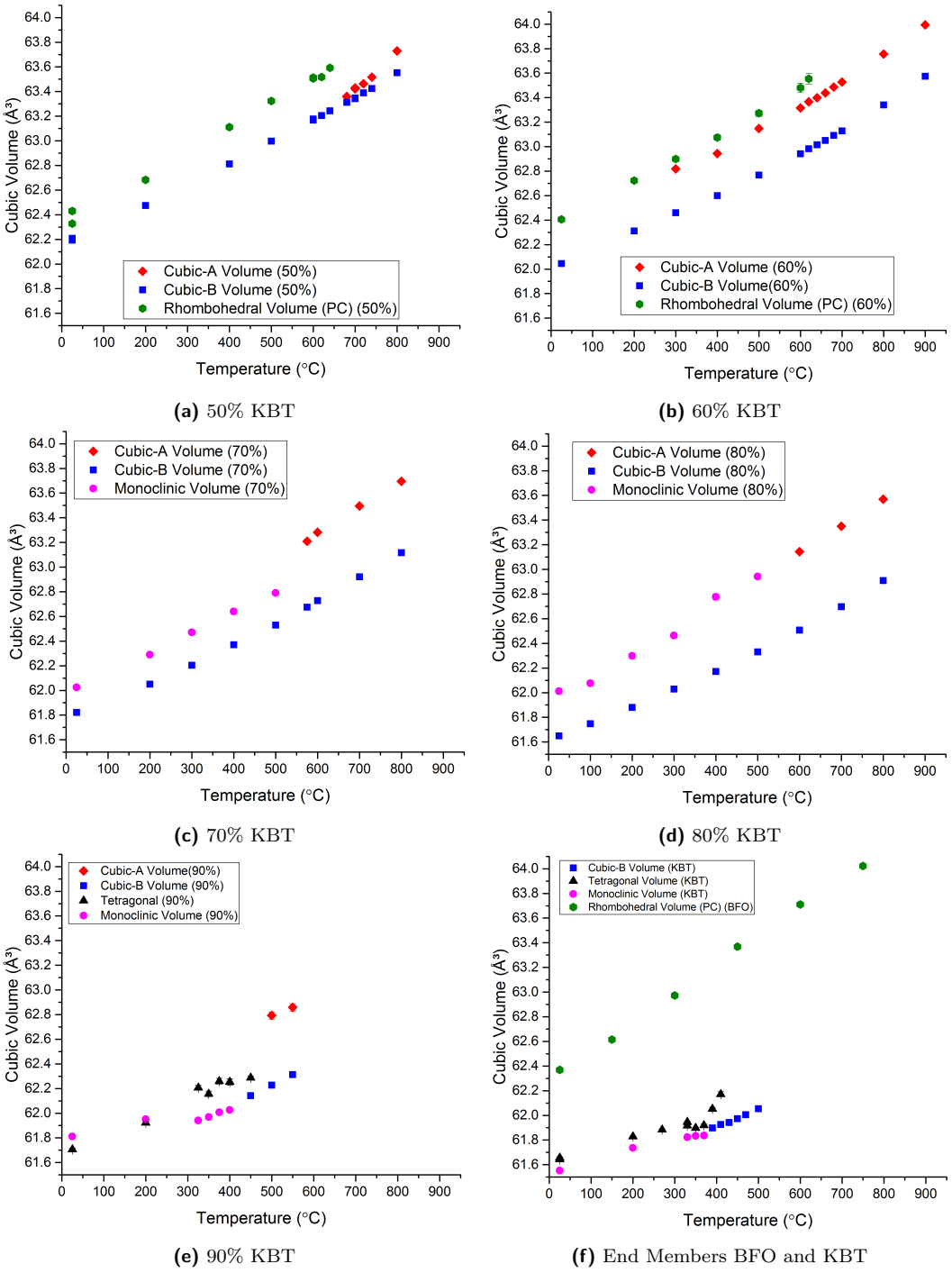

(a) 50% KBT **(b)** 60% KBT

(c) 70% KBT **(d)** 80% KBT

(e) 90% KBT **(f)** End Members BFO and KBT

Figure 4.22: Volume with respect to temperature for the noted compositions. The different phase volumes are presented. The axes are the same to allow for easy direct comparison. The rhombohedral volume is presented as a pseudocubic volume.

The graphs in Figure 4.21 are all extremely similar, showing a larger rhombohedral volume and a smaller cubic volume. Comparing the rhombohedral volume with Figure 4.22f, it can be seen that the volumes are extremely close, and there is little change in the rhombohedral volume from the end member volume. There is thermal expansion in the material, resulting in a regular volume increase; both the cubic and rhombohedral volume changes can generally be modelled well with parallel lines. In all but the 15% KBT sample, Figure 4.21a, there comes a point where a single cubic phase is presented and the volume expansion of this is consistent with the cubic volume at lower temperatures. In Figure 4.21d it can be seen that just before this change to just a cubic phase, the rhombohedral volume shows a decline in its rate of expansion with temperature, which would mean the rhombohedral and the cubic volume would eventually converge. This is discussed further in Section 4.4.6.2. In summary, the changes in volume seen in Figure 4.21 are all very consistent with one another, which is consistent with the observed nature of the 15% to 40% KBT region in Rietveld refinements.

The graphs in Figure 4.22 are significantly more varied. The subfigures of Figure 4.22 all display some level of thermal expansion. Another commonality between the graphs of Figure 4.22, with the exception of the end members, is the fact that at high temperature they all form a two-cubic mixed phase rather than a single cubic phase as in Figure 4.21. These cubic phases were found to have different compositional values, depending on whether they were closer to being like a BFO cubic peak or a KBT cubic peak, which is discussed in depth in Section 4.4.6.4. The Cubic-A phase has a larger unit cell and thus a larger volume than the Cubic-B phase, meaning Cubic-A is closer to the rhombohedral volume. Where a cubic phase is present at room temperature this can be considered to be a Cubic-B phase. Other than these similarities, it is useful to group them into smaller groups.

Figure 4.22a and Figure 4.22b show a similar early progression of volumes to those found in Figure 4.21, but are set apart by the inclusion of two separate cubic phases. The splitting of the cubic phase actually begins in each before the rhombohedral phase has fully diminished, but in the case of the 50% sample the contribution is too low to allow for a good refinement. The two-cubic mixed phases expand in parallel fashion in Figure 4.22b, but not in Figure 4.22a. This could be a result of the second cubic peak in the 50% sample being less well defined. The splitting between the volume of the Cubic-A and Cubic-B phases is larger in the 60% KBT powder than the 50% KBT powder.

Figure 4.22c and Figure 4.22d while being similar in terms of phase composition are also quite different in terms of volume changes between these phases.

In both cases, the change from a monoclinic and cubic mixed phase model to a two-cubic mixed phase model is poorly defined. The results presented here represent a best estimate for the composition at which it is expected that there would be a change, but several measurements above and below are equally viable. Figure 4.22c shows a sudden change in volume at the point at which it is represented by the two-cubic mixed phase rather than a cubic and a monoclinic phase, but this discontinuity between representations is independent of the point chosen. Figure 4.22d shows no such discontinuity at the chosen point of change. In both graphs, Cubic-B is quite consistent throughout, showing a marginal change in gradient between the range from room temperature to 400°C and showing thermal expansion above this parallel and comparable with all other high temperature graphs.

Figure 4.22e shows a change from a tetragonal and monoclinic phase to a two-cubic mixed phase. The monoclinic phase becomes increasingly cubic with temperature, becoming indistinguishable from cubic at the temperature where it is represented by the Cubic-B phase. At this point, some tetragonal phase remains as shoulders on the peak, but this too is becoming more cubic. Like the 50% sample, there is actually some evidence of the double cubic central peak surrounded by the tetragonal shoulders before the change from tetragonal to cubic is complete, but the deviation from a single cubic peak is too low to fit satisfactorily until the tetragonal phase has become undetectable. In this case, the monoclinic phase has a lower volume than the tetragonal phase, whereas in the 70% and 80% KBT samples, the monoclinic phase represented the larger volume phase at low temperatures. This is consistent with the monoclinic phase in the 70% and 80% KBT samples fitting a different phenomenon to the monoclinic phase in the 90% KBT sample. In the 70% and 80% KBT samples, the monoclinic phase is fitting the remnants of the larger volume rhombohedral phase, whereas in the 90% KBT sample it is fitting a slightly widened form of the monoclinic phase of the KBT end member. The tetragonal phase shows a change in volume with respect to temperature consistent with becoming part of the Cubic-B phase. The leftover Cubic-A phase then has a very different volume to the other phases present in the measurements, with a volume very similar to that of the cubic phase of the 60% KBT. In Section 4.4.6.4 this Cubic-A can be seen to be composed mostly of BFO-like material.

Figure 4.22f shows the end members, BFO and KBT, for comparison with the other data displayed in Figure 4.21 and Figure 4.22. The BFO end member data was formed experimentally, utilising the best of the BFO powders synthesised in Chapter 3. While the powder had more impurity phase (around 3%), it was considered to be of sufficient quality to determine the pseudocubic volume for comparison with these

measurements. At low temperature there is thermal expansion and the monoclinic volume (again, like the 90% KBT, lower than the tetragonal volume), which form towards convergence of an average cubic volume between the two. However, the tetragonal phase persists after the monoclinic phase has already converged to cubic, and observing the diffraction patterns, is still vital for an adequate fit. The volume of these final tetragonal phase contributions increase rapidly with temperature, before they become part of the single cubic phase.

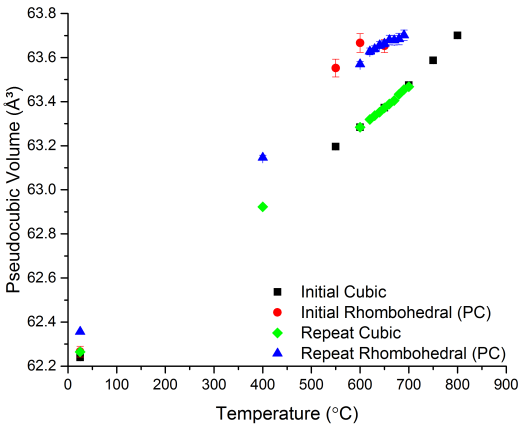

(a) Pseudocubic volume (40% KBT), with data from an initial experiment with wide steps and the repeat experiment with finer steps at high temperature.

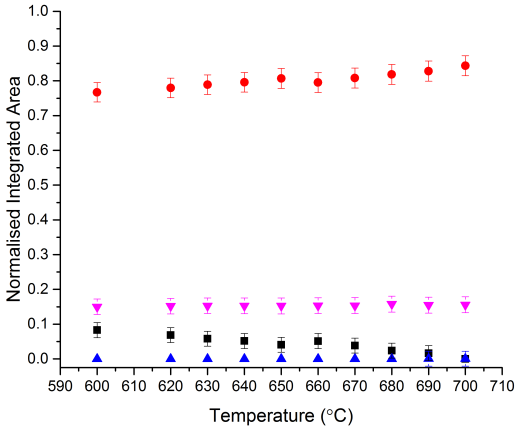

(b) {110} peak integrated intensity comparisons. The red circles are the cubic phase area, the black squares are the rhombohedral phase area, the blue triangles are the impurity phase area, the pink downwards triangles are the background area. Values are normalised to the total integrated area of the peak.

Figure 4.23: Comparison of the change in PC volume in the 40% KBT measurements with the change in the integrated intensity of the phases in the measurements with respect to temperature.

4.4.6.2 Integrated Intensity of Structural Changes

Figure 4.23a shows the change in the volume, adjusted for a pseudocubic cell, with respect to temperature for the 40% KBT sample. There were two experiments; the first established the approximate transition temperature, which is shown as the red circles (rhombohedral) and the black squares (cubic), and the second which investigated changes in volume around the transition temperature specifically, shown as the blue triangles (rhombohedral) and green diamonds (cubic). The results are consistent between the two experiments, with the different schemes aligning within the errors with few outliers. In the second measurement, around the transition temperature found from the prior measurement, it was found that the lattice parameters of the rhombohedral phase changed gradient with respect to

temperature, which would ultimately result in a convergence between the cubic and rhombohedral phase volumes. The rhombohedral phase intensity becomes too low to measure before this point is reached.

Figure 4.23b shows the integrated intensities of the {110} peak, measured from 31° 2θ to 32.5° 2θ to ensure that all intensity in the peak was accounted for, normalised by dividing the areas by the total area, with respect to temperature. The red circles are the cubic phase area, the black squares are the rhombohedral phase area, the blue triangles are the impurity phase area, the pink downwards triangles are the background area. The rhombohedral component decreases with increasing temperature. The cubic component increases with temperature. The impurity phase has a very small contribution in the {110} peak. The background remains unchanged, meaning that the intensity from the rhombohedral peak is not lost by the formation of an amorphous phase, but is instead transferred to the increasing cubic peak intensity.

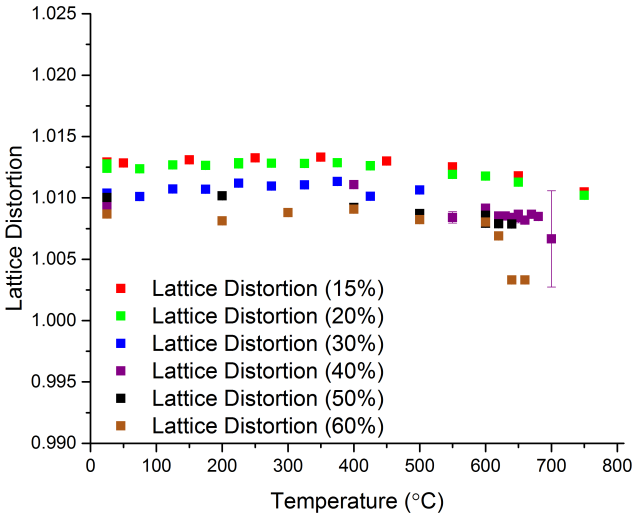

Figure 4.24: Plot of the rhombohedral lattice distortion vs temperature. The samples which were modelled as being cubic do not have lattice distortion values. A trend of decreasing lattice distortion with increasing temperature is generally noted in all samples.

4.4.6.3 Rhombohedral Lattice Distortion

Figure 4.24 shows the changes in the lattice distortion with respect to temperature. The distortion was estimated as Distortion $= \frac{c}{a}/\sqrt{6}$ [7] and is a metric for the divergence of the cell from a cubic cell, with a higher distortion representing a less cubic cell. Comparing this with Figure 4.21 and Figure 4.22 it can be observed that while the volume is increasing with temperature from thermal expansion, this

is not evenly present in the a and c rhombohedral lattice parameters, showing a noticeable decrease in the lattice distortion with increasing temperature, offering further evidence of the rhombohedral phase of the mixed phase material becoming more cubic at high temperature.

The lattice distortions show a trend of decreasing above 500°C. This is consistent with the rhombohedral phase itself taking on a more cubic form in addition to the decreasing intensity. Because of this gradual shift, a sharp transition from mixed rhombohedral and cubic to just cubic would not be expected and has not been observed.

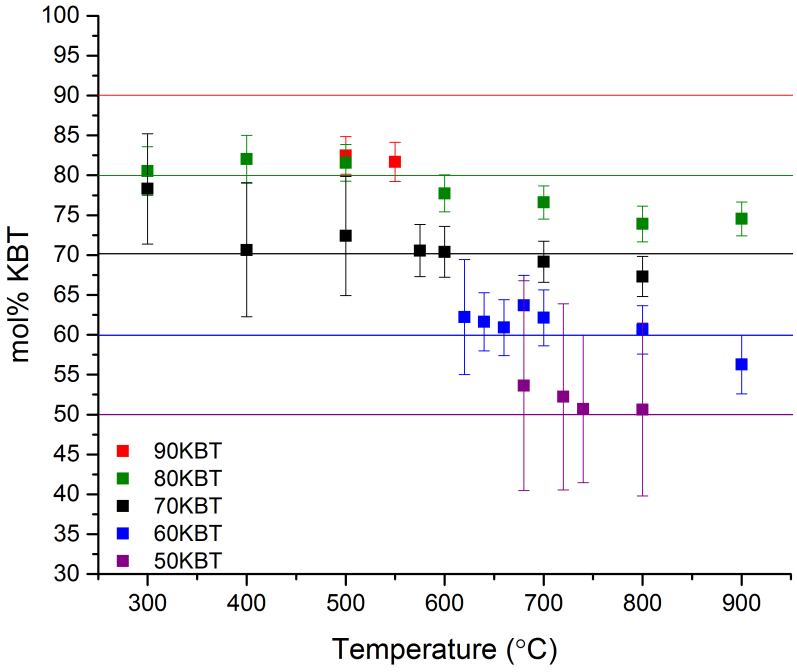

Figure 4.25: A diagram displaying the mol% of KBT determined in each measurement by the occupancy methodology. Of note is that most compositions show a good agreement with the synthesis composition, with the exception of 90% KBT and the large errors on 50% KBT. In both cases, the second cubic phase contribution is minimal.

4.4.6.4 Compositional Analysis of Cubic-A and Cubic-B Peaks

With the compositional region from 50% KBT to 90% KBT showing a different reaction to high temperature than the lower mol% KBT compositions, this region was investigated as one major region of the phase diagram. It was determined to be best fitted at high temperature with a two-cubic mixed phase model over any single phase, so it was considered that there could be phase separation or break down occurring in this region. Room temperature measurements taken after the

heating to this temperature agreed well with room temperature measurements made before heating, so it was clear that the process was reversible. It was thought that there could be a difference in the phase % of KBT in each of the cubic peaks, so they were allowed to refine in such a way that the % of BFO in each peak could be ascertained, along with the total composition for that sample. The results of the total composition experiments agreed well with the actual composition of the material, displayed in Figure 4.25. The exceptions, 90% and 50%, with a large difference in occupancy derived composition and large errors respectively, occur in the two end samples of this separation region, where the secondary cubic peak is quite small, making measurements less reliable.

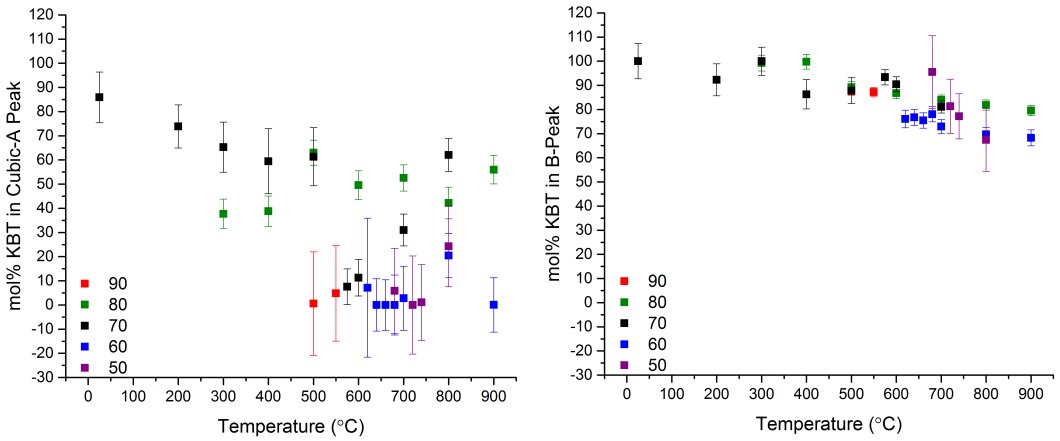

(a) A-Cubic Peak **(b)** B-Cubic Peak

Figure 4.26: Comparison of the A-Cubic Peak and B-Cubic Peak compositions, determined through occupancy refinements during Rietveld refinements. In general, the the A-Cubic Peak was found to be BFO rich and the B-Cubic Peak was found to be KBT rich.

It was found that the Cubic-A peak was richer in BFO compared with the Cubic-B peak, seen in Figure 4.26. Given that the Cubic-A peak was the peak closer in lattice parameters to unmixed BFO and the Cubic-B peak was closer to the unmixed KBT lattice parameters, it can be argued that the splitting of these peaks gives rise to a BFO-Like peak (Cubic-A) and a KBT-Like peak (Cubic-B); while some of the data analysis has given values of 100% BFO or KBT respectively, the uncertainties in the values are larger for smaller values, so it is likely that both peaks contain some level of both BFO and KBT like behaviour. Since the splitting is reversed by cooling, it is unlikely that the material is chemically changed from a mixed BFO-KBT powder to unmixed BFO and KBT. This difference in composition would explain the differences in volume seen in the two cubic phases in Figure 4.21 and Figure 4.22.

4.4.6.5 Percentage Cubic and Rhombohedral

From the Rietveld refinements, as in the room temperature experiments, it was possible to get a value for the rhombohedral and cubic relative phase percentages of the mixed phase. These values were included in the tables describing the Rietveld refinements. In the cases where it was determined that the cubic fitting was better than the mixed phase, these have been included as 100% cubic 0% rhombohedral. In all other cases, the values are those obtained directly from TOPAS ACADEMIC Rietveld refinements, as in the room temperature section.

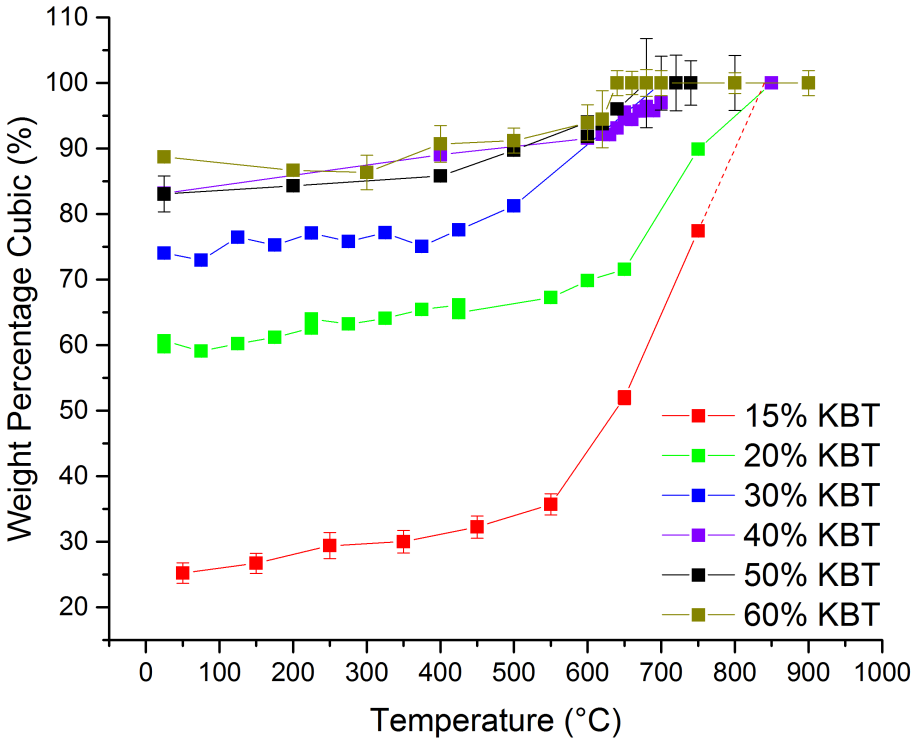

Figure 4.27: Comparison between the values for the cubic proportions of the powders with respect to temperature, drawn from the Rietveld refinement tables, from Table 4.2 to Table 4.14, and all other data obtained in the course of this thesis. The 50% KBT and 60% KBT samples have the Cubic-A and Cubic-B phase contributions summed together. The dashed line shows an extrapolation of the 15% KBT plot.

Figure 4.27 shows the data of the cubic percentage values from the Rietveld refinement tables. It can be seen from this graph that as the temperature is increased, the model tends towards cubic. This appears to be a small effect initially, with the overall phase ratio between cubic and rhombohedral remaining steady between room temperature and a temperature in the range of 500°C to 600°C depending on the composition, with higher %mol KBT powders starting to become

more rapidly cubic at lower temperatures. All of the samples except the 15% KBT sample reach a point of being 100% cubic by 800°C, though the only reason 15% KBT does not is likely that it was not heated above 750°C; an extrapolation of the 15% KBT data suggests that it very likely would have also reached the cubic phase by 900°C. The 40% KBT, 50% KBT and 60% KBT all have very similar cubic progressions. The 50% KBT and 60% KBT have the Cubic-A and Cubic-B phases added together.

The higher mol% KBT samples have not been added because they become cubic at a lower temperature and do not follow an analogous change in composition to the rhombohedral-cubic room temperature measurements. The fact that the higher % KBT materials not only start at a higher cubic weight percentage but also transition to being fully cubic at lower temperatures is consistent with the additional disorder introduced to the system by the addition of KBT, which is seen in the long range order as the cubic (and, at higher mol % KBT, monoclinic) phase, and it is known that KBT transitions to a cubic phase at lower temperature than BFO (450°C [2] and 931 °C [1] respectively).

4.5 Cubic-Comparison Single Peak Method

Since the Rietveld refinement measurements took 6 hours to complete, it was impractical to have a finely graduated set of temperature experiments with this method. The {110} peak was seen to have one of the largest changes over the temperature range, so was the focus of the shorter scans, taking 30 minutes each to complete. During the experiments where these shorter measurements were taken, several longer measurements were also taken concurrently, which were analysed by Rietveld refinements to allow the direct comparison of these two different methods.

These shorter measurements allowed temperature steps as low as 10°C to be realised around prospective regions of interest from prior experiments. The issue with these measurements was that they were unable to be analysed through Rietveld refinement, so an alternative method of quantifying the data had to be employed. To this end, a Split Pearson VII peak analysis methodology [8] was used in ORIGIN.

Figure 4.28 shows the progression from the high temperature fitting on a 40% KBT sample {110} peak to the room temperature fit from the same model. Here the observed data is given by the black data points, with error bars, while the fitted cubic model is shown by the blue line. The degree to which the cubic model represented the data was investigated by comparing the areas covered by the calculated and observed {110} peak; it should be noted that this does not measure

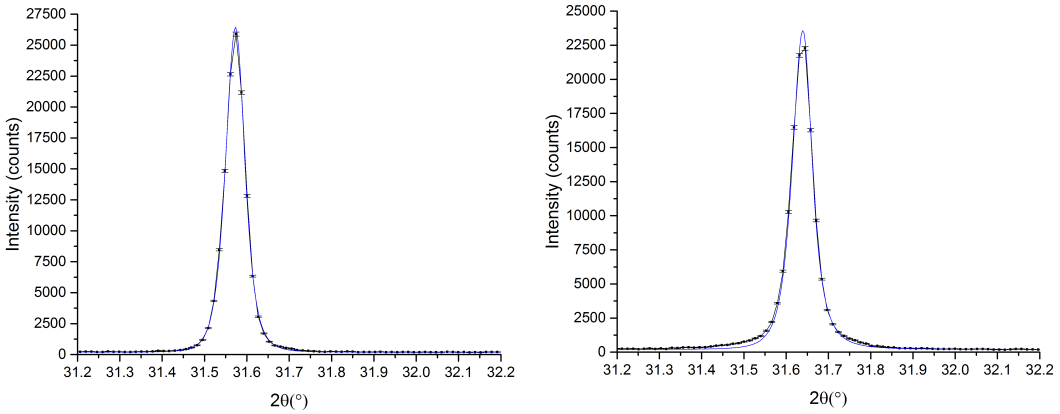

(a) 850°C. 99(2) % Area fit

(b) 700°C. 94(2) % Area fit

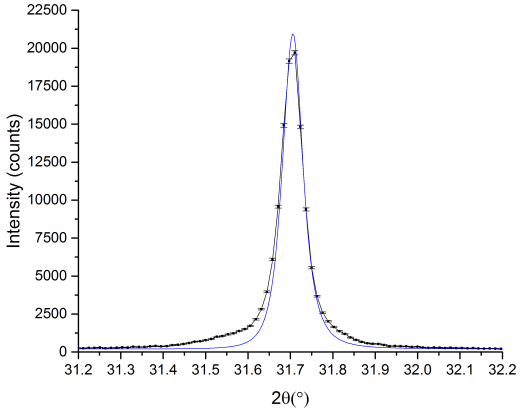

(c) 500°C. 84(3) % Area fit

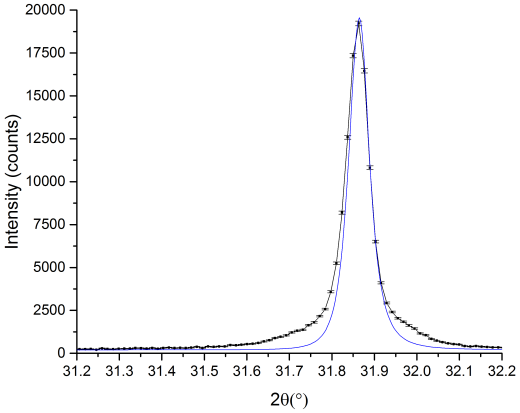

(d) 25°C. 77(3) % Area fit

Figure 4.28: 40% KBT {110} single peak graphs with changing temperature, arranged from high temperature to low temperature. It can be seen that while a single cubic fit matches the observed data well at high temperatures, the percentage overlap decreases as the temperature is decreased. The data points are in black, connected with straight lines and the single cubic peak model to the data is in blue.

the overlap of the areas, simply a comparison between the total peak area of the model and the total peak area of the data. As will be seen later, while this means the percentage is quite abstract, its evolution does follow the same trend as changes in the actual phase ratio.

The highest temperature measurement was taken to be essentially cubic in nature, and so the peak was fitted as purely cubic, seen in Figure 4.28a, measured at 850°C. Visually, it is clear that the cubic model fits this data well, and the value of the area of the model compared with the value of the area of the data is 99(2)% of the value. The parameters from this model were then used as the baseline model for the rest of the temperature fittings. The peak position and peak area were able to refine freely. The background should be within a similar range for all measurements taken in any single temperature experiment, so was constrained. The mL, mR, wL and wR parameters were restrained to ensure that the cubic peak shape would be retained. It can be seen that at lower temperatures, this cubic model fits less well.

It can then be seen that at lower temperatures, the model fits the observed data less well, with slight deviation at 750°C (94(2)% area), larger deviation at 500°C (84(3)% area) and a large deviation at room temperature (77(3)% area) where only the central intensity of the peak was fit. Figure 4.28d also shows some signs of diffuse scatter in with the residual rhombohedral intensity, with the peak FWHM larger than the cubic model can accommodate even in the main peak.

By taking the percentage difference between the areas covered by the cubic model and the observed data, it was possible to construct graphs showing with smaller step size how the system evolved with increasing temperature, since the systems were either cubic, or a mix of rhombohedral and cubic; essentially, by measuring the difference in area covered, it was possible to obtain a rough graph of how the cubicness of the system progressed with respect to temperature. This data is shown in Figure 4.29. It shows the progression of the peak fitting, from close to 100% coverage at high temperature, where the peak should be purely cubic, down to a much lower level at room temperature. It can be seen that at low temperatures there is significantly larger disagreement between the data, which implies that this methodology is not a good representation for low temperature data.

It was not possible to use this method on the 15% KBT sample, because even at the highest temperature measured the system was not fully cubic, meaning that there was no baseline measurement to work from. Likewise for most of the two-cubic mixed phase region at high temperature, since these aside from the 50% sample were not able to be represented by a single cubic peak. In the 50% KBT sample the second cubic peak is mostly needed for higher angle peaks, so since this

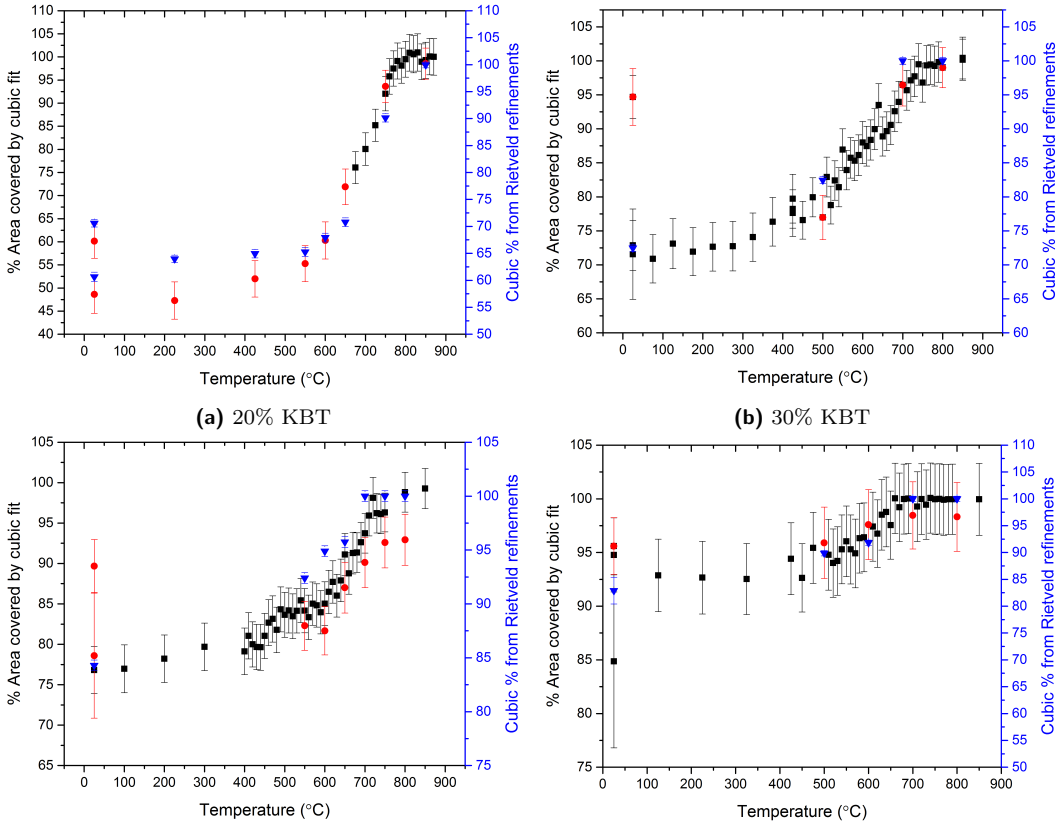

(a) 20% KBT

(b) 30% KBT

(c) 40% KBT

(d) 50% KBT

Figure 4.29: BFOKBT powder measurements on the {110} peak, displayed as the % area that a purely cubic fit of the data was able to cover of the total observed area. Both the pure {110} measurements (black squares) and the {110} measurements from the longer scans (red circles) are included here. In addition, the % cubic from the Rietveld refinements (blue triangles) are included for comparison.

Table 4.15: Stable and transition temperatures from single peak method, values all ±20°C due to step size.

% KBT	Stable mixed until/°C	stable cubic after/°C
20	550	810
30	500	740
40	450	710
50	500	650

method focusses on the {110} peak it can be estimated as a single cubic peak.

Figure 4.29a shows the data obtained with this method for the 20% KBT powder sample. When compared with the cubic phase percentages from the Rietveld refinements it can be seen that this methodology shows changes in gradient around the same temperatures. While the actual values appear to agree well with the Rietveld refinement percentages above 600°C, this is coincidental, as the other graphs in this section show. What is consistent is that both the Rietveld and single-peak measurements agree on the points where the structure changes from a steady mix of phases, to increasing cubic phases, to a stable entirely cubic phase.

Figure 4.29b, Figure 4.29c and Figure 4.29d show the data obtained with this method for the 30% KBT powder sample, the 40% KBT powder sample and the 50% KBT powder sample respectively. When compared with the cubic phase percentages from the Rietveld refinements it can be seen that this methodology shows changes in gradient around the same temperatures in each case, providing confirmation that the changes in the phase structure can be approximated by the single peak methodology. As such, this method can be used to track the approximate points where the stable temperature region gives way to the rapidly changing temperature region, before the samples then become cubic. This allows a more nuanced view of the points at which major changes in the phase structure of the system can be mapped. The outliers at 25°C are measurements taken post heating.

4.5.0.0.1 Summary

In summary, these measurements allowed for a clearer view of the point at which the BFO-KBT samples switched from their stable state to their increasingly-cubic-phase state, to their stable cubic state. From this, it can be seen that the increasingly-cubic-phase state tends to extend approximately 200°C, seen in Table 4.15. While below the increasingly-cubic-phase temperature, this method is less reliable, it does help to confirm the stability of the powders below this temperature, despite the fact that KBT is known to start becoming cubic at (280°C), becoming fully cubic at 450°C [2], close to the temperature at which the increasingly-cubic-phase begins.

4.6 High Temperature Decomposition

It was noted that during the high temperature experiments, it was possible for impurity phases to form in the powders. See the 40% KBT powder for the clearest example of this phenomenon, since the sample did not show signs of having a impurity phase until part way through the heating experiment. In addition, it was noted that the sample holder was becoming discoloured by the experiments, in the same way as was noticed in the alumina crucibles in Section 3.2. It was suspected that, given the reported volatility of bismuth oxide [9, 10, 11, 12] that there was a possibility that material was being lost during the heating, which would explain the discolouration and the formation of impurity phases. The stoichiometry of the sample would be affected by this decomposition. This was investigated by thermal analysis, using a *Mettler Toledo DSC1-Star* system.

The temperature was set to increase at a gradient of 1°C per minute, until reaching 800°C. It remained at this temperature for 2 hours before being cooled at the same rate. This was chosen to mirror the heating and cooling process in the high temperature experiments. When the post heating mass was compared to the pre-heating mass, it was found that the sample had lost <0.1% of its initial mass (±0.01%). In addition, mass spectroscopy recorded no bismuth, titanium, iron or potassium being released by the sample, though with a maximum detectable atomic mass <160, it is possible that some heavier compounds, such as Bi_2O_3 could have been missed. From the extremely small change in mass it seems unlikely that this would be a significant amount.

In addition to the high temperature measurements generating impurity phases in the samples, it was also noticed that when the room temperature measurements were repeated on the same samples after they had cooled the peaks had changed. The rhombohedral intensities had decreased, and the cubic intensities had increased, as was found to happen as the temperature was increased, or the KBT % was increased. In order to investigate this further, an experiment was carried out on a sample of 40% KBT which involved heating the sample twice; the first time around, as normal, heating up to 850°C with measurements at regular intervals; When the temperature was then decreased back down to room temperature, measurements were taken at fixed intervals, like in the heating example; Once at room temperature, a second heating run was initiated, with measurements again taken at fixed intervals; Once the highest temperature was reached, 850°C as in the first run, the temperature was once again decreased to room temperature with measurements taken at fixed intervals.

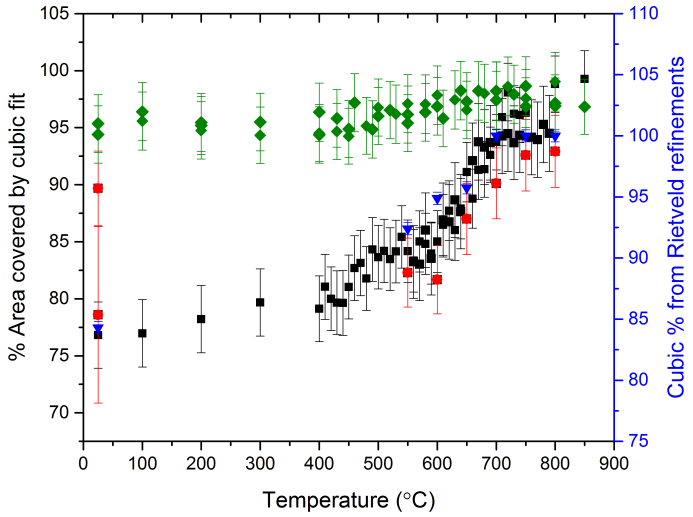

Figure 4.30: 40% KBT {110} measurements, displayed as the % area that a purely cubic fit of the data was able to cover, as in Figure 4.29c. Here, the black squares represent data from two separate heating experiments of a powder that has not been heated. The red circles represent those data points taken from longer-measurement datasets, for which there also exist Rietveld refinements (shown as blue triangles). Finally, in addition to this, which was mostly present in Figure 4.29c, the green diamonds represent the data taken post heating. This includes two sets of measurements taken while the system was being cooled, and one set of data describing the effects of heating the sample a second time.

From these four sets of measurements, a graph was constructed, shown in Figure 4.30. In addition to these measurements, data from another 40% KBT heating experiment is included for comparison with the data obtained from this experiment, and the Rietveld refinements; it can be seen that the initial heating measurement set matches very well with the prior heating experiment to high temperature. The initial cooling measurement set, the second heating measurement set and the final cooling measurement set all match up well with one another, suggesting that any changes which have taken place do not alter any further after the initial heating experiment. The changes seen here suggest that after the initial heating, the diffraction pattern is consistently more cubic.

Figure 4.31 shows a direct comparison of the initial and final room temperature measurements of a set of measurements included in Figure 4.30. From this comparison, it's clear that a significant change in the diffraction data has occurred during the heating process as the final measurement, shown as the blue dashed line, is more intense with a smaller base, and thus, smaller contributions from a rhombohedral phase than the solid red line, representing the pre-heating measurement. This confirms the conclusion to be drawn from Figure 4.30 that there is a difference between the pre-heating and post-heating measurements, with

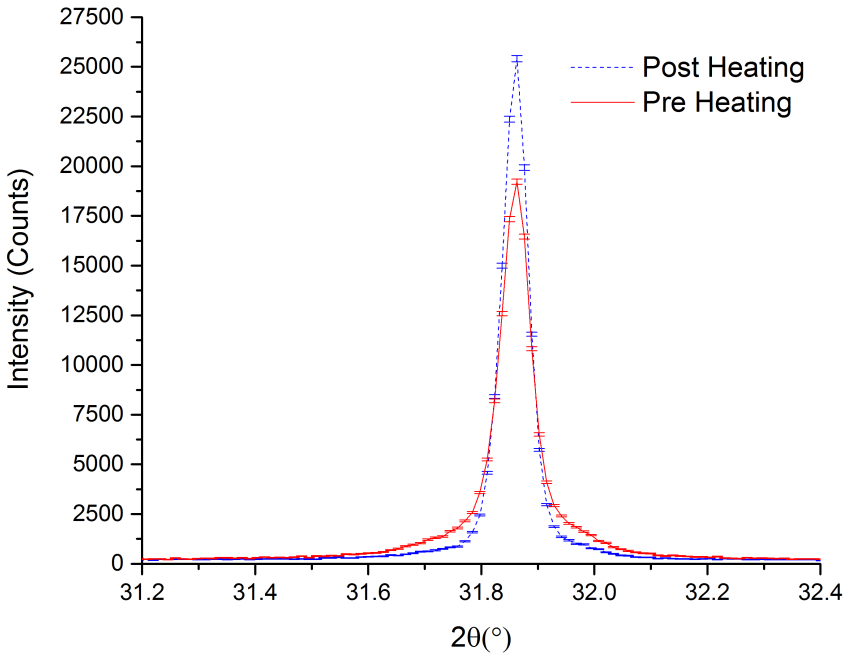

Figure 4.31: Two 40% KBT {110} measurements at room temperature, taken as part of the same set of measurements. The red solid line is the initial measurement, taken before the sample was heated. The blue dashed line is the final measurement, taken after the sample had been heated and cooled back to room temperature twice.

the post-heating measurements appearing to be more cubic than the pre-heating measurements.

4.6.0.0.1 Summary

In summary, since it was found that very little mass was lost during these heating experiments it is unlikely that sufficient material was vaporised from the powder sample to alter the stoichiometry enough to explain the changes seen. It was found that the samples were each becoming more cubic after being heated, suggesting that some sort of change to the phases was occurring. The fact that the impurity phase was seen to change or appear, depending on the initial phase purity of the sample, would seem to be the key to this. The main impurity phase was Bi_2O_3, which would suggest that the main phase was no longer fully stoichiometric. If the bismuth of this impurity phase was mostly formed from the BFO, or evenly from both the KBT and the BFO, this would shift the ratio closer to the KBT end of the spectrum, since KBT contains half the bismuth that BFO does. From the compositional investigation in Chapter 3, this would mean that the diffraction pattern of samples in the experimental range would become more cubic, matching

with the observation that post-heating samples showed signs of being more cubic than analogous pre-heating measurements did.

4.7 Phase Diagram and Conclusions

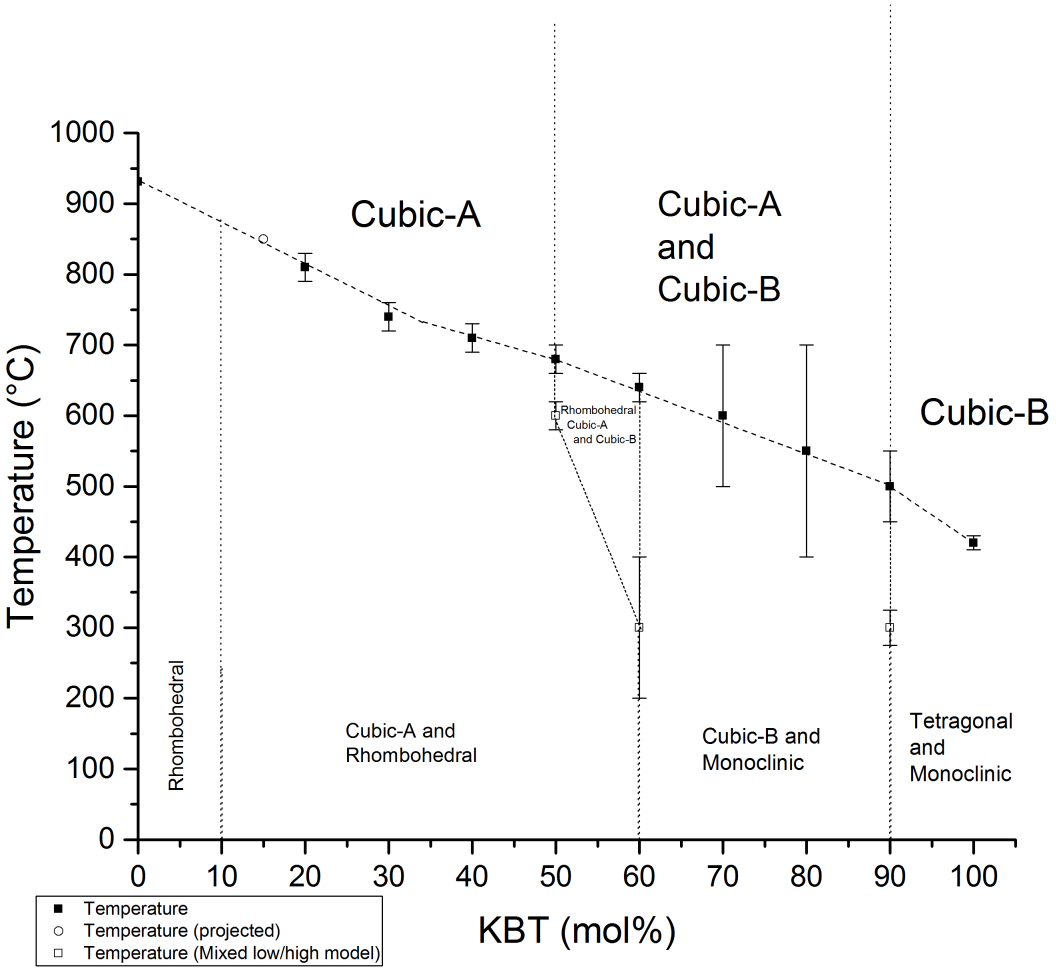

Figure 4.32: Phase diagram constructed from the data in this chapter and the room temperature powder chapter (Chapter 3). Like the phase diagram presented in Chapter 3, the dashed lines used do not represent sharp phase transitions but rather the point where a different model is a better representation for the data; no sharp phase transitions were observed, with the system tending to become more cubic with an increase in temperature, until all other phases were too small to be properly represented.

Figure 4.32 is constructed from the data in Chapter 3, Section 4.4 and with Section 4.5 providing more nuanced data about the point of cubic transition for the lower mol% KBT region. With increasing temperature, the system tends towards a more cubic phase composition, though between 50% KBT and 90% KBT, at high

temperature it in fact forms two overlapping cubic phases, which was discussed in Section 4.4.6.4.

As such, excluding the end members, there are seen to be two major regions in the phase diagram. The first is that below 50 mol% KBT, which has a relatively simple phase diagram. The cubic and rhombohedral room temperature phase changes under heating thus increasing the intensity of the cubic phase fraction and decrease the rhombohedral phase fraction, while the rhombohedral phase fraction undergoes a change in lattice parameters to become more cubic in its own right. As the cubic phase percentage at room temperature is increased, with increasing mol% KBT, the change to a cubic phase at high temperature happens at lower temperature. The 15% KBT powder was not able to reach the cubic phase in the measurements undertaken, due to concerns about the potential for the material to melt, but the point at which it would be considered cubic has been extrapolated from the measurements which were undertaken.

The second is the region above and including 50 mol% KBT, within which the high temperature phase becomes a mix of two overlapping cubic phases. This region is further split into three sub-regions: (a) the sub-region including 50% and 60% KBT, which at room temperature and under initial heating acts like the first major region; (b) the sub-region consisting of the 70% and 80% KBT measurements, which are a mix of monoclinic and cubic at room temperature, although alternative models are also viable; (c) the third sub-region consisting of just 90% KBT, which at room temperature shows a similar composition to the KBT end member.

The first sub-region shows some deviation from the first major region even before the rhombohedral phase has fully disappeared below the detection threshold, requiring an additional phase between the upper and lower temperature phase regions, which consists of Cubic-A and Cubic-B peaks, as well as a rhombohedral peak surrounding them.

The second sub-region is the hardest to properly characterise; at room temperature, there are already multiple possible phase compositions, and this confusion does not diminish with temperature until above 700 °C; the peaks are so similar to two cubic peaks even at low temperature that it is hard to ascertain the point at which it is optimal to represent the data with two cubic peaks over any of the other models. This becomes somewhat clearer above 700 °C, where the model is fitted better with two cubic phases than any other model, but the confusion range on the model is wide, resulting in large error bars in Figure 4.32.

The third sub-region has a similar phase composition to the KBT end member at room temperature, but at high temperature forms a two-cubic phase,

and like the first sub-region shows a split of the cubic-like monoclinic phase into two cubic phases before the tetragonal phase has diminished to the point of disappearing.

The cubic phases were modelled as $Pm\bar{3}m$ phases, with Cubic-A phases found at low mol% KBT and Cubic-B phases found at high mol% KBT, with a combination in between where a phase separation was observed to occur. The rhombohedral phases were modelled as $R3c$, the monoclinic phases were modelled as $P1m1$ phases and the tetragonal phases were modelled as $P4mm$ phases.

From the phase diagram, it would be expected that the optimal composition for device applications would be around 60% KBT, as this is where the phase is seen to change, and piezoelectric properties increase in the region of phase transitions. It is strange that the actual improvement in piezoelectric properties is found at 40% KBT, a stable region far from any transitions. It should be noted again however that even at the locations indicated in the phase diagram, there is not a sharp phase transition; the BFO-KBT system is very stable with respect to both composition and temperature.

4.7.1 Contour Plots

Figure 4.33 shows the phase diagram constructed by combining the data from the compositional study in Chapter 3 and the thermal studies in Section 4.4. The contour lines represent the cubic percentage of the mixed phase, extrapolated from the Rietveld refinements, which are shown on the graph as the single points. Because of this, the contours will show a closer agreement to the data the closer they are to a point of datum. The Cubic-A and Cubic-B phases have been summed to give the total cubic contribution in this graph.

From the contour plot it can be seen that in the low KBT compositional region, below 500°C the percentage of cubic contribution to the total phase is relatively stable. At higher temperature, it can be seen that the contribution from the cubic phase increases rapidly until the structure can be represented entirely by the cubic phase with no need for a rhombohedral component. As the mol% KBT is increased, there is a rapid change between 15% KBT and 20% KBT, though no data points were actually taken between those materials so the exact nature of the change between them has not been characterised, but instead has been assumed in this plot to be essentially a linear progression.

Since lower mol% KBT samples are unlikely to reach the cubic phase before the risk of melting becomes prohibitive, it may not be possible to extend this phase diagram to lower mol% KBT samples in a meaningful way. In the higher KBT compositional region, the relatively stable region extends to around 400°C,

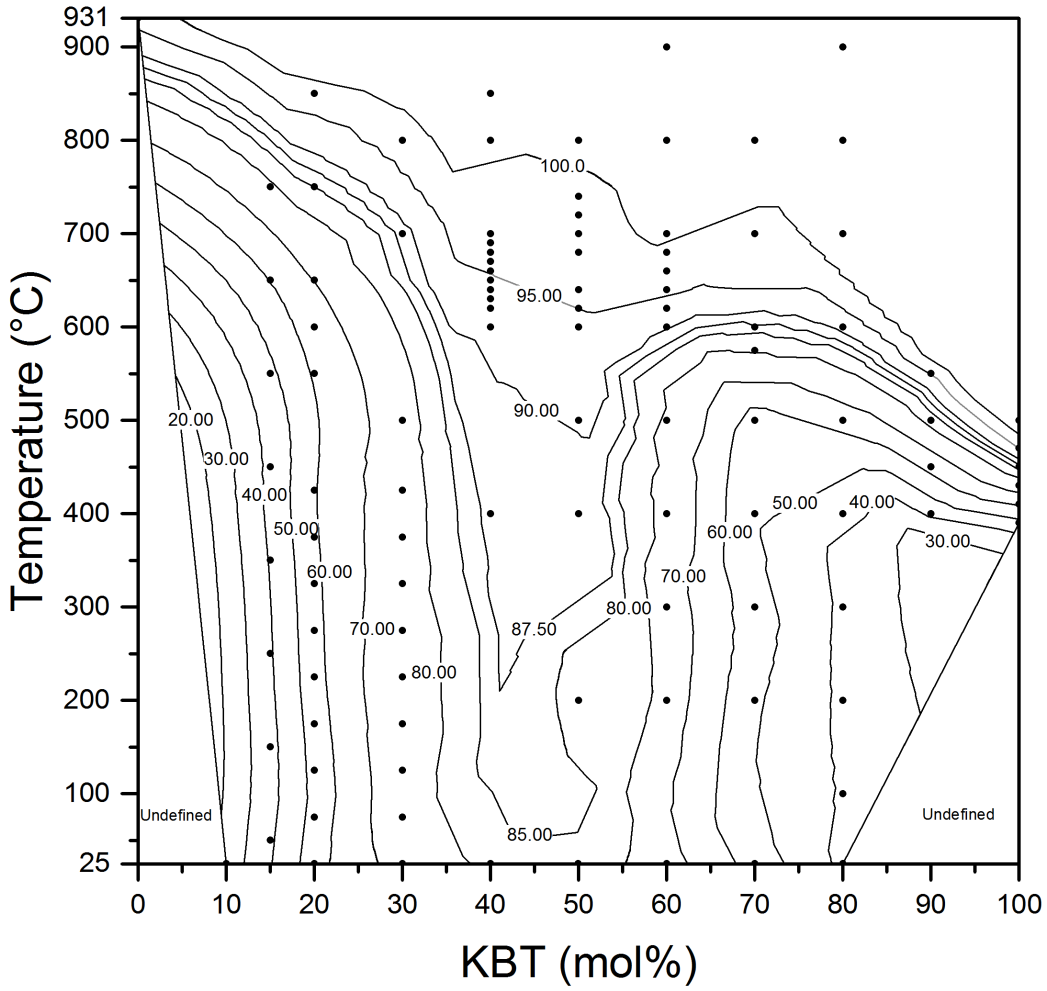

Figure 4.33: Contour plot of the phase diagram for the BFO-KBT system, displayed in terms of the cubic percentage of the mixed phase in the material. Cubic-A and Cubic-B have been summed together for this representation. This contour plot is extrapolated from the data gathered, which are represented as black spots; the further from these, the less reliable the data, so the graph can not be taken verbatim, but it does provide a visual representation of the change in phase composition with respect to temperature and chemical composition.

then showing a more rapid conversion to a fully cubic region. Cubic-A exists only at higher temperatures, normally of the order of 500°C, except in 60% KBT, which exhibited a splitting in the cubic peaks at much lower temperature. The Cubic-A phase percentage is quite stable with respect to temperature. Cubic-B by comparison exists at room temperature and its phase percentage can be seen to increase with increasing temperature.

At high temperature, the compositions of Cubic-A and Cubic-B are noted to change slowly with respect to changes in composition, with higher Cubic-A contributions at lower mol% KBT compositions and lower Cubic-A contributions at higher mol% KBT compositions. In all cases, Cubic-B is the dominant phase of the two. Cubic-A and Cubic-B phases were both modelled as $Pm\bar{3}m$ cubic phases.

As in the room temperature powder chapter, Chapter 3, it is useful to compare the results of the changes in the morphotropic phase boundary (MPB) seen in the BFO-KBT system with respect to changing temperature with other materials displaying an MPB. As the archetype material, it makes sense to first look at this system in comparison with $PbZr_{1-x}Ti_xO_3$ (PZT), using the phase diagram generated compared to a known phase diagram of the archetype material [13]. Comparing Figure 4.32 with the phase diagram described by Jaffe [13], displayed in Section 1.3.2, it can be seen that the phase transitions in BFO-KBT are less well defined than those found in PZT, with the differences between for instance the cubic and rhombohedral mixed phase and the cubic and monoclinic mixed phase being quite subtle, both appearing as almost cubic phases with small discrepancies. The change from cubic and monoclinic to tetragonal and monoclinic does appear better defined. In PZT, the short range order is known to expand to become the long range order around the phase transition [14] and in the BFO-KBT system the mixed phases observed are likely a result of short range order effects. The temperature range in which BFO-KBT is stable is greater than in PZT, which could be useful for high temperature device applications, and a combination of the properties of both materials would potentially be quite attractive, as researched by Bennett et. al [15].

In summary, the BFO-KBT system has proven to form a complicated phase diagram. No sharp phase transitions have been recorded, but at different compositions and temperatures, different models have been found to fit better, with gradual transitions between them. The high temperature part of the phase diagram shows a decline in the temperature at which the system ceases to have non-cubic phases with increasing mol% KBT, with an almost straight line possible to be drawn from the point at which BFO becomes cubic to the point at which KBT becomes cubic. It has two major compositional regions of its phase diagram; the low mol%

KBT region (up to and including 40% KBT), mixed rhombohedral and cubic phases stable with respect to temperature up to 500°C and rapidly forming a single cubic phase above this, and the high mol% KBT region (50% KBT and up), which phase separates at high temperature leaving a BFO-like cubic phase (Cubic-A) and a KBT-like cubic phase (Cubic-B). The high mol% KBT region is split into subregions dependant on the phase composition at room temperature. The 50% to 60% KBT subregion shows a similar low temperature phase diagram to the low mol% KBT compositional region, with the cubic part of the peak profile becoming split into two peaks at high temperature. This creates a three-phase region in the crossover between the room temperature mixed phase of rhombohedral and Cubic-B and the two-cubic Cubic-A and Cubic-B mixed phase at high temperature. The 70% and 80% subregion presents as a cubic and monoclinic mixed phase composition at room temperature and gradually forms into a Cubic-A and Cubic-B phase at high temperature. It passes through a region in which the phase composition is indeterminate between the end states. The 90% KBT subregion shows similarities with the KBT end member at room temperature, but forms into a Cubic-A and Cubic-B phase at high temperature. Here, the BFO-like Cubic-A phase has a significantly higher volume, comparable with the 60% KBT Cubic-B phase.

4.8 References

Bibliography

[1] Catalan, G., Scott, J. F., *Advanced Materials*, **21**:2463 (2009).

[2] Otoničar, M., Škapin, S. D., Jančar, B., Ubic, R., Suvorov, D., *Journal of the American Ceramic Society*, **93**:4168 (2010).

[3] Hagiwara, M., Fujihara, S., *Journal of Applied Crystallography*, **54** (2015).

[4] Li, Z. F., Wang, C. L., Zhong, W. L., Li, J. C., Zhao, M. L., *Journal of Applied Physics*, **94**:2548 (2003).

[5] Arnold, D. C., Knight, K. S., Morrison, F. D., Lightfoot, P., **027602**:1 (2009).

[6] Matsuo, H., Noguchi, Y., Miyayama, M., Suzuki, M., Watanabe, A., Sasabe, S., Mori, S., Torii, S., Kamiyama, T., **104103**:1 (2011).

[7] Zhang, W.-B., Deng, Y.-H., Hu, Y.-L., Han, K.-L., Tang, B.-Y., *Solid State Communications*, **142**:6 (2007).

[8] Krill, C., Haberkorn, R., Birringer, R., *Specification of microstructure and characterization by scattering techniques*, vol. 2 (2000).

[9] Zurbuchen, M. A., Lettieri, J., Fulk, S. J., Jia, Y., Carim, A. H., Schlom, D. G., *Applied Physics Letters*, **82**:4711 (2003).

[10] Barz, R., Neumayer, D., Majhi, P., Wang, C., Dey, S., *Integrated Ferroelectrics*, **39**:61 (2001).

[11] Mubarak, T. H., Azhdar, B., Hassan, K. H., Kareem, C. H., *International Journal of Innovative Research in Science, Engineering and Technology*, **03**:17034 (2014).

[12] Morozov, M. I., Einarsrud, M.-A., Grande, T., *Applied Physics Letters*, **101**:252904 (2012).

[13] Jaffe, B., Cook, W. R., Jaffe, H. L., in 'Piezoelectric Ceramics,' (136), (Academic Press, London; New York1971).

[14] Glazer, A. M., Thomas, P. A., Baba-Kishi, K. Z., Pang, G. K. H., Tai, C. W., *Physical Review B - Condensed Matter and Materials Physics*, **70**:1 (2004).

[15] Bennett, J., Bell, a. J., Stevenson, T. J., Comyn, T. P., *Applied Physics Letters*, **103**:152901 (2013).

Chapter 5

Single Crystal Investigation

5.1 Introduction

Single crystal x-ray diffraction measurements are an important tool in crystallographic structure determination, because in a single crystal diffraction experiment the equivalent Bragg peaks are indexed separately, meaning that distinguishing between similar space groups is more reliable than in powder diffraction. In powder diffraction, all symmetry equivalent reflections have the same d-spacing and thus are indistinguishable in a one dimensional powder pattern. This allows single crystal diffraction to more easily discern details such as whether a structure is centrosymmetric or not. In this case, however, the expected structure was already known, with the single crystal diffraction being used more as a separate confirmation of the powder diffraction results, though in single crystal diffraction it should be noted that refinement of the lattice parameters is less accurate than in powder diffraction.

During these refinements, it is important to know the chemical compositions of the materials in question, since the refinements will take place after absorption corrections and rely upon a least-squares fitting between modelled data and observed data. Significant changes in the absorption will alter the model greatly, and this absorption is reliant on the composition. In the BFO-KBT system, the higher the KBT quotient, the lower the absorption as the bismuth is the most absorbing component of the system. This work builds on the analysis from Chapter 3 and Chapter 4 which investigated the structure of the system through powder x-ray diffraction, so a good starting model for the structure in the BFO-KBT system was already obtained, and the nominal composition of the investigated crystals were checked with SEM measurements to confirm the composition. This was discussed

in Section 5.3.1.

The diffractometer used in this study was an Oxford Diffraction (now Rigaku Oxford Diffraction) *Gemini R* CCD diffractometer. Measurements taken on this system were then processed, first with the CRYSALIS PRO software [1] for data reduction, then with SHELXL [2] for the refinement of the structure. A refinement was also conducted in JANA2006 [3] to allow for the refinement of a mixed state of rhombohedral and cubic phases being present in the crystal and anharmonic thermal parameters. Diamond Light Source beam line i15 was utilised for the synchrotron measurements discussed in Section 5.3.5.

5.2 Refinement of End Members

In order to understand the end members of the mixed BFO-KBT system, BFO and KBT, these were initially determined through the same single crystal x-ray methods as would be used in the mixed material. A suitable BFO crystal was obtained from a sample grown by the group of Marin Alexe of the University of Warwick, with a KBT crystal later found in a crystallite system grown by a previous PhD student in the department, G. O. Jones, University of Warwick, 2002 [4] by a flux growth method, specifically spontaneous nucleation.

5.2.1 Structure Refinement of BFO End Member

The calculation of ideal size of a BFO single crystal was described in Section 2.2.1.1. This methodology resulted in a size of 50 µm for a wavelength of 0.0709 nm (molybdenum source), which was used throughout this chapter unless specifically noted otherwise. A larger single crystal of BFO was cut down to this size with a scalpel under an *Olympus SS61* microscope (zoom ratio: 6.7:1, zoom range: 0.67x-4.5x). Care was taken to find a crystal likely to be a single crystal by looking for optically homogeneous samples. While thicker samples were completely opaque, at the size scale investigated enough light was transmitted through the samples to judge whether they were likely a single crystal. The samples were cut to be as close to cubes as possible, to reduce the absorption corrections necessary in particular directions due to sample anisotropy, though most of the crystals tended towards thin plates. At the size scale investigated, most of the tools were significantly larger than the crystals being manipulated, with even the scalpel blade mostly crushing rather than cutting at that size. As such, clean cuts were rarely possible, meaning that actually cube-shaped samples could not be obtained. Fortunately, the empirical absorption corrections can take account of non-cubic shapes [5].

These crystals were then mounted on a *MiTeGen* head, which are of known diameter allowing an initial estimate of the size to be undertaken, with either vacuum grease or *Fomblin Y* (Sigma-Aldrich) to hold them steady for room temperature analysis. For low temperature analysis, a glass fibre was used to avoid ice forming on the sample, with the end of the fibre broken such that it formed a sharp point ensuring that the crystals would not be significantly smaller than the glass they were mounted on. The *MiTeGen* head or glass fibre were then attached to a goniometer head. Care was taken to position this in the centre of the x-ray beam, small adjustments made in the height of the crystal and the x and y directions, observed through a camera calibrated to have cross hairs in line with the beam, which ensured that the crystal was in focus and fully within the beam. Being in focus for the camera was also necessary for the absorption correction, as the faces needed to be constructed as discussed in Section 2.2.1.1.

A screening measurement was taken, to determine whether the crystal obtained may be suitable for diffraction and, if so, a further measurement was taken as a pre-experiment. Here it could be seen if there was obvious twinning in the sample, or if the crystal did not fit the expected structure well.

Once a suitable crystal was found, mounted and checked as described above, it was measured on the single crystal diffractometer for >12 hours in order to ensure that a sufficient signal to noise ratio was obtained. It was also necessary to take measurements with a high enough coverage to cover half of reciprocal space at room temperature, with another measurement later being taken in the same way at 200K.

5.2.1.1 Data Reduction

The data obtained were first processed in CRYSALIS PRO, a program from Rigaku made specifically to process the data from their diffractometers. First, the raw data were processed to identify peaks in the data through the internal tool in CRYSALIS PRO. These data were then used to construct a proposed lattice size and shape; in the case of the unmixed BFO sample, the constrained cell was found to be $a = 5.5881(9)$Å, $c = 13.856(3)$Å, with angles of 90° 90° and 120°, close to the parameters for BFO found in the literature of $a = 5.57874(16)$Å, $c = 13.8688(3)$Å [6], $a = 5.5799(3)$ Å and $c = 13.8670(5)$ Å [7]. The Ewald sphere was constructed, to see how well the proposed lattice fits the data in reciprocal space, where a good model should fit most of the peaks, and the remaining peaks should not form a second lattice, else the sample is twinned. The data itself can also be examined frame by frame, mostly done in this project to observe signs of twinning or of tilt peaks in measurements.

From this point, the data were further refined; given the parameters for the lattice determined already, a space group was determined, found to be $R3c$ from the tilt peaks seen in the unwarp images and the $R3c$ reduction giving the best R_{Int}, also in line with the findings in the literature [8]. Absorption corrections were carried out through CRYSALIS PRO using the Clark and Reid method [5], utilising the video of the sample being rotated to build the faces necessary for the correction during the refinalisation step. An R_{Int} factor of 8.5% was obtained and this was then output into SHELXL for further processing.

5.2.1.2 SHELXL Analysis

In SHELXL, the cell was constructed following the *International Tables for Crystallography* [9] for an $R3c$ cell, with the bismuth in the A-site position and the iron in the B-site position, surrounded by an oxygen octahedron. From this structure, an R_1 of <7% was obtained, which indicates a good refinement. The results were observed as a residual electron density difference map.

A residual electron density difference map based on $F^2_{obs} - F^2_{calc}$ shows the regions in a unit cell where the observed data is mismatched from the calculated model; peaks indicate that more electron density is required in the model, while holes indicate a surplus of electron density. One of the possible causes for these peaks and holes would be an incorrect structure; heavier atoms, excess atoms or excess occupancy in the model compared with the sample will result in holes, while lighter atoms, insufficient atoms or insufficient occupancy in the model compared with the sample will result in peaks. The structure of BFO is well known, and the atomic positions in Table 5.2 are consistent with prior refinements, shown in Section 5.2.1.4. This means that the peaks and holes in the residual electron density maps were not indications of missing or incorrect atoms, but rather indicate thermal motion, which in the other samples would also include the disorder from the shared sites.

This map is shown in Figure 5.1; the maximum was 8.6 electrons $Å^{-3}$ and the deepest hole was -5.7 electrons $Å^{-3}$. The red represents a density of 2 electrons $Å^{-3}$, the blue represents a hole of -2 electrons $Å^{-3}$ and the green represents a hole of -4 electrons $Å^{-3}$.

Multiple phenomena could result in residual electron peaks like those seen in Figure 5.1, with large amounts of residual electron density around the A-site and B-site. One possibility is that they could be due to an inadequate absorption correction, as bismuth containing substances are well absorbing, requiring a very small sample size. Furthermore, different diffraction angles are subject to different levels of absorption, which may not be fully rectified even with a faces absorption

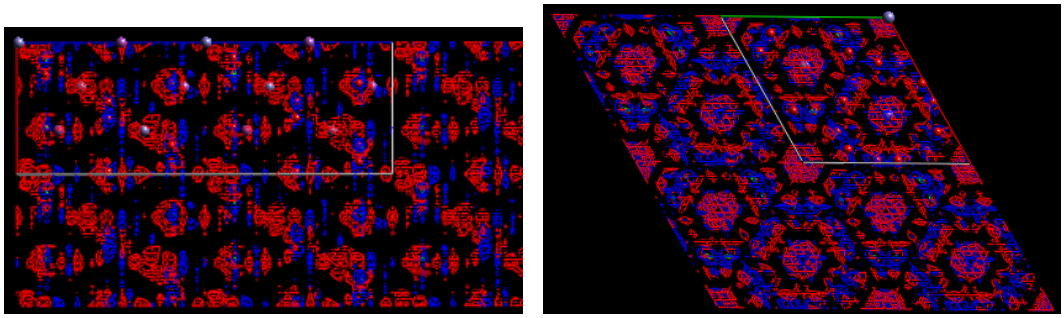

(a) (100) **(b)** (001)

Figure 5.1: Residual electron density Fourier map of a room temperature sample of unmixed BFO in MARCHING CUBES ELD[10]. It can be seen that there is a lot of residual electron density both above and below the bismuth position. The red represents a density of 1.5 electrons $Å^{-3}$, the blue represents a hole of -1.5 electrons $Å^{-3}$ and the green represents a hole of -4 electrons $Å^{-3}$. A single unit cell is highlighted.

correction. Another possibility is that the peak could be a result of anharmonic thermal parameters, which when fitted with harmonic thermal parameters would lead to patterns of residual electron density being observed around the atomic positions, which was observed. This hypothesis was tested in JANA2006 [3], but when the room temperature BFO samples were refined with anharmonic thermal parameters, no improvement was found, both in the R-factors and in the residual electron density. Since the anisotropic thermal parameters showed no signs of deviations from a spherical shape it was thought that anharmonic parameters would be unlikely to improve the refinement as you would expect to see highly anisotropic parameters in the case of anharmonic refinement, but it was still possible.

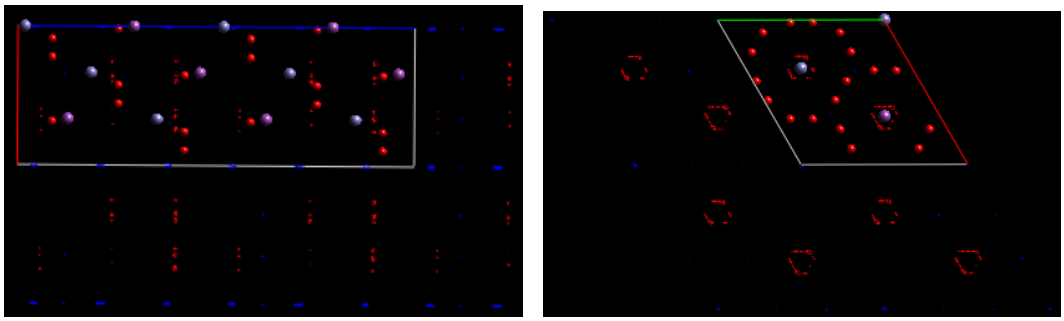

(a) (100) **(b)** (001)

Figure 5.2: Residual electron density Fourier map of the same sample of unmixed BFO as in Figure 5.1, now at 200K. In contrast to Figure 5.1, the electron density around the bismuth position is comparable to background noise. The scale is the same as before; the red represents a density of 1.5 electrons $Å^{-3}$ and the blue represents a hole of -1.5 electrons $Å^{-3}$. The green is no longer present. A single unit cell is highlighted.

Table 5.1: Tilt parameters from Megaw and Darlington [11] and Fischer *et al.* [12] compared with the calculated values from Table 5.2.

Parameter	Table 5.2	Megaw [11]	Fischer [12]	Table 5.2	Fischer [12]
Temperature (K)	273	273	273	200	77
ω	11.6(3)°	10.6°	12.2(2)°	12.5(2)°	12.3(2)°
d	-0.004(2)	-0.004	-0.0043(3)	0.003(2)	-0.0045(3)
s	0.041(2)	0.045	0.0487(5)	0.041(2)	0.0493(6)
t	0.016(2)	0.017	0.0196(5)	0.015(2)	0.0203(6)

5.2.1.3 Low Temperature BFO Analysis

A measurement on a BFO crystal was completed at low temperature (200K) over the course of 54 hours, to investigate whether the residual electron density peaks may be thermal in nature. The measurement was processed and refined in the same way as above. Comparing this again with the results in Table 5.1 shows that there is generally a good agreement between the atomic positions determined for the sample and those determined by published papers for other low temperatures. It was necessary to switch from harmonic ADPs for the iron to isotropic since the parameter becomes very small at this temperature. This prevents it refining well, leading to non-positive-definite (NPD) parameters, which are non-physical.

The low temperature SHELXL refinement was otherwise conducted in the same way as the room temperature refinement. This gave an R_{int} factor of <6% while the SHELXL refinement was conducted in the same way, using the prior atomic positions as a template, which produced an R_1 of <6%. The residual electron density peaks surrounding the A-site were greatly reduced to approximate background levels, seen in Figure 5.2. With the improved R_1 value, and the decreased presence of residual electron density, it can be said with some level of confidence that this disorder was thermal in nature. The residual electron density maximum was 2.7 electrons $Å^{-3}$, while the deepest hole was -1.7 electrons $Å^{-3}$.

5.2.1.4 BFO Refinement Comparison with Literature

Table 5.2 shows the SHELXL refinement outputs from the room temperature and low temperature refinements, allowing them to be easily cross referenced with examples from the literature. These are compared with the Megaw tilt parameters (see Section 2.2.2.3) in Table 5.1 as these provide a compact way to compare results.

Comparing the room temperature set of atomic positions with the work of Megaw *et al.* [11], it can be seen that the tilt peaks resolved from the BFO measurement are in good agreement with the expected positions. Comparing these

Table 5.2: BFO end member SHELXL refinement parameters tabulated.

Temperature (K)	293	200
Lattice Parameters		
a (Å)	5.5837(5)	5.582(5)
c (Å)	13.821(2)	13.808(1)
Quality Parameters		
R_{int}	8.50	7.10
R1	6.41	4.53
GoF	1.13	1.02
Highest Peak (electrons $Å^{-3}$)	8.69	2.4
Deepest Hole (electrons $Å^{-3}$)	-5.51	-1.0
Refined Parameters	16	10
A		
$x = y = 0, z =$	0.291(2)	0.291(2)
Ueq/Beq ($Å^2$)	0.0211(5)	0.0145(6)
$U_{11} = U_{22}$	0.0207(5)	0.0141(7)
U_{33}	0.0221(8)	0.015(1)
$U_{23} = U_{13}$	0	0
$_{U12}$	0.0103(3)	0.0070(3)
B		
$x = y = 0, z =$	0.016(2)	0015(2)
Ueq/Beq ($Å^2$)	0.013(1)	0.005(1)
$U_{11} = U_{22}$	0.011(2)	-
U_{33}	0.017(3)	-
$U_{23} = U_{13}$	0	-
$_{U12}$	0.0057(8)	-
O		
x	0.235(5)	0.225(5)
y	0.351(7)	0.322(8)
z	0.083(0)	0.083(0)
Ueq/Beq ($Å^2$)	0.031(5)	0.010(5)
U_{11}	0.03(1)	-
U_{22}	0.02(1)	-
U_{33}	0.04(1)	-
U_{23}	-0.00(1)	-
U_{13}	0.01(1)	-
U_{12}	0.01(1)	-

with the work of Fischer *et al.* [12] which used neutron diffraction (which has better oxygen sensitivity) it can be seen that the room temperature measurement is also in good agreement with their findings.

Comparing the low temperature results are more difficult; there are few low temperature BFO structural measurements, and fewer still that use the location conventions necessary to calculate Megaw tilt parameters. Thus, to compare the results taken at 200K, the results from Fischer *et al.* at 77K have been used to add a lowest bound along with the room temperature measurements; the 200K measurements would be expected to be within these bounds. These are generally in good agreement with the exception of the d parameter. It was necessary to move from harmonic to isotropic ADP values for the B-site at low temperature, since the values were very low in isotropic form and gave NPD values for harmonic refinements.

5.2.2 Structure Refinement of KBT End Member

The KBT crystals by contrast to the BFO crystals were not available as single phase pure crystals. It was determined by crushing a selection of these crystals into a fine powder and using powder diffraction that KBT single crystals were likely present amongst the mixed crystals and indeed seemed to be the main component of the powder, but there were also other phases present. It was important to determine that the samples chosen were actually phase pure KBT before much time was invested into measuring or analysing them, adding an additional step to the selection when compared with the BFO and BFO-KBT crystals. The first part of this was to involve the use of birefringence in the crystal selection, looking for single birefringent crystals in the clusters of crystals observed. The crystals thus obtained were extremely small, suitable for single crystal diffraction but not for experiments with a birefringence microscope.

The most likely crystals were then measured in pre-experiments on the diffractometer to determine the lattice parameters. KBT is reported as having $P4mm$ tetragonal structure, with lattice parameters $a = 3.9247(0)$Å and $c = 3.9844(3)$Å [13] or $a = 3.933(3)$Å and $c = 3.975(4)$Å [14], but was found in Chapter 3 to have lattice parameters or $a = 3.9184(2)$Å and $c = 4.0146(2)$Å , quite different from the measurements quoted above. In addition to this, KBT was found to have a mixed phase of tetragonal $P4mm$ and monoclinic $P1m1$. Due to the small tetragonal and monoclinic deviation from cubic, the simplest method was to find near-cubic crystals and then observe how well they would fit with the expected KBT cell. An example of this type of crystal was found, and measured in the same way

as the BFO crystal mentioned in the prior section had been.

An R_{int} factor of 5.9% confirmed that the suggested tetragonal structure was a reasonable fit with the data as far as the reduction and refinalisation processes in CRYSALIS PRO were concerned, including absorption corrections.

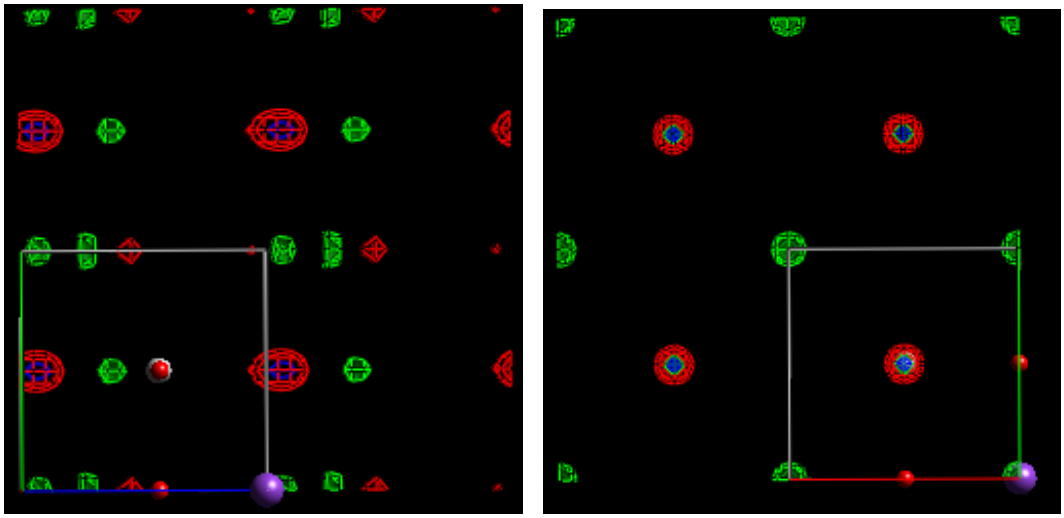

(a) (100) **(b)** (001)

Figure 5.3: Residual electron density Fourier map of a room temperature sample of unmixed KBT. It can be seen that there is a lot of residual electron density both above and below the bismuth position. The red represents a residual electron density of 4 electrons $Å^{-3}$ and the blue represents a residual electron density of 8 electrons $Å^{-3}$, while the green represents a hole of -3 electrons $Å^{-3}$.

Refining this output structure with SHELXL was attempted, but it was not possible to get the R_1 factor <14%, which implied that the refinement would not be resolved by this method. It is hypothesised that this was because of the mixed Bi-K atoms on the A-site, which adds an inherent level of disorder to the system. Figure 5.3 shows the residual electron density of the sample in MARCHING CUBES ELD[10]. The highest residual density was found to be around 9 electrons $Å^{-3}$, which was around the oxygen position on the [001] face and the deepest hole was found to be around -5 electrons $Å^{-3}$ around the A-site and B-site, distributed along the z-axis.

Unlike in the BFO crystal, this disorder was not decreased significantly by reducing the temperature to 200K. This can be seen in Figure 5.4, and from Table 5.3 comparing the room temperature and low temperature refinements. In the lower temperature KBT measurement, the same scale was used as in the room temperature version, meaning that while the residual electron density map seems more complicated, the highest residual electron densities in blue are diminished with

Table 5.3: KBT end member SHELXL refinement parameters tabulated.

Temperature (K)	293	200
Lattice Parameters		
a (Å)	3.9213(4)	3.9288(8)
c (Å)	3.9960(8)	3.960(1)
Quality Parameters		
R_{int}	6.70	8.10
R_1	14.32	15.44
GoF	3.17	4.964
Highest Peak (electrons Å^{-3})	9.45	9.55
Deepest Hole (electrons Å^{-3})	-5.79	-4.67
Redundancy	7.1	26.5
Completeness	100% (0.8)	100% (0.8)
Refined Parameters	14	14
A		
$x = y = 0, z =$	-0.002(2)	-0.004(2)
Ueq/Beq (Å^2)	0.073(5)	0.043(3)
$U_{11} = U_{22}$	0.057(3)	0.035(2)
U_{33}	0.011(1)	0.060(6)
$U_{23} = U_{13} = U_{12}$	0	0
B		
$x = y = 0, z =$	0.563(3)	0.507(2)
Ueq/Beq (Å^2)	0.017(2)	0.010(1)
$U_{11} = U_{22}$	0.015(2)	0.010(2)
U_{33}	0.020(4)	0.0122(3)
$U_{23} = U_{13} = U_{12}$	0	0
O1		
x	0.5	0.5
y	0	0
z	0.59(1)	0.61(1)
Ueq/Beq (Å^2)	0.041(8)	0.027(7)
U_{11}	0.02(1)	0.02(1)
U_{22}	0.02(1)	0.004(9)
U_{33}	0.08(2)	0.05(2)
$U_{23} = U_{13} = U_{12}$	0	0
O2		
$x = y = 0.5, z =$	0.14(5)	0.12(2)
Ueq/Beq (Å^2)	1.1(3)	0.17(3)

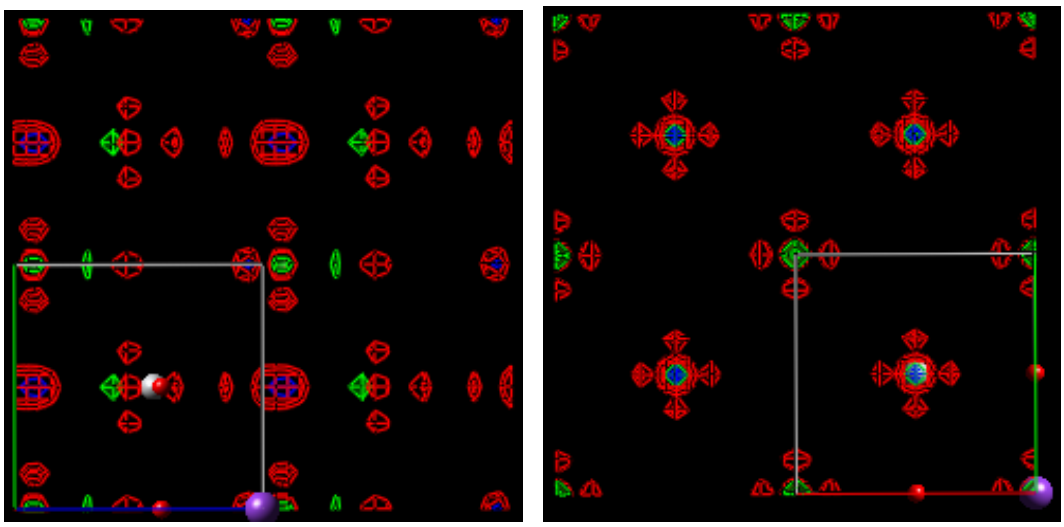

(a) (100) **(b)** (001)

Figure 5.4: Residual electron density Fourier map of a 200K sample of unmixed KBT. It can be seen that there is a lot of residual electron density both above and below the bismuth position. The red represents a residual electron density of 4 electrons $Å^{-3}$ and the blue represents a residual electron density of 8 electrons $Å^{-3}$, while the green represents a hole of -3 electrons $Å^{-3}$.

lower temperature. The R-factors between the two are very similar though, as there is still very high disagreement between the observed and calculated models. In the 200K residual electron density map, there is more distribution along the x-axis and y-axis, but the majority can still be seen to be along the z-axis, with the highest residual density being in a similar position. The highest density and deepest hole were of comparable sizes to the room temperature measurement.

In summary, the refinement of the KBT crystals as a single tetragonal phase was not successful. With the model proposed in Section 3.4.1 the poorness of the simple fit was expected, as it doesn't take account of the significant volume of monoclinic phase found to exist in the powder sample, which is likely also present in the single crystal. The tabulated data from these measurements is included in Section 5.4.

5.3 Structure Refinement of BFO-KBT Crystals

The analysis of the BFO-KBT crystals was more complicated than the unmixed BFO crystal refinements. The starting model from Chapter 3 meant that the nature of the crystals were known, like the KBT crystals, to be more complex than the BFO crystals, consisting of two phases which would be difficult to separate in a single

Table 5.4: BFO-KBT crystal nominal compositions in mol% KBT for the different designations of crystal used in this project. The 3A and 2B crystals are the most heavily used.

Designation	Nominal Composition
1A	40
1B	40
2A	36
2B	36
2C	36
3A	32
3B	32

crystal refinement.

5.3.1 Introduction of BFO-KBT Crystals Used

The KBT-BFO crystals used in this study are nominally between 30% KBT and 40% KBT (0.32, 0.36, 0.4 crystals were available, with 2-3 of each nominal composition) and so was in the region where prior research suggested there would most likely be a shift from rhombohedral to a pseudocubic regime. However, as discussed in Chapter 3 and Chapter 4, this region actually corresponds to a stable mixed phase of rhombohedral and cubic phases with little structural variation relative to composition, which is dominated by the cubic phase.

Table 5.4 shows the crystal designations matched with the nominal compositions of those crystals, in terms of the mol% KBT. The crystals were grown by Noguchi's group at Tokyo University by flux growth. Flux growth has the potential to result in crystals which vary from their nominal composition, so it was important to check the actual composition before absorption corrections could be carried out. This used the same measurement and calculation methods of Section 3.2.2, using EDX measurements to test the nominal compositions.

Table 5.5 shows the results of one such experiment on the 3A crystal, highlighted since it was one of the most experimented-upon samples. Compared with the powder samples, the single crystal measurements had more variance and thus higher uncertainty in their exact composition on average, as can be seen from the spread of results from 32% KBT to 40% KBT. While the powder uncertainties were ±2-4%, the single crystals are ±4-8% as well as being further from the nominal compositions. The nominal value for this sample was 32% KBT, but the SEM measurements place the composition around 36% ±4%. The uncertainty range

Table 5.5: BFO-KBT 3A crystal composition by SEM, compared with the mol% KBT that this composition implies. It can be seen from this that compared with the powder SEM results, the uncertainties in the single crystal results are much larger. Uncertainty represented as 1 Standard Deviation of the data.

Element	Composition %	KBT %
Bi	40.1(4)	40
K	09.0(4)	36
Ti	16.9(8)	34
Fe	34.0(9)	32

means that the single crystal samples lie somewhere between 30% KBT and 40% KBT, which is a stable region in terms of the phases from Chapter 3, but could have had some effect on the absorption corrections. The high uncertainties were caused by charging in the sample from the electron beam, which means a low conductivity in the crystal samples, unlike unmixed BFO samples.

In summary, it was known from Chapter 3 and Chapter 4 that for the compositions the single crystal samples represented, the diffraction pattern would be mostly cubic. The resolution on a single crystal diffractometer is not sufficient to discern the overlapping peaks of the rhombohedral phase and the pseudocubic phase, though the additional rhombohedral intensity was still expected to result in high residual factors in the refinements.

5.3.2 Data Reduction

The basic operations used to determine the structure of the BFO-KBT crystals were the same as those used for the determination of the end member crystals; single crystals of BFO-KBT were isolated and cut down to size, mounted on a goniometer and measured with the *Gemini R* single crystal CCD x-ray diffractometer. The data from these measurements were then reduced in CRYSALIS PRO and then further processed.

In CRYSALIS PRO, the unit cell was obtained as it was in unmixed BFO and unmixed KBT. From the raw data measurements, the data looked like they should fit to a cubic lattice well, so initial fits began by attempting to fit the crystal to a cubic structure. As other structures were tried, this step was repeated with each of those structures: cubic, tetragonal, rhombohedral and monoclinic.

The cubic lattice parameters were found to be $a = b = c = 3.9631(7)$Å, $\alpha = \beta = \gamma = 90.0°$. Following this, the shape of the crystal was determined from the video taken at the beginning of the data collection, the results of which were

Table 5.6: BFO-KBT crystal structures and the R_{int} and R_1 factors for 3A crystal output as a result of different lattice types, $Pm\bar{3}m$, $P4mm$, $R3c$ and $P1m1$.

Structure	R_{int}	R_1
Cubic	9.8	19.4
Tetragonal	8.4	18.3
Rombohedral	9.5	19.8
Monoclinic	8.0	19.5

then used to construct the polyhedra nescessary for the Clarke and Reid method for absorption correction [5]. The R_{int} for these fits were calculated and are represented in Table 5.6.

5.3.3 SHELXL Analysis

In SHELXL, again similar to the unmixed BFO and unmixed KBT samples, the atomic locations within the cell were determined from the space group and least-squares refinements. It was known that the potassium and bismuth would share a site, as would the titanium and iron, so these constraints were used in the refinements.

The 3A crystal was refined with different structures; first with cubic, which has the most constraints in its atomic positions, then with tetragonal which allowed some freedom in the z-axis, then with a rhombohedral cell, and finally with a monoclinic cell. Despite having the most freedom of movement, this still had a very high R_1 value. These were based on the other phases seen in Chapter 3, so were $P4mm$, $R3c$ and $P1m1$ respectively. The R_1 factors, displayed in Table 5.6, are all above 18, which is unreasonably large, and show little difference between them. Ultimately, from the powder measurements it was most likely that the structure would be some mix of cubic and rhombohedral, with cubic as the majority, so these were the refinements which were focused on.

The Fourier difference maps of the models were examined, looking for clues about the structure; all of the residual electron density tended to be focussed around the disordered A-site and B-site, suggesting it was the nature of the disorder that was preventing a good refinement. This was especially true around the A-site, but was also observed around the B-site, seen in Figure 5.5a. There was a significant amount of residual electron density around each atom, especially the A-site and B-site atoms, forming shells of excess intensity up to 25 electrons $Å^{-3}$ and holes as deep -6 electrons $Å^{-3}$, which is an extremely high variance, meaning a large disagreement between the model and observed data.

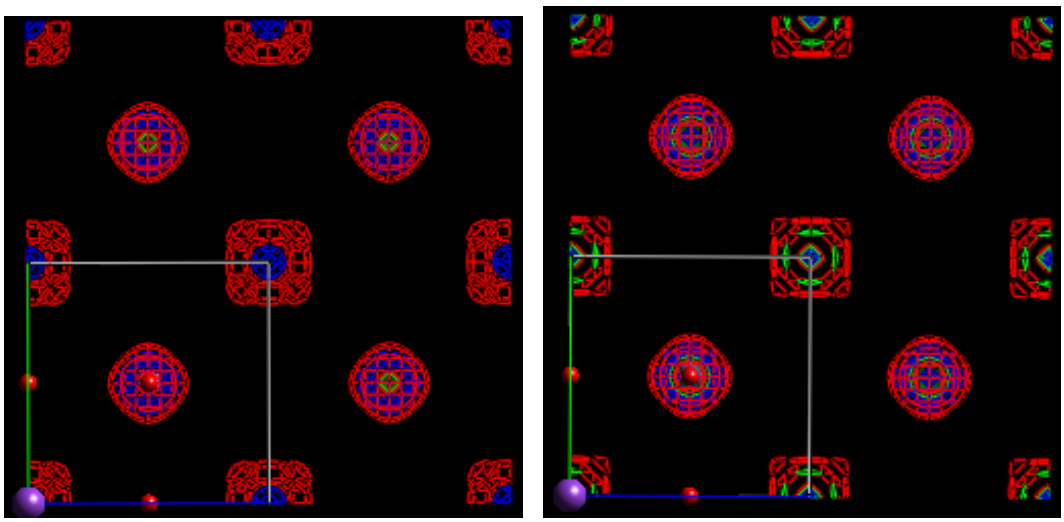

(a) (100) Room temperature. **(b)** (100) 100K.

Figure 5.5: Residual electron density Fourier map of a room temperature (Figure 5.5a) and 100K (Figure 5.5b) measurement of BFO-KBT 3A. It can be seen that there is a lot of residual electron density both above and below the bismuth position. The red represents a residual electron density of 5 electrons $Å^{-3}$ and the blue represents a residual electron density of 10 electrons $Å^{-3}$, while the green represents a hole of -5 electrons $Å^{-3}$. The maximum residual electron density was at 25 electrons $Å^{-3}$. Being cubic, the (010) and (001) directions are identical.

A low temperature measurement was taken to observe whether this improved the data fit, but unlike unmixed BFO, this did not improve the fitting of the data in the Fourier maps. At low temperature there were still large amounts of electron density around the Bi/K position, and the Fe/Ti positions, which can be seen in Figure 5.5b. This is similar to the result found in unmixed KBT; the shells are still present around the A-sites and B-sites, and the highest residual density and deepest hole values were very similar.

It was found that the lower temperature measurement did not significantly decrease the disagreement between the observed data and the calculated model, even 100K below where the residual electron density in BFO was found to diminish to background levels. Therefore other potential models for the residual electron densities seen had to be considered.

A wider integration mask for each peak in a frame was used in an attempt to suppress the observed disorder, since it was possible that there was some variance in the peak positions which was being missed with the default size. However, this was not found to improve the data.

Since it is known that BFO-KBT could exhibit some form of nano-region structure [15, 16], which would complicate attempts to refine as any one structure, it

was suggested to split the data such that reflections that would be expected in cubic but not rhombohedral structures could be refined, with the remaining reflections being used to determine the other structure. Unfortunately, once these data were removed, there were insufficient data left to work with for either phase, so this method provided no insights into the refinement and even if there had been sufficient data remaining they would have had too low a resolution to properly separate the phases. A different technique to investigate this is discussed in Section 5.3.4.

There was also some consideration about the absorption of the samples, so some experiments were also run on the higher intensity diffractometer which allowed for a smaller sample size to be used, and thus less absorption. These measurements did not successfully decrease the disorder in the system. This was also the reasoning behind the synchrotron measurements discussed further in Section 5.3.5.

5.3.4 JANA2006 Analysis

Further analysis was proposed using the program JANA2006 [3], which allows for multiple crystalline phases to be refined in one measurement. In the powder diffraction measurements, multi-phase analysis had been shown by Rietveld refinement to improve the fit of the data, so needed to be implemented here for the single crystal data as well.

Since it was known from the powder diffraction measurements that the structure in the compositional range represented by the single crystals would be dominated by the cubic structure, the data was reduced in CRYSALIS PRO first as a $Pm\bar{3}m$ cubic structure, though no diffraction data were rejected. The CRYSALIS PRO data reduction otherwise proceeded as normal. The HKL files were then imported to JANA2006, and the cell was constructed manually from the 30% and 33% KBT powder diffraction refinements.

Once the basic cell was completed, the atoms were added in; since all of the atoms were on special positions, the information could again be taken from the refined model, which had been taken from the *International Tables of Crystallography* [9]. This cubic-only structure was initially refined with the A-site and B-site atomic positions and thermal parameters linked appropriately. The refinement for an entirely cubic structure in JANA2006 was not found to provide an improvement over the same refinement in SHELXL. Checking the internal residual electron density visualisation software in JANA2006, it was also clear that the residual electron density was comparable to that found in SHELXL refinements.

The second phase was added once the model quality was shown to be comparable to the SHELXL models produced. The new phase was added to the

model, with the $R3c$ rhombohedral lattice parameters from the same powder diffraction refinements. In addition, a matrix is needed to convert from the hexagonal-based rhombohedral cell to the cubic cell, shown with the inverse in Equation 5.1. The proposed cell from the matrix acting on the cubic cell was checked to ensure that the proposed cell agreed well with the known rhombohedral cell. This was found to be the case.

$$M_{Cubic\rightarrow Hex} = \begin{bmatrix} \overline{1} & 1 & 0 \\ 0 & \overline{1} & 1 \\ 2 & 2 & 2 \end{bmatrix} \qquad M_{Hex\rightarrow Cubic} = \begin{bmatrix} \overline{\frac{2}{3}} & \overline{\frac{1}{3}} & \frac{1}{6} \\ \frac{1}{3} & \overline{\frac{1}{3}} & \frac{1}{6} \\ \frac{1}{3} & \frac{2}{3} & \frac{1}{6} \end{bmatrix} \tag{5.1}$$

The atom positions were then added in to the rhombohedral cell from the positions in the powder diffraction refinement. The A-site atoms and B-site atoms in the second phase were linked in position and thermal parameters, and both phases were refined together. It was found that this refinement did not improve the R-factors and in fact made them worse on many attempts. When checked against the residual electron density maps no significant improvements were observed. Multiple attempts were made at these refinements, but ultimately since the refinements produced were no better than the SHELXL refinements, the mixed models in JANA2006 were not able to successfully describe the observed data.

5.3.5 Synchrotron Measurements

One of the largest potential issues with characterising a material with heavy atoms is absorption. The use of a higher energy x-ray beam, such as the beam available at a synchrotron, can provide a better way to examine the material.

A crystal of 2B BFO-KBT was examined on the I15 beam line at Diamond Light Source. The beam wavelength was 0.2227Å, which meant that the absorption coefficient was an order of magnitude lower, being 5.52 mm^{-1} instead of 63.9 mm^{-1} obtained with the molybdenum sources used in previous experiments. This meant that the data gathered at the synchrotron was far less susceptible to absorption effects. Technical issues during data collection meant that the data coverage and redundancy were lower than intended (100% of necessary data coverage and 8.2 respectively for cubic, 70% of necessary data coverage and 4.0 for rhombohedral). This meant that it was not possible to use the data obtained to refine a rhombohedral cell, as resolving a rhombohedral cell requires a hemisphere of reciprocal space to be collected in order to have sufficient data to resolve each of the Bragg peaks present in a rhombohedral structure. There was enough data to refine a cubic model from the data. The R_{int} of this model for the 2B BFO-KBT crystal examined was 10.2,

which was comparable to the R_{int} obtained from the laboratory-based equipment for a 3A BFO-KBT sample.

The synchrotron equipment did not allow the capturing of a video necessary for absorption correction calculations via the Clark and Reid method [5]. In order to simulate this, the samples used had videos taken on the equipment in the lab which did allow for these videos to be made. These were then matched up with the orientation of the crystal at the beam line by two stills of known orientations 90 degrees apart. The videos from the lab-based system were modified manually to correspond to the correct angles on the synchrotron system, and faces were drawn on in CRYSALIS PRO as normal.

The data were refined in SHELXL as prior data had been, and were found to have an R_1 of 5.6%, which was a significant improvement over previous experiments. It was noted, however, that residual electron density pattern obtained was similar to the ones obtained from the laboratory experiments, though now more detailed and of lower intensity. Whereas before, simple spherical shells of residual electron density and holes were observed, there were now lobes of each arranged around the A-site and B-site. It was decided to utilise the anharmonic refinement method in JANA2006 to investigate whether these could be mitigated. The maximum residual electron density peak and deepest hole in these syncrotron measurements are compared in Section 5.4 and it can be seen that this lower intensity corresponds to the lower R_1 value.

The JANA2006 refinement was conducted on a reduction output directly from CRYSALIS PRO. The data was loaded as normal, and the structure was input into JANA2006 in a form consistent with the *International Tables of Crystallography* [9] and the output from CRYSALIS PRO for the lattice parameters. The A-site atoms were linked together, as were the B-site atoms, both in position (though they were both on special positions) and thermal parameters.

The structure was refined first with harmonic thermal parameters, to give a baseline for the refinement. A 4th rank tensor was used for the A-site and B-site anharmonic thermal parameters, based on the system described by Yamanaka *et al.* [17], which allowed the residual electron density to be fitted well. The O position was still represented by an isotropic thermal parameter.

While the residual electron density was decreased by this refinement, the R_1 factor was increased slightly rather than improved. This increase was small, so it is possible that the uncertainty allowed by the harmonic thermal parameters were masking errors in the data, the parameters swollen in some way which overrode a more subtle difference on average.

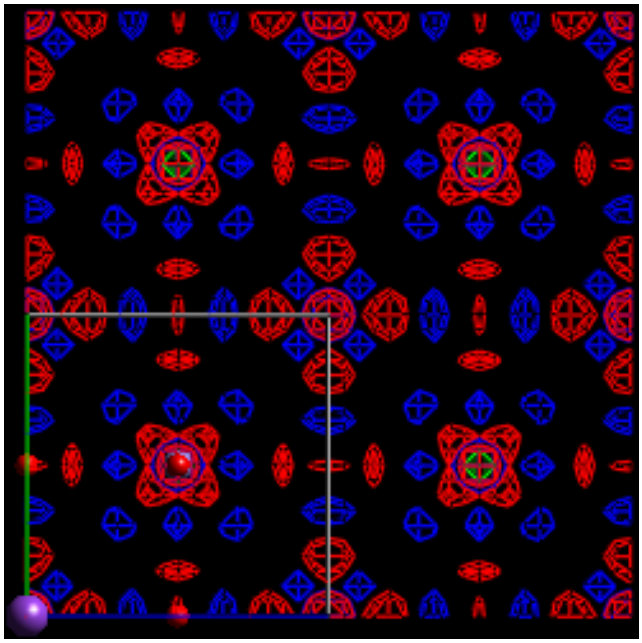

(a) Harmonic thermal parameters.

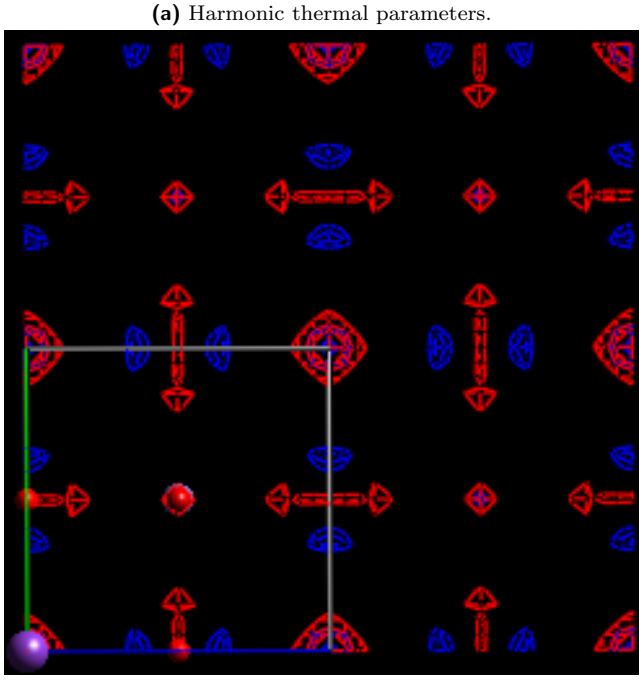

(b) Anharmonic thermal parameters (4th rank tensor).

Figure 5.6: Comparison between the harmonic (Figure 5.6a) and anharmonic (Figure 5.6b) residual electron density graphs for the 2B crystal investigated at the synchrotron, viewed along the {001} direction of the $Pm\bar{3}m$ structure. In these diagrams, the green areas correspond to regions with -3 electrons $Å^{-3}$, blue corresponds with regions showing -1 electrons $Å^{-3}$, and red showing regions of +1 electrons $Å^{-3}$. Both diagrams show 4 cells. At the bottom left, one of these cells is highlighted.

Figure 5.6 shows a comparison between the synchrotron data fit with harmonic thermal parameters (Figure 5.6a) and anharmonic thermal parameters (Figure 5.6b). In both cases, 4 unit cells are shown. One single cell is highlighted at the bottom left of the images. The different colours represent specific contours; the green corresponds to the deepest holes of at least -3 electrons $Å^{-3}$. It is notable that the anharmonic thermal parameters do not produce holes so deep. The blue corresponds with significant holes of at least -1 electrons $Å^{-3}$, while the red corresponds with significant residual electron density of at least +1 electrons $Å^{-3}$. It is notable that even with the harmonic thermal parameters, the values of the residual electron densities are far lower than those found in the earlier lab-based measurements, such as those in Figure 5.5a, with a maximum residual electron density around 2 electrons $Å^{-3}$ and a deepest hole of -1.5 electrons $Å^{-3}$ in SHELXL.

Starting with the harmonic thermal parameters from Figure 5.6a, there are many interesting features to be found in the residual electron density. First, examining the B-sites, the largest holes, in green, correspond directly with the B-sites. These sites are surrounded by positive electron density arranged as a body-centred cube, with lobes at the corners. This body-centred cube is itself surrounded by a cube of negative electron density, with lobes at the corners as well as along each edge. There is a distant octahedron of positive electron density around this.

Examining the A-sites, there is nothing about the 1 electrons $Å^{-3}$ threshold at the actual A-site itself, but surrounding it is first a cube of negative electron density, with nodes on the corners. Outside of this is an octahedron of positive electron density, with the highest residual electron density found at the centre of these octahedral nodes above 2 electrons $Å^{-3}$.

There is no residual electron density above the 1 electrons $Å^{-3}$ threshold or holes below the -1 1 electrons $Å^{-3}$ threshold on the O-site. There are regions of increased residual electron density surrounding them however.

The residual electron density lobes and holes in the harmonic refinement correspond to specific crystallographic directions. In the B-site, the closest lobes correspond to the {111} directions. The {110} directions show a set of holes and distant lobes that could correspond to a different atom. There are also lobes in the {100} directions, though these are closer to the oxygen atoms so could correspond to these instead. In the A-site, the {111} direction corresponds with a set of holes. The {110} direction has no obvious relation to the residual electron density. The {100} direction has nearby lobes, with further holes beyond this and a distant lobe equally places between the A-sites in the {100} direction.

Comparing this to the refinement with anharmonic thermal parameters in

Figure 5.6b, it's immediately clear that there is less in the residual electron density at the thresholds chosen. Starting again from the B-site positions, these now show much smaller holes, around -1 electrons $Å^{-3}$. The green, deeper holes, are not present in the anharmonic model at all. The B-sites are surrounded be a distant octahedron of positive electron density, approximately 1 electron $Å^{-3}$.

The A-sites in this system show the highest positive residual electron density, over 2 electrons $Å^{-3}$. There is little over the threshold examined here immediately surrounding the A-sites, although it could be argued that the holes near the O positions may be related to the A-site, since they can be formed into an octahedron around this site.

The O-site has a flat disc of residual electron density around the position of the O atom, with edges towards the B-site. On either side of this disc, towards the A-site, is a hole, meaning that the flat side of the disc is facing a hole on each side.

In the anharmonic refinements, in the B-site there is nothing in the {111} direction, nor arguably in the {110} direction, though it's possible that one of the lobes attributed to another atom could be related here, despite being so distant that it's on the edge of the cell. In the {100} direction, there is a distant lobe, though this is much closer to the oxygen position. In the A-site, there is a minor lobe on the A-site itself, which shows no true direction. In the {100} direction, there is a distant hole, followed by a more distant lobe equidistant between the A-site positions. The lobes and holes in the {100} directions in both A-site and B-site correspond roughly with those of the harmonic refinement.

From this, it can be agreed that most of the directional features around the A-site and B-site have been accounted for by the anharmonic refinement. The poor resolution for oxygen atoms in x-rays could explain some of the remaining electron density and holes. The interesting features in the harmonic refinement would mean that the remaining electron density once the average cubic positions are accounted for involve the B-site having other potential positions in the {111} direction and to a lesser extent, the {110} direction, while the A-site has remaining movement in the {111} direction. Since both A-site and B-site show potential displacement in the {111} direction, the most likely form this would take would be a cubic cell stretched in the {111} direction, namely a rhombohedral cell.

This could then mean that the residual electron density in the harmonic model, which is lost in the anharmonic model, potentially corresponds to to a difference between the long range order and the short range order in the BFO-KBT MPB. This is similar to that described by Glazer and Thomas in PZT [18], which would fit with the idea of nanoregions within the crystals, (consistent with relaxor

materials). This would be consistent with the rhombohedral nanoregions expected from Matsuo *et al.* [16] and the structure refined in Chapter 3. Local chemical disorder is known to result in anharmonic atomic displacements [17], which would correspond with the short range order being different from the long range order. It should be noted that it is not generally possible to discern between dynamic disorder (such as thermal effects) and static disorder (such as the nanoregions suggested) [19], so since no low temperature measurements were taken at the synchrotron, it is not possible to rule out anisotropic thermal effects rather than nanoregions as a possibility.

The residual electron density lobes in the {100} direction around the A-site correspond to a tetragonal symmetry, which was not resolved by anharmonic atomic displacement parameter refinement.

A measurement on the same sample, mounted in the same way as at the synchrotron was conducted on a Rigaku Oxford Diffraction *SuperNova* diffractometer. Analysing the data from this same 2B BFO-KBT crystal, it was found to have a higher R_{int} than most BFO-KBT crystal refinements of 10.8, but in SHELXL analysis was found to have a relatively low R_1 factor of 10.2. Since the same crystal was not able to be refined as well on the laboratory-based equipment, it seems likely that the absorption of the material is a large contributor to the difficulties in refining the material.

5.4 Summary of Single Crystal Data

The single crystal BFO-KBT x-ray diffraction refinements are summarised in Table 5.7. For the sake of brevity in the table, the measurements have been given an identifier, where: (i) is a 3A crystal, measured with the Rigaku Oxford Diffraction *Gemini R* diffractometer at room temperature, using Mo radiation. (ii) is the same crystal as (i), measured on the same machine at 100K. (iii) is a measurement of a 2B crystal, taken at beamline I15 (Diamond Light Source) using 0.2772Å wavelength radiation with an Oxford Diffraction *Atlas* detector at room temperature. (iv) uses the same crystal as (iii), but was measured using a Rigaku Oxford Diffraction *SuperNova* diffractometer.

5.5 Conclusions

Single crystal x-ray diffraction of the BFO-KBT system has not been undertaken prior to this project and is as such a novel element of this thesis. The same is true

Table 5.7: Summary of BFO-KBT single crystal data obtained through refinements in cubic $Pm\bar{3}m$ space group.

Identifier	(i)	(ii)	(iii)	(iii)	(iv)
Crystal Designation	3A	3A	2B	2B	2B
Temperature (K)	273	100	273	273	273
Refinement Program	SHELXL	SHELXL	SHELXL	JANA2006	SHELXL
Refined Parameters	5	4	4	9	4
Completeness	100% (0.8)	100% (0.6)	100% (0.8)	100% (0.8)	100% (0.7)
Redundancy	96.5	73.3	8.2	8.2	21.7
Lattice Parameters					
a (Å)	3.9698(2)	3.9534(8)	3.9648(6)	3.9648(6)	3.9671(9)
Volume	62.548(5)	61.81(2)	62.33(2)	62.33(2)	62.60(3)
(Model Quality)					
R_{Int} (%)	10.4	11.4	10.2	10.2	10.8
R1 (%)	19.44	18.85	5.63	6.13	10.21
R1(all) (%)	19.44	18.85	5.63	8.23	10.21
wR2(%)	4.31	4.07	1.54	8.28	2.56
GoF	4.73	4.27	1.03	1.12	2.35
Highest Q Peak	24.7	25.5	2.4	2.8	9.3
Deepest Hole	-6.4	-6.7	-1.6	-1.4	-3.1
Atomic Positions					
Bi/K: $x = y = z = 0$					
Isotropic thermal (Å^2)	0.030(2)	0.025(2)	0.052(2)	-	0.035(2)
$U_{11} = U_{22} = U_{33}$	-	-	-	0.045(3)	-
$d_{1111} = d_{2222} = d_{3333}$ (10^{-5})	-	-	-	0.03(4)	-
$d_{1122} = d_{2233} = d_{1133}$ (10^{-5})	-	-	-	-0.05(2)	-
Fe/Ti: $x = y = z = 0.5$					
Isotropic thermal (Å^2)	0.078(2)	0.07(2)	0.046(4)	-	0.070(9)
$U_{11} = U_{22} = U_{33}$	-	-	-	0.034(5)	-
$d_{1111} = d_{2222} = d_{3333}$ (10^{-5})	-	-	-	-0.24(8)	-
$d_{1122} = d_{2233} = d_{1133}$ (10^{-5})	-	-	-	-0.00(5)	-
O: $x = y = 0.5, z = 0$					
Isotropic thermal (Å^2)	0.09(7)	0.08(6)	0.13(3)	-	0.13(6)
$U_{11} = U_{22}$	-	-	-	0.11(2)	-
U_{33}	-	-	-	0.09(2)	-

for end member KBT crystals. These experiments have allowed for an independent verification of the structure refined in the powder chapter, utilising samples which are single crystals seen to be optically homogeneous, and allows for further refinement of the system with investigations into the residual electron density.

The refinement of a well known and well studied material such as room temperature BFO allows an initial baseline for the refinement of more complex structures to be established. It was shown in Table 5.1 that the refinements for the single crystals of BFO were consistent with the results of Megaw and Darlington [11] and the results of Fischer *et al.* [12]. The tilt parameters are derived from the atomic positions, which single crystal refinements are more sensitive to than lattice parameters, so these values provide a good confirmation of the structure at room temperature. At low temperature, most of the values also agreed with those of Fischer *et al.* [12], aside from the s parameter. The room temperate R_1 value was calculated to be 6.4, while the low temperature R_1 value was calculated to be 4.5, the low values of which are consistent with a good agreement between the model and the observed data. In addition, the residual electron densities were found to be low at low temperature, which is also consistent with this.

The refinement of unmixed KBT demonstrated some of the challenges that would be facing the refinement of BFO-KBT. Despite having a good R_{int} of 5.9%, it was found that the refinement of the model in SHELXL could only provide an R_1 of around 14%. This was found to support the powder x-ray diffraction result that KBT may itself be a mixed phase material, as the mixed phase nature of the crystal could be the source of the disparity between the model and the data. This high R_1 factor could also be a result of high absorption, like in BFO-KBT, so it would be beneficial to experiment similarly with KBT at a synchrotron.

From the refinements on the single crystals obtained in this chapter, it can be said that the structure of BFO-KBT is not simple to refine. While a part of this is likely the existence of the nanoregions found in relaxor materials [16], the synchrotron refinements show that much of this can be overcome, suggesting strongly that there is a strong component of absorption causing major problems in the study of these single crystals.

With the structure already known from powder diffraction methods in Chapter 3, the $Pm\bar{3}m$ could be used immediately. Since in this space group all of the atoms in the system are on special positions, the only refinements possible are to determine the nature of the thermal parameters.

Observation of the residual electron density after the refinements showed that

there were systematically lobes of electron density surrounding the B-site position containing a mix of iron and titanium depending on the KBT content of the crystal, and to a lesser degree also around the A-site position containing a mix of bismuth and potassium also depending on the KBT content of the crystal. Around the B-site, these were found to form an octahedral shape, while around the A-site these were found to form a cubic shape. Since the atomic positions were fixed by special positions, it was decided that to investigate these, it would be necessary to use JANA2006 to represent the thermal parameters as a 4th rank tensor anharmonic system. As a starting position for this, a similar set of values was used to Yamanaka et al [17], the residual electron density maps of which showed a similar pattern to that observed in BFO-KBT. From there, it was possible to refine the anharmonic thermal parameters for the measurements taken at the synchrotron. These refinements solved the issue of the residual electron density around the B-site.

This structure had an R_1 of 5.6%, but still showed a similar residual electron density map profile. This was able to be resolved through the use of anharmonic thermal parameters in JANA2006, as had previously been attempted with data from the laboratory based diffractometer, which showed an interesting pattern of residual electron density and holes potentially corresponding to a rhombohedral structure and a tetragonal structure. It is possible that these systematic residual electron densities around the A-site and B-site could potentially be due to a difference between the long range order and the short range order in the BFO-KBT MPB, similar to that described by Glazer and Thomas in PZT [18], which taken with the potentially rhombohedral nature of the disorder, is in agreement with the findings of Matsuo *et al.* [16] with BFO-KBT being represented as polar rhombohedral nanoregions and non-polar cubic nanoregions, though the anharmonic refinement did not remove the tetragonal residual electron density. In addition, the BFO-KBT crystals were observed through a birefringence microscope. Since this was only able to determine long range order, and the compositions for which crystals were available were dominated by the cubic phase, the birefringence observations also appeared highly cubic.

KBT powder was found in Chapter 3 to have a mix of tetragonal $P4mm$ and monoclinic $P1m1$ phases. The $P1m1$ phase was found to be 31(1)% of the diffraction profile. This should be detectable in a single crystal as though it were a multi crystal. Instead, a single $P4mm$ crystal structure was found. While the refinement of this did not yield a suitably low R1 value, this is due to absorption, as in the BFO-KBT crystals. In order to investigate the possibility of observing the other crystal structure in the KBT crystals, measurements should be carried out at

higher detector distances than was available during this thesis, so that any Bragg peaks observed would not overlap fully, preferably with a wavelength less strongly absorbed by the KBT crystal for a better refinement, such as at a synchrotron. If the monoclinic phase is still not observed even at a larger detector distance, this would imply that the phase structure is synthesis dependent. In contrast, the lower percentage of the rhombohedral phase in BFO-KBT at the composition of the crystals (15% to 25%) means that it would be unlikely that the rhombohedral phase could be resolved even with a larger detector distance.

5.6 References

Bibliography

[1] {Agilent Technologies Ltd, Yarnton, Oxfordshire, England}, 'CrysAlis PRO,' (2014).

[2] Sheldrick, G. M., *ACTA CRYSTALLOGRAPHICA SECTION A*, **64**:112 (2008).

[3] Petíček, V., Dušek, M., Palatinus, L., *ZEITSCHRIFT FUR KRISTALLOGRAPHIE*, **229**:345 (2014).

[4] Jones, G. O., *Investigation of the Structure and Phase Transitions in the Novel A-site Substituted Perovskite Series (Na1-xKx)0.5Bi0.5TiO3.*, Ph.D. thesis, University of Warwick (2001).

[5] Clark, R. C., Reid, J. S., 'The Analytical Calculation fo Absorption in Multifaceted Crystals,' .

[6] Kubel, F., Schmid, H., *ACTA CRYSTALLOGRAPHICA SECTION B-STRUCTURAL SCIENCE*, **46**:698 (1990).

[7] Bucci, J., Robertson, B. K., James, W. J., *JOURNAL OF APPLIED CRYSTALLOGRAPHY*, **5**:187 (1971).

[8] Catalan, G., Scott, J. F., *Advanced Materials*, **21**:2463 (2009).

[9] Hahn, T. (Ed.), *International tables for crystallography volume A: space-group symmetry*, (The International Union of Crystallography2005), fifth edn.

[10] Rohlíček, J., Hušák, M., *Journal of Applied Crystallography*, **40**:600 (2007).

[11] Megaw, H. D., Darlington, C. N. W., *Acta Crystallographica Section A*, **31**:161 (1975).

[12] Fischer, P., Polomska, M., Sosnowska, I., Szymanski, M., *J. Phys. C: Solid State Phys.*, **13**:1931 (1980).

[13] Otoničar, M., Škapin, S. D., Jančar, B., Ubic, R., Suvorov, D., *Journal of the American Ceramic Society*, **93**:4168 (2010).

[14] Wefring, E. T., Morozov, M. I., Einarsrud, M. A., Grande, T., *Journal of the American Ceramic Society*, **97**:2928 (2014).

[15] Ozaki, T., Matsuo, H., Noguchi, Y., Miyayama, M., Mori, S., *Japanese Journal of Applied Physics*, **49**:09MC05 (2010).

[16] Matsuo, H., Noguchi, Y., Miyayama, M., Suzuki, M., Watanabe, A., Sasabe, S., Mori, S., Torii, S., Kamiyama, T., **104103**:1 (2011).

[17] Yamanaka, T., Ahart, M., Nakamoto, Y., Ye, Z.-g., Gramsch, S. A., Mao, H.-k., Hemley, R. J., **174108**:1 (2012).

[18] Glazer, A. M., Thomas, P. A., Baba-Kishi, K. Z., Pang, G. K. H., Tai, C. W., *Physical Review B - Condensed Matter and Materials Physics*, **70**:1 (2004).

[19] Boysen, H., in 'Accuracy in Powder Diffraction II,' (165–175) (1992).

Chapter 6

Conclusions

6.1 BFO-KBT Conclusions

Conclusions on the nature of the BFO-KBT system from this thesis must be discussed with reference to the phase diagram, which provides context for all other discussions of the system. From there, the results of the powder diffraction and single crystal diffraction will be discussed.

6.1.1 Phase Diagram

Figure 6.1 shows the phase diagrams constructed as a part of this thesis, both at room temperature (Figure 6.1b) and with respect to temperature (Figure 6.1c), compared with the phase diagram constructed from the literature (Figure 6.1a). As was noted when these phase diagrams were introduced, there are no sharp transitions, so the lines are where one model becomes a better description of the system than another rather than a phase transition. It can be seen that the phase diagram constructed for the BFO-KBT system from the data obtained in Chapter 3 and Chapter 4 is more complicated than the expected phase diagram from Chapter 1, with all samples aside from the BFO end member represented by multiple phases, including the KBT end member, which was found in Chapter 3 to not have a purely tetragonal structure as was previously reported [8], but was instead found to be formed of a mix of tetragonal $P4mm$ and monoclinic $P1m1$ phases.

The phases found within the phase diagram were rhombohedral ($R3c$), cubic ($Pm\bar{3}m$), monoclinic ($P1m1$) and tetragonal ($P4mm$), where both the cubic and monoclinic phases were considered to be an effect of long range order only and not necessarily an accurate representation of the short range order. The room temperature phases present varied with composition: At low mol% KBT, up to 60%

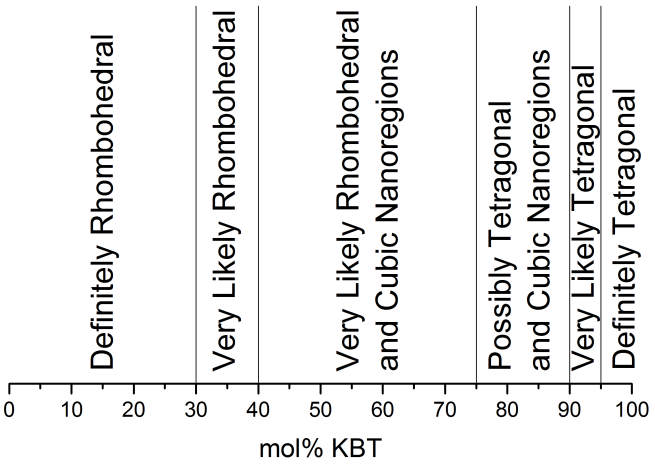

(a) Phase diagram from literature sources.

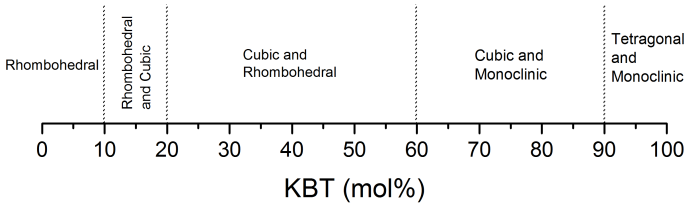

(b) new phase diagram at room temperature

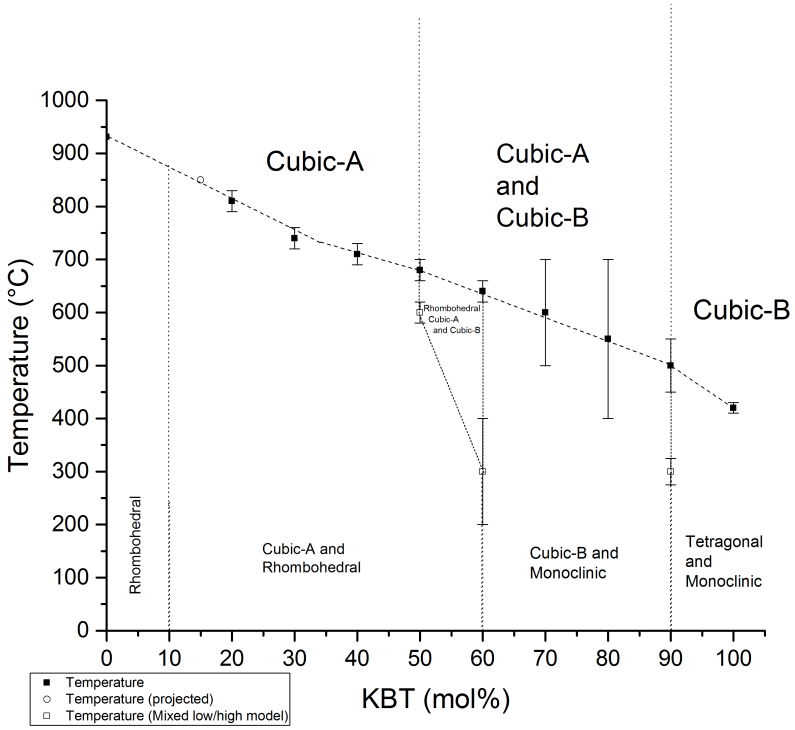

(c) new phase diagram including high temperature measurements.

Figure 6.1: Comparison of the phase diagram constructed from the literature (Figure 6.1a) in Chapter 1 [1, 2, 3, 4, 5, 6] with the phase diagrams proposed from the diffraction measurements in this thesis for room temperature KBT (Chapter 3) and over a temperature range (Chapter 4), with BFO end member cubic transition included [7].

KBT, the room temperature phases found were a mix of cubic and rhombohedral phases, with the phase percentage of rhombohedral decreasing with increasing mol% KBT. The balance of evidence suggests that 70% KBT and 80% KBT are a mix of monoclinic and cubic phases, and this is the conclusion that has been reached in this thesis, given the slightly improved fit, the lack of evidence to strongly suggest any other phase and the fact that a monoclinic phase is certainly found at higher mol% KBT compositions, seen in Figure 6.1c (it can however still be argued that correct phase structure could be a tetragonal and cubic mixed phase or a two-cubic mixed phase, given the small change in fitting by using these instead). 90% KBT and the KBT end member were found to be a mix of monoclinic and tetragonal phases; this was unexpected for the KBT end member, as previous research had indicated a tetragonal phase only. This is discussed further in Section 3.4.1.

MPBs have been reported at 40% KBT [3], 75% KBT [5] and 94% KBT [2], which places one in each of the major regions identified, but there are no sharp transitions from one structure to another and there is significant phase coexistence. The existence of the monoclinic phase in the BFO-KBT phase diagram and the mixed phase at all points are not found in any other reported experiments.

The composition-temperature phase diagram shown in Figure 6.1c shows the expected cubic phase for low mol% KBT and the KBT end member at high temperatures. The BFO-KBT mixed oxide system can be seen from the phase diagram to be very stable with respect to composition and temperature. An unexpected phase separation was found for high temperature BFO-KBT between 50% KBT and 90% KBT, with a two-cubic mixed phase present. These cubic phases were named Cubic-A and Cubic-B. Cubic-A was found to be more BFO-like, in lattice parameters and composition, while Cubic-B was found to be more KBT-like in lattice parameters and composition, which is consistent with a phase separation in the material. This process was reversible, and further room temperature measurements were back to their prior form, aside from small changes from volatilised material becoming part of the impurity phase, which was noted to be true for all samples post-heating. In the low mol% KBT samples, this caused the room temperature phase to be more cubic post-heating. Observing the lattice parameters as a function of temperature, it was found that the room temperature cubic phases are consistent with Cubic-B peaks. It should be noted that the line between the cubic and non-cubic phases with respect to temperature is not a sharp phase transition, but rather the point at which the other mixed phases are not required to model the data. The compositions of Cubic-A and Cubic-B were refined by their occupancy, and it was found that their compositions were dominated by

BFO and KBT, respectively.

Comparing the temperature at which this ending of the non-cubic mixed phase region with the phase diagram of Bennett *et al.* [9], who use the temperature of maximum permittivity to calculate T_C, the results presented here give a structural change to a cubic phase several hundred °C higher on average. Using this temperature as an analogue to T_C is not suitable for relaxor ferroelectrics, and so these results may not be inconsistent.

6.1.2 Powder X-ray Diffraction

In order to build on the existing powder x-ray diffraction experiments in the literature, powder diffraction with a high resolution powder diffractometer was utilised. This allowed a thorough investigation of the phases present in the BFO-KBT system, including their associated transitions by careful analysis of their Bragg peak intensities, splittings and asymmetry, both with respect to composition and with respect to temperature. In order to extract this data, extensive use of Rietveld analysis (conducted in TOPAS ACADEMIC [10]) was used, which provides a significantly more analytical approach than the powder x-ray diffraction measurements of BFO-KBT in the literature, which rely on visual inspection; these two factors allowed different phases to be observed in all BFO-KBT compositions. Up until this, the only reported Rietveld refinement was of the neutron powder diffraction data of Bennett *et al.* [1].

It was found that the lattice parameters of the rhombohedral phase were quite stable with respect to composition. Volume increased at a constant rate with respect to temperature, until at high temperature where the rate of increase dropped. This is consistent with a second order phase transition from rhombohedral to cubic, but further testing would be extremely difficult with the low phase fraction at the point where this occurs.

All compositions formed some form of cubic structure at high temperature, though it was found that almost all of the room temperature structures were quite stable with respect to temperature, most (aside from the 60% KBT and 70% KBT) persisting to around 500°C with little change before becoming significantly more cubic, meaning that the multiphase structure of BFO-KBT is very stable with respect to temperature. The cubic lattice parameters decreased with increasing mol% KBT, both at room temperature and relative to different compositions at high temperature.

The monoclinic cells were found to decrease in volume with increasing mol% KBT at room temperature. At high temperature, the monoclinic phases are less well

defined than other phases, but do still tend to decrease in volume with increasing mol% KBT.

The tetragonal phase is only found in the 90% KBT sample and KBT end member, but the tetragonal cell representing them still decreases in volume with increasing mol% KBT at room temperature, and generally also does so at high temperature.

A very rough estimate of a linear plot of the cubic volume vs. temperature from Figure 4.22f (at high temperature, so that both are represented by a single phase) gives $y_{bfo} = 0.0022(1)x + 62.35(4)$ and $y_{kbt} = 0.0012(4)x + 61.37(4)$. From this, the difference in gradient between the BFO and the KBT can be seen to be large; the BFO gradient is around 1.5 to 2 times higher than the gradient of the KBT. This would result in increasing strain as the sample is heated and the unit cells expand at different rates. Given the small changes in the rhombohedral lattice parameters with respect to composition shown in Figure 3.12, it seems it is easier to deform the KBT lattice to match the BFO lattice than the reverse. This would explain why when the compositions equalise or become dominated with the KBT, the phase shows separation at high temperatures into the two-cubic mixed phase model, which can result from strain [11]. This would mean that the system is under considerable strain, an idea reinforced by the necessity of Stephens parameters in the refinements. If that is the case, the strain would likely vary as a function of composition. Since the 50% KBT to 90% KBT samples exhibit a two-cubic mixed phase at high temperature, indicating a phase separation which would lower the remaining strain, the maximum strain would be found in the 40% KBT system, which still forms a single cubic phase at high temperature. Intrinsic strain is known to enhance the piezoelectric properties of materials exhibiting an MPB [12], which would then explain the enhanced piezoelectric properties observed by others at 40% KBT [3], and may also mean that the high temperature phase separation region ends in the region of 94% KBT where a local peak in the piezoelectric coefficient was also observed [2].

The atomic positions of the cells were also determined through Rietveld refinement. It was found that for high mol% KBT, the oxygen positions in the monoclinic phase became more distorted from the octahedron with increasing mol% KBT except in the KBT end member, while the tetragonal atomic positions were roughly equivalent between the 90% KBT sample and the KBT end member, despite the change in the tetragonality. At low mol% KBT, the changes in the oxygen atom positions were tracked by the changes in the octahedron. The oxygen octahedra were investigated with respect to composition but it was found that with the low phase

percentage of the rhombohedral phase and the relative insensitivity of x-rays to oxygen atoms, the errors on most of the values were too large to extract meaningful data. When compared with neutron powder diffraction data by Bennett *et al.* [1], it was found that the values for the tilt were of a similar size for the 20% KBT powder, but with the very large errors on the higher mol% KBT powders a useful comparison was not possible.

6.1.3 Single Crystal X-ray Diffraction

To supplement this work on BFO-KBT powders, analysis of single crystals of (1-x)BFO-(x)KBT were also undertaken with samples at x = 0.32, x = 0.36 and x = 0.4 available. From Chapter 3, this compositional range was found to be dominated by the cubic phase, which would result in cubic diffraction patterns, which was consistent with the results obtained. While the R_{int} factors for data reduction in CRYSALIS PRO [13] of the single crystal x-ray experiments were found to be reasonable, with both cubic and rhombohedral symmetry below 10% (9.8% and 9.5% respectively), the R_1 factors for the refinements in SHELXL [14] were higher than acceptable, both for cubic and rhombohedral symmetry, in the range of 17-20%. Once the mixed phase nature of the powders was understood, attempts were made to represent the single crystals as a mixed phase in JANA2006 [15], but was not able to significantly improve the refinement model. A breakthrough was made by utilising different energies which were less absorbed by the sample at Diamond Light Source (Harwell Campus, Oxfordshire, UK), which overcame the absorption issues with the sample. This allowed a sample with an R_{int} of 10.2% and an R_1 of 5.6% to be refined, a significant improvement in R_1.

It was found that anharmonic atomic displacement parameters were required to model the single crystal diffraction data, with disorder along the {111} direction in particular found to be remedied with this, which is consistent with a rhombohedral distortion of a cubic cell. In addition, disorder consistent with a tetragonal distortion from a cubic cell was found along the {001} direction, but was not removed through refinement with anharmonic atomic displacement parameters.

6.2 KBT Conclusions

Results obtained indicate a multi-phase refinement is the best fit to the data, with a mix of $P4mm$ tetragonal and $P1m1$ monoclinic phases. Analysis of literature reports on KBT show little Rietveld refinement data, and what there is of it has higher residual factors than other investigated compositions in the same paper [16].

Said paper is the paper on which the accepted tetragonal cif file is based. Most other papers on KBT do not include Rietveld refinement and the small monoclinic contribution could easily be missed in a visual inspection of a 'known' tetragonal material. In addition to this, KBT shows relaxor dielectric properties, which would generally be inconsistent with a simple tetragonal structure. With all this taken into account, the proposed multiphase interpretation is plausible.

It should also be noted that with the volatility of the bismuth and potassium components, the generation of a stoichiometric KBT sample is extremely unlikely, and EDS and Wavelength Dispersive X-ray (WDS) measurements in the literature have found that KBT synthesised from stoichiometric powders can form KBT that is non-stoichiometric [17]. The general trend of the material seems to be that as the composition of the KBT gets further from the ideal stoichiometric composition, with excess bismuth or potassium, the tetragonal splitting of the peaks is decreased [18], with a decrease in the overlap between them and a lowering of the residual intensity between the peaks indicative of the monoclinic phase in KBT. The diffraction patterns of KBT formed with different methodologies are very similar, so the results gathered in this thesis are consistent with the measurements taken in the literature.

At high temperature, KBT becomes cubic. In the literature, it was claimed that the cubic phase starts at 280°C [19] and then is present as a mixed phase material with the tetragonal phase as the temperature is increased until it is a single cubic phase at 450°C. The analysis in this thesis, however, shows it to be a mix of tetragonal and monoclinic phases at room temperature, and this mixed phase structure evolves with temperature, both phases becoming more cubic with increasing temperature. It was found that the monoclinic phase could be represented by a cubic phase at 390°C, leaving a cubic and tetragonal mixed phase system. At 430 °C, system could be modelled as a single cubic phase.

6.3 Future Work

During the course of this thesis, many questions about the BFO-KBT system have been addressed, but in the process, many have also been uncovered. As the answers to these are outside of the scope of this thesis, they would require further in depth study. Three main areas have been identified; further studies into the local structure of BFO-KBT, which was identified as being different to the long range structure observed; further research into the phase diagram itself, with more sensitive steps around regions where the system changes more rapidly and extending

the temperature range to lower temperatures; and further studies into the BFO-KBT system with a view towards device applications, including discussing doping BFO-KBT with other materials to improve the properties.

6.3.1 Local Structure of BFO-KBT

It was found very likely that the local structure of the BFO-KBT system was not the same as the long range order observed in the powder x-ray diffraction and single crystal x-ray diffraction measurements, and as a relaxor material it is very likely that it contains nanoregions.

TEM and SAED measurements of the low KBT end of the BFO-KBT system by Matsuo *et al.* [3] indicated that these nanoregions consisted of polar rhombohedral nanoregions and non polar cubic nanoregions [4]. It would be interesting to investigate the nature of the system at higher mol% KBT compositions, such as 70 % KBT and 80% KBT, to determine the state of the nanoregions that result in the mixed phase long range order. While SAED measurements have been made on KBT samples by Otoničar *et al.* [19], it would also be worth doing such an experiment with the possibility of a tetragonal-like monoclinic and tetragonal mixed phase state in mind during the analysis, as these measurements showed tetragonal twinning and it is hard to distinguish tetragonal twinning from a tetragonal-like monoclinic and tetragonal mixed phase [20].

A further way to investigate the local structure would be through a total scattering experiment, such as a pair distribution function (PDF) measurement. PDF allows refinement across different length scales, making it extremely well suited for this kind of crystallographic observation. The complexity of the system may mean that this is not a feasible option however, certainly outside of synchrotron experiments which have significantly better signal-to-noise ratios than laboratory-based systems [21].

6.3.2 Expansion of the Phase Diagram

Given that the current study only goes from room temperature to around the Curie (or Burns, since these are relaxors) temperature in the materials studied, it would be beneficial to systematically investigate the lower temperature end of the BFO-KBT phase diagram; especially since it is known that in some similar materials (PZT for example [22, 23]), lower temperatures exhibit lower symmetry structures. Given that the system already has some monoclinic elements, it would be interesting to see whether these appear at other compositional ratios at low temperature. It would

be especially interesting to observe whether the 70% KBT - 80% KBT region has more definition at lower temperature, as those phases are poorly defined at room temperature.

It would also be interesting to further investigate the areas of the phase diagram most sensitive to compositional changes, such as between 15% KBT and 20% KBT, where the diffraction pattern changes from being dominated by the rhombohedral phase to the cubic phase, or between 80% KBT and 90% KBT, where the diffraction pattern goes from a poorly defined pair of near-cubic phases to a clear monoclinic and tetragonal phase. In addition to these, investigating how much mixing is required for changes to be observed in the end member would also be interesting, between 0% KBT and 10% KBT, and between 90% KBT and 100% KBT. In each of these cases, to check the obtained composition a more sensitive method of determining the composition compared to the currently used EDS would be necessary, such as WDS.

6.3.3 BFO-KBT for Device Applications

The BFO-KBT system is extremely promising in its potential to form useful, functional materials for device applications, being a material with MPB properties and a large temperature range in which those properties are stable. It is a good candidate for doping with other materials to enhance the piezoelectric properties of the system.

One such system has already been investigated in 2013 by Bennett *et al.*, who reported the exceptionally large piezoelectric response from BFO-KBT doped with lead titanate [24]. If similar piezoelectric strains could be found when BFO-KBT is doped with lead-free materials, utilising a material with a high piezoelectric strain, it could be possible to synthesise an improved lead-free piezoelectric material. It would be interesting to test this with various lead-free ferroelectric tetragonal materials to see if such an improvement can be found with these.

If as hypothesised the phase separation is caused by the lattice mismatch resulting in strain, introducing a dopant with a lattice size between the two could maintain the highly strained single cubic phase high temperature state. At room temperature, BFO has a pseudocubic volume of 62.37Å^3, while KBT has a volume of 61.66Å^3 (tetragonal) and 61.55Å^3 (monoclinic), so volumes between 61.55Å^3 and 62.37Å^3 would be ideal. $BiScO_3$ could be a potential lead-free dopant of the BFO-KBT system. One of the values reported for its volume in a cif file is 62.15Å^3 [25]. In addition, it has already shown similar properties to BFO when doped with KBT [26], which could make it a suitable dopant, and is known to form an MPB with lead

titanate [27]. Its structure is generally reported as cubic or rhombohedral, and like BFO it tends towards a higher than ideal conductivity, so other materials may be more suitable for doping the MPB properties around 40% KBT, but for higher mol% KBT materials, with an intermediate pseudocubic volume and properties similar to BFO, it would be interesting to dope the BFO-KBT system by replacing a quantity of BFO with $BiScO_3$.

Given the known issues of bismuth and potassium volatility, examined in KBT by Sung *et al.* [28] and Wicheanrat *et al.* [18], investigating the effects of doping KBT and BFO-KBT with excess reagents to alter the resultant synthesised powder bismuth and potassium content, it would be interesting to combine such a study with EDS and WDS techniques to find the optimum starting materials with which to produce truly stoichiometric BFO-KBT samples, and also to determine whether non-stoichiometric or stoichiometric BFO-KBT samples exhibit the strongest dielectric and piezoelectric effects.

In addition to these proposed doping experiments, it would be interesting to compare the structures discerned through high resolution powder x-ray diffraction with the dielectric and piezoelectric properties of the material, which can then be compared with the dielectric and piezoelectric measurements reported by Bennett *et al.* [1] and Morozov *et al.* [5].We are currently working on a paper comparing these properties, with a further paper with explicit focus on the high temperature observations also planned.

6.4 References

Bibliography

[1] Bennett, J., Bell, A., Stevenson, T., Smith, R., Sterianou, I., Reaney, I., Comyn, T., *Materials Letters*, **94**:172 (2013).

[2] Kim, J. M., Sung, Y. S., Cho, J. H., Song, T. K., Kim, M. H., Chong, H. H., Park, T. G., Do, D., Kim, S. S., *Ferroelectrics*, **404**:88 (2010).

[3] Matsuo, H., Noguchi, Y., Miyayama, M., Suzuki, M., Watanabe, A., Sasabe, S., Mori, S., Torii, S., Kamiyama, T., **104103**:1 (2011).

[4] Ozaki, T., Matsuo, H., Noguchi, Y., Miyayama, M., Mori, S., *Japanese Journal of Applied Physics*, **49**:09MC05 (2010).

[5] Morozov, M. I., Einarsrud, M.-A., Grande, T., *Applied Physics Letters*, **101**:252904 (2012).

[6] Pushkarev, A. V., Olekhnovich, N. M., Radyush, Y. V., *Inorganic Materials*, **47**:774 (2011).

[7] Catalan, G., Scott, J. F., *Advanced Materials*, **21**:2463 (2009).

[8] Kreisel, J., Glazer, A. M., Jones, G., Thomas, P. A., Abello, L., Lucazeau, G., *Journal of Physics: Condensed Matter*, **12**:3267 (2000).

[9] Bennett, J., Shrout, T. R., Zhang, S., Owston, H. E., Stevenson, T. J., Esat, F., Bell, A. J., Comyn, T. P., *IEEE transactions on ultrasonics, ferroelectrics, and frequency control*, **62**:33 (2015).

[10] DiChristina, M., *Scientific American*, **302**:4 (2010).

[11] Pesquera, D., Barla, A., Wojcik, M., Jedryka, E., Bondino, F., Magnano, E., Nappini, S., Gutiérrez, D., Radaelli, G., Herranz, G., Sánchez, F., Fontcuberta, J., *Physical Review Applied*, **6**:034004 (2016).

[12] Fan, L., Chen, J., Ren, Y., Pan, Z., Zhang, L., Xing, X., *Physical Review Letters*, **116**:1 (2016).

[13] {Agilent Technologies Ltd, Yarnton, Oxfordshire, England}, 'CrysAlis PRO,' (2014).

[14] Sheldrick, G. M., *ACTA CRYSTALLOGRAPHICA SECTION A*, **64**:112 (2008).

[15] Petíček, V., Dušek, M., Palatinus, L., *ZEITSCHRIFT FUR KRISTALLOGRAPHIE*, **229**:345 (2014).

[16] Jones, G. O., Kreisel, J., Thomas, P. A., *Powder Diffraction*, **17** (2002).

[17] König, J., Spreitzer, M., Jančar, B., Suvorov, D., Samardžija, Z., Popovič, A., *Journal of the European Ceramic Society*, **29**:1695 (2009).

[18] Wicheanrat, C., Laowanidwatana, A., Bongkarn, T., *Integrated Ferroelectrics*, **149**:9 (2013).

[19] Otoničar, M., Škapin, S. D., Jančar, B., Ubic, R., Suvorov, D., *Journal of the American Ceramic Society*, **93**:4168 (2010).

[20] Schierholz, R., Fuess, H., *Journal of Applied Crystallography*, **45**:766 (2012).

[21] Billinge, S. J. L., in Dinnebier, R. E., Billinge, S. J. L. (Eds.), 'Powder Diffraction: Theory and Practice,' chap. 16, (Royal Society of Chemistry, Cambridge2008).

[22] Noheda, B., Gonzalo, J. A., Caballero, A., Moure, C., Cox, D. E., Shirane, G., *Ferroelectrics*, **237**:237 (2000).

[23] Noheda, B., Gonzalo, J., Cross, L., Guo, R., *Physical Review B*, **61**:8687 (2000).

[24] Bennett, J., Bell, a. J., Stevenson, T. J., Comyn, T. P., *Scripta Materialia*, **68**:491 (2013).

[25] Ghebouli, M. A., Ghebouli, B., Fatmi, M., Bouhemadou, A., *Solid State Communications*, **151**:908 (2011).

[26] Martín-Arias, L., Castro, a., Algueró, M., *Journal of Materials Science*, **47**:3729 (2012).

[27] Eitel, R. E., Randall, C. A., Shrout, T. R., Rehrig, P. W., Hackenberger, W., Park, S.-E., *Japanese Journal of Applied Physics*, **40**:5999 (2001).

[28] Sung, Y. S., Kim, J. M., Cho, J. H., Song, T. K., Kim, M. H., Chong, H. H., Park, T. G., Do, D., Kim, S. S., *Integrated Ferroelectrics*, **114**:92 (2010).